

Combustion of Alternative Fuels:
Opto-Mechanical Design and Optical
Investigation



Balazs Ihracska

School of Engineering and Material Sciences
Queen Mary University of London

Supervisors:

Professor Theodosios Korakianitis

Professor Dongsheng Wen

Professor Roy Crookes

A thesis submitted in conformity with the requirements for the degree of
Doctor of Philosophy to the University of London

Statement of originality

I, Balazs Ihracska, confirm that the research included within this thesis is my own work or that where it has been carried out in collaboration with, or supported by others, that this is duly acknowledged below and my contribution indicated. Previously published material is also acknowledged below.

I attest that I have exercised reasonable care to ensure that the work is original, and does not to the best of my knowledge break any UK law, infringe any third party's copyright or other Intellectual Property Right, or contain any confidential material.

I accept that the College has the right to use plagiarism detection software to check the electronic version of the thesis.

I confirm that this thesis has not been previously submitted for the award of a degree by this or any other university.

The copyright of this thesis rests with the author and no quotation from it or information derived from it may be published without the prior written consent of the author.

Signature:

A handwritten signature in black ink that reads "Waska Boley". The signature is written in a cursive style with a long, sweeping underline that extends to the right.

Date: 11th of February 2016

Details of collaboration and publications:

Ihracska, B., T. Korakianitis, P. Ruiz, D. R. Emberson, R. J. Crookes, A. Diez and D. Wen (2014). "Assessment of elliptic flame front propagation characteristics of iso-octane, gasoline, M85 and E85 in an optical engine." Combustion and Flame 161(3): 696-710.

Ihracska, B., D. Wen, S. Imran, D. R. Emberson, L. Maria Ruiz, R. J. Crookes and T. Korakianitis (2013). "Assessment of elliptic flame front propagation characteristics of hydrogen in an optically accessible spark ignition engine." International Journal of Hydrogen Energy 38(35): 15452-15468.

Imran, S., D. R. Emberson, **B. Ihracska**, D. S. Wen, R. J. Crookes and T. Korakianitis (2014). "Effect of pilot fuel quantity and type on performance and emissions of natural gas and hydrogen based combustion in a compression ignition engine." International Journal of Hydrogen Energy 39(10): 5163-5175.

Korakianitis, T., A. M. Namasivayam, R. J. Crookes, S. Imran, **B. Ihracska**, A. Diez and N. A. Malik "Compression-ignition engine performance and emissions in single and dual fuelling modes with sustainable fuels" (2011) Power and Energy Systems and Applications

Under review:

Ihracska, B., R. J. Crookes, P. A. Ruiz, G. Haritos, D. Montalvão, T. Korakianitis, D. Wen "Design of optical access on pressurised chambers" International Journal of Pressure Vessel and Piping

Imran, S., D. R. Emberson, A. Hussain, H. Ali, **B. Ihracska**, T. Korakianitis "Performance and specific emissions contours throughout the operating range of hydrogen-fuelled compression ignition engine with diesel and RME pilot fuels" Alexandria Engineering Journal

Abstract

There is a considerable body of work based on observations and measurements obtained from optically accessible high pressure reactors, such as piston engines and constant volume combustion chambers. However, there are still important aspects of design and relevant information regarding optical access that are missing or are insufficiently explored or not readily accessible in the existing literature. A comprehensive review of requirements for optical access to such high-pressure, high-temperature systems has been conducted. It is presented in a readily navigable format, with data and technical correlations hitherto not found in a 'user-friendly' style, along with a comparison of optical materials, relevant properties and guidelines for application.

It was found that optical materials often have sufficient mechanical strength, but that there were limiting factors of design, namely: working temperature, required electro-magnetic (EM) wave range and cyclic loading. It is especially difficult to carry out accurate design with cyclic loading as in a running engine, as the relevant data for optical materials is lacking in the literature. As a result of the significant uncertainty arising from inconsistency of design data, it is found that a safety factor is required, between two and five, depending on the probability of failure and associated risk. The opto-mechanical design process of pressure vessels is shown in detail for two real case- studies: a high-pressure steady-flow combustor

and the combustion chamber of a spark ignition engine. The latter system is then adopted and utilised for further diagnostic analysis.

Utilising the optical access, a high-speed imaging system was used to record the ignition and flame kernel formation in the internal combustion engine. A range of fuels were investigated, including gasoline, isooctane, and a few alternative renewable fuels: E85, M85, and hydrogen. The experiments were conducted at stoichiometric conditions for the liquid fuels and $\varphi = 0.67$ for hydrogen at various engine speeds and compression ratios.

A novel analysing method was proposed to process the acquired raw optical data, where ellipses, rather than conventional spheres, were fitted onto image projections of the visible light emitted by the flames. A cross-comparison of the results with the available data from the literature was also conducted. The large amount of optical data allowed the statistical evaluation of the flame area, flame speed and a flame-shape descriptor.

The image analysis showed that the ellipse fitting method provided a 50–100 % better fit and thus allowed a more accurate description of the flame propagation properties. The results indicated that gasoline and isooctane had similar flame propagation behaviour, but a significant difference was observed between these fuels and E85, M85 and hydrogen. Similarities were found between the propagation characteristics of M85 and hydrogen, showing the fastest

propagating flames among all the fuels. The statistical analysis found that the precision of the flame speed measurement and the roundness of the flames increase with the engine speed, compression ratio, and time elapsed after ignition.

.

Table of Contents

Statement of originality.....	I
Abstract	IV
Table of Contents	VII
List of Tables	XIII
Table of Figures	XV
Acknowledgements	XXII
Nomenclature.....	XXV
1 Introduction: literature review and motivation	1
1.1 Environmental issues.....	1
1.2 Optical research on flame speed measurements and flame kernel formation	5
1.2.1 Flame structure, propagation and its relation to the work done	5
1.2.2 Visualisation of initial flame kernel growth in SI engines	8
1.2.3 Flame structure analysis.....	16
1.2.4 The necessity of optical research and measurement methods	18
1.3 Design of optical access: materials; practical solutions; mechanical and optical performance.....	28

1.3.1	High temperature optical materials: mechanical, optical and chemical properties.....	28
1.3.2	Optical access on ICE	35
1.3.3	Mounting methods of optical element	46
1.3.4	Allowable or design stress in pressurised vessels and in the optical element, safety factors	51
1.3.5	Deflection and stress	53
1.3.6	Failure estimation by statistical tool, variability in strength.....	59
1.3.7	Cyclic loading	59
1.3.8	Birefringence and maximum optical path difference (OPD).....	61
1.3.9	Other design considerations	63
1.4	Research aims and objectives	64
1.4.1	Summary of flame propagation literature review	64
1.4.2	Summary of opto-mechanical design literature review.....	65
1.4.3	Aims and objectives.....	65

2	Design of optically accessible internal combustion engine and experimental setup.....	68
2.1	Design requirements	68
2.2	The engine and its general instrumentation	70
2.3	Design of the optical element	76
2.3.1	Geometric design and compression ratio	76
2.3.2	Material and determining the design stress and temperature	79
2.3.3	The design stress	86
2.3.4	Minimum required thickness	89
2.3.5	Optical power of the distorted window	93
3	Imaging system and data process.....	95
3.1	Experimental procedure.....	95
3.2	Quality of collected optical data	96
3.3	Pixel errors or optical aberrations.....	98
3.3.1	Defocus	99
3.3.2	Motion blur.....	101

3.3.3	Reflection.....	105
3.4	Repeatability.....	107
3.5	Fitting an ellipse to an arbitrarily shaped region, fitting methods, flame speed and shape factor.....	109
3.6	Determining flame speed from fitted ellipses	112
3.7	Shape factor	113
3.8	The data processing code.....	115
4	Experimental results and discussion	120
4.1	Statistical analysis.....	120
4.1.1	Sources of systematic and random error in measurements.....	120
4.1.2	Data distribution and relative standard error	121
4.2	Flame speed curves as function of fuel type and engine conditions...	126
4.2.1	Isooctane and gasoline	135
4.2.2	Alcohol blends	141
4.2.3	Hydrogen	146
4.2.4	Cross comparison of results	150

4.3	Flame shape analysis and comparison of equivalent radius and ellipse fitting methods.....	155
5	Conclusions	161
6	Future work.....	168
7	Appendices.....	170
	Appendix A.	170
	Appendix B.	174
	Appendix C.	188
	Appendix D.	189
	Appendix E.	190
	Appendix F.	191
	Appendix G.	192
	Appendix H.	194
	Appendix I.	195
	Appendix J.	196
	Appendix K.	197

Appendix L.....	198
8 Bibliography.....	199

List of Tables

Table 1. Selected fuel properties.....	14
Table 2. Summary of prior related publications.....	15
Table 3. Optical measurement methods in relation to ICE	20
Table 4. Optical material properties.....	33
Table 5, Classical mechanics of plane-parallel circular elements	53
Table 6, Classical mechanics of plane-parallel rectangular elements.....	57
Table 7. Constants for rectangular window geometries	58
Table 8. Maximum allowed OPD and deflection for windows.....	62
Table 9. Some engine data for the Briggs and Stratton engine used for the research	71
Table 10. List of measurement related devices and fuels.....	76
Table 11. Optical aberrations	99
Table 12. Summary of pixel error analysis	104

Table 13. Geometric and thermodynamic conditions in the combustion chamber at the time of spark onset 128

Table 14. Data matrix of IMEPs and the corresponding COVs for all conditions and fuels. 132

Table 15. Flame speed values calculated using the EQR method and along the major and minor axes at 1000 μ s after ToI; for an easy comparison of fuels the EQR method speed values were normalised to flames speeds values of isooctane. 133

Table 16. Flame speed values along the major and minor axes at 1000 μ s AIT; for an easy comparison of the results from different engine conditions, a normalised value is shown for each result and condition..... 134

Table 17. Summary of flame speed, EQR, values for cross-discussion purposes 152

Table of Figures

Figure 1. Global production of oil, gas and coal over time, within the 2°C-limit scenario, separated by different kinds of oil and gas, retrieved from [10]	3
Figure 2. Energy reserves and mixture of the world (a); growth of renewable energy consumption, still a relatively small portion compared to fossil fuels, retrieved from [5]	4
Figure 3. Illustration of the flame structure and temperature distribution of a flame, identifying the reaction and preheat zones (the image was taken at 1200 rpm, compression ratio: 5.00, with isooctane)	6
Figure 4. Spherical propagation assumption and prediction. (a) and (c) spherical propagation assumption; (b) isotropic propagation predicted by combustion model.....	11
Figure 5. The OAICE used in this study with its instrumentation.....	22
Figure 6. A typical structure for a RCM used for PLIF, retrieved from [79]	23
Figure 7. A schematic drawing of an HPCF experimental rig [80-83]	24
Figure 8. The optical access for the HPCF rig shown above, the design and development of this rig was conducted by the author	25

Figure 9. A schematic of a typical set-up of a CVTR, retrieved from [85] 26

Figure 10. CVTR at the Queen Mary University of London; optical access via three circular sapphire windows (blue) 27

Figure 11. Transmittance of the reviewed optical materials; relative responsivity and wavelength of interest are also shown (for Design requirements section).. 34

Figure 12. Four stroke overhead valve engine 35

Figure 13. Fully accessible combustion chamber on a two – stroke engine..... 37

Figure 14. L-head optical ICE constructed from a Briggs and Stratton engine 38

Figure 15. Four–stroke engine equipped with a side chamber 39

Figure 16. A Bowditch type OAICE used to investigate the influence of butanol addition to gasoline, retrieved from [112] 41

Figure 17. Four-stroke engine with side access and small viewing opening fitted in the head..... 42

Figure 18. The schematic of the MIT optical engine with flat windows and a square piston, retrieved form [25] 44

Figure 19. Fixed volume combustion chamber with circular window that is positioned by a guided clamp [80]. 47

Figure 20. Four-stroke optical engine, the rectangular window is sandwiched by the clamp and soft gaskets [13, 14]. 48

Figure 21. Special sodium chloride free sitting window for a high-temperature, high pressure difference, infra-red (IR) spectra [121] 48

Figure 22. a, Using adhesives for a low pressure application [122]; b, Using adhesives for a moderate pressure application [123]. 49

Figure 23. Window integrated in the vessel body, O-ring and tapered methods [124, 125]..... 50

Figure 24. Optically accessible engine setup for liquid fuels 70

Figure 25. Optically accessible engine setup for hydrogen fuel 70

Figure 26. Valve timing diagram of the modified Briggs and Stratton engine..... 73

Figure 27. Section and top views of combustion chamber with fitted ellipse to the flame front..... 74

Figure 28. An isometric view of the lowest clearance volume achievable with the chosen window geometry; larger clearance volumes were achievable by the means of spacers placed under the window..... 79

Figure 29. A typical pressure curve of in-cylinder pressure measurement as function of crank position (0° is start of inlet), high load setup CR: 8.14 at 1500 rpm with gasoline fuel, ignition time 20° BTDC 81

Figure 30. Cooling air flow around and inside the modified research engine (engine block and impeller not shown)..... 83

Figure 31. Temperature distribution in the middle plane of the window parallel to side b, CR:8.14 at 1500 rpm 83

Figure 32. Temperature distribution of the outer surfaces of the window..... 84

Figure 33. CFD simulation results: maximum temperature found (discrete data points) in the window as a function of engine speed; trend line was also added 85

Figure 34. Design stress as a function of the operating temperature of selected materials 86

Figure 35. Failure stress at a number of cycles for glass on a linear and a logarithmic scale, experimental data adapted from [150] 89

Figure 36. FEA deflection result for an $a \times b - tck$ rectangular window, maximum distortion occurred in the centre 93

Figure 37. Noise distribution on a recorded image..... 98

Figure 38. Nozzle and spray, (a) blurred image with low SNR, (b) sharp image with good sharpness and contrast edge detection possible, retrieved from [189]... 102

Figure 39. Noise and blurring of a M85 flame at CR: 8.14, 1500 rpm; image was taken 402 μ s after ignition. 105

Figure 40. Major axis length distribution of the first data point - 67 μ s – for M85 at 1500 rpm and CR:8.14..... 106

Figure 41. Spark core and light reflected from the bottom of the combustion chamber, image was processed for better visibility 107

Figure 42. Repeatability validation; flame area measured at different recording condition with the same fuel and same engine conditions; LMS AVE: least mean square average 108

Figure 43. Flow chart of the analysing computer code..... 115

Figure 44. A typical histogram of pixel values on recorded raw image 117

Figure 45. Sample .png binarised image, E85 at CR: 5.00 and 1500 rpm, this image is the 9th in the series after spark onset..... 118

Figure 46. Sample data distribution, in this case for M85, 1200 rpm, CR = 5.00, 804 μ s, **St = 804 = 5.9 \pm 0.15m/s** 121

Figure 47. RSE in calculated flame speed along the major axis at selected CRs and engine speeds for a, isooctane b, gasoline c, E85 d, M85 e, Hydrogen 125

Figure 48. Apparent flame speed and roundness values of a spark discharging at 1500 rpm and CR: 8.14 in a non-combustible charge (air, plasma was considered to be flame) 130

Figure 49. Instantaneous flame speed and roundness curves of isooctane and gasoline at different engine conditions; a, CR: 5.00 engine speed: 1200 rpm; b, CR: 5.00 engine speed: 1500 rpm; c, CR: 8.14 engine speed: 1200 rpm; d, CR: 8.14 engine speed: 1500 rpm..... 138

Figure 50. Instantaneous flame speed and roundness curves of E85 and E85 at different engine conditions; a, CR: 5.00 engine speed: 1200 rpm; b, CR: 5.00 engine speed: 1500 rpm; c, CR: 8.14 engine speed: 1200 rpm; d, CR: 8.14 engine speed: 1500 rpm..... 144

Figure 51. Instantaneous flame speed and roundness curves of hydrogen at different engine conditions; a, CR: 5.00 engine speed: 1200 rpm; b, CR: 5.00 engine speed: 1500 rpm; c, CR: 8.14 engine speed: 1200 rpm; d, CR: 8.14 engine speed: 1500 rpm..... 149

Figure 52. Development of a hydrogen flame kernel at 1500 rpm and CR: 8.14 with fitted ellipses and circles; fit ratios are also shown 156

Figure 53. Sample flame images a, isooctane, conditions: 1200 rpm and CR = 5.00
b, gasoline conditions: 1500 rpm and CR = 5.00 157

Acknowledgements

There are a large number of people who had an important effect on my career that eventually led to the completion of this work. I first want to express my gratitude to my family – my parents; Sandor Ihracska and Sandorne Ihracska, for their patience, love and constant support during my hectic teenage years and early education, and my brother, Andras Ihracska, for helping me learn the basics of science and engineering. Our many fruitful conversations of manufacturing and engines shaped my research immensely. I am also grateful to my cousin, Peter Revai, for the countless advice and help given on computer and electronic related problems.

This work would not have reached completion without my wife Paula Ruiz's support. Paula's advice, guidance and encouragement were absolutely vital in the earlier stages of my research. During these years, she also gave birth to our wonderful twins, Tina and Alexis, and took good care of them when I had to concentrate on my work. The three of them provided me the strength to keep going during the toughest times.

I am especially grateful to my personal tutor Ms Szilva Danyi. She provided me with a great amount of help and taught me to enjoy maths and physics. Her direct influence got me interested in research and academia.

I believe I would not have become a practicing engineer without the help of my first boss, Mr Pal Romhanyi. He took me on as a trainee mechanical engineer and taught me during my first years of working education. An equal amount of gratitude goes to the Head of Engineering, Mr Janos Ozsvart. I shared a room with Janos for three years and in those times, learnt more about engineering than I ever have since. Every single drawing or calculation of mine has been influenced in some way by these two excellent engineers.

I have had the privilege to work alongside some exceptional people at Queen Mary University of London (QMUL). My sincere appreciation goes to the technician team at QMUL, for without their assistance, it would have been impossible to complete my research. I am especially grateful to Mr Vince Ford and Mr Anthony Otten, for their endless patience and explanations when I was constantly breaking tools on the lathes or milling machines.

I would like to thank the management of the Engineering department at QMUL, in particular, the school manager Ms Jayne Hawkins and my ex-line manager Mr Chris Straw. They supported me and allowed me to start my part-time postgraduate education.

Finally, I would like to thank my supervisors, Professor Theodosios Alexander, Professor Crookes and Professor Dongsheng Wen for their patient guidance,

encouragement and advice. I hope they found me worthy of their attention and I am looking forward to more shared projects.

Nomenclature

Latin

A	area
a	distance
A_L	laminar flame front area
A_T	turbulent flame front area
B	arbitrary region
b	distance
BLR	image blur
C_V	isochoric specific heat capacity
d	infinitesimal difference operator
D_0	aperture
D_3	three dimensional fractal dimension
d_a	semi axial length
D_F	Feret's diameter
E	Young's modulus
f	arbitrary function
FOV	size of field of view
K_I	stress intensity factor
K_{IC}	critical stress intensity factor
K_w	constant
K_x	constant
L	integral length scale
LHV	lower heating value
m	mass
M	moment of a two dimensional region
m_w	Weibull modulus
n	refractive index
n_{cr}	constant
no	number
O	parameter

OPD	optical path difference
p	pressure
P_{lens}	optical power of a lens
Q_{ht}	heat transfer to walls
r	radius
R	deflection radius
R_m	tensile strength
RNS	roundness
$R_{p0.2/t}$	0.2% proof strength
S	average flame speed
SA	semi axes of an ellipse
Sf	shape factor
SF	safety factor
S_n	flame speed
T	T temperature
t	time
t_{ck}	thickness
t_{ex}	exposure time
U	central moment
u_n	turbulent burning velocity
V	volume
V_c	clearance volume
v_{cr}	crack propagation rate
V_d	displacement or swept volume
v_g	gas expansion velocity
V_0	constant
v_{part}	fluid or object velocity
\bar{x}	x centroid
x	deflection
\bar{y}	y centroid

Subscripts

b	finite difference operator
bdg	axis orientation angle
des	efficiency
l, p, w	q density
maj	summation operator
max	maximum
min	minor or minimum
pix	pixel
vol	volumetric
x,y,z	Cartesian coordinates

Greek

Δ	finite difference operator
ε	axis orientation angle
η	efficiency
ρ	q density
Σ	summation operator
σ	stress
σ_0	specific stress level

Acronyms and abbreviations

BTDC	before top dead centre
CA	crank angle
CFD	computational fluid dynamics
CH	clearance height
CMOS	complementary metal-oxide semiconductor
COV	coefficient of variance
CR	compression ratio
CVTR	constant volume test rig
D	dimension
EM	electro magnetic
Eol	end of imaging period
EQR	equivalent radius
EVC	exhaust valve closes
EVO	exhaust valve opens
FAR	normalised fuel to air ratio
FEA	finite element analysis
FRc	fit ratio for circle
FR _e	fit ratio for ellipse
HC	hydrocarbon
HICE	hydrogen fuelled internal combustion engine
HPCF	high pressure constant flow rig
ICE	internal combustion engine
IMEP	indicated mean effective pressure
IR	infra red
IVC	intake valve closes
IVO	intake valve opens
NIR	near infrared
OAICE	optically accessible internal combustion engine

RCM	rapid compression chamber
rpm	revolutions per minute
RSE	relative standard error
RSE	relative standard error
SAFS	spherical assumption flame speed
SI	spark ignition
SNR	signal to noise ratio
TAI	time after ignition
TDC	top dead centre
Tol	time of ignition
UV	ultra violet

1 Introduction: literature review and motivation

1.1 Environmental issues

Over the past two decades, the issues with our hydrocarbon-based economy and its effects on climate change and human life have been well-documented. Growing concern about global warming and the depletion of the ozone layer has driven researchers to find better alternatives to meet the high energy consumption demand [1-8]. Recently, the Intergovernmental Panel on Climate Change published a Summary for Policymakers, and reported that cumulative emissions of carbon dioxide were the main driving factor behind the average global surface warming, and suggested a rigorous scenario that aims to keep global warming below a 2°C rise in the average global temperature in comparison to the temperature in the pre-industrial era [9]. At present, there is a contradiction in policymakers' position with regards to the increased unconventional oil production, and the suggested target of 2°C throughout the twenty-first century [10]. In order to have at least a 50% chance of meeting the 2°C target, the carbon budget between 2011 and 2050 should not exceed 1100 gigatonnes of carbon dioxide; however, current estimates of greenhouse gas emissions resulting from the use of global fossil fuel reserves are above this value by a factor of three [10]. A modelled solution to maintain the 2°C limit is shown in Figure 1. The International Energy Agency has forecasted that carbon dioxide emissions are expected to increase from 29 gigatonnes per year to 36 about under the current policies [5]. Figure 2 shows a statistical review of world

energy reserves and consumption, which demonstrates that 86 % of the world's main energy consumption is of the fossil fuel type [5].

With the combustion of fossil fuels and the subsequent production of carbon dioxide being accounted for as the main contributors to the current release of greenhouse gases into the atmosphere [11, 12], and taking into consideration that a solution to the current energy supply problems remains as yet distant, improvements in the understanding of the chemical reactions and flame-propagation processes and reduction of the emissions of these engine-fuel combinations should be implemented as a short-term solution [13, 14]. These environmental and socio-political issues are among the most motivating research drivers, providing an impetus for research into renewable energy and design-to-specification fuels. Nevertheless, both developed and developing countries still rely heavily on conventional fuels powering conventional engines [15] and it is highly probable that the internal combustion engine using liquid fuels will continue to be a relevant transportation tool over the next few decades [5]. There is still plenty of room for considerable improvement in the understanding of the chemical reactions and flame-propagation processes, reducing the emissions of these engine-fuel combinations, and increasing performance. One of the important ways to analyse combustion processes in engines is to employ three-dimensional computational fluid dynamics simulations, with the incorporation of various well-refined fuel oxidation and flame propagation mechanisms [16-18]. The models and codes need validation

with experimental work, in order to accurately describe the exact nature of these in-cylinder processes.

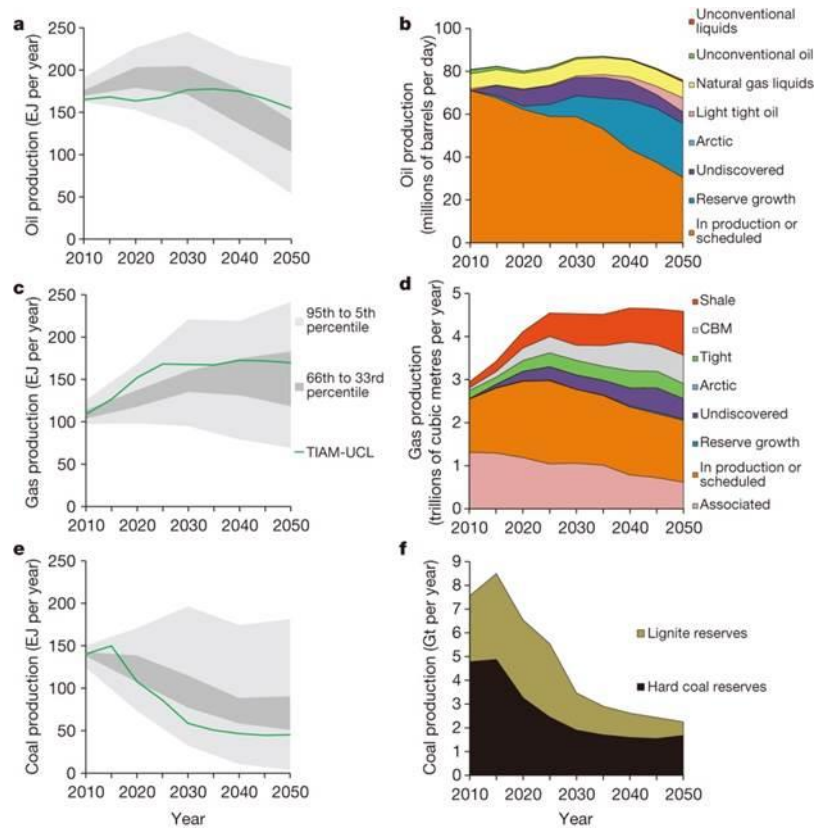


Figure 1. Global production of oil, gas and coal over time, within the 2°C-limit scenario, separated by different kinds of oil and gas, retrieved from [10]

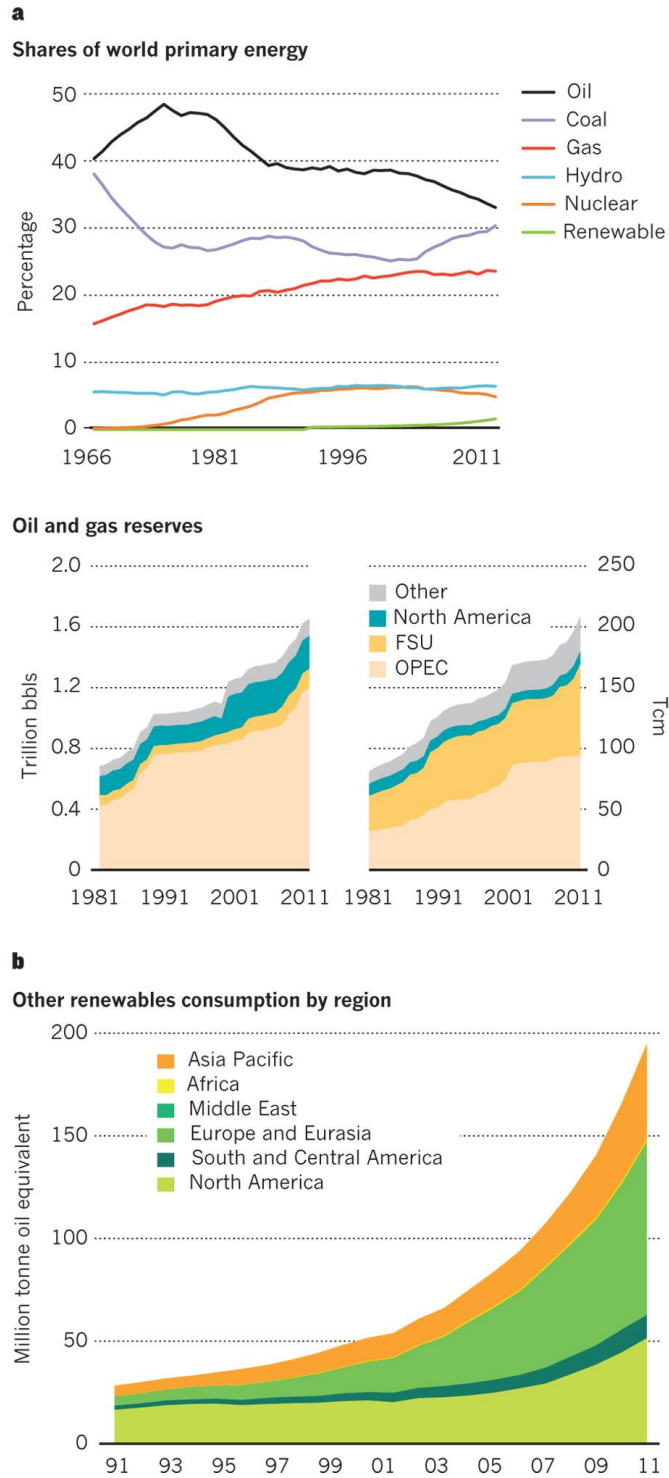


Figure 2. Energy reserves and mixture of the world (a); growth of renewable energy consumption, still a relatively small portion compared to fossil fuels, retrieved from [5]

1.2 Optical research on flame speed measurements and flame kernel formation

1.2.1 Flame structure, propagation and its relation to the work done

Although the flame is defined as the luminous part of the burning gases, caused by highly exothermic, rapid oxidation [19], for the sake of simplicity in this study, the earliest and relatively short plasma state of the glowing charge is also considered as a flame. For both moving and standing flames, the flame front is the indicator of where gases heat up and start emitting light [20, 21]. This front is considered to consist of two regions: the preheat zone and the reaction zone. For instance, Figure 3 illustrates the top view of the reaction and the preheat zone in the chamber of the optical-access engine used in this paper. The combustion process in SI engines can be divided into four main stages: spark and flame initiation; initial flame kernel development; turbulent flame propagation; and flame termination [22]. The first two stages are of high importance in terms of in-cylinder pressure development [23-27]. The four stages are influenced by: spark energy and duration [28]; spark plug design and orientation [29]; in-cylinder flow field [30]; cyclic cylinder charging [31]; in-cylinder composition [32]; and other related factors. A detailed literature survey on the effects of these parameters on the four stages of combustion is presented [26].

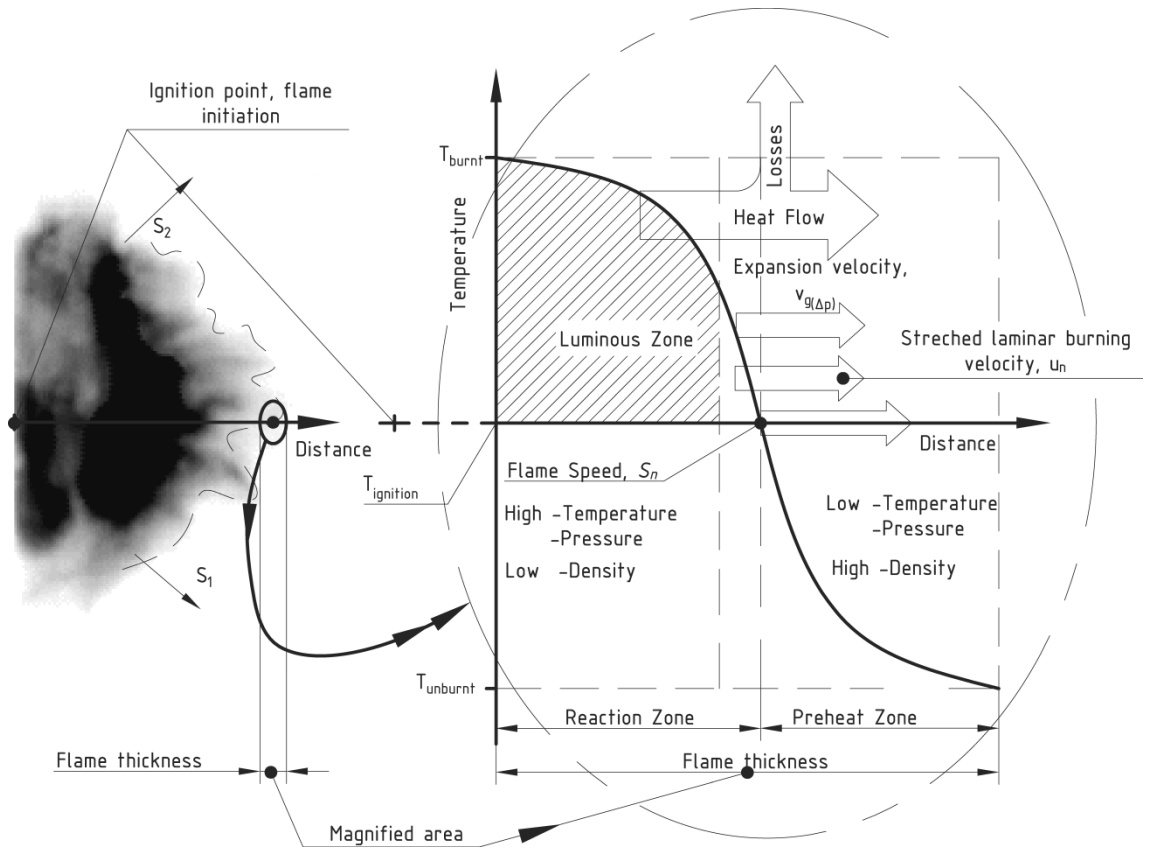


Figure 3. Illustration of the flame structure and temperature distribution of a flame, identifying the reaction and preheat zones (the image was taken at 1200 rpm, compression ratio: 5.00, with isooctane)

Turbulent flames in a spark ignition engine can be assumed to be an array of laminar flamelets with simple or non-turbulent structures, [33, 34]. The flame speed S_n is not a unique property of the given mixture but a sum of the burning and expansion velocities. The flame speed can be measured from images of the spatial-temporal development of the flame and it is given by [21, 34]

$$S_n = v_g + u_n \quad (1)$$

where, v_g is the gas expansion velocity immediately adjacent to the flame front and u_n is the burning or transformation velocity, [21]. u_n was termed as the stretched laminar burning velocity of combusting air fuel mixture by Bradley, [35].

In contrast to flame speed, the laminar burning velocity is an intrinsic property of a combustible fuel, air and burned gas mixture. That is defined as the velocity, relative to and normal to the flame front, with which unburned gas moves into the front and is transformed to products [36].

The turbulent burning velocity equals the laminar velocity with the added effect of the flow field, geometry; wrinkling of the flame front; pressure effects on flame thickness; and the history of the flame [37]. The effect of the turbulent flow field is crucial for the first and second stage of combustion. It has been demonstrated that the smallest flame kernels are distorted shortly after ignition [38].

Turbulent burning velocity plays a prime role and directly effects the in-cylinder pressure development, i.e., engine performance. Turbulent burning velocity and laminar burning velocity are important physical properties of fuel air mixtures. It is essential that both of these velocities are derived experimentally from flame speed and in-cylinder pressure measurements [21, 22, 24, 34]. The work produced by an engine is related to the flame speed as can be inferred from the following. The burned mass of charge is given by

$$m_{b(t)} = (\bar{S}_x \bar{S}_y \bar{S}_z)_{(t)} \rho_{b(t)} S_{f(t)} \quad (2)$$

where, \bar{S}_x , \bar{S}_y and \bar{S}_z are the average flame speeds in the x ; y ; z directions. These can be determined by dividing the flame radius along an axis by the elapsed time from ignition. S_f is a shape specific function. The burning of fuel releases energy to the working fluid in the cylinder, given by [21, 36, 39]:

$$m_b LHV - (mc_V dT) - \Sigma h_i dm_i - dQ_{ht} = pdV \quad (3)$$

The rate of burning of the air–fuel mixture affects the chemical energy change of the fluid, and this directly affects the indicated work and power output. In Equation (3) the work done on the piston pdV equals the energy released from the burning fuel $m_b LHV$, minus the energy required to heat up the charge $mc_V dT$, minus the heat transfer to walls dQ_{ht} , and adjusted by the masses leaving or entering the chamber $\Sigma h_i dm_i$. Note: term $\Sigma h_i dm_i$ can be positive (during fuel injection) or negative (flow to crevice volumes or blow by). Therefore engine performance is highly dependent on flame propagation characteristics within the cylinder.

1.2.2 Visualisation of initial flame kernel growth in SI engines

Previous engine research images of flames in cylinders showed a significant enflamed volume, but the pressure measurements were not accurate or sensitive

enough to indicate the evolving flame kernels [25, 32]. Therefore, optical investigation of combustion is preferred to pressure tracing at the early combustion stages.

The practical realisation of visual access to a combustion chamber of a working piston engine is not easy, with any of the visible, ultra violet spectra or laser radiation approaches [40-44]. The fluctuating pressure at high temperature, the limited strength of transparent materials and the geometrical constrains kept investigators from studying optical engines at real working conditions. In most cases, the engine speed and CR were kept low in order to observe the propagating flames. In previous investigations, the effect of changing engine speeds and equivalence ratios were studied. However, because of the tight cylinder geometries, there has been no optical data recorded in the same engine at different compression ratios. Another major difficulty is the time scale of rapid oxidation. The average of temporal resolution that can be found in the literature is about 0.2–0.4 ms. Only one paper included data at higher temporal resolution, which could potentially provide insight to the earliest and faintest flames [45]. It has also been reported that fouling of the optical ports limits the length of operation time [29]. The experimental conditions and a general summary of the most relevant work on flame speed measurements and other investigations in optical engines can be found in Table 2. A comprehensive review of experimental investigation techniques used in reciprocating-piston engines is presented in [46].

It has been shown that combustion or combustion related measurements taken in any internal combustion engines would have a relatively large standard deviation and therefore low precision. This is caused by a number of processes which are both global and local, low- and high-dimensional; these include the air-fuel mixture, turbulent flow field, and combustion instability variations. The high level of uncertainty introduced by these phenomena in the thermal efficiency – and thus in the engine performance – is called cycle-by-cycle variation or cyclic variation. Cycle-by-cycle variation in engines is a widely studied phenomenon [26, 29, 47, 48].

It has been proved that the position and shape of the flame kernel and flame speed significantly affect cycle-by-cycle variation and thus the overall engine performance, [25, 40, 47]. However, previous studies have assumed that the propagation of spark-initiated oxidation is isotropic, i.e. spherical flame propagation [25, 27, 29, 32, 38, 45, 49-58], i.e. isotropic propagation was assumed. Beretta [32] investigated flame propagation and used circles to calculate the flame speed, as seen in Figure 4 (a). As indicated in Figure 4 (b), isotropic propagation was predicted by a combustion model applied by Rakopoulos [16] on hydrogen combustion. The three images indicate three different moments before top dead centre as shown. Keck [25] investigated cycle-by-cycle variation, and concluded that the flame shape has a significant effect; but the measurements and evaluation was carried out by using circles, as shown in Figure 4 (c).

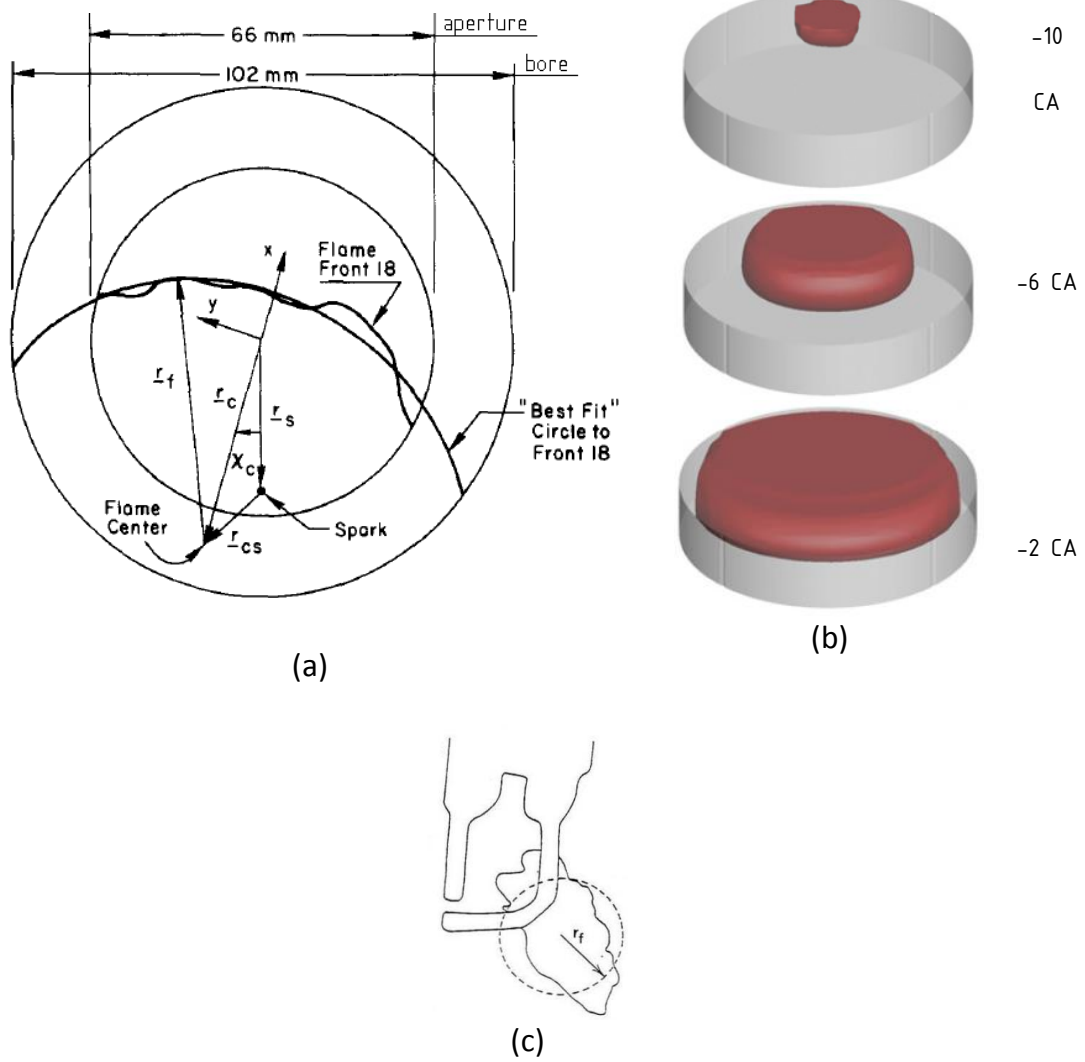


Figure 4. Spherical propagation assumption and prediction. (a) and (c) spherical propagation assumption; (b) isotropic propagation predicted by combustion model

Only a few studies have mentioned different flame-front geometries [24, 25, 51, 54] or looked into the implications arising from the assumption that the flame front surface has a spherical geometry. However, these shapes have not been described mathematically and detailed analyses have not been carried out. No attempt has

been made to check the spherical propagation assumption. Thus, a validation of this accepted method is required.

There is notably little data available on the properties of in-cylinder flame propagation and combustion rate, and even less work has been published examining such flames using alternative fuel types (alcohols, their mixtures, and hydrogen). Moreover, the work so far done targets fully developed flames, little attention has been paid to flame kernel development and propagation. However, these data are essential for engine-combustion modellers, for validation purposes [59, 60] and to enhance the understanding of the fundamental mechanisms governing real-life engine combustion. Even though the in-cylinder flame front is a three-dimensional flame, in most studies flame-speed measurements are measured from two-dimensional projections of the images. Applying the isotropic propagation assumption, the two-dimensional projected contours of spherical flames can be digitised and their various geometrical properties determined. Actual flame speeds and flame shapes were measured in a small number of studies, where the flame radii were calculated using the “equivalent radius” (EQR) method [25, 27, 29, 38, 45, 51, 52, 58, 61, 62] which determines the radius from the measured area:

$$r = \sqrt{\frac{A}{\pi}} \quad (4)$$

where r is the flame radius and A is the area of the projected region. There has been no attempt to refine this assumption. Many of the early investigators (who established the fundamentals of optical engine work) used hand tracing methods, due to limitations of available tools to delineate the boundaries and/or had low number of samples (3–6 measurements averaged) [30]. Later papers do have a larger number of measurements, but the statistical distribution of their findings was not documented [63].

In previous studies with optical-access engines, the main choice of fuels was pure hydrocarbons (HC) such as propane and isooctane. Less attention was paid to practical fuels such as gasoline and alcohol blends. It is a usual practice to use isooctane as a surrogate of gasoline in engine-related research purposes as these two fuels have similar physical properties. Moreover, gasoline is a mixture of hydrocarbons with a composition that is not guaranteed, whereas isooctane is an easily available pure chemical. Previous flame-propagation studies in optical engines did not compare flame propagation characteristics of gasoline and isooctane to verify that the two fuels behaved in a similar fashion. Alcohols and blends with gasoline (or isooctane) have been used in piston engines since the engine itself was invented. At present, bio-alcohols are among the proposed candidates for future fuels. Many studies have investigated their emission and performance qualities [7, 61, 64-66], but the literature is lacking the relevant optical, engine data. Usually each published study concentrates on one engine geometry (e.g. one compression ratio)

and one fuel. There is very little optical data available on comparison of different fuels in the same engine operating conditions. Table 1 lists some of properties of the fuels tested in these engines, [17, 36, 67-70]. Laminar burning velocity is a function of pressure, temperature and the air fuel ratio (A/F). In Table 1 the data corresponds to 100 kPa of pressure at 298 K but instead of choosing a fixed A/F for each fuel, the maximum values are shown. These maximum values occur at different A/F ratios but typically for slightly rich mixtures.

Table 1. Selected fuel properties

	Formula	Molecular weight	Density	Lower heating value	Stoic. A/F ratio	Max. laminar burning velocity	Flammability limits in air	
	-	(g)	(kg/m ³)	(MJ/kg)	(kg/kg)	(m/s)	(V %)	
							lower	upper
Gasoline (approx.)	$C_nH_{1.87n}$	110	720-780	44.2	14.60	-	1.0	8.0
Isooctane	C_8H_{18}	114.23	692	44.3	15.13	0.34	1.1	6.0
Ethanol	C_2H_6O	46.07	785	26.9	9.00	0.41	3.3	19.0
Methanol	CH_4O	32.04	792	20.0	6.47	0.44	6.0	36.0
E85	$C_nH_{2.88n}O$	56.29	771	29.6	9.92	-	3.0	17.1
M85	$C_nH_{3.74n}O$	44.37	777	23.6	7.77	-	5.3	31.5
Hydrogen	H_2	2.02	0.08	120.0	34.20	2.90	4.0	75.0

Table 2. Summary of prior related publications

Research ID		Imaging details			Engine conditions			
		Method description	Frame rate (frame/s)	Speed (rpm)	Fuel	FAR	CR	
Rashidi	[48]	Luminous	H.sp. c. images	2000	1096	Isooctane	1.08	-
Berreta	[32]	Luminous	H.sp imaging, hand traced, NaCl seeding	5000	872, 1233	Isooctane	1.13-1.08	7.86
Heywood	[49]	Schlieren	Each picture is from different cycle	1380	1380	Propane, hydrogen	1.00	7.00
Gatowski	[50]	Schlieren	H.sp. c. images	2000	740,1400	Propane	0.90	5.75
zur Loye	[38]	Luminous	Laser scattering, TiO ₂ , ZrO ₂ seeding	-	300-3000	Propane	1.00 0.50	8.00
Keck	[25]	Schlieren	H.sp. c. images, Hand traced	2000	1400	Propane	0.87	5.75
Pischinger	[27]	Schlieren	H.sp. c. images	25000	1400	Propane	1.00 0.77 0.71	6.70
Bates	[24]	Luminous	Multi exposure in one frame	30	500, 1000	Propane	0.75	9.10
Nakamura	[54]	Luminous	H.sp. c. images	10000	1500	Gasoline	1.00	9.30
Herweg	[53]	Schlieren	Images from different cycles	Flash light, pulse 40 ns	800-2000	Propane	0.77	7.30
Bates	[23]	Luminous	Multi exposure in one frame	30	500, 1000	Isooctane	0.75	9.10
Shen	[45]	Schlieren	H.sp. c. images, Hand traced	20000	500, 1000	Isooctane	1.00 0.91	7.70
Aleiferis	[29]	Luminous	Double-exposed images	25	1500	Isooctane	0.68	7.90
Aleiferis	[58]	Luminous	Double-exposed images	25	1500	Isooctane	0.68, 1.00	7.90
Lee	[57]	Laser deflection and Schlieren	A comparison between the 2 methods	3000	1200, 1500, 1800	Liquefied petroleum gas		10.00

Conte	[55]	Optical and ion sensors	Mapping (no image processing)	-	2000	Gasoline and gas mixtures	1.00	8.70
Gerke	[56]	OH-chemi.	H.sp. imaging	10000	Comp. machine	Hydrogen	0.36-2.50	(5-45 bar)
Tahtouh	[63]	Luminous	H.sp. imaging	6000	1200, 2000	Isooctane, methane	1.00, 0.80	9.50
Baritaud	[52]	Schlieren	H.sp. c. images, Hand traced	6000	50, 1040	Propane	0.65, 0.85	6.00
Tagalian	[51]	Schlieren	5 cycles	1400	1400	Propane	0.90	-
Aleiferis	[61]	Shadowg.	H.sp. c. images, 100 cycles	9000	1500	E85, gasoline	1.00	11.15
Aleiferis	[62]	Chemi.	H.sp. c. images, 100 cycles	9000	1500	Alcohols, other HCs	1.00	11.15
Herweg	[71]	Luminous	Side chamber	-	300, 500, 750, 1000, 1250,	Propane	1.00, 0.77, 0.67	7.30

H.sp. c., high speed consecutive

1.2.3 Flame structure analysis

Databases of in-cylinder turbulent flame characteristics and flame front propagation rates are essential for further understanding of combustion fundamentals. This study covers the evaluation of the isotropic propagation assumption and contribution to the flame speed database for flame kernels of conventional and alternative fuels. However, additional measurements would be required to see a more complete picture. In order to describe and understand the turbulent behaviour of the flame, the level of wrinkling and flame front distortion needs to be measured with respect to the integral length scales and flow-field properties. This can be done by means of laser-light based optical velocimetry methods (Laser Doppler Velocimetry or Particulate Image Velocimetry). The author had no means to carry out these tests

during this research. However, the combustion propagation rate data collected and presented in this work contributes to the combustion database and verifies the finding of others. Moreover, it supports the work of modellers.

The first step to model in-cylinder flames (i.e. turbulent combustion) is to consider turbulence. Three different approaches to turbulence modelling include: direct numerical simulation, Reynolds-averaged Navier-Stokes and large eddy simulation. All of these approaches are accepted, and certain studies have compared their advantages and shortcomings [72, 73]. Large eddy simulation works well for non-reacting flows and seems to be the favoured method to model premixed turbulent flames. However, the chemical kinetics is confined in a thin reaction zone, Figure 3, and this zone is typically difficult to get resolved. This problem can be dealt with an assumption where the turbulent flame speed is considered to be equal to the laminar flame speed corrected for the stretch and flame wrinkling. In one of the interesting methods considering flame wrinkling, the wrinkling is assumed to have a self-similar geometry. Then, the surface area of the wrinkled – turbulent – flame front can be calculated as follows:

$$A_T = \left(\frac{L_{max}}{L_{min}} \right)^{D_3-2} A_L \quad (5)$$

where, A_T is the area of the turbulent flame front, A_L is the laminar flame front, L is the integral length scale and D_3 is the fractal dimension in the three-dimensional space [74-76].

The aim of this work was not detailed combustion analysis and investigation of the underlying fundamentals, but to measure and compare the overall characteristics of flame kernels for various fuels at the spark-assisted stage. However, the aforementioned short introduction and references cited provide a bridge between the experimental work presented here and the more theoretical side of combustion science.

1.2.4 The necessity of optical research and measurement methods

A major advantage of optical engine instrumentation is its fast response. In general, EM waves travel at the speed of light and sensors recording them have a high response rate - which is crucial when fast combustion related processes are investigated. ICEs have been developed significantly in the past few decades as a result of active research. It is known that a significant mass fraction of air-fuel mixture burns before any pressure rise or temperature change can be detected [36]. It has also been shown that the properties of the evolving flame kernel at the earliest stages of ignition have a major effect on the in-cylinder combustion processes [24].

One of the main processes that play an important role in the working of an ICE is the fluid flow. Volumetric efficiency, in-cylinder charge motion, residual gas content and

so on have a fundamental effect on every aspect of the performance of an ICE. These flows have been studied by using optical methods, visualising the flow field or pressure boundaries. These methods provide vital information and cannot be replaced by any other instrumentation.

Other areas of engine research where visualisation is important are:

- injection, spray and mixture development
- flame propagation and combustion
- pollutant formation studies

There are a number of optical methods that can be used to investigate the processes listed above. It is not the aim of this study to detail and describe these rather complex measuring techniques. In order to provide an overview, a comprehensive list of these methods is shown in Table 3. A couple of exhaustive review books have been published on the background and findings of the relevant measurement techniques [46, 77].

Table 3. Optical measurement methods in relation to ICE

Engine process	Measurement type	Technique
Fluid flow		Laser Doppler Anemometry (LDA)
		Particle Image Velocimetry (PIV)
Injection, spray and mixture development	Droplet sizing and atomization	Direct back lit imaging
		Fraunhofer diffraction
		Phase Doppler Particle Analyser (PDPA)
		Two-dimensional visualisation by Mie scattering
		Laser sheet droplet sizing by Mie scattering
		Laser-Induced Exciplex Fluorescence (LIEF)
	Fuel vapour concentration	Planar Laser-Induced Fluorescence (PLIF)
		Laser Rayleigh Scattering (LRS)
	Mixture composition	Spontaneous Raman Scattering (SRS)
Flame propagation and combustion	Mixture composition	Spontaneous Raman Scattering (SRS)
	Visualisation of combustion species	Planar Laser-Induced Fluorescence (PLIF)
	Flame geometric properties and speed	Spectroscopy: Light Emission and absorption
		Chemiluminescence: optical emission from the oxidation process (this technique was chosen for the flame analysis in this work)
		Chemiluminescence: optical emission from the oxidation process enhanced by emission from additives
		Schlieren method and shadowgraphy
	Temperature measurement	Radiation thermometry
		Laser Rayleigh Scattering (LRS)
		Spontaneous Raman Scattering (SRS)
		Coherent Anti-Stokes Raman Scattering (CARS)
		Planar Laser-Induced Fluorescence (PLIF)
Pollutant formation	Soot concentration and temperature	Two-colour method
	Soot concentration	Light-extinction
	Soot distribution and size measurement	Laser-induced incandescence

These techniques can be applied on a number of different optical rigs that are able to provide insight into the combustion process. A more detailed review of the different experimental procedures, and a comparison among them, can be found in the literature, [78] Results acquired from optically accessible internal combustion engines (OAICE) provide the closest simulation to the in-cylinder processes in real engines, Figure 5. On the other hand, the combustion chamber of a real engine is surrounded by all the necessary auxiliaries (cooling, mechanisms, injection and ignition systems), making the physical realisation of the access to be a complex task.

When the investigation focuses on a particular aspect of an in-cylinder process and a larger access is required, then some of the aforementioned auxiliaries can be removed to provide the required space. This way the OAIC becomes a rapid compression machine (RCM), as illustrated in Figure 6. RCMs are not heat engines anymore; it is not possible to maintain the cycles of ICE strokes by them. Usually, the power stroke is tested only with a RCM with thermal convection, mixture distribution and flow characteristics that are dissimilar to the ones found in production engines. However, the better access to these processes in time and space provides an opportunity to take more accurate measurements.

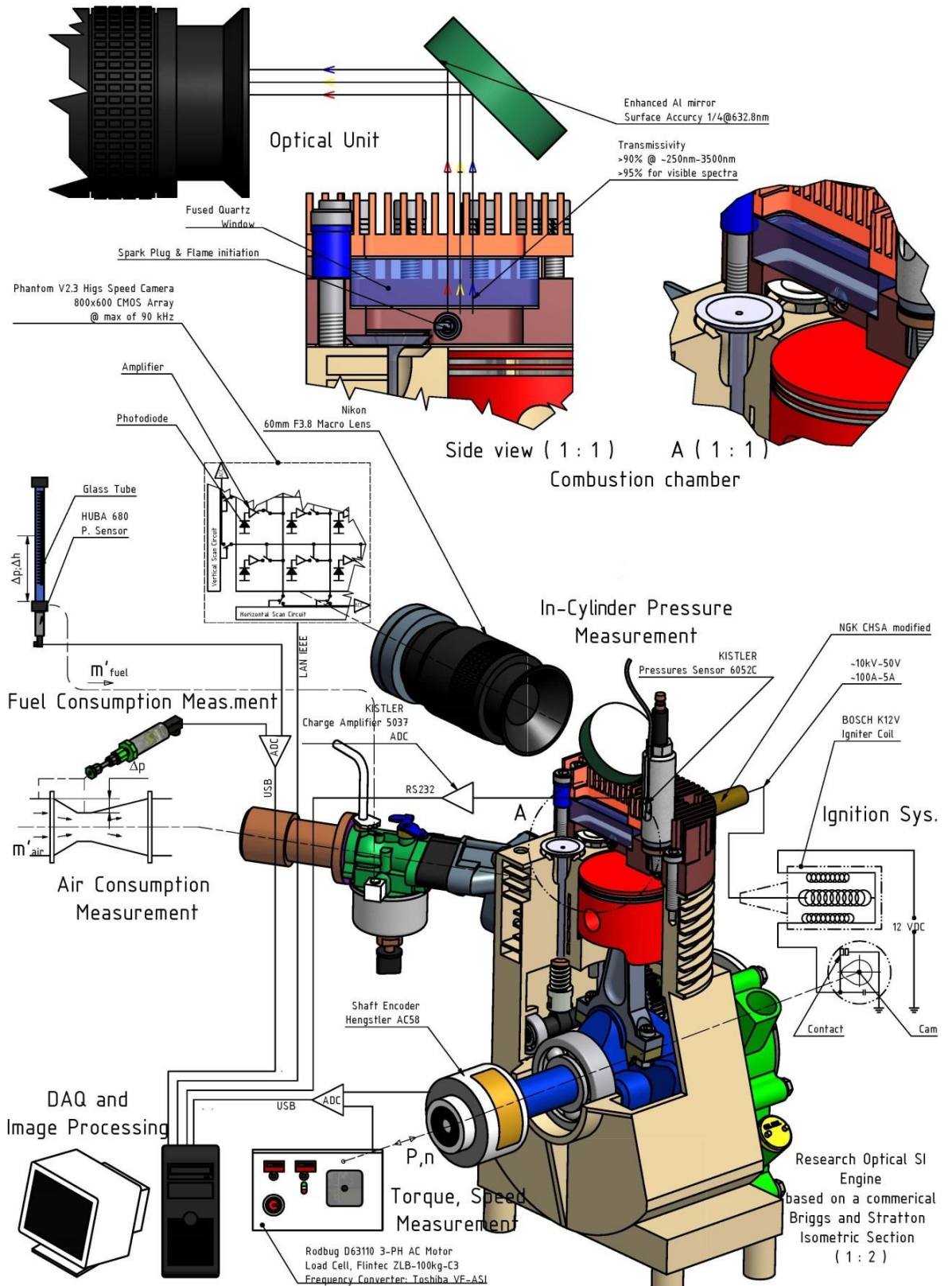


Figure 5. The OAICE used in this study with its instrumentation

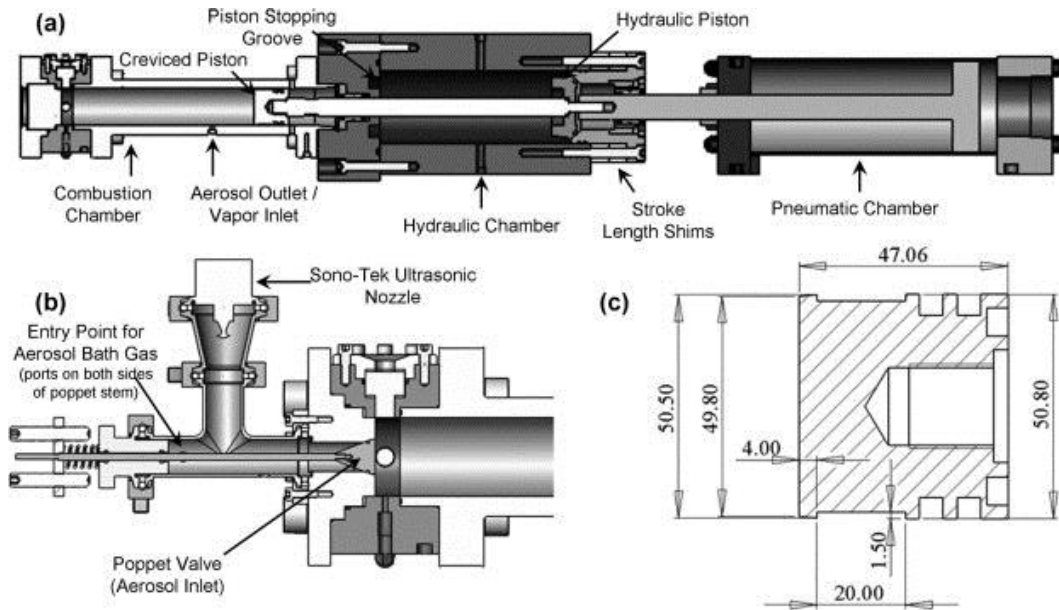


Figure 6. A typical structure for a RCM used for PLIF, retrieved from [79]

High pressure constant flow devices (HPCF) were developed to model and test the working of industrial furnaces, external and internal combustion engines and gas turbines, Figure 7. These rigs can accept virtually any combustible substance with a high accuracy of air-fuel ratio and a control of residence time. Moreover, the internal flow pattern can be set to the specific requirements. HPCF experiments usually acquire data for emission, fuel spray and soot formation related studies. The flames are usually accessed by probes and by optical instrumentation. The illustrated rig was developed by the author, and a summary of this design process is presented in Appendix A. The findings and details of that design work will be published, as was detailed in the Statement of Originality section. The actual optical access for this HPCF rig is shown in detail in Figure 8.

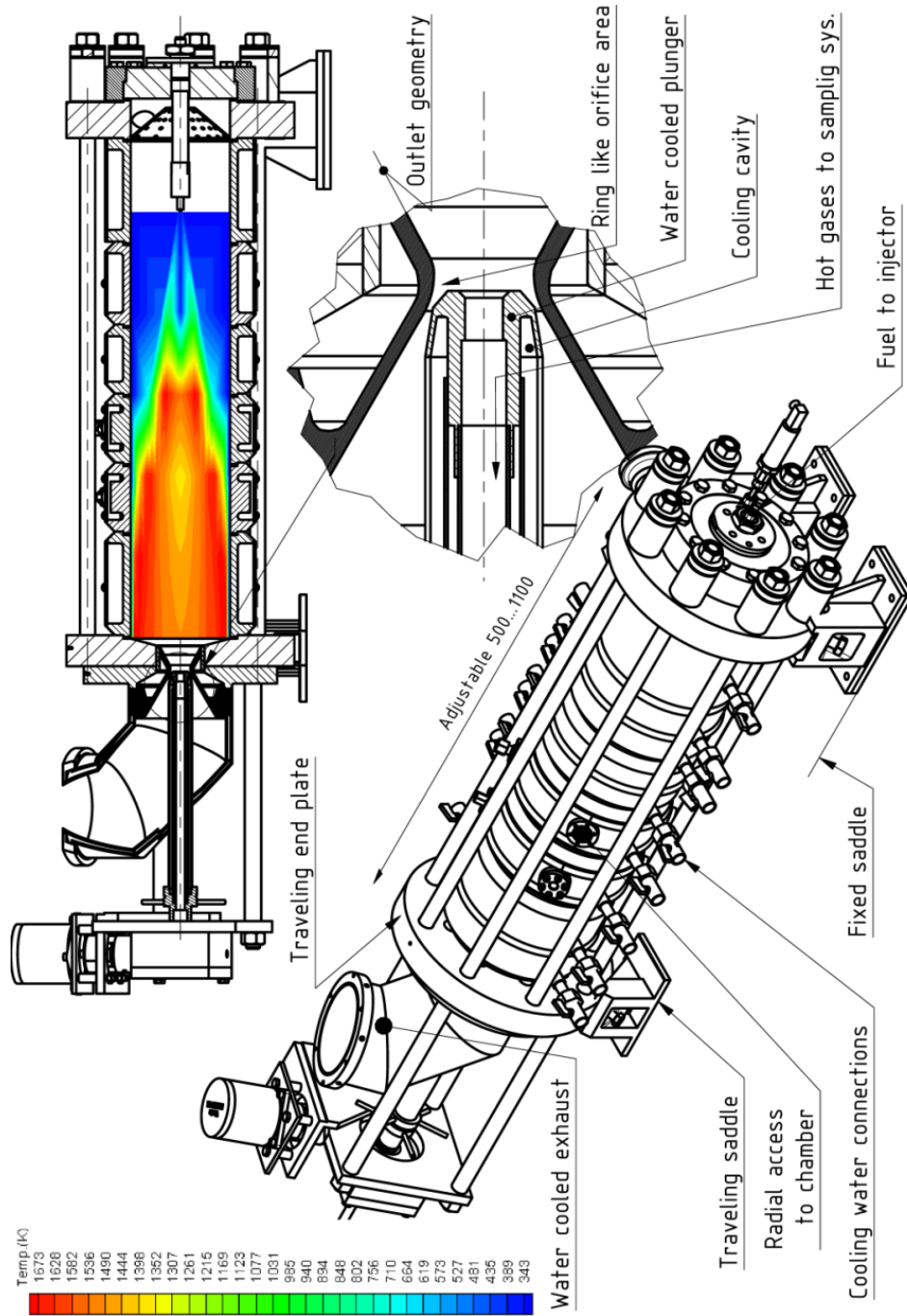


Figure 7. A schematic drawing of an HPCF experimental rig [80-83]

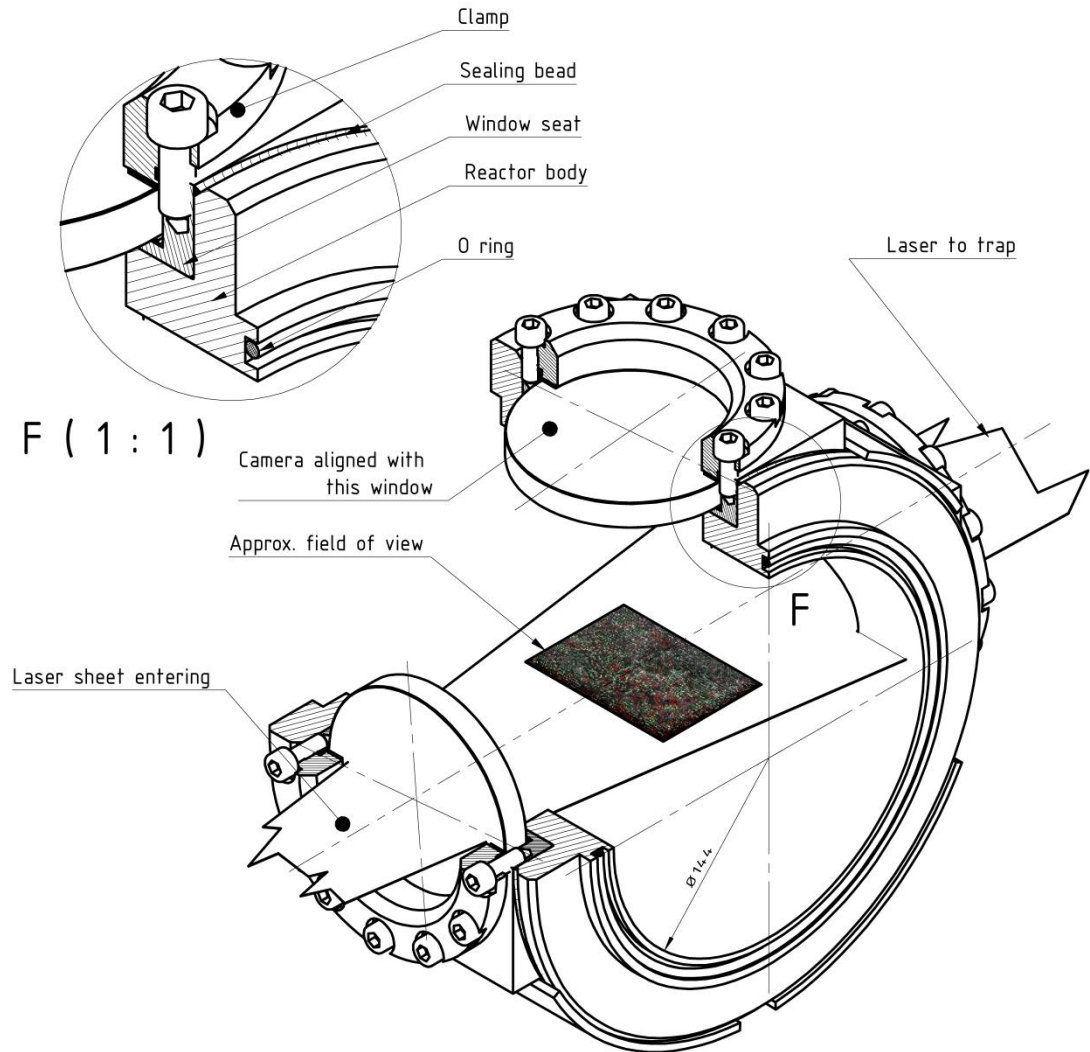


Figure 8. The optical access for the HPCF rig shown above, the design and development of this rig was conducted by the author

The constant volume test rig (CVTR) was used to support similar research as the HPCF test cells. They are extensively used to determine laminar and turbulent burning velocity; a large number of studies were published based on the data collected from CVTRs. The author also contributed to the design of an optical CVTR, Figure 10. The

research carried out on this rig was led by Emberson and investigated a number of aspects of the spray formation of diesel, bio-diesel and emulsion fuels [84].

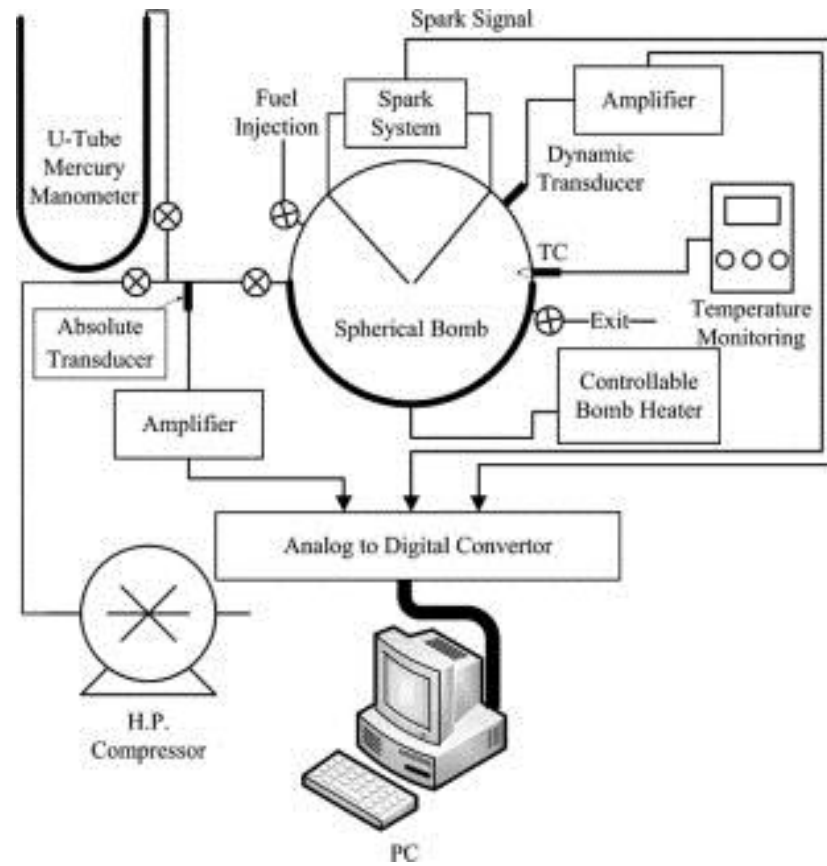


Figure 9. A schematic of a typical set-up of a CVTR, retrieved from [85]

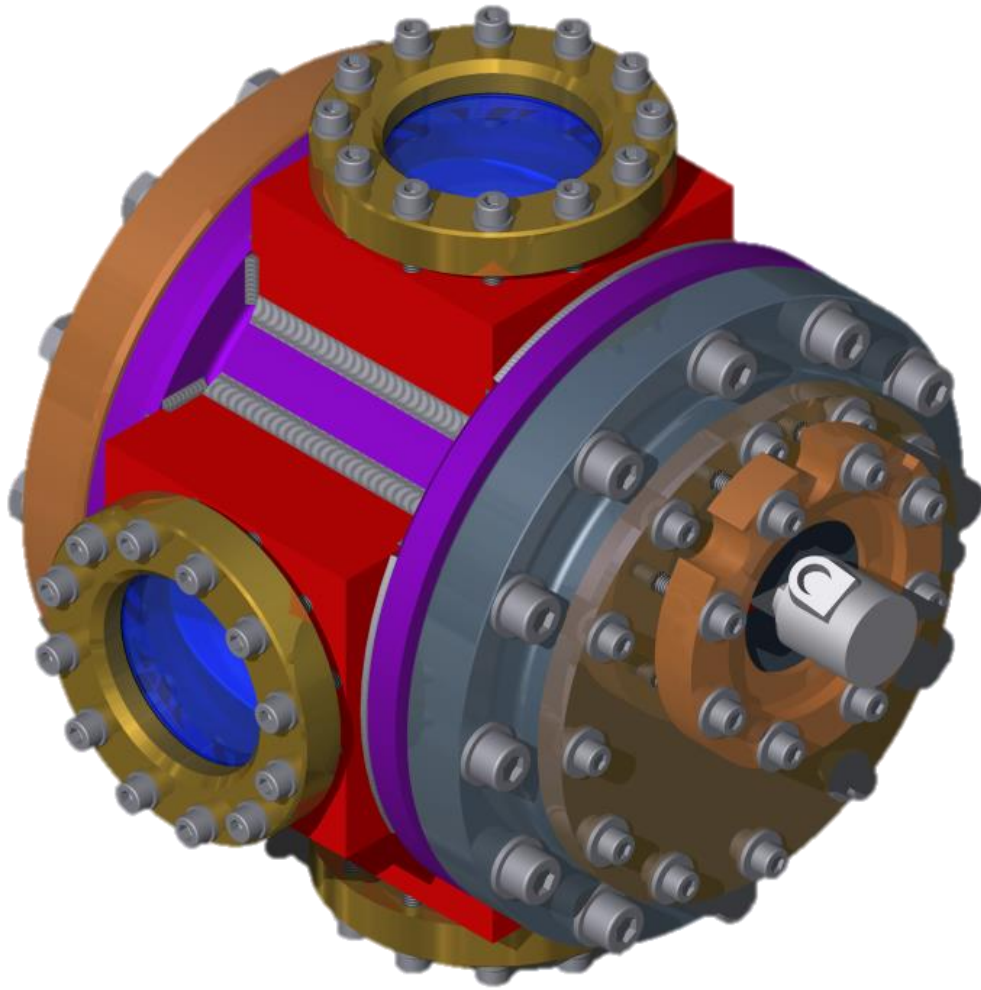


Figure 10. CVTR at the Queen Mary University of London; optical access via three circular sapphire windows (blue)

1.3 Design of optical access: materials; practical solutions; mechanical and optical performance

1.3.1 High temperature optical materials: mechanical, optical and chemical properties

There are a large number of materials that can be considered for sight windows on pressure vessels, from ordinary plastics to exotic ceramics. In this work, only the most common and most practical optical materials, which are suitable for high temperature operation, were chosen for comparison.

The underlying design criteria for selecting the optimal optical material type are: useful transmittance range, operating temperature and mechanical load. In Table 4, only high-operating-temperature materials are listed. It is important to note there are other choices available for specialised tasks, such as silicon or germanium, but their availability is limited and they are costlier. In low-temperature environments, plastics like acrylic and polycarbonate can be used. During design, it is essential to consider the working temperature and obtain a good estimate of it from simulations or experiments.

Although unusual in mechanical engineering, it is important to choose the right material for the required electromagnetic band. It is also vital to consider the ratio of the electromagnetic energy falling on a body to that transmitted through it. This ratio is called the transmittance of the material [86]. Transmittance values for each

wavelength vary significantly among material. For example, a larger selection of materials can be considered if the investigated radiation is in the visible or in the near infra-red (NIR) regions. Due to the availability of a wider range of materials, the implication is that sight windows for high speed imaging or laser-aided measurements can be designed more easily, and more complex shapes with larger dimensions are therefore possible. Choosing an optimal material is more complex when longer wavelengths have to be captured for both spectroscopy and thermal imaging. For wavelengths over 2500 nm, the transmittance curves start fluctuating or becoming discontinuous. If this, then, is the electromagnetic wave band region of interest, careful planning will be needed to select the right material type. The transmittance of common optical materials for wavelengths under 200-250 nm falls rapidly. Yet, it is an important region in combustion science as some radicals have their peak emissivity in this electromagnetic band. Researchers and designers are practically left with fused silica and a number of fluorides (MgF_2 , CaF_2 , BaF_2) to use. Figure 11 shows the transmittance curves of selected materials.

Once the material candidates are shortlisted by wavelength transmittance, the more conventional design process follows this when further mechanical, thermal and chemical resistance properties are of interest.

Finally, the cost analysis needs to be taken into account when the material type providing the optimal solution is chosen.

Table 4 summarises some of the most related properties of a selection of practical optical materials. As expected, all of the listed properties are functions of temperature, size and shape, exact composition, heat treatment, surface finish, and other manufacturing processes. It is important to note that there are significant differences (10-15%) between the claimed values by different manufacturers and textbooks.

Soda lime glass is the common glass type that can be found everywhere. It is mass-manufactured by floating the hot raw material on a bed of molten tin. It is the least expensive material of all, and being softer than other glasses, it is easy to make a complex part out of it. It is a hard material with good scratch resistance, but is significantly softer than other glasses or sapphire. It is not resistant to many chemicals, and its higher coefficient of expansion makes it sensitive to uneven temperature distribution [87-91].

Borosilicate glass is 2-3 times more expensive than soda lime glass but still considerably less expensive than fused quartz or silica. It has the same easy manufacturing properties as soda lime but usually has a lower thermal expansion coefficient, hence making it more resistant to thermal shock. Leaching can occur but it is more resistant to chemicals [87-90, 92, 93].

Fused quartz and silica have very similar properties as they have an almost identical composition. The main difference between them is in the amount of contamination

caused by the different manufacturing processes. Quartz is made from melted and cleansed naturally occurring quartz sand with larger amount of contamination in the product, while fused silica is a pure version of quartz synthesised from various gases. However, their mechanical and electrical properties are identical. The only contrasting (and significant) advantage is that, silica has an excellent transmittance in the ultra violet (UV) region. This property makes it unique among silicon oxides. A major advantage of quartz and silica, when compared to cheaper glasses, is their increased stability. Their mechanical properties are significantly less sensitive to temperature changes than borosilicate or float glasses. For instance, for a borosilicate, the linear thermal expansion at 500 °C increases its ambient value a few hundred times; silica, however, faces an increase of about 40 times and then stays constant with further increase of the temperature. This makes the evaluation of thermal stresses a lot easier when implementing quartz and silica. Nevertheless, their excellent properties come at a price: the material cost is significantly higher than the aforementioned glasses and their higher temperature resistance makes fabrication more complex. They have a reasonably good resistance to chemicals but break down with some caustics, fluorinated acids and plasmas [87-90, 92-95].

Sapphire is a single crystal and a very versatile material. It is the second hardest material on Earth, which makes it best choice of material whenever wear and abrasion are the main constraints. Its high mechanical strength and modulus of elasticity provides good resistance against impacts. It is virtually impervious to all

corrosive materials and its thermal stability outperforms all other optical materials. Yet, sapphire raw material is not significantly more expensive than fused silica. On the other hand, its extreme hardness and a high melting point make the manufacturing process challenging and costly. In conclusion, sapphire is not suitable for large windows and for complex shapes [96-100].

Magnesium fluoride is an excellent material choice for application in the UV bandwidth (the cheaper CaF_2 has similar properties but with slightly reduced useful transmittance range). Larger size crystals can be grown, and it is possible to machine it with standard diamond tools as this material can be polished well. Thus, complex shapes and geometries can be achieved. It has a wide range of transmissivity but it is not as wear-resistant as the other materials, and its surface will degrade in a humid environment at elevated temperatures (over 500 °C) [92, 98, 101-103].

Table 4. Optical material properties

	Unit	Soda Lime Glass	Borosilicate	Quartz	Fused Silica	Sapphire	Magnesium Fluoride
General							
Chemical Formula, Composition	(weight %)	SiO ₂ :74, Na ₂ O:15, CaO:5, others	SiO ₂ :80+, B ₂ O ₃ :7-13%, Na ₂ O, others	SiO ₂ :99	SiO ₂ :99	Al ₂ O ₃ :99	MgF ₂ :99
Density	(g/cm ³)	2.2-2.52	2.2-2.4	2.2	2.2	3.98	3.18
Optical							
Useful Transmission	(nm)	320-2300	325-2100	200-2400	180-2200	150-5000	110-7500
Refractive index (588 nm)	-	1.52	1.47	1.46	1.46	1.76	1.38
Mechanical ^I							
Young's Modulus	(GPa)	72	64	73	73	335	138
Tensile Strength	(MPa)	~41	27-62	50	50	275 ^{II}	140
Hardness, Vickers	-	550	520-580	1000-1200	1000-1200	1940	400
Poisson's ratio	-	0.23	0.21	0.17	0.17	0.25	0.27
Weibull variability of strength	-	6 ^{III}	30 ^{IV}	8.82 ^V	10.2 ^{VI}	5	5
Weibull stress	(MPa)	129 ^{III}	71 ^{IV}	115 ^V	180 ^{VI}	485	96
Thermal							
Softening Point	(°C)	1450	800-850	1730	1600	2300 ^{VII}	1255
Max. Continuous Operating Temperature	(°C)	260	280-350	950-1150	950-1100	1200	500
Thermal Conductivity at 300 K	(W/mK)	0.96	1.1-1.2	1.38	1.38	27.21	11.6
Coefficient of Expansion	(10 ⁻⁶ /K)	3.5-9	3.25-4	0.55	0.55	8.4	8.9

properties perpendicular to optical axis

materials are birefringent for exact refractive indexes see references

^I mechanical and optical properties are dependent on fabrication method and surface finish; ^{II} fractural strength; ^{III} Kimble R-6; ^{IV} BK-7; ^V standard polish; ^{VI} "super polish"; ^{VII} melting point

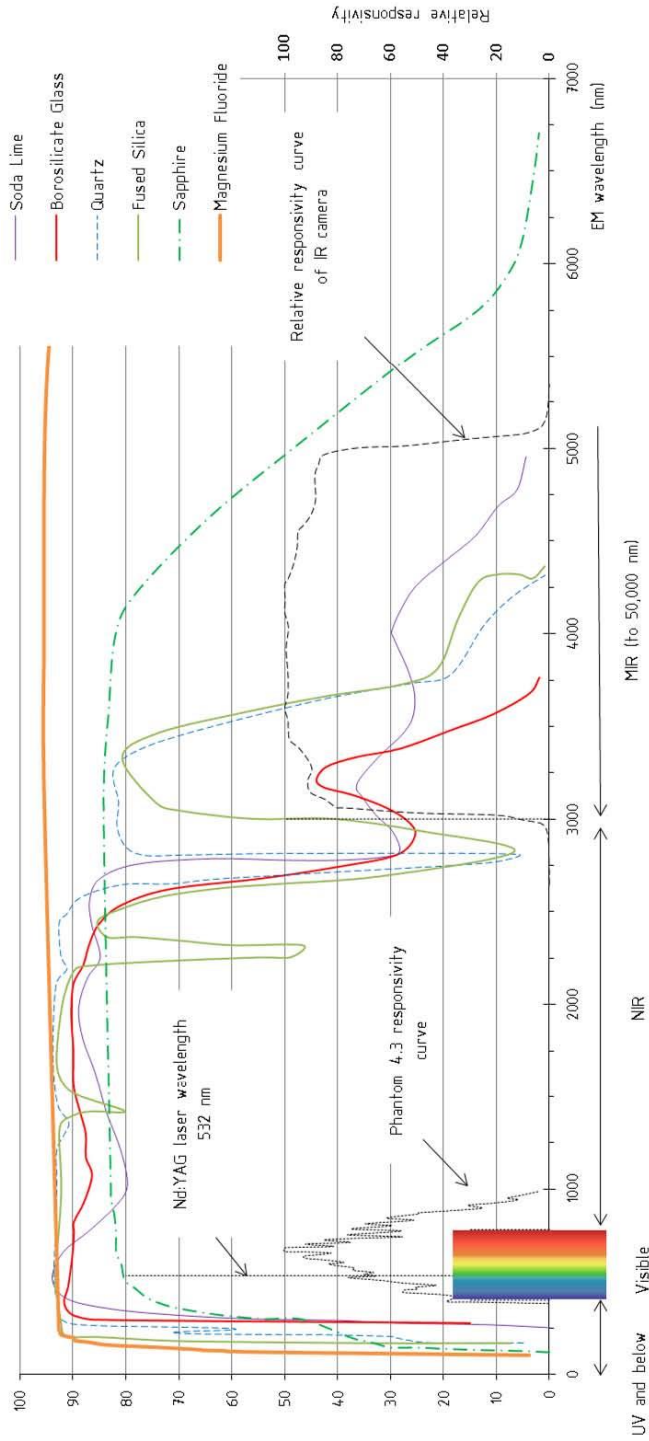


Figure 11. Transmittance of the reviewed optical materials; relative responsivity and wavelength of interest are also shown (for Design requirements section).

1.3.2 Optical access on ICE

In a typical production, ICE every side of the combustion chamber is utilised. On the top, the cylinder head provides space for the ports for gas exchange, fuel injection, sensors and for the ignition system (SI only). At the bottom, the moving piston-crank mechanism assembly borders the chamber. At the side, the barrel and its cooling channels/fins are the simplest part of the engine, as shown in Figure 12.

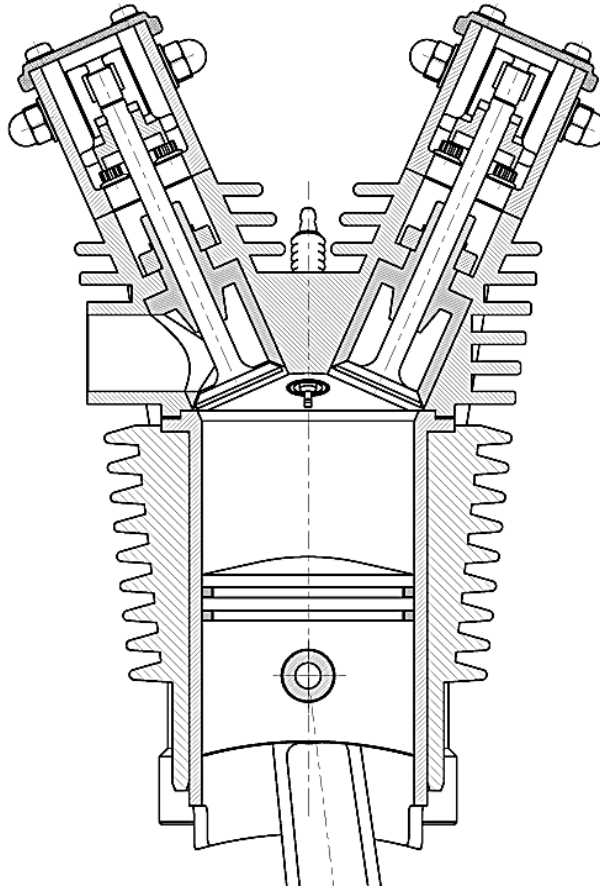


Figure 12. Four stroke overhead valve engine

To gain access to the combustion, at least one of these three components of the engine has to be significantly modified. Certain types of laser-based techniques require multiple access points, [104].

1.3.2.1 Optical element placed in the cylinder head

Undoubtedly, the most complex assembly of components on an ICE is the overhead valve cylinder head. It is nearly impossible to fit a large enough window in here. If an optical passage is required through the head then the only option is to modify the number or size of gas exchange ports. Clearly, this would greatly affect the in-cylinder flow, mixture formation and combustion chamber volume geometry. The validity of data obtained from such an engine would of course be limited. On the other hand two-stroke engines have a relatively simple cylinder head design. The intake and exhaust process take place in the crank case and engine block. This permits the modification of the head without having to pay major penalties. Combustion studies have been carried out in this type of research test engines for a long time for compression and spark ignition (SI) studies [105-107].

A two-stroke optical engine is shown in Figure 13. This engine has been developed by the author and has a circular window on the top the side of the combustion chamber is made out of a transparent quartz rig. The shape and size of the volume enclosed by the piston, ring and top flat is nearly identical to the engine's combustion

chamber keeping the in-cylinder flow realistic and closely comparable to the unmodified version.

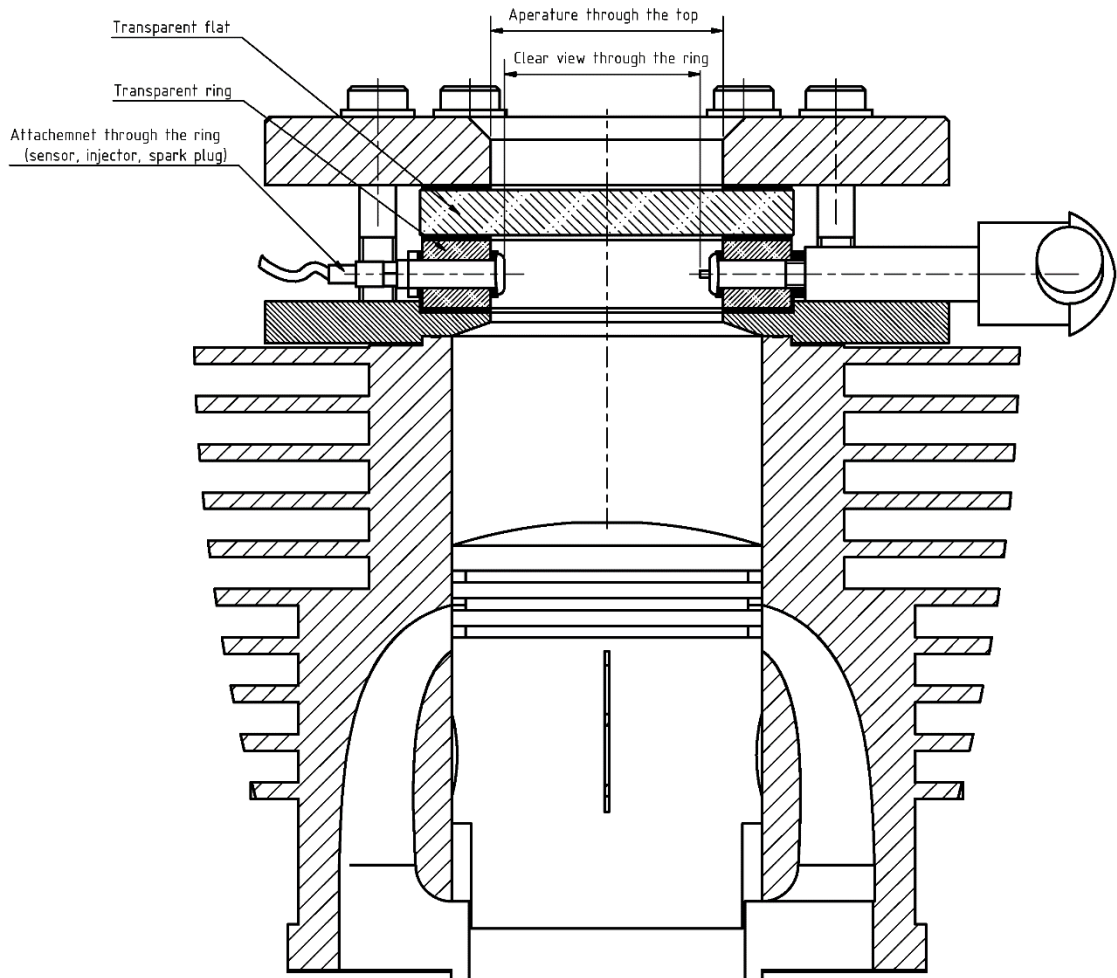


Figure 13. Fully accessible combustion chamber on a two – stroke engine

Another suitable cylinder head design for optical modification is the so called L-head. Where, the valves not above the piston embedded in the head but next to the piston fitted inside the cylinder block. These types of test rig have been used for engine research since permitted by advancements in photography and optical data recording – Withrow and Rassweiler made the whole combustion volume visible and

recorded movies of the flame propagation in 1936-38 [108, 109]. In this study, the data was also taken in an optical L-head engine. A cross-section of this engine is shown in Figure 14. This image describes the structure of other L-head engines well. The optical element is placed above the piston and potentially can cover the whole combustion volume. The valves are placed on the side; therefore the flow patterns inside the overhead valve production engines are not closely simulated by the ones in an L-head engine.

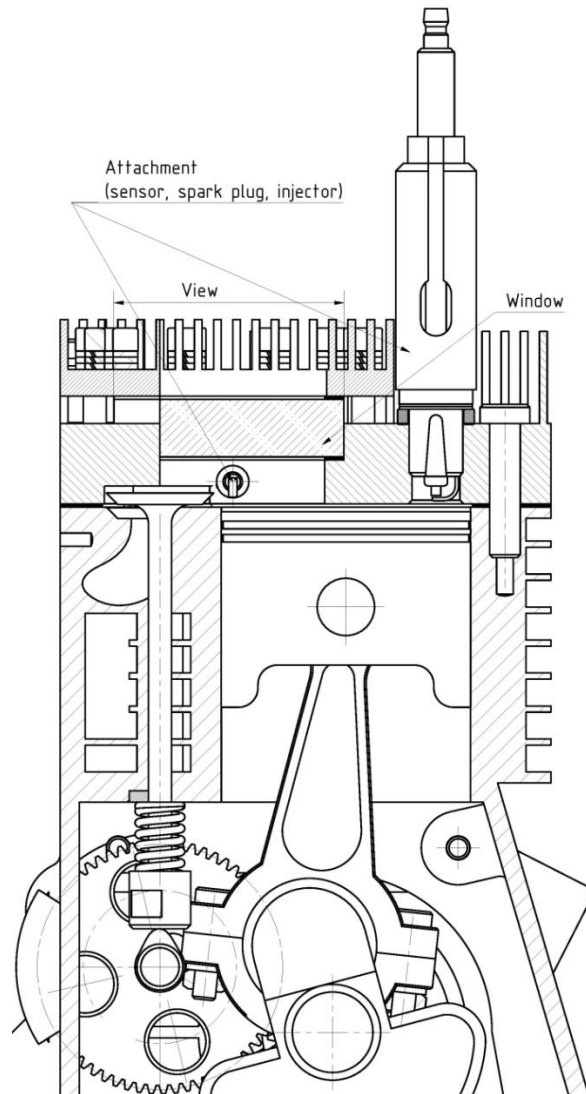


Figure 14. L-head optical ICE constructed from a Briggs and Stratton engine

In optical research carried out on compression ignition and diffusion flames, a swirl chamber is usually used as a tool. A swirl chamber in usage and research capabilities is similar to a RCM, but it is mounted on an ICE and the working fluid passes between the ports and the chamber via a connection throat. Spray interaction, ignition delay and flame lift studies have been published using this test rig, [80].

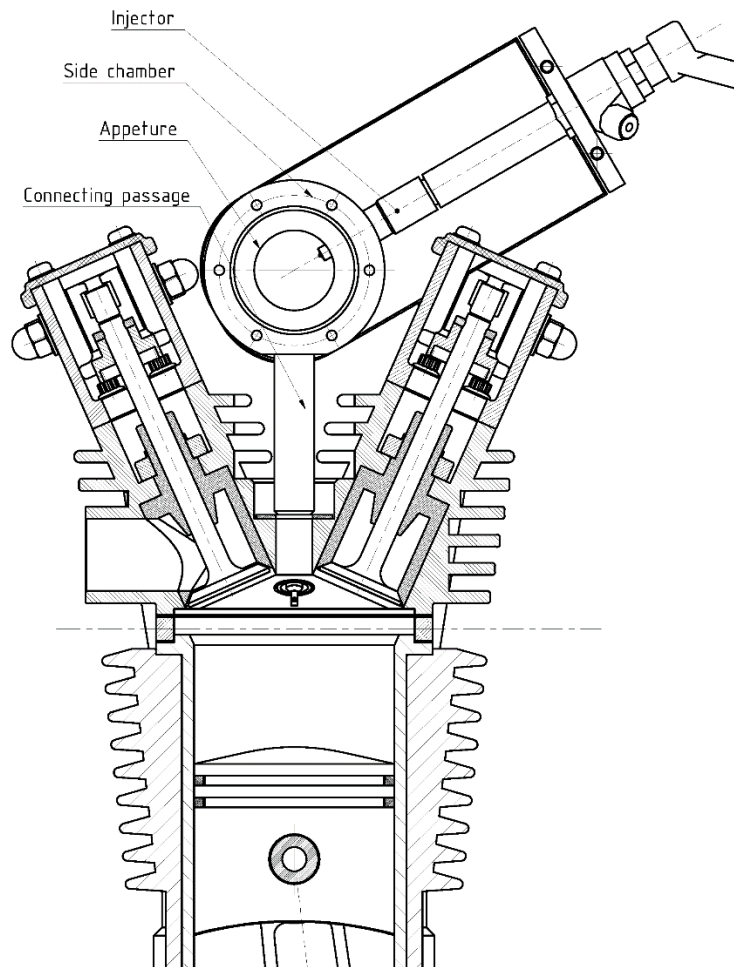


Figure 15. Four-stroke engine equipped with a side chamber

1.3.2.2 The Bowditch type engine: access via the piston

The extensive use of overhead valve engines required an optical engine where the in-cylinder flow structures were less disrupted by the modifications. In the sixties, Bowditch at General Motors improved the optical engine design by placing the optical element inside the piston, [110]. Since then, the method has been grown to be well-established and popular among engine researchers, [111]. The basic structure of the Bowditch engine is illustrated in Figure 16. The window is fitted inside the crown of an elongated piston. The EM radiation emitted from the combustion passes through the window and is reflected by a mirror mounted at 45°. The reflected rays then leave the elongated piston via a cut out to the optical sensor.

Real-engine conditions are well-simulated by the Bowditch type optical engine as long as the piston geometry is simple. Completely flat top pistons can only be found in a small number of engines. Modern CI and SI engines usually have complex geometry supporting fuel mixing and recesses to permit higher valve lift values. Therefore, in the mixture formation of these engines cannot be investigated by using the Bowditch type engine. Another problem is the quick deposit formation on the surface of the window when the direct injection system spays the fuel straight on the hot optical piston.

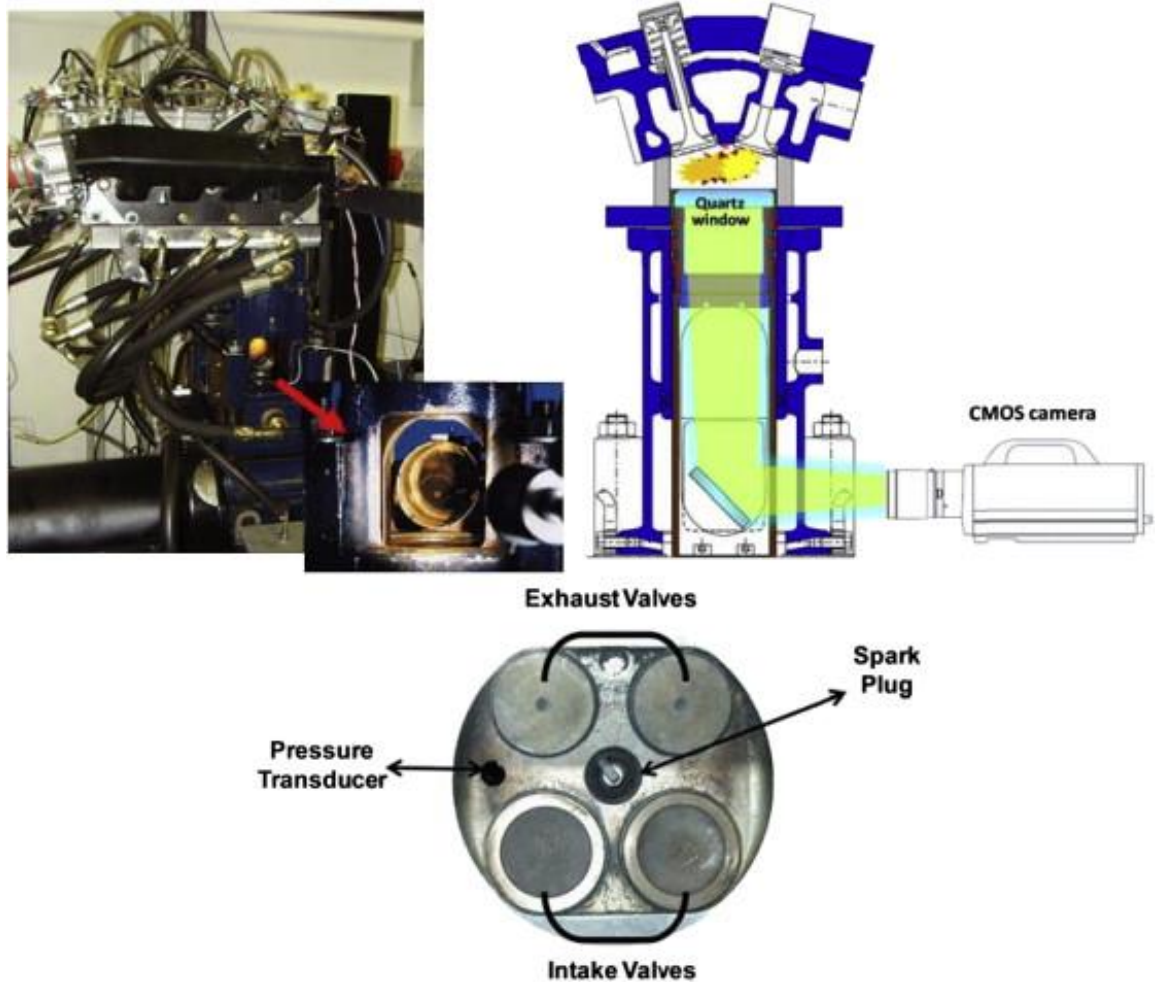


Figure 16. A Bowditch type OAICE used to investigate the influence of butanol addition to gasoline, retrieved from [112]

1.3.2.3 Optical access gained through the liners

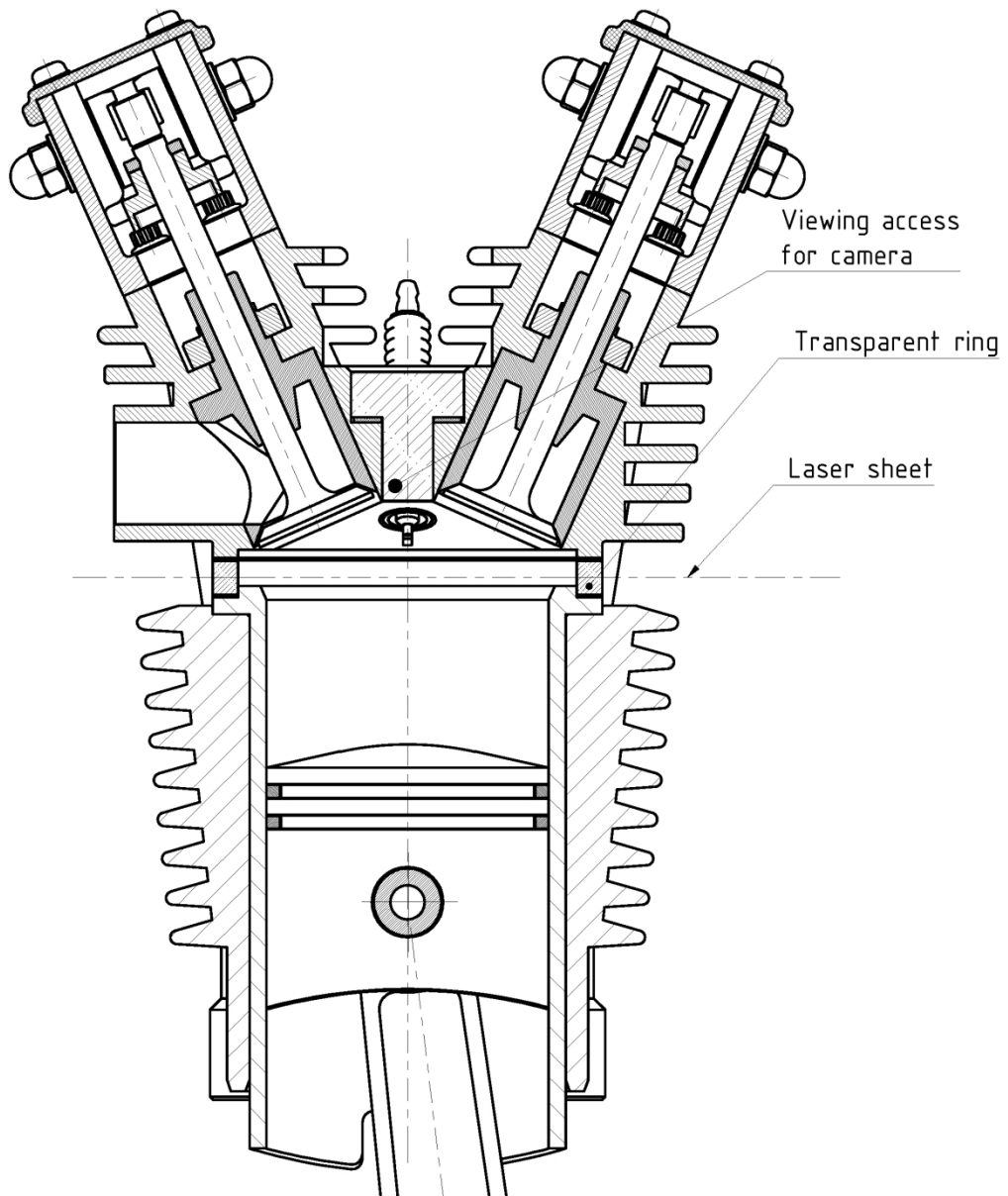


Figure 17. Four-stroke engine with side access and small viewing opening fitted in the head

As mentioned before and demonstrated in Figure 13, certain laser-based measurements require multiple access to the combustion – therefore, a transparent side is required. The easiest design option is to place the optical elements above the

top dead centre (TDC) to make sure that there will be no contact between them and the working piston, as indicated in Figure 13. The design becomes challenging when a large view is required, so that the full stroke, or a significant part of it, has to be visible. The main design consideration is the possible contact between the brittle window and the moving piston. The piston trajectory has to be carefully designed with the piston slap and thermal effects taken into account.

Lubricants cannot be used between the piston ring and the liner as their film on the window would obstruct the view. Self-lubricating polymer rings, polyamide-imide, were used to overcome this problem by Lee [113]. Polyamide-imide has high strength: 192 MPa (tensile) and high working temperature 260 °C (continuous) which make it a versatile material, especially suitable for environments with elevated temperatures.

When large pieces of ceramic or glass are used in a heat engine application, the uneven temperature distribution needs to be considered – which can lead to high thermal stresses. A more thorough work on the specifics of design and installation of a large sized sapphire was published by Bates [114].

Image distortion by the curved liner is also a difficulty to overcome. A complex optical set-up was employed by a couple of researchers to correct the results obtained from transparent liner engines [115, 116]. Another approach for recording distortion free images is to use flat liners. A square piston engine was designed and

built at MIT. The engine is indicated in Figure 18; it was the base of a number of optical studies related to laser based and Schlieren combustion measurement and flow visualisation studies [25, 50, 117]. The drawback of this arrangement, when compared to the curved liner engine type, is the less realistic in-cylinder flow pattern.

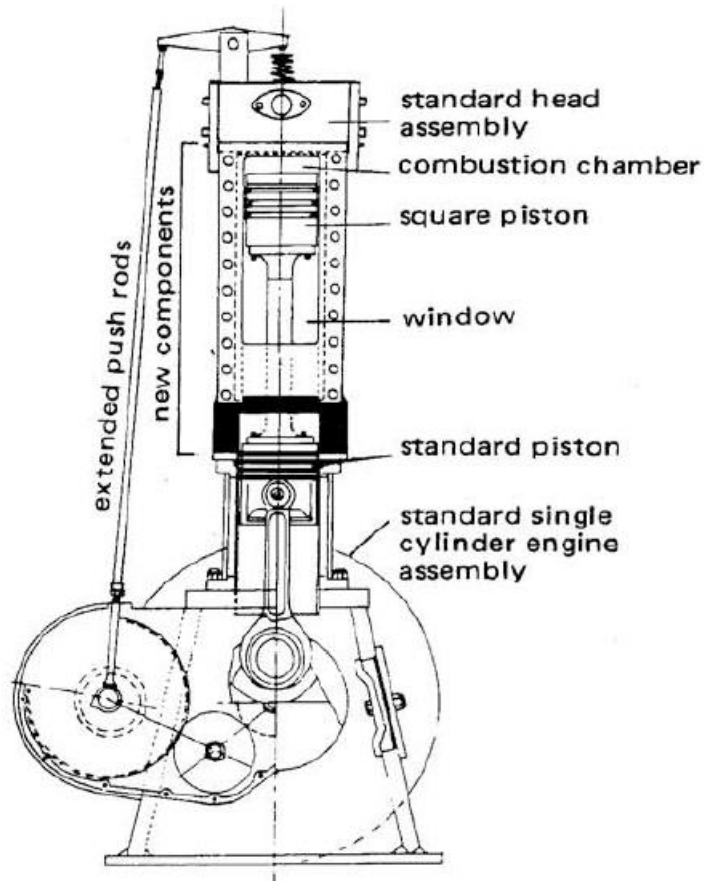


Figure 18. The schematic of the MIT optical engine with flat windows and a square piston, retrieved form [25]

1.3.2.4 Validation of measurements form optical engines

In addition to the issues caused by the obvious macro geometry differences, namely piston and combustion chamber shape design, a detailed comparison of OAIC and

production engines was made by Kashdan [118]. It was concluded that higher surface temperature occurs on glass engine parts as a result of the lower thermal conductivity. So, in optical engines higher in-cylinder pressures can be measured as a result of the increased heat flux to the charge caused by the higher surface temperature. Indeed, glasses have thermal conductivity coefficients that are lower by one or two magnitudes than steel and aluminium, respectively. The effect of this was demonstrated by showing in-cylinder pressure curves, with higher pressure values for engines equipped with glass parts. Skip-firing was suggested as a solution to keep the temperature at the level that is normally found in production engines. Unfortunately, there was no detailed analysis included for cases where the optical element was sapphire – which has the same range of thermal conductivity as steel and cast iron. The value of thermal conductivity of magnesium fluoride is also comparable to some steel grades, and is somewhat lower than cast iron. Therefore, when achieving similar thermodynamic conditions in an OAICE to a production engine is one of the main concerns, sapphire or magnesium fluoride material should be chosen as the optical element.

It was also pointed out that a correction factor should be applied to the engine geometry to compensate for the effects of the deflection of parts under pressure and for the effects of geometry change due to thermal expansion. This concern mainly applies to Bowditch type engines where the elongated piston can suffer from the aforementioned phenomenon.

As the “key challenge”, the issue of the limited operating range of OAICEs was identified. It was suggested that the future development of these OAICEs should aim to achieve closer load and engine speed levels to the ones in standard production engines.

1.3.3 Mounting methods of optical element

There are a number of different ways to hold the optical element within an optical apparatus. A particular mounting method can be selected considering the geometric constraints, the sealing requirements, position accuracy, the orientation of optical axis, stress and the deformation caused by pressure difference, and birefringence. In this work, sight optics is investigated only; their mounts are less complex than lenses that need more degrees of freedom.

1.3.3.1 Optical element kept in place by clamp.

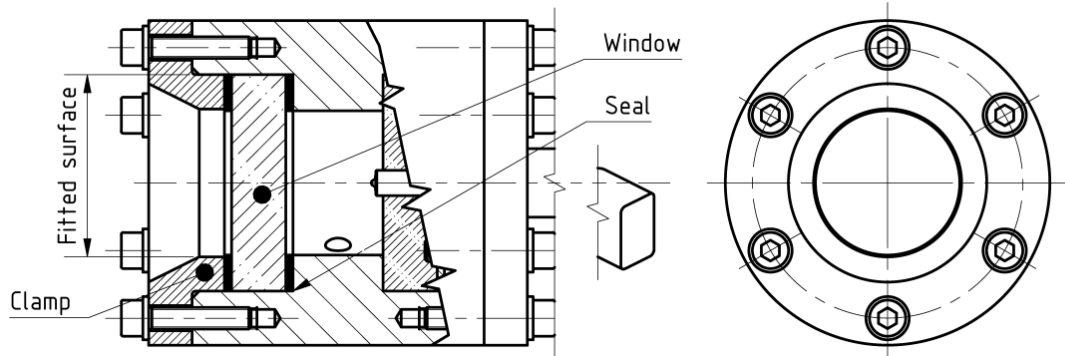


Figure 19. Fixed volume combustion chamber with circular window that is positioned by a guided clamp [80].

Figure 19 shows the usual clamping method where the retainer is fitted and guided in the direction of the displacement of the window. The radial position of the retainer is fully defined by the contact forces. The advantage of this solution is the simple tensile load on fixing bolts, and simplified dismantling and re-assembly. Details of loaded bolted joints can be found in the literature [119]. The disadvantage here is that the larger the size in the direction of the optical axis, the more complex is its design and the more difficult is the manufacturing [120].

1.3.3.2 Optical element kept in place by a free sitting clamp

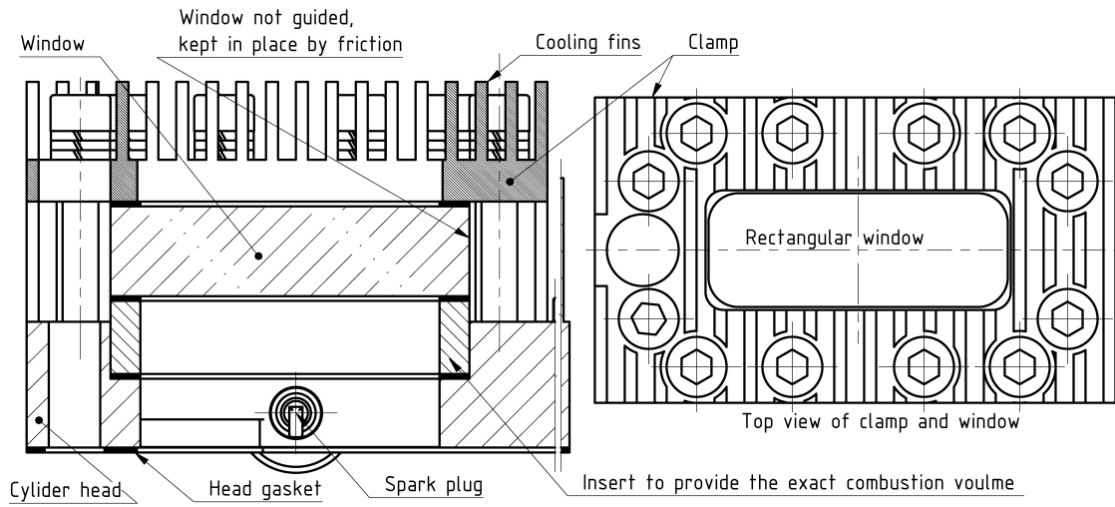


Figure 20. Four-stroke optical engine, the rectangular window is sandwiched by the clamp and soft gaskets [13, 14].

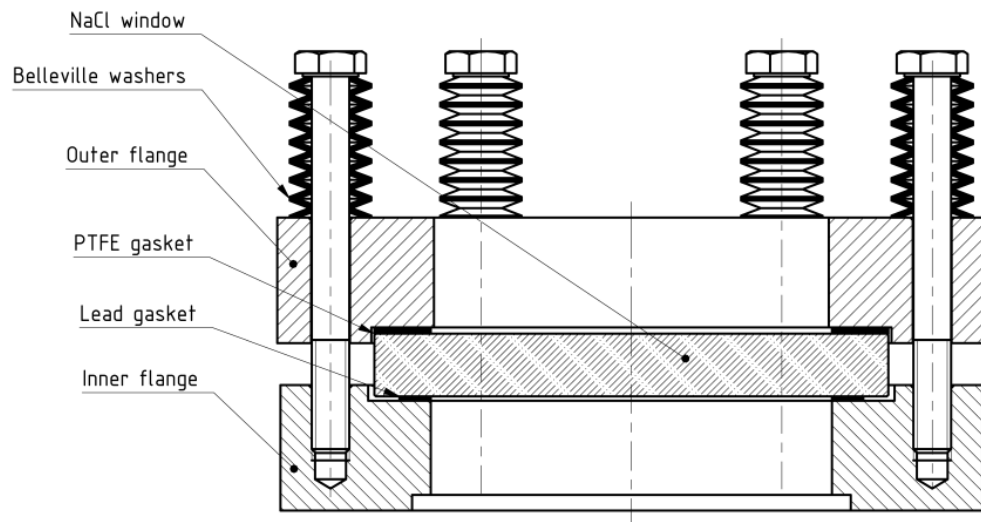


Figure 21. Special sodium chloride free sitting window for a high-temperature, high pressure difference, infra-red (IR) spectra [121]

The simplest design solution is illustrated in Figure 20 and Figure 21. The clamp is not guided but constrained by contact in one axis and constrained by friction along the other two axes; its position is defined by fixing bolts. Its advantages are: a simpler design, easier to manufacture, smaller in size along the optical axis, and that its position along the optical axis can easily be varied. Its disadvantage is that a greater amount of mechanical (bending) load on bolts is required; since the window can freely move, bringing the assembly together can also be problematic.

1.3.3.3 Adhesives

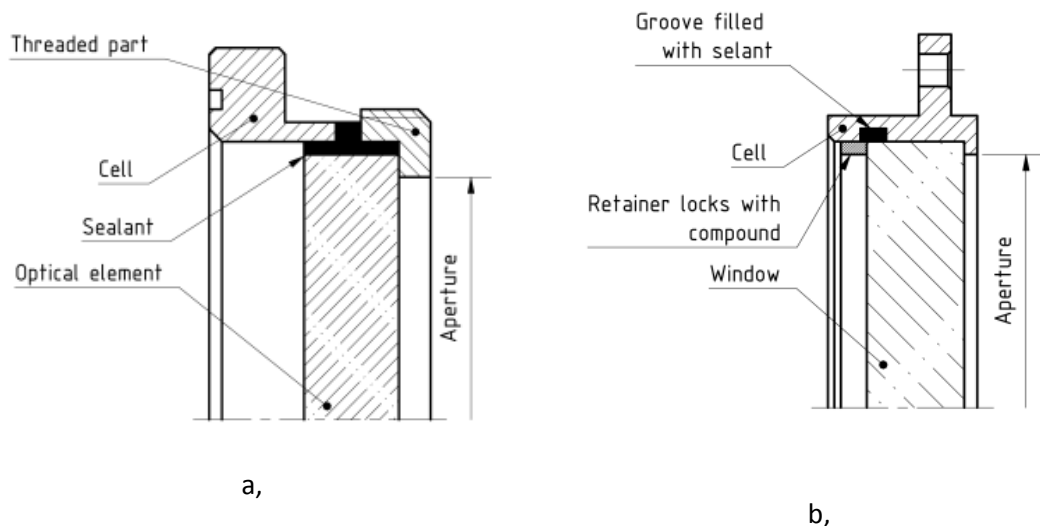


Figure 22. a, Using adhesives for a low pressure application [122]; b, Using adhesives for a moderate pressure application [123].

Fixing an optical element in a carrier frame using adhesives, as indicated in Figure 6 is a convenient solution for lower pressure and temperature environments. In both cases, the window sits against a shoulder which provides an accurate positioning. All mechanical loads rising from the pressure differential are taken by the adhesive. In

the second case, the adhesive acts as a sealant and retainer; only, the stress is induced, but the pressure difference is taken by the shoulder on the frame cell. The main advantage of this solution is the modest space requirement. Its only disadvantage is that the performance of the assembly is proportionally dependent on the properties of the adhesive, which are usually limited.

1.3.3.4 Fitted inside the shell of the vessel

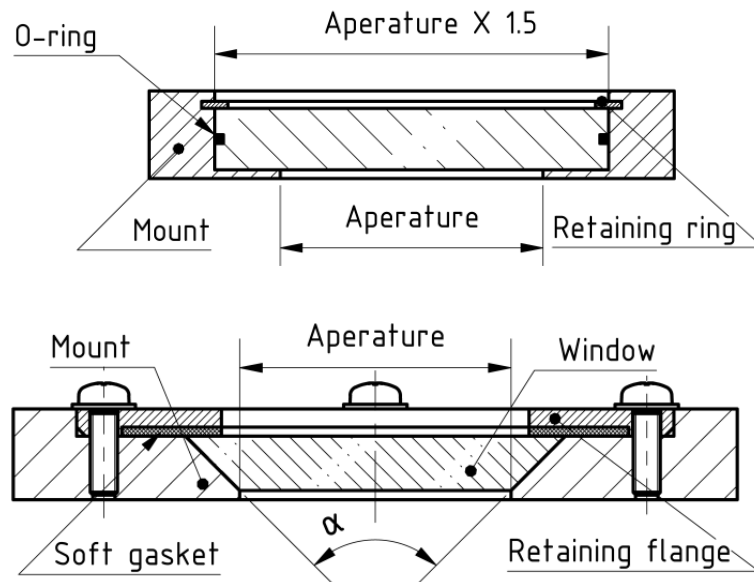


Figure 23. Window integrated in the vessel body, O-ring and tapered methods [124, 125]

The optical element can be fitted inside the housing, a typical application area is the deep submergence vehicles, Figure 23. There is no need for bolts as the major load-bearing element. Its advantage is that this setup can take large pressure differences, while the vessel geometry can also be made more simply. Its disadvantage is that the

window can only be dismantled from the pressurised side, and more complex window geometry is required.

1.3.4 Allowable or design stress in pressurised vessels and in the optical element, safety factors

The estimation of the allowable or design stress is among the most important and sometimes challenging tasks, especially at elevated temperatures [126-128]. The data of mechanical properties can be found in the literature for the more common materials; however, there often is no consistency in the given values. It becomes even more difficult to find information when practical issues are being considered, such as the effects of temperature, humidity, manufacturing technology, surface finish, and loading rate. Pressure vessel codes provide suggestions for high strength alloys which can then be taken as a first guidance for optical materials. According to BS EN 13445-3 [127] and ASME Boiler and Pressure Vessel Code Section VIII [128], the design stress should be calculated as:

$$\begin{aligned}
 \text{(EN)} \quad \sigma_{des} &= \min\left(\frac{R_{p0,2/T}}{SF} ; \frac{R_m/20}{SF}\right) \\
 &= \min\left(\frac{R_{p0,2/T}}{1,5} ; \frac{R_m/20}{2,4}\right)
 \end{aligned} \tag{6}$$

$$\begin{aligned}
 \text{(ASME)} \quad \sigma_{des} &= \min\left(\frac{R_{p0,2/T}}{SF} ; \frac{R_m/20}{SF}\right) \\
 &= \min\left(\frac{R_{p0,2/T}}{1,5} ; \frac{R_m/20}{2,14}\right)
 \end{aligned} \tag{7}$$

where, σ_{des} is the allowable design stress; SF is the safety factor; $R_{p0,2/t}$ is the 0,2% proof strength at T temperature; R_m is the tensile strength at 20 °C [129]. As optical materials discussed in this work have brittle characteristics, it is only the safety factors that are associated with the tensile strength that are applicable. It is suggested that the safety factor for optical design should always exceed 2. The general value for a well-designed system is between 2 and 3, when failure is not expected to cause major damage. When, there is more uncertainty in the design the value exceeds 3, the usual and conservative safety factor value is 4. The value can be as high as 5 for non-optimum or possible unplanned conditions (manufacturing or usage) or when failure can cause a significant damage [122, 130].

1.3.5 Deflection and stress

1.3.5.1 Plane-parallel circular window

Table 5, Classical mechanics of plane-parallel circular elements

Non supported case	Supported case
$\sigma = \frac{3(3 + \mu) \Delta p r^2}{8 t_{ck}^2} = K_w \frac{\Delta p r^2}{t_{ck}^2} \quad (8)$	$\sigma = \frac{3 \Delta p r^2}{4 t_{ck}^2} = K_w \frac{\Delta p r^2}{t_{ck}^2} \quad (9)$
$K_w = 0.125 \quad (10)$	$K_w = 0.75 \quad (11)$
$x = \frac{3}{16} (-\mu^2 - 4\mu + 5) \frac{\Delta p r^4}{E t_{ck}^3} \quad (12)$	$x = \frac{3}{16} (1 - \mu^2) \frac{\Delta p r^4}{E t_{ck}^3} \quad (13)$
$= K_x \frac{\Delta p r^4}{E t_{ck}^3}$	$= K_x \frac{\Delta p r^4}{E t_{ck}^3}$
$K_x = 0.96 \quad (14)$	$K_x = 0.17 \quad (15)$

Equations relating deflection to the applied pressure difference can be found in the literature for a number of shapes and support modes [131, 132]. A summary of the most closely related relations is presented in Table 5. Where, K_w is a generalised constant suggested by textbooks [122, 123, 130]. In these works, K_w is chosen

conservatively to cover a wide range of optical materials. This conservative method was chosen in this study to make a suggestion for values of K_x . In the rest of the equations, (8)-(15) σ is the stress; μ is the Poisson ratio; Δp is the pressure differential; r is the radius which is half of the aperture or diameter D_0 ; x is the deflection; t_{ck} is the thickness of the optical element; E is Young's modulus. If the stress equations are rearranged and the safety factor, the diameter and design stress are inserted, then the minimum required thickness of the optical element can be calculated.

$$t_{ck|\sigma \min} = \left(\frac{1}{2}D_0\right) \left[\frac{K_w SF_\sigma \Delta p}{\sigma_{des}}\right]^{1/2} \quad (16)$$

where, $t_{ck|\min}$ is the minimum thickness of the circular optical element; D_0 is the diameter of the aperture; SF_σ is the safety factor; Δp is the applied pressure difference on the optical element; σ_{des} is the allowable design stress. Using Equations (12) and (13), the deflection can be calculated or the rearranged version with the maximum allowable deflection can be used to find the minimum required thickness:

$$t_{ck|x \min} = \left[\frac{SF_x K_x \Delta p D_0^4}{16 E x_{max}}\right]^{1/3} \quad (17)$$

where SF_x is the safety factor. In general, as SF_σ is associated with complete breakdown and failure and SF_x has an effect on only the quality of the image produced by the optical element. SF_x can have a significantly lower value than the SF_σ . Equation (80) provides results for a simple case of a mechanical load. When, there is a combined load from thermal and mechanical loads, the deflection needs to be calculated using Finite Element Analysis (FEA). The result of the simulation can be used to calculate the outer radius (R) of the window that turned into a divergent meniscus lens under the loads (assuming the same deflection on both sides of the window):

$$R = \frac{x^2 + D_0^2}{8x} \quad (18)$$

Then with the known thickness the lens power (P_{lens}) can be calculated:

$$P_{lens} = (n - 1) \frac{-t_{ck}}{R^2 + Rt_{ck}} \quad (19)$$

The maximum deflection of a window is a function of allowable image distortion. In an optical system with lens and sensor, the lens focusing error usually gives the

tolerance in dioptres. It is hard to find tolerances published, but as a rule of thumb some values are summarised in Table 8, [133-136].

1.3.5.2 Plane-parallel rectangular window

Equations relating deflection to the applied pressure difference can be found in the literature for a number of shapes and support modes [131, 132]. The detailed analysis of bending of rectangular plates is not the aim of this work and it can be found in the literature, [137, 138]. Similarly to the case of the circular plates, if the Poisson ratio is assumed to be a convenient and conservative constant then, the equations can be presented in a simplified form that is easier to apply. It is worth noting that all the equations have similar forms regardless from window shape or support type.

Table 6, Classical mechanics of plane-parallel rectangular elements

Non-supported case	Supported case
$\sigma = \frac{K_W \Delta p b^2}{t_{ck}^2} \quad (20)$	$\sigma = \frac{K_W \Delta p b^2}{t_{ck}^2} \quad (21)$
$x = \frac{K_x \Delta p}{E t_{ck}^3} \quad (22)$	$x = \frac{K_x \Delta p b^4}{E t_{ck}^3} \quad (23)$

where, a and b are the length of the sides of the rectangle, with b being the shorter side.

Table 7. Constants for rectangular window geometries

a/ b		1.0	1.2	1.4	1.6	1.8	2.0	3.0	4.0	5.0	∞
Non-supp.	K_w	0.287 4	0.376 2	0.453 0	0.517 2	0.568 8	0.610 2	0.713 4	0.741 0	0.747 6	0.750 0
	K_x	0.044 4	0.061 6	0.077 0	0.090 6	0.101 7	0.111 0	0.133 5	0.140 0	0.141 7	0.142 1
Supported	K_w	0.307 8	0.383 4	0.435 6	0.468 0	0.487 2	0.497 4	0.500 0	0.500 0	0.500 0	0.500 0
	K_x	0.013 8	0.018 8	0.022 6	0.025 1	0.026 7	0.027 7	0.028 4	0.028 4	0.028 4	0.028 4

Similar equations can be used to derive the minimum thickness of a rectangular window as a function of maximum allowable stress and deflection.

$$t_{ck|\sigma min} = \left[\frac{K_w SF_\sigma \Delta p b^2}{\sigma_{des}} \right]^{1/2} \quad (24)$$

$$t_{ck|x min} = \left[\frac{K_x SF_x \Delta p b^4}{Ex} \right]^{1/3} \quad (25)$$

The calculated or simulated deflection can be used to estimate the curvature of the deformed window.

$$R = \frac{x^2 + b^2}{8x} \quad (26)$$

The power can then be calculated in the same way as it was introduced for circular windows, Equation (19).

1.3.6 Failure estimation by statistical tool, variability in strength

It is a common practice to implement Weibull statistics to estimate the probability of failure (P_f) when a given σ load is applied on a brittle material.

$$P_f = 1 - \exp \left[- \left(\frac{\sigma}{\sigma_0} \right)^{m_W} \right] \quad (27)$$

where m_W is a constant describing the variability in strength; their values having been experimentally determined and published. σ_0 is a stress level at which 63 % of the samples fail, m_W is the so-called Weibull modulus and indicates the scatter of fracture stress around σ_0 [122, 139-142]. The acceptable values can differ significantly and they should be determined for each application individually. Some suggested examples: for a cheap easily replaceable cutting tool – 10^{-2} ; for an expensive part that upon failure can cause serious damage – 10^{-4} ; when personal injury is at risk – 10^{-6} ; when the outcome of a failure could be fatal then – 10^{-8} .

1.3.7 Cyclic loading

It is well-known that repetitive or fluctuating mechanical loads lower the strength of materials. Steady state reactors are less affected, but ICE parts – by nature – are cyclically loaded machine components.

There are a number of design methods explained and procedures suggested in standards and text books to handle these load cases, [127, 128, 143-145]. The effects of cyclic loading for metals are well-investigated. Test results, strength–life diagrams and modification factors are readily available in the literature, [127, 143]. The design task becomes more complex when unconventional materials such as transparent materials have to be used. There is data available for glass and ceramic materials that describe their cyclic fatigue behaviour at room temperature. However, when the mechanical load is applied at elevated temperatures, the estimation of permissible design stress becomes guesswork as the result of limited data on specific materials, [146, 147].

Numerous publications that aimed to investigate the fatigue behaviour of ceramics and glasses were reviewed here, [145, 148-151]. Interestingly, the conclusion of experimental work was that the test failure stresses showed good agreement with the prediction of equations of slow crack growth, described by:

$$v_{cr} = v_0 \left(\frac{K_I}{K_{IC}} \right)^{n_{cr}} \quad (28)$$

where, v_{cr} is the rate at which crack propagates, v_0 and n_{cr} are constants describing the environment, K_I is the stress intensity factor and K_{IC} is the critical stress intensity factor. A detailed introduction of fracture mechanics was made by Hertzberg [152].

The aforementioned good agreement shows that the assumption of slow crack growth is valid. This suggests that, unlike many other materials, sapphire and glass have no additional cyclic loading characteristics that need to be taken into consideration during design, at least for temperatures close to ambient.

1.3.8 Birefringence and maximum optical path difference (OPD)

It is usual for most practical optical materials to have two indices of refractions. Their refractive index is a function of the propagation-direction and polarisation of the incident electro-magnetic wave. Furthermore, it is a function of the mechanical stress in the medium. Optical substances having this property are called birefringent materials [19]. The level of birefringence is expressed as a difference in the optical path of two perpendicular states of the polarised wave. This inequality in distance is called the OPD and it is measured in nanometres. The OPD has been previously investigated for plane-parallel circular plates with a pressure differential applied on them; Sparks et al., [153] derived an approximate relation:

$$\text{OPD} = 8.89 \times 10^{-3}(n - 1) \frac{\Delta p^2 D^6}{E^2 t^5} \quad (29)$$

where, OPD is the optical path difference; n is the refractive index of the material; Δp is the pressure difference applied across the planes of the optical element; D is the aperture, the unsupported diameter of the optical element; E is Young's

modulus of the medium; and t is the thickness of the window. This OPD caused by an applied stress called the stress birefringence. It is measured as OPD per unit travel path; its unit is nm/cm. The details of the maximum allowable tolerances on birefringence for some applications are given in ISO 10110-8 [154] and Kimmel and Parks [155]; a summary is presented in Table 4. Equation (29) can be rearranged to find the minimal required thickness:

$$t_{ck|ODP\ min} = \sqrt[5]{8.89 \times 10^{-3}(n - 1) \frac{\Delta p^2 D^6}{OPD \cdot E^2}} \quad (30)$$

Table 8. Maximum allowed OPD and deflection for windows

Precision	Application	Maximum power of a deflected window (dioptrre)	Maximum OPD per unit path length (nm/cm)
Extreme	Polarisation and interference instrumentation, deep-space instrumentation	no data	2
High	Photolithography optics and astronomical telescopes	no data	5
Good	Photographic and microscope optics, visual telescope	0.01	10
Low	Eyepieces, viewfinders, magnifying glasses	0.1	20
Commercial	Illumination optics, condenser lenses	No requirement	No requirement

It is important to note that there are always some residual stresses in optical materials, depending on the quality of the manufacturing processes. More details relating the manufacturing process to stress birefringence can be found in the references.

There is no analysis available in the literature on OPD in rectangular windows. Therefore, Equation (30) was altered to make it suitable for a rectangular geometry:

$$t_{ck|ODP \min} = \sqrt[5]{8.89 \times 10^{-3}(n - 1) \frac{\Delta p^2 a^6}{OPD \cdot E^2}} \quad (31)$$

This is a conservative approach, when ODP becomes crucial in a design procedure a more detailed analysis can be carried out refine Equation (31).

1.3.9 Other design considerations

In this section further design considerations are listed and referenced. They are not of interest to this study, but they can be potentially important for other designs, for instance, in applications where the pressurised chamber is used with high accuracy polarisation or interference instruments or deep space applications.

- Compressive stress caused by sharp edges on the surface of an optical element [156, 157]
- Transmittance change as a function of material thickness [86]
- Effect of a temperature gradient on adhesive bonds [123, 158]
- The tensile stress in a brittle material due to a compressive load on its surface [123, 132, 159]
- Focus shift in thick parallel plane optical elements [160]
- Distortion caused by a temperature gradient [141, 161, 162]

1.4 Research aims and objectives

1.4.1 Summary of flame propagation literature review

There is notably little data available on the properties of in-cylinder flame propagation, and even less work has been published examining such flames using alternative fuel types (alcohols, their mixtures, and hydrogen). However, these data are essential for engine-combustion modellers, for validation purposes [59, 60] and to enhance the understanding of the fundamental mechanisms governing real-life engine combustion.

The existing literature also lacks data for the comparison of flame propagation as a function of engine speed and compression ratio, with different fuels tested in the same engine. In the vast majority of the previous studies, the temporal resolution is not sufficient to provide an insight into the earliest stages of kernel formation. A large number of optical studies have been carried out on ICEs, but there are only a handful of experiments in which a statistically sufficient amount of flame propagation data was collected. Detailed statistical analysis has not yet been carried out on flame behaviour. Flame propagation can be quantitatively described in terms of the rate of propagation: flame speed or flame growth speed. In previous studies, despite the asymmetric in-cylinder flame photos, the propagation has been assumed to be isotropic. Further, this assumption has not been checked or validated.

1.4.2 Summary of opto-mechanical design literature review

In order to address the aforementioned gaps in the literature, and to observe and evaluate processes of combustion, optical access had to be designed for an engine. During the review of literature, in the survey of related opto-mechanical publications, it was found that the design methods and procedures used in industrial pressure vessels are well-documented, with comparisons of the methods and standards available for industrial applications [163-170]. These provide good guidelines even for an unconventional design task; but of course they do not provide comprehensive data for one-off special cases like experimental rigs. Thus, the available literature lacks data and case studies regarding optical access to pressurised vessels. Information on design practices and material properties is scattered in the literature, and is hard to find and often inconsistent.

There do exist a limited number of works examining the design procedures [50, 51, 110, 171], but to the authors' knowledge, there is no detailed design study on optically accessible pressure vessels at elevated temperatures and/or where fatigue failure is to be considered.

1.4.3 Aims and objectives

1.4.3.1 Aims

One of the main aims of this study is to contribute to the existing data on the subject of combustion, by adding flame speed data acquired from various types of fuels at

different engine operating points. Moreover, the widely used assumption of spherical flame propagation needs to be verified and quantified.

This work also aims to provide a comprehensive overview of the design standards, procedures and databases relevant to the design of an optically accessible pressure vessel. The study intends to show the application of the compiled information in the solution of a couple of practical problems, and interprets this information in a novel way that provides guidelines for opto-mechanical design. Furthermore, some additional constants and relations need to be derived in order to complete these guidelines.

1.4.3.2 Specific objectives

Collect a statistically satisfactory amount of flame speed data for standard fuels (isooctane, gasoline) and for some proposed future fuels (alcohol blends, hydrogen) at different engine operating points. The sample needs to be large enough to keep the precision at an acceptable level. The operating points need to be chosen as stoichiometric mixture, 1500 rpm, and CR of 8.14 – these are similar to the operating points usually chosen in existing research, in order to facilitate cross-comparison. Furthermore, some combinations of the standard conditions with a lower engine speed and CR values should be tested, to provide an insight into the effect of the engine conditions on combustion characteristics. The collected data should be

presented in a way that allows an easy comparison between the chosen engine operating points.

As an addition to the accepted method (circle fitting), a more advanced flame boundary analysis (ellipse fitting) is to be applied, in order to evaluate and verify the assumption of isotropic flame propagation. The evaluation should be carried out quantitatively as a function of time after ignition, and the results should be discussed for all the tested fuels.

A detailed literature review needs to be carried out on the topics of industrial pressure vessel design standards and procedures, case studies on the design of optical access, and optical material properties. The findings should be compiled and presented in a way that is relevant to the procedure of designing optical access for pressure vessels. Recommendations for the necessary design criteria should be provided; for example: safety factor values, allowable stress, deflection and OPD. The mechanical, thermal and optical properties of the selected materials need to be presented in a table to allow direct comparison.

Some complementary material should be provided in order to make the design procedure straightforward. Explicit equations are to be derived for calculating the minimum required material thickness for an optical element as a function of the design criteria. Especially, to address the gap in the literature, the relations and constants need to be shown for rectangular window geometries.

2 Design of optically accessible internal combustion engine and experimental setup

2.1 Design requirements

The aim of the research activity was to investigate the earliest stages of in-cylinder combustion, i.e. the ignition and early flame kernel formation at various engine speeds and compression ratios with different fuels. Therefore:

- It was essential that the spark was visible. The spark plug was placed at the centre of the field of view.
- As further beneficial feature, it was requested that a significant part of the piston and the valves can be seen on the recordings.
- As usual, the largest possible field of view was necessary while maintaining the highest possible compression ratio.
- The window had to perform sufficiently for only the visible EM range.
- The optical power of the distorted window must stay under an acceptable level.

- The optical element had to withstand a reasonable amount of loading cycle of mechanical and thermal loads with – preferably – no modification to the cooling impeller.
- The rig had to be equipped with general engine instrumentation in order to measure and record the produced torque, engine speed, in-cylinder pressure, air intake flow, fuel flow, and temperature (multiple points on head and block, intake and exhaust).

2.2 The engine and its general instrumentation

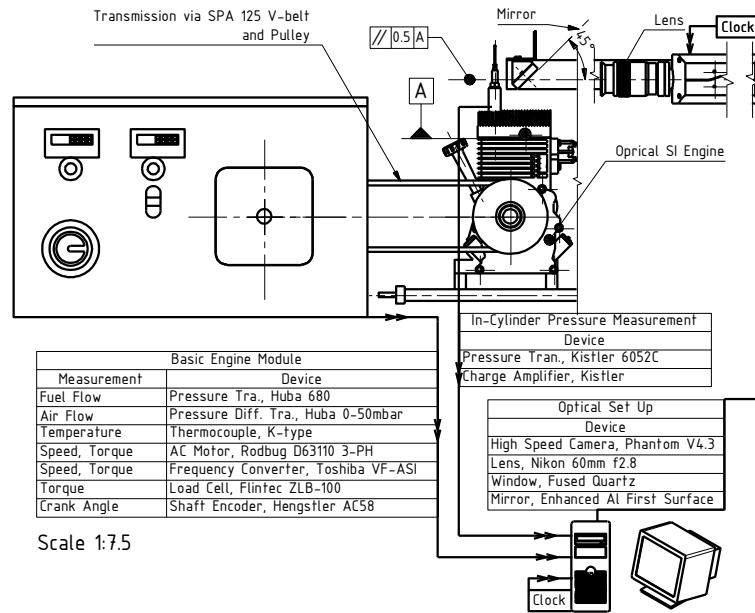


Figure 24. Optically accessible engine setup for liquid fuels

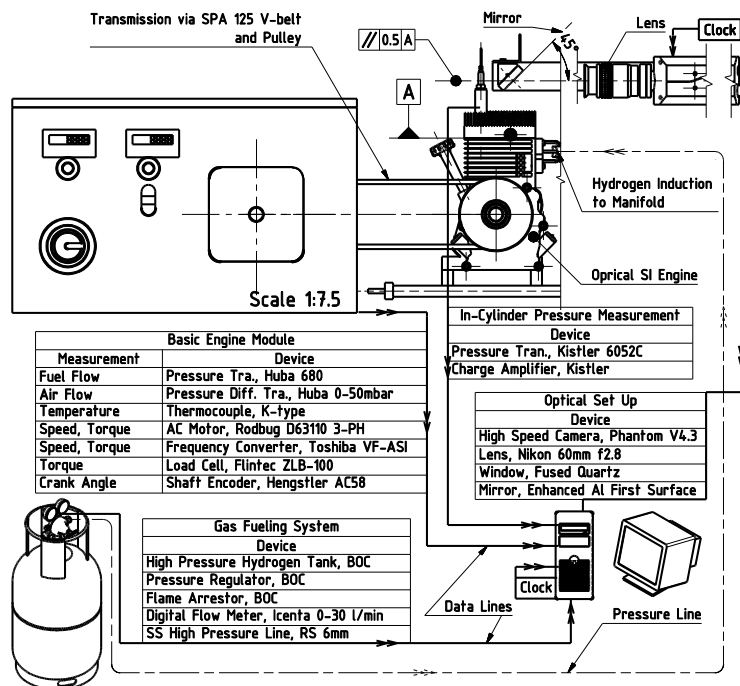


Figure 25. Optically accessible engine setup for hydrogen fuel

Table 9. Some engine data for the Briggs and Stratton engine used for the research

Attribute	Unit	Value
Make	-	Briggs and Stratton
Model no.	-	093432
Type	-	4-Stroke, Air Cooled, Wet Sump
No. of valves, head arrangement	-	2-Valve, L-head
Bore; stroke	(mm)	65.1; 44.4
Connecting rod ratio: $\frac{\text{rod length}}{\text{stroke}}$	-	2
Displacement	(cm ³)	148
Intake valve diameter	(mm)	28
Intake valve lift	(mm)	4.5
Intake valve opens; closes	(mm)	0.4 BTDC; 40 ATDC
Exhaust valve diameter	(mm)	25
Exhaust valve lift	(mm)	4.5
Exhaust valve opens; closes	(mm)	39 ATDC; 0 TDC
Field of view	(mm)	19 X 50
Compression ratio	-	5.0...8.14

Experiments were carried out in a modified single-cylinder four-stroke Briggs & Stratton engine. Some parameters of the engine are shown in Table 9. Many properties of this research engine are comparable with commercial engines. The engine's original lubrication and cooling systems, the valve train, and timing were not modified. The exhaust muffler was taken off and the exhaust port was connected straight into a laboratory extractor. The nozzle of the original carburettor was replaced with a variable area nozzle, so that any air-fuel mixture could be set by varying the fuel and/or air flow. The fuel flow and air flow were measured electronically. The volume change of the fuel stored in a small tank above the carburettor was measured, and the fuel flow rate was determined with known fuel density. The air consumption was measured using an orifice plate based on the

Bernoulli's principle, Figure 24. In case of the hydrogen, the fuel was supplied from a standard K-type cylinder via the usual safety, pressure and mass flow regulator system. The stainless pressure line fed the gas to a digital flow meter calibrated to hydrogen, as indicated in Figure 25. The measurements were taken every half second, and the air/fuel ratio was calculated subsequently and stored on the data acquisition computer. During the whole operation period of the engine, the air/ fuel ratio was monitored to keep constant. The rig had a 12 V ignition system containing a BOSCH K12V TCI coil to supply high voltage to the NGK CHSA spark plug. The geometry of the plug had to be modified so as fit in the cylinder head. The thread, sealing mode and electrical connection had to be changed, however, the electrodes and their gap of 0.7 mm were not altered. The ignition timing was kept the same (20 CA degree BTC) for all fuels and operating conditions. Therefore, at the time of ignition, the flow field adjacent to the spark was similar for the tested fuels at a given operating point. The position and orientation of the spark plug is illustrated in Figure 27, and the azimuthal orientation of the spark-plug gap was kept constant in all the experiments.

It is a complex task to obtain accurate values for residual gas volume, so it was estimated by using valve timing and clearance volumes. It can be seen in Figure 26, that there was only a short period of valve overlap. Moreover, the low volumetric efficiency (at wide open throttle) and positioning of the valve with respect to the

head walls suggest that the effect of short-circuiting was not significant. The dynamic effects of the oscillating working fluids could be neglected.

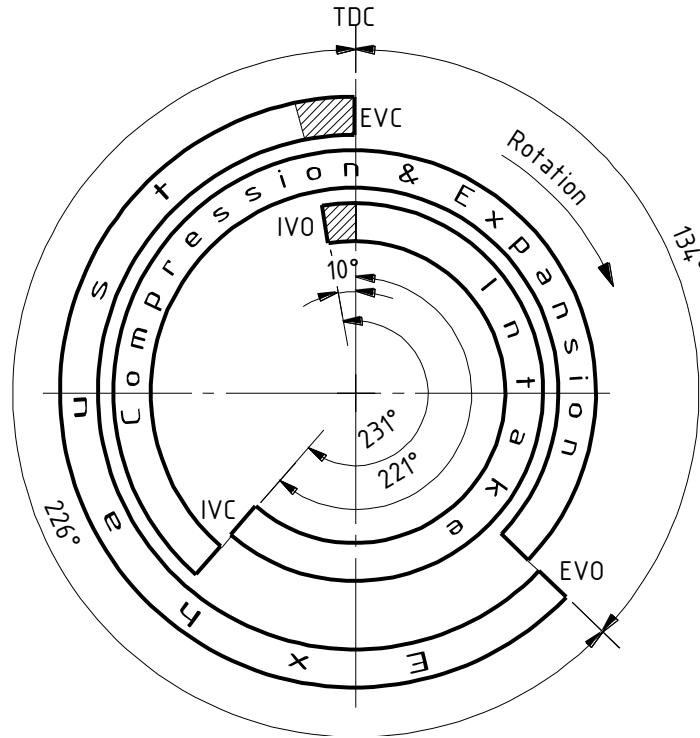


Figure 26. Valve timing diagram of the modified Briggs and Stratton engine

The optical access was gained by a specifically designed cylinder head. The chosen Briggs & Stratton engine had an air-cooled and side-valved configuration, which resulted a simpler head design.

One of the main design goals was to keep the compression ratio close to ones that real engines have. This restricted the maximum achievable size of field of view. The location and size of optical access was found by ensuring that some portion of the valves and piston were visible and the spark plug placed in the middle. Finally, the required grades of materials, minimum wall thickness and cooling surface were

determined by Finite Element Analysis. The final version of the research head had similar internal and outer geometrical design to the original one, but the compression ratio grew variable using spacers from 5.00 up to its maximum value 8.14. The detailed in-cylinder geometry is illustrated in Figure 27.

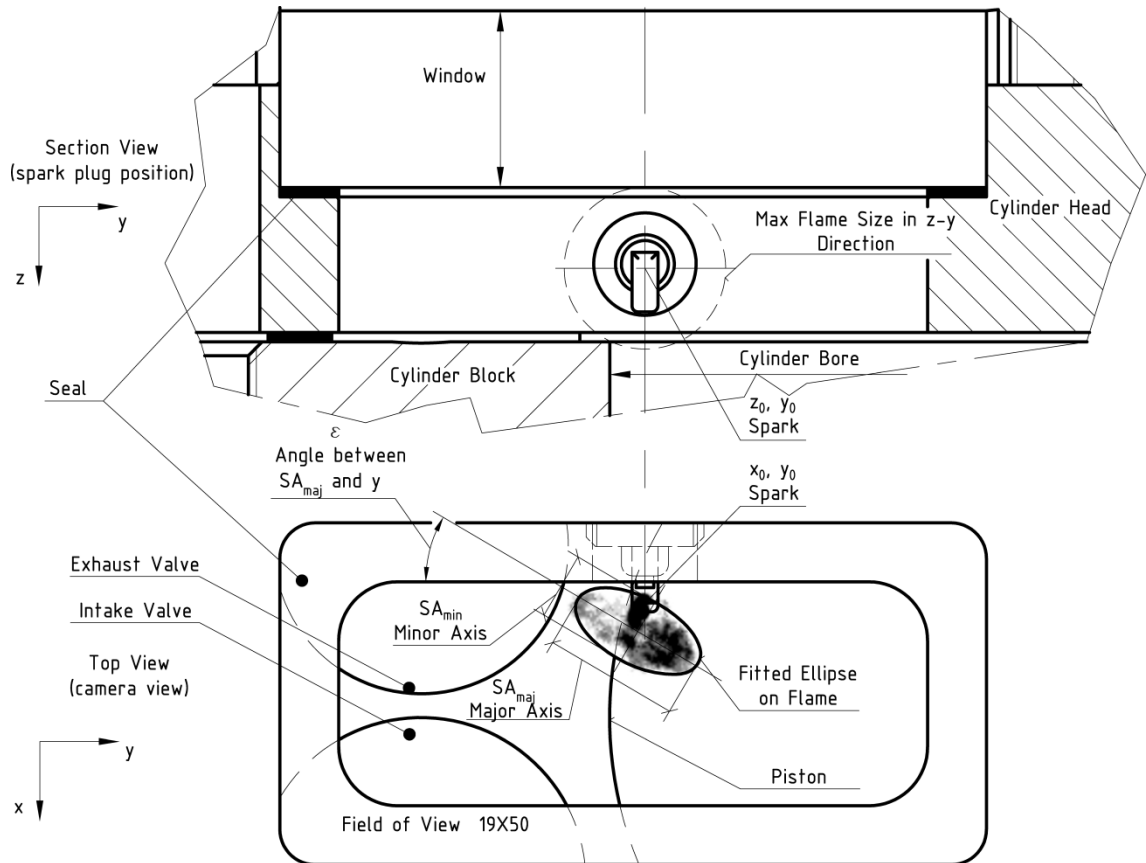


Figure 27. Section and top views of combustion chamber with fitted ellipse to the flame

front

At this stage, only a qualitative characterisation of the engine can be provided. This engine resembles the production engines more than the rapid compression machines or fixed volume combustion chambers. Moreover, it is believed that the quality of description of real engine processes, at least for the investigated time

range, is on the same level as in square piston engines, side chambers or direct injection engines with a Bowditch-type piston.

Detailed information on specification and properties can be found in the appendix for the equipment and fuels that had a direct effect on the results, the references are provided in Table 10.

Table 10. List of measurement related devices and fuels

Measurement	Device	Appendix / Ref.
Flame speed	Optical cylinder head	B
	Briggs and Stratton original engine block and head	C
	High speed camera, Phantom V4.3	D
	Lens, Nikon 60 mm f2.8	E
	Window material, Fused quartz	Table 4
	Mirror, Enhanced Al first surface	F / [172]
In-cylinder pressure measurement	Pressure transd., Kistler 6052C	G
	Charge amplifier, Kistler	H
	Shaft encoder, Hengstler AC58	I
Fuel flow-liquid	Pressure transds., Huba 680	J
Fuel flow-hydrogen	Digital thermal mass flow meter, Icenta Redycompact GCM	K
	Air flow	Pressure differential transds., Huba 0-50 mbar
Fuels	Isooctane, Chromasolv- >99%	[173]
	Ethanol, Fluka- >99.8%	[173]
	Methanol, Sigma-Aldrich >99.9%	[173]
	Hydrogen, BOC- >99.9%	[174]

2.3 Design of the optical element

2.3.1 Geometric design and compression ratio

Based on the literature review (summarised in Table 2), an overall average flame speed value – 10 m/s – was assumed as the design base input. This work aimed at

studying the early flame kernel formation and the ignition process. Therefore, it was assumed that the first $1750 \pm 250 \mu\text{s}$ after time of ignition (ToI) would be investigated – meaning that the expected flame travel, i.e. the design distance, was around 15-20 mm. From the requirement of valves and piston being visible, it was decided that the most suitable shape for the aperture was a rectangular one ($a \times b$). It was also given that the spark should be visible at the centre of the field view. Therefore, based on the design distance and the spark plug position, the field of view had to be at least 40 by 20 mm. In order to capture the possible largest portion of the valves and piston, the length of the field of view was increased to 50mm.

$$a \equiv 50\text{mm} \quad (32)$$

Then, utilising the accurately made 3D solid model including the crevice volume around the piston, spark plug and pressure sensor, iterations with Boolean operations were carried out, see Figure 28. The width of the field of view was varied to find the optimum solution for a low clearance volume but having large aperture (width) window geometry. Then, using the clearance volume values from the CAD analysis and the known displacement/swept volume the compression ratios (CRs) were calculated:

$$CR = \frac{V_d + V_c}{V_c} \quad (33)$$

where, V_d is the displacement or swept volume and V_c is the clearance volume.

After a number of trials, the width of the aperture was chosen to be

$$b \equiv 19\text{mm} \quad (34)$$

Thus, the maximum achievable CR in the engine was limited to 8.14.

$$CR = 8.14 \quad (35)$$

The height of the main combustion volume and the chamber under the window, were variable. A series of spacers was manufactured that could be placed under the window to increase the height of the chamber and, thus, lower the CR. The CR as function of spacer height is shown on the manufacturing drawing of the spacer in Appendix B, drawing number: ONE-02-04-00.

All computer aided design work was carried out with Inventor by Autodesk under an educational licence [175].

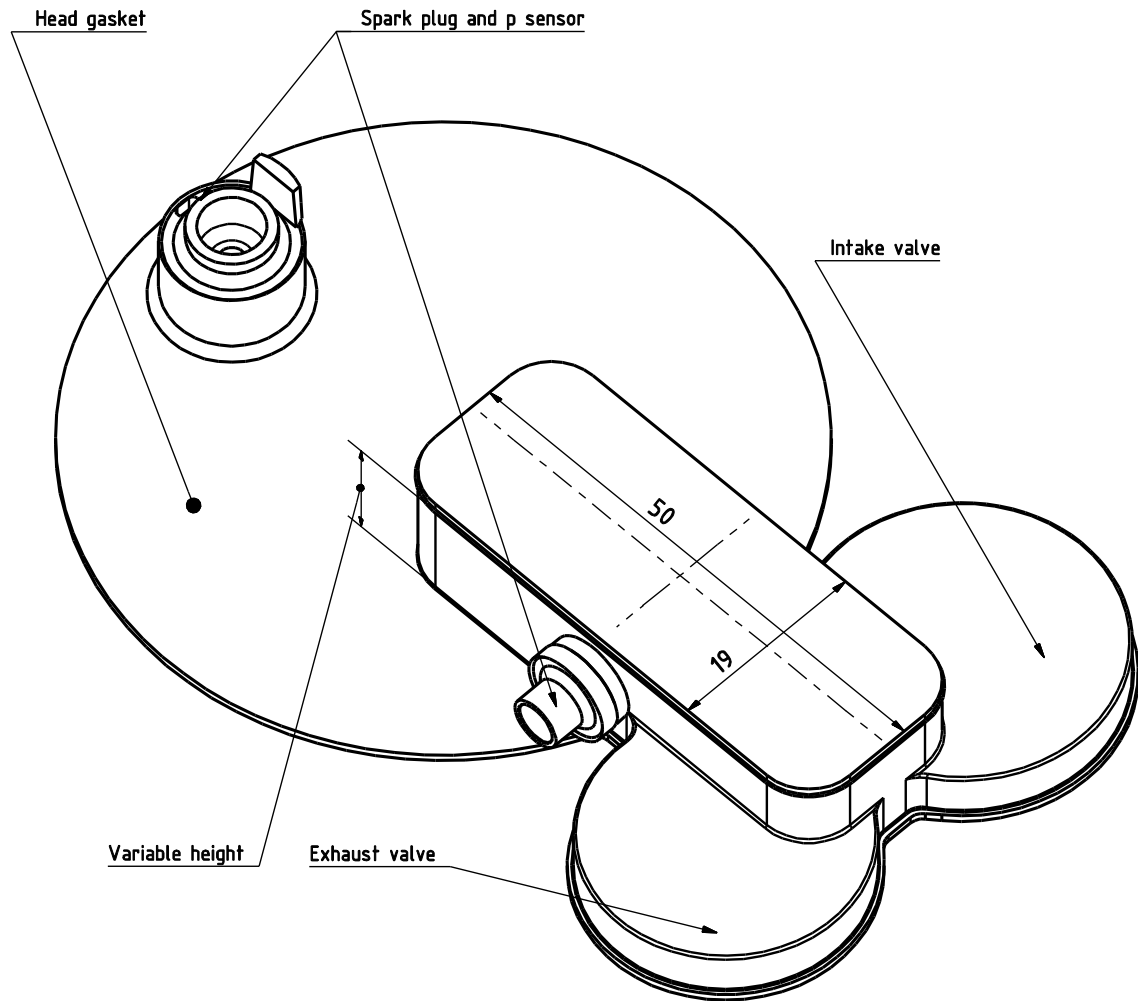


Figure 28. An isometric view of the lowest clearance volume achievable with the chosen window geometry; larger clearance volumes were achievable by the means of spacers placed under the window

2.3.2 Material and determining the design stress and temperature

The minimum required thickness is a function of the mechanical and thermal properties of the chosen material. As the required EM range was limited to the narrow visible spectra, any of the reviewed optical material would have been suitable. The evident cost-effective solution was to choose the optical material to be

quartz. An example for a design of optical element for a wider EM range is outlined in Appendix A.

After determining the geometry, sealing method and mount type, the necessary thickness of the window can be calculated as a function of loads. The mechanical load was an evenly distributed, repeated pressure. Furthermore, there was a thermal load applied on the window, namely a heat flux originating from the burning charge.

The magnitude of the maximum pressure was determined by measurements. The averaged pressure curve of 120 cycles is shown in Figure 29 along with the corresponding error bars. From Figure 29, the maximum in-cylinder pressure can be predicted to be 30 bar. Therefore, the design pressure was

$$\Delta p \equiv 3 \text{MPa} \quad (36)$$

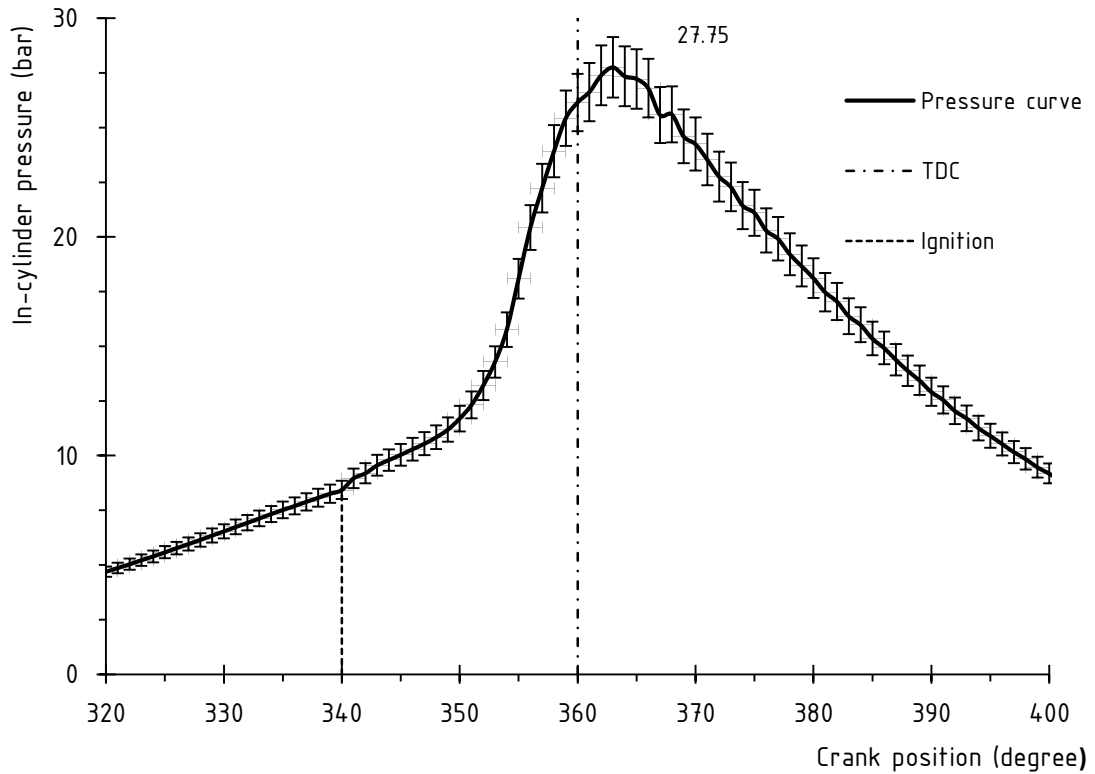


Figure 29. A typical pressure curve of in-cylinder pressure measurement as function of crank position (0° is start of inlet), high load setup CR: 8.14 at 1500 rpm with gasoline fuel, ignition time 20° BTDC

It was more challenging to get a prediction of the temperature distribution. In order to get a reasonably accurate estimation, CFD studies were run on the engine model. The rotation of the air-cooled engine's impeller was simulated in the study to provide the cooling flow, as shown in Figure 30, and an averaged heat flux was applied to the cylinder head. In order to prevent failure, it was necessary to obtain the temperature distribution. As well-known, the mechanical properties are functions of the temperature. Moreover, in order to prevent failure, the maximum permitted operating temperature of the optical material must not be exceeded. All simulation

work was carried out with SolidWorks by Dassault Systems under an educational licence [176].

The theory of heat transfer in ICE to the engine parts has been well-described in experimental and computational studies, [177, 178]. The initial heat flux data was taken from published papers where the authors collected data from a very similar sized L-head engine [179] and from another study that used a Briggs and Stratton L-head engine [180]. Temperature measurements were taken from the cylinder head during normal operation. This experimental data was used to support and correct the simulation results.

The simulations were carried out with engine speeds ranging from 1000 to 2000 rpm. A set of samples of results is indicated in Figure 31 and Figure 32, where the temperature distribution of the window is shown. It was expected, but still interesting to see the temperature drop around the areas of contact.

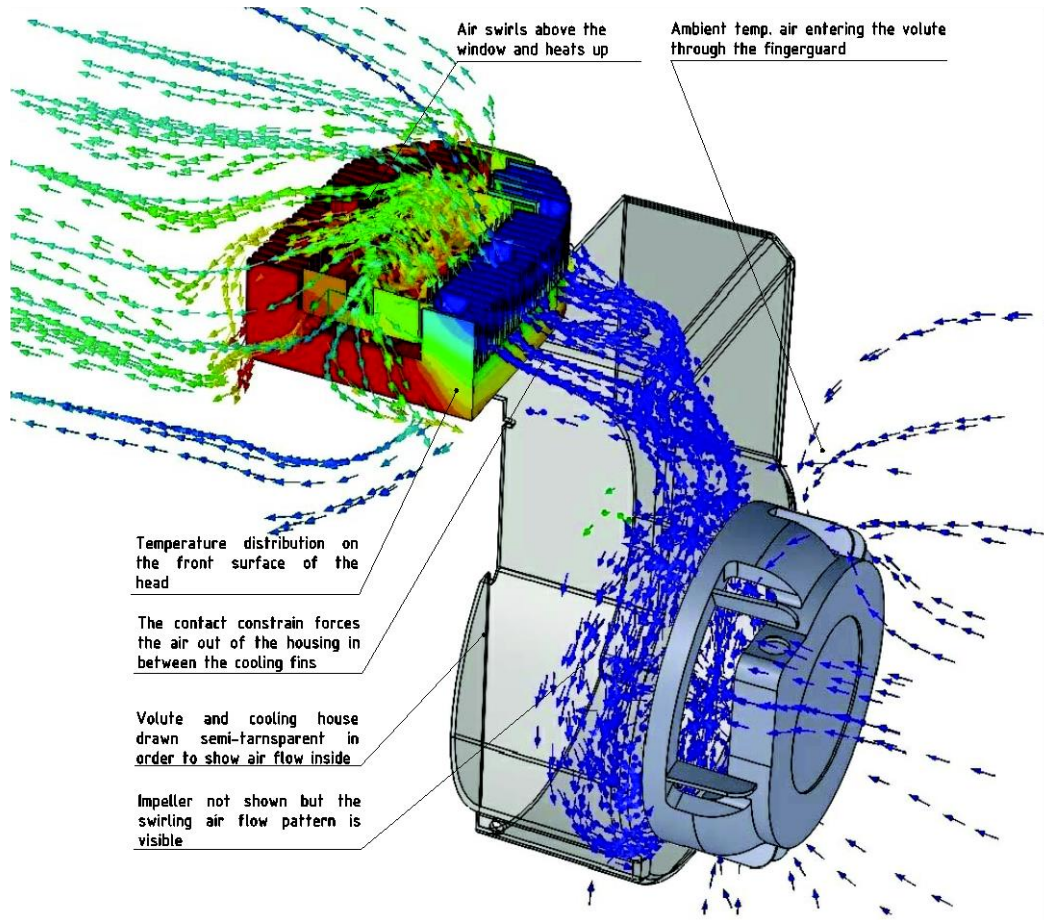


Figure 30. Cooling air flow around and inside the modified research engine (engine block and impeller not shown)



Figure 31. Temperature distribution in the middle plane of the window parallel to side b, CR:8.14 at 1500 rpm

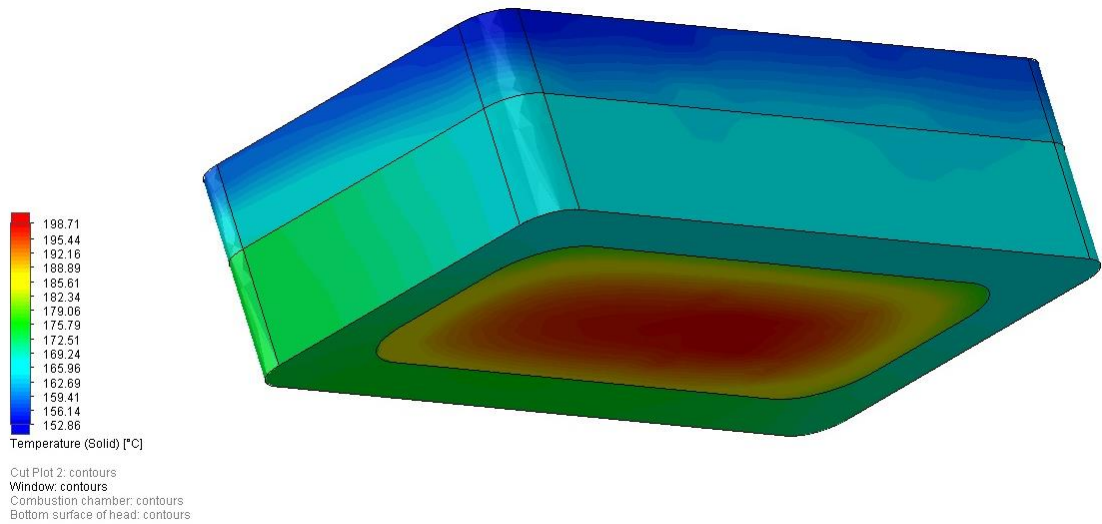


Figure 32. Temperature distribution of the outer surfaces of the window

In Figure 31, the bottom shows the local maximum as it is in direct contact with the flame, the top corners were cooler where the clamp provided cooling. Regardless of the engine conditions, the maximum temperature difference was found to be about 35-40 °C. Based on this temperature gradient, and considering the relatively low coefficient of expansion of quartz, it was concluded that the design was not under high thermal stress. There was no risk of destructive thermal shock for any operating point. In Figure 32, an isometric view of the window is shown. The heated bottom surface showed the peak temperature and a cooler band can be seen around the edges where the window was fixed to the cylinder head. The temperature difference was smaller than the one estimated inside the window – therefore, this was not a concern.

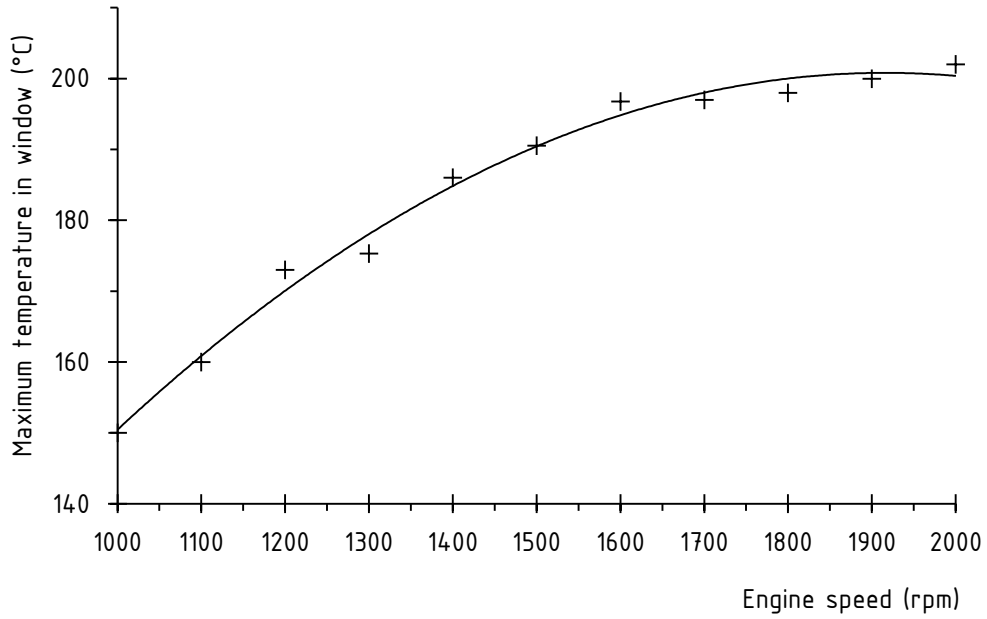


Figure 33. CFD simulation results: maximum temperature found (discrete data points) in the window as a function of engine speed; trend line was also added

The summary of the temperature simulations can be seen in Figure 33. From this, it was concluded that the maximum design temperature of the window was 203 °C.

2.3.3 The design stress

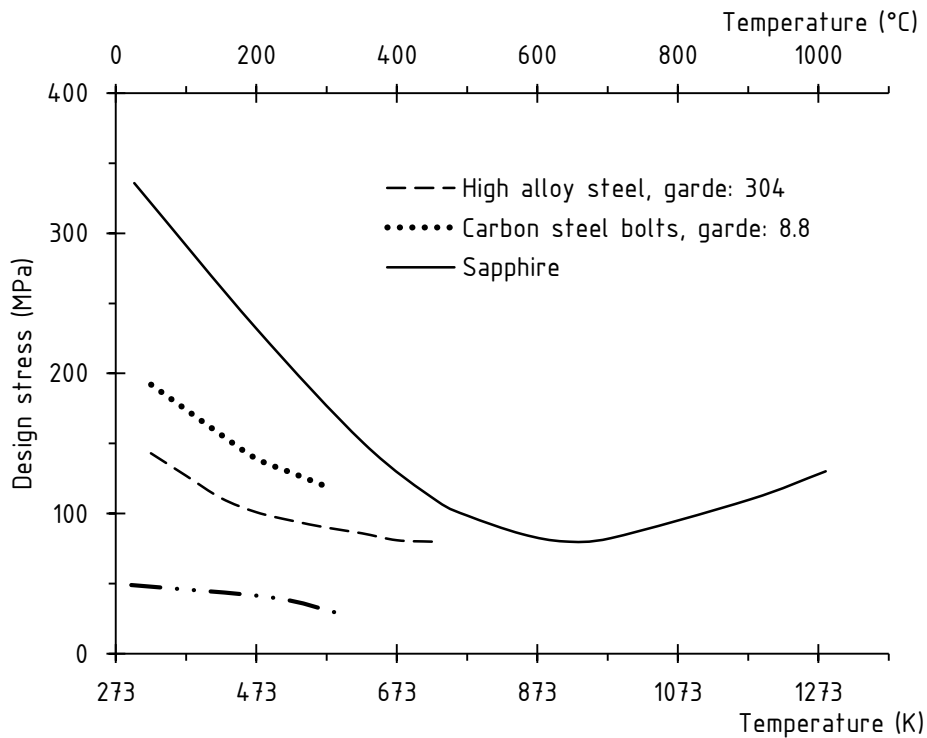


Figure 34. Design stress as a function of the operating temperature of selected materials

In Figure 34, the permissible design stress is indicated for some of the most common engineering materials based on the literature review. The maximum possible temperature of the window was determined to be 203 °C. This value was used to trace the maximum design stress for quartz for static loading. The permissible stress was estimated to be 47 MPa.

As previously mentioned, the ICE parts are under cyclic loading. This also applies to an optical element; therefore, fatigue needs to be considered. In the literature review it was found that there were no additional cyclic loading characteristics that

needed to be taken into consideration during the design for glasses. Therefore, the stress can be simply obtained from a stress-number of cycles curve. Experiments investigating the fatigue behaviour of glass was carried out by Sglavo et al., [150]. This obtained data was plotted in Figure 35 along with a prediction line for higher number of loads.

It was a clear requirement that the optical element needed to operate safely for a satisfactory number of tests. On the other hand, a part of an experimental rig is not expected to last for an infinite number of times. Thus, it was decided that the window should survive at least 200 flame speed measurement tests at the average load frequency. The average load frequency occurred at the middle of the engine speed range, at 1500 rpm, and each test took about two minutes to complete. Since the engine used a four-stroke engine cycle, it can be calculated that the required number of load cycles was 3×10^5 . Finally, the design stress was found to be 26 MPa using the logarithmic prediction curve in Figure 35.

It is important to note that the experimental data was collected at an ambient temperature of the test room; therefore, the prediction is only valid for that temperature. Ideally, this analysis should have been carried out with experimental data collected at elevated temperatures, but such data is not available in the literature. However, the design temperature, 203 °C, is about the one-fifth of the maximum operating temperature of glass. It was an educated guess that for this relatively small temperature rise, a brittle material – like quartz – would lose some

of its stiffness, but its fracture toughness would actually increase. Based on this the chosen 26 MPa design stress was an acceptable and conservative estimate.

The permissible design stress was estimated for static loading at elevated temperatures, and for a cyclic loading case at room temperature. Out of the two values, the more conservative 26 MPa was finally chosen for this application.

$$\sigma_{des} \equiv 26\text{MPa} \quad (37)$$

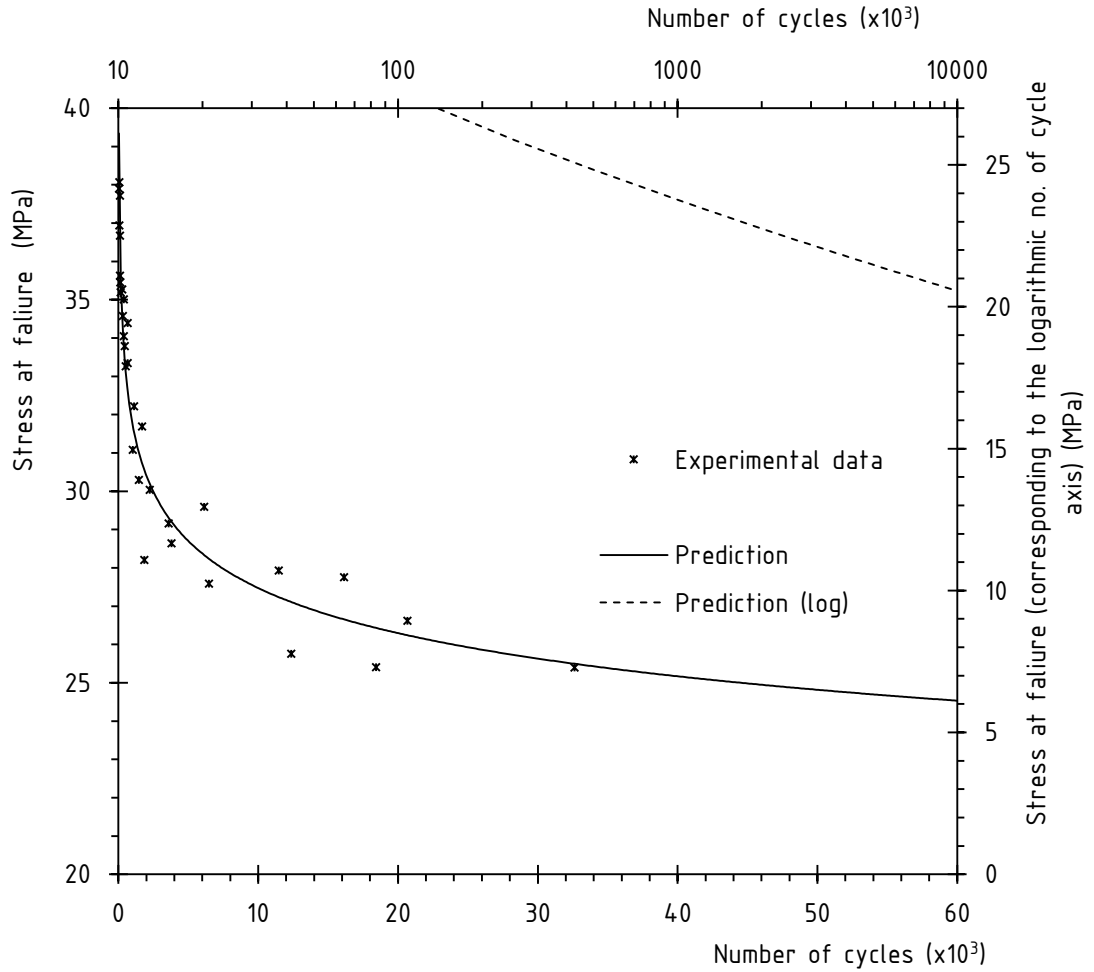


Figure 35. Failure stress at a number of cycles for glass on a linear and a logarithmic scale, experimental data adapted from [150]

2.3.4 Minimum required thickness

The minimum required thickness was estimated by substituting the data into Equation (24). The dimensions of the base of the rectangular-shaped window were

determined earlier, Equations (32) and (34). Their ratio was used in Table 7 to find a value for K_w .

$$K_w = 0.65 \quad (38)$$

Based on the careful design and optical grade manufacturing, it was concluded that there was no need to take any unplanned condition into consideration. As explained earlier, the design stress was determined in a conservative way. Moreover, a possible failure would not have caused personal injury or serious damage. Thus, a for the safety factor a relatively low value was chosen:

$$SF_\sigma \equiv 2.1 \quad (39)$$

The design pressure was defined in Equation (37).

$$\therefore t_{ck|\sigma min} = \left[\frac{K_w SF_\sigma \Delta p b^2}{\sigma_{des}} \right]^{1/2} \quad (40)$$

$$t_{ck|\sigma min} = \left[\frac{0.65 \cdot 2.1 \cdot 3 \cdot 10^6 \text{Pa} \cdot (19 \cdot 10^{-3} \text{m})^2}{\sigma_{des}} \right]^{1/2} \quad (41)$$

$$t_{ck|\sigma min} = 19.84 \text{mm} \quad (42)$$

In order to determine the minimum thickness for OPD the relevant values were substituted in Equation (31). High-speed imaging can be considered to be a relatively low-precision measurement among the optical techniques. Thus, 20 nm/cm was selected as the design criteria from Table 8.

$$\text{ODP} \equiv 20\text{nm} \quad (43)$$

The Young's modulus and refraction coefficient were found during the literature review and were listed in Table 4. The Young's modulus is a function of temperature for all solids. In the case of high quality glasses such as quartz and silica the change in the value of the Young's is negligible, [181, 182].

$$\therefore t_{ck|ODP \min} = \sqrt[5]{8.89 \times 10^{-3}(n - 1) \frac{\Delta p^2 a^6}{\text{OPD} \cdot E^2}} \quad (44)$$

$$t_{ck|ODP \min} = \quad (45)$$

$$= \sqrt[5]{8.89 \times 10^{-3}(1.46 - 1) \frac{(3 \cdot 10^6 \text{Pa})^2 (50 \cdot 10^{-3} \text{m})^6}{20 \frac{10^{-9} \text{m}}{10^2 \text{m}} \cdot (73 \cdot 10^9 \text{Pa})^2}}$$

$$t_{ck|ODP \min} = 6.41\text{mm} \quad (46)$$

As

$$t_{ck|\sigma min} > t_{ck|ODP min} \quad (47)$$

the required thickness of the window was decided to be

$$t_{ck} = 20\text{mm} \quad (48)$$

Then, with the known temperature distribution in the window, FEA was carried out on the geometry to determine the maximum deflection. The result is shown in Figure 36, from which the deflection was estimated to be

$$x = 0.005\text{mm} \quad (49)$$

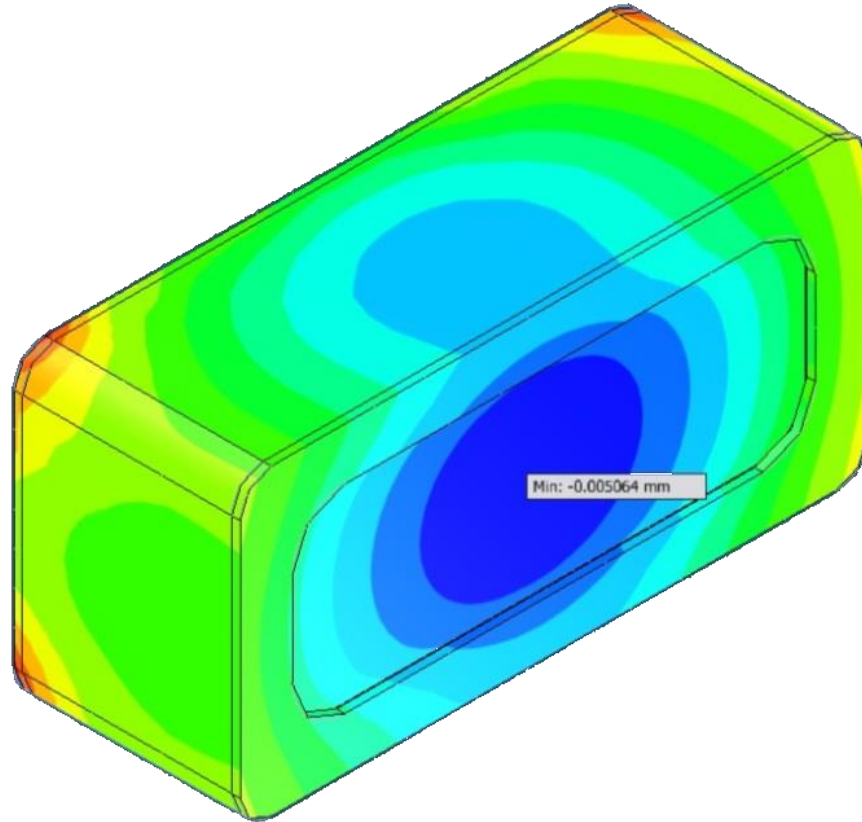


Figure 36. FEA deflection result for an $a \times b - t_{ck}$ rectangular window, maximum distortion occurred in the centre

2.3.5 Optical power of the distorted window

The radius of the lens can be calculated by inserting the geometry and deflection values into Equation (26).

$$R = \frac{x^2 + b^2}{8x} \quad (50)$$

$$R = \frac{(5 \cdot 10^{-6} \text{m})^2 + (19 \cdot 10^{-3} \text{m})^2}{8 \times 5 \cdot 10^{-6} \text{m}} \quad (51)$$

$$R = 9.03 \text{m} \quad (52)$$

Then, the power of the lens was calculated by using Equation (19).

$$P_{lens} = (n - 1) \frac{-t_{ck}}{R^2 + Rt_{ck}} \quad (53)$$

$$P_{lens} = (1.46 - 1) \frac{-20 \cdot 10^{-3} \text{m}}{(9.03 \text{m})^2 + (9.03 \text{m})(20 \cdot 10^{-3} \text{m})} \quad (54)$$

$$P_{lens} = -1.13 \times 10^{-4} \text{ dipotre} \quad (55)$$

This value is well below the power tolerance of the photographic range, 0.01 dioptre, as shown in Table 8. Therefore, it was concluded that the design was satisfactory. The manufacturing drawing of the window was added to Appendix B, drawing number: ONE-02-03-00.

3 Imaging system and data process

3.1 Experimental procedure

Figure 24 shows a schematic representation of the engine test bed. The optical assembly is at the top right corner. Fused quartz was chosen for the optical window as it has the appropriate mechanical, thermal and optical properties. An adjustable first-surface Aluminium mirror passed the emitted light to the Nikon f2.8 Macro lens. The lens had the maximum diameter aperture setting to allow as much light into the camera as possible. With the given focal length, the aperture setting, the subject distance and circle of confusion, the estimated depth of field (i.e. sharp region) is ± 6 mm.

Prior to image recording the engine was heated up using a metal blank instead of the window. It was found that when a heated window was used the obtained image quality was significantly better. The better image quality was a result of the notably less amount of condensation of liquids on the window. Therefore, prior to installation the optical elements were preheated by a blower torch at the beginning of the research, and then a more sophisticated temperature controlled furnace was used. The design of the window clamp allowed swapping the blank to the window in a few seconds, preserving the temperature of the system. Then, the engine was run an additional five minutes to reach steady operating conditions. For statistical analyses, over 100 sets of data were obtained at each engine operating point. The

camera memory could only store about 30 sets of data at a time. Therefore each time about 30 sets of data were recorded, and while the engine was running at the same operating point the camera memory was copied to the computer over about 30 seconds. Then a subsequent set of about 30 data points was obtained, and the process was repeated four times at each operating point.

The Phantom V2.3 camera was set to record at 15 kHz. At this rate the exposure time was 65 μ s and the flame image was recorded in a 256 x 128 pixel array. The spatial and temporal resolution was found to be 0.19 mm/pixel and 67 μ s respectively. From the camera's internal memory the images were sent to a PC in 24-bit bitmap format. These images were fed into a C language code for analysis, which after some filtering and noise reduction determined the position of useful combustion cycles. The following geometric properties were then calculated for each picture that contained useful data: area; perimeter; mass centre coordinates; x-y terminal points coordinates; best fit circle; best fit ellipse; circularity; roundness; solidity; ratio of perimeters; and different shape factors.

3.2 Quality of collected optical data

The overall quality of the images was evaluated by calculating the signal-to-noise ratio (SNR). As described in [183-185], the SNR can be determined using the following equation

$$SNR = \left[\frac{(\bar{i}n - \bar{i}n_{dgd})}{\sigma_{sig}} \right] \sqrt{no_{pix}} \quad (56)$$

where, $\bar{i}n$ is the mean signal intensity; $\bar{i}n_{dgd}$ is the mean intensity for background; no_{pix} is the number of pixels in the region; σ_{sig} is the standard deviation of the intensity of the signal. The images taken closer to ignition time were found to have a SNR of approximately 80, i.e., at this contrast level the signal could be detected by the computer with small uncertainty. For well-developed flames, the SNR was found to be between 150 and 200; when the values of SNR exceeded approximately 130, the flame region had a high contrast, even to the naked eye. A detailed discussion and explanation of the SNR can be found in the literature [185].

A raw image was inserted below to illustrate noise distribution, Figure 37. In order to make the noise visible, the value of the pixels of the two rectangular shapes on both sides of the flame was multiplied by a factor of 10. The image processing started with reducing the areas where systematic errors were likely to occur. Firstly, the top edge was removed where some reflection of the spark was visible. Then, both sides were cropped (a five pixel wide region each side) where there were vertical lines of noise. This systematic uncertainty was on all images, probably caused by the CMOS sensor

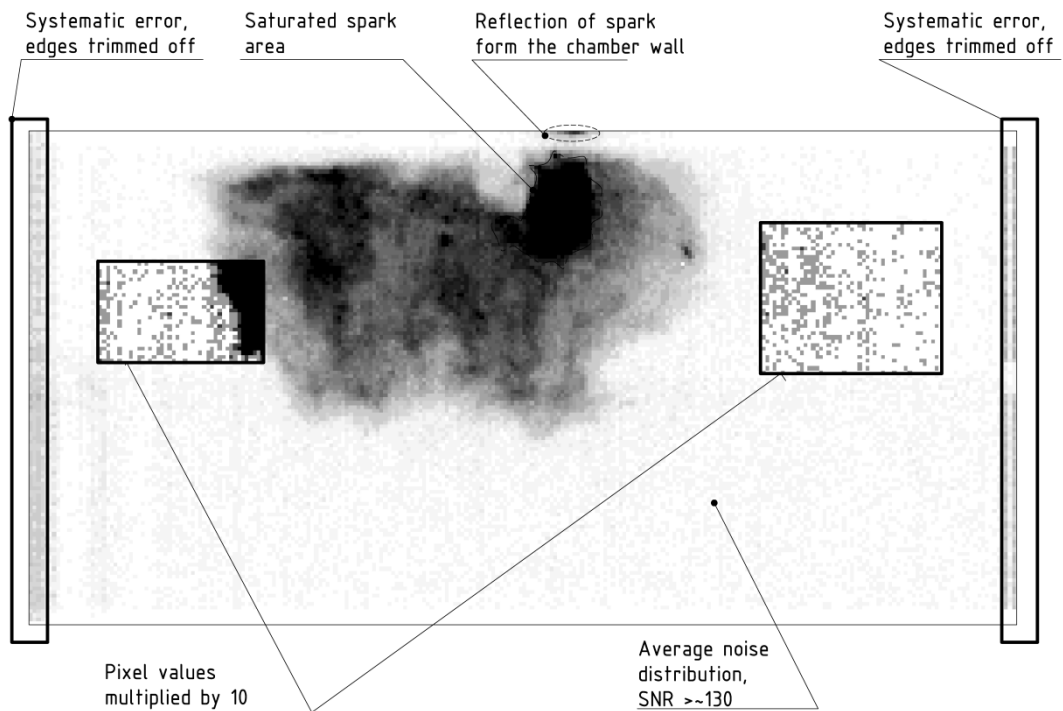


Figure 37. Noise distribution on a recorded image

3.3 Pixel errors or optical aberrations

The errors in an image can be defined as a distortion formed by the imaging system used. They can be caused by a number of faults or as their combined result. It is important that even a perfect or faultless set up introduces a measurable amount of aberration to the image due to the wave nature of the EM radiation. The design and evaluation of the current system was carried out with the assumption that light propagates as a ray. This approximation does not take into account a number of sources of error. However, the measured physical phenomenon: combustion in an ICE, is affected by a number of other non-optical uncertainties. The errors arising from these uncertainties (for example: the random behaviour of spark onset or turbulent

flow field) are likely to be significantly higher than the errors introduced by the optical system. Therefore, only aberrations that are the most relevant or have the most direct effect on the measurements were analysed in details. Others are only listed in Table 11 to provide a full overview, [186, 187].

Table 11. Optical aberrations

Name	Caused by	Result
Tilt	Wavefront tilted relative to reference plane	Incorrect magnification
Spherical	Spherical geometries in the system, increased refraction	Static blur
Coma	Imperfections	Distorted shape
Astigmatism	Multiple focal points	Static blur
Filed curvature	Non-uniform power or power distribution of optics	Image is only perfect on a curved image plane
Distortion	Extremely short focal distance,	Deviation of the rectilinear projection
Edge position variation	Variation in latency in the acquisition of the image	Incorrect edge display
Defocus, Motion blur and Reflection are analysed in details		

3.3.1 Defocus

It is important consider the properties of focal range of an imaging system that attempts to record boundaries (could be solid edges or fluid) that move in space. The aberration, defocus occurs when the moving target edge leaves the field that is in focus. The sharpness and contrast of these edges (or SNR) in defocus reduces as a function of distance along the optical axis away from the plane of best focus.

The region between the nearest and farthest planes in the scene where the image is acceptably sharp is called the depth of field or focus range. It is estimated as,

$$D_{oF} \approx \frac{2F_{no} C_{oC} d_{obj}}{f_{lens}} \quad (57)$$

where, D_{of} is the total length of the depth of field, C_{oC} is the circle of confusion which describes the smallest image element that has identifiable features, d_{obj} is the object distance and f_{lens} is the focal length of the lens, [188].

The successful high-speed imaging of the low light intensity, early flame kernels requires a high-sensitivity camera coupled with a fully open aperture and low f-number lens. These properties of the elements of the current optical set up make the system to be a shallow focus type; i.e. depth of field is expected to be relatively short. In order to capture the flame boundaries with an acceptable sharpness it is required that the size of the focus range is comparable to the combustion chamber depth. The total depth of field of the used imaging system was estimated by using Equation (57), it was found to be 12 mm. Then, estimated size of the depth of field was compared with the thickness of the combustion chamber, 13mm. The difference was found to be less than 10 % which suggests that the edges of propagating flames were expected to be in focus for the measurements; no errors introduced by defocus.

3.3.2 Motion blur

One of the main concerns when one designs or evaluates a high-speed imaging system is the possible error caused by trying to capture a still image of a moving object or fluid. If this process of “freezing” of the motion is not carried out sufficiently well, then non-sharp edges form on the images with low SNR. This effect is called blurring, and it makes the image processing and analysis more complex and less accurate. Figure 38 shows two images of a spray development of the same conditions. However, the two images were taken with different exposure times. The relatively low exposure time of 222 μs on picture (a) resulted in blurred image; edge detection or similar image processing techniques cannot be applied. Picture (b) was recorded with a significantly reduced exposure time of 25 ns. The effect of the short exposure time can be seen as frozen motion, the structure of the spray and droplets can be observed with good SNR.

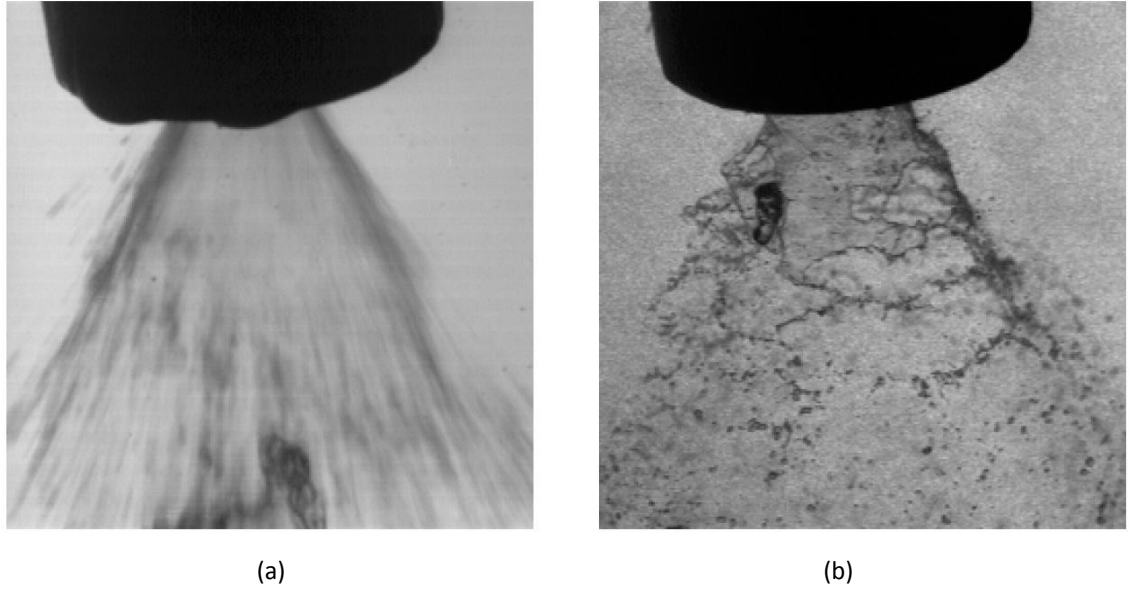


Figure 38. Nozzle and spray, (a) blurred image with low SNR, (b) sharp image with good sharpness and contrast edge detection possible, retrieved from [189]

The magnitude of the possible blur depends on the rate of part motion, exposure time, and the size of the field of view [190], and it can be calculated as

$$BLR = v_{part} t_{ex} \frac{n_{pixels}}{FOV} \quad (58)$$

where, BLR is the image blur in pixels, v_{part} is the velocity of the object (part or fluid), t_{ex} is the exposure time, n_{pixels} is the number of pixels spanning the field of view, and FOV is the physical size of the field of view. The term $\frac{n_{pixels}}{FOV}$ is the inverse of spatial resolution. It is suggested by the literature that for high-precision measurements, the effect of the blur is negligible if its magnitude less than one pixel. If the value is over one, then further analysis is required. According to Whybrew [189]; an acceptable level of blur is when the object moves less than 10% of the

characteristic linear length during the exposure time, in this case the axes of the ellipse i.e.:

$$t_{ex} \leq \frac{l_{ch}}{10v_{part}} \quad (59)$$

where, l_{ch} is the characteristic length.

The blur evaluation analysis was carried out for the optical system used in this study. It was found that the slower propagating flames, typically less than 3 m/s, satisfy the one pixel criterion. These slower propagating flames usually occurred in the setup with a low engine speed and low CR along the minor axis. The analysis showed that in the case of flames traveling faster than 3 m/s but slower than 6 m/s, the magnitude of the blur was over one pixel. However, the 10 % criterion – detailed in Equation (59) – was satisfied from about 200 μ s after ignition, for these flames. The results obtained for the first few images had an unsatisfactory amount of blurring, and therefore further analysis was required. In the case of the fast flames, those travelling at 6 m/s and above, typically the first seven data points were affected by blurring, but from about 500 μ s after ignition, the level of blurring dropped to an acceptable level.

Additional evaluation was carried out for a selection of the images that did not satisfy the criteria outlined above. It was found that the maximum blur was about 25 % of the characteristic length, but most of the pixels of the blurred area had significantly

higher intensity values than the noise. Therefore, those were easily detectable as flame. Only 3–5 % of the blurred area was found to have low intensity values close to the level of noise, and these pixels were considered as noise and were removed during analysis. A summary of this analysis is shown in Table 12.

Table 12. Summary of pixel error analysis

Flame Boundaries at condition of:	Criterion satisfied	Result of error analysis
Flame speed < 3 m/s	one pixel	negligible
3 m/s < Flame speed < 6 m/s	10%	acceptable
Flame speed > 6 m/s and TAI > 500 μ s	10%	acceptable
Flame speed > 6 m/s and TAI < 500 μ s	none	$BLR \approx l_{ch} \cdot 0.25$ As a result of the properties of the imaging system less than 5% of the blurred area was removed as noise.
Flame speed >> 6 m/s	none	Error caused by these conditions is investigated in Section 3.3.3

An example of the analysis is shown in Figure 39. The image shows an M85 flame recorded at 1500 rpm with a CR of 8.14, 402 μ s after the spark onset. The black, saturated area was considered as flame and the scattered grey spots as noise. The grey ragged band around the flame could have been noise or part of the flame, due to blurring. The resolution of the current imaging-analysis system was not able to distinguish between noise and flame for this band, which was approximately 3.5 % of the whole flame area.

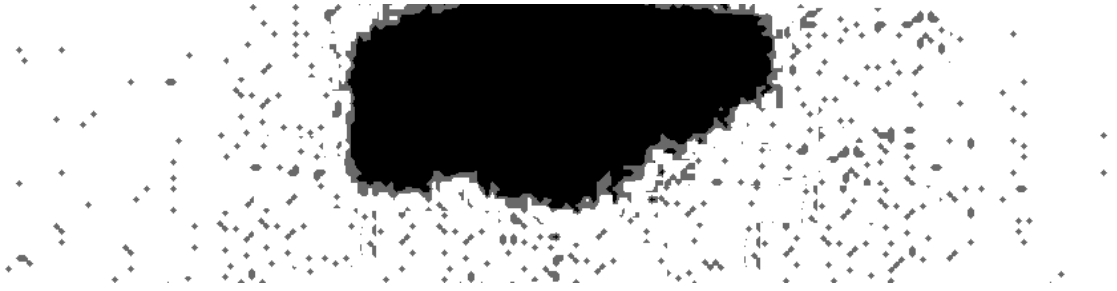


Figure 39. Noise and blurring of a M85 flame at CR: 8.14, 1500 rpm; image was taken 402 μ s after ignition.

3.3.3 Reflection

Preliminary analysis showed unexpectedly high initial flame speeds, only occurring at the first data point. These high values could not be explained solely by the high energy input by the spark; further analysis was required to uncover this randomly occurring phenomenon.

Histograms of samples corresponding to the first data point calculation were examined. It was found that around the mean value, the data distribution resembled a Gaussian function; but overall, the distribution was skewed to the high side, as in the example shown in Figure 40. This non-symmetric characteristic only occurred in the histograms of samples for the first image, and seemed to be random (more details are provided in the Statistical analysis section). No correlation was identified between the skewed nature of these distributions and the fuel type or the engine conditions.

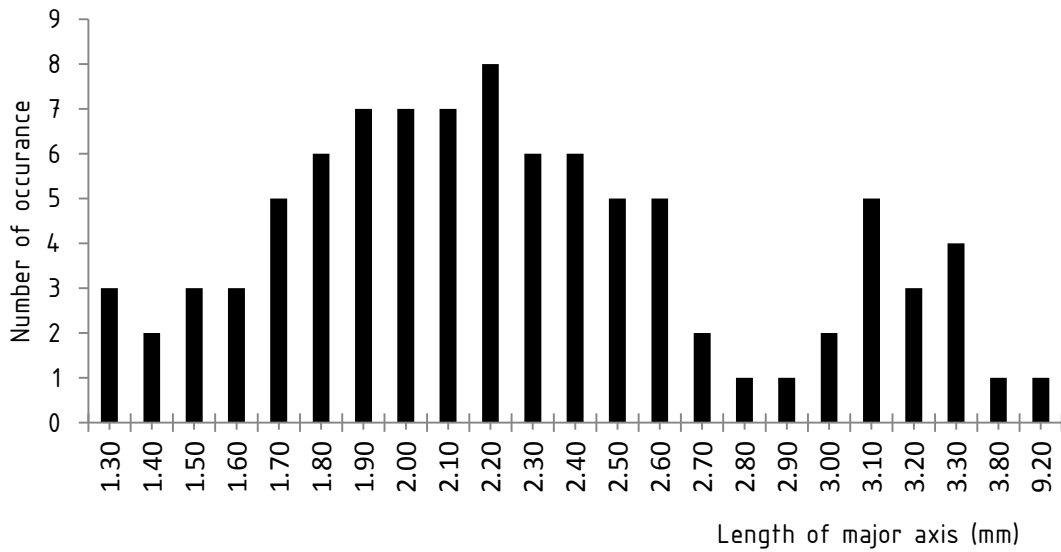


Figure 40. Major axis length distribution of the first data point - $67 \mu\text{s}$ – for M85 at 1500 rpm and CR:8.14

The combustion chamber had a black matt finish, in order to minimise the uncertainties arising from reflections. However, further investigation of the raw images suggested that some of the images captured a spark that was significantly brighter than the sparks or the flames seen in any other images recorded later. These bright flames saturated more pixels on the recorded pictures, and there was a round-shaped bright area around the flame core, as illustrated in Figure 41. The shape and size of this reflection seemed to be completely random, similar to the random nature of the spark discharge. As the intensity of the reflection was close to the intensity of the flames, the reflected area was considered to be a flame by the analysing system. This caused a random, asymmetrical error which was significant in its relative

magnitude. Based on the detailed analysis, the estimated effect of this error on the flame speed measurement was +0 % and -48 %.

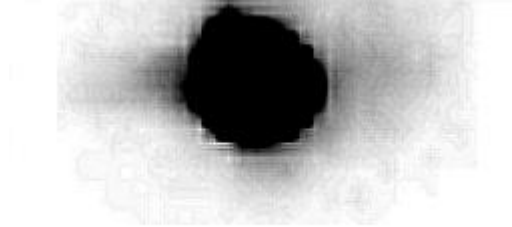


Figure 41. Spark core and light reflected from the bottom of the combustion chamber, image was processed for better visibility

3.4 Repeatability

The camera optical data analysing setup was tested for repeatability. The engine was set to run on isooctane at 1200 rpm with CR: 8.14. Then three time 30 combustion event was recorded, each with different optical setups. The camera rates were 4, 8 and 12 kHz for the recordings with 256 x 512, 256 x 256 and 128 x 256 resolution respectively. Therefore, the temporal and spatial inputs were different but the expected flame growth curves were expected to be nearly identical as the same combustion event was filmed.

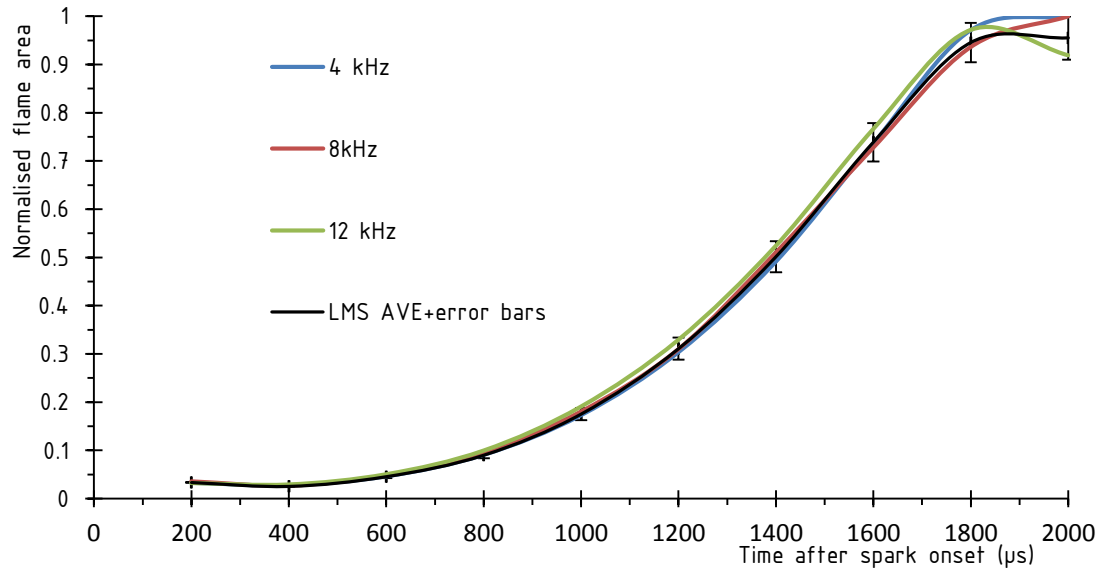


Figure 42. Repeatability validation; flame area measured at different recording condition with the same fuel and same engine conditions; LMS AVE: least mean square average

The results of the repeatability test are presented in Figure 42. As is seen, the curves for the three recording settings showed reasonably good agreement. For further analysis the least square fit method for an overall average of the 90 combustion events was also plotted with the corresponding error bars. All the original curves fitted inside the error band around the average value, proving satisfactory repeatability.

3.5 Fitting an ellipse to an arbitrarily shaped region, fitting methods, flame speed and shape factor

A fundamental task of automated image analysis and computer vision techniques is to fit geometries to regions or set of points. In two-dimensional space, the most primitive approach to model a 2D shape is to fit a circle. The next level to retrieve more information from the model is to fit an ellipse, which (unlike a circle) is not symmetrical about every one of its diameters. In this work ellipses are used to model and analyse the non-isotropic propagation of in-cylinder flames.

Fitting an ellipse to an arbitrarily shaped region has been studied in considerable detail. There are two basic methods for fitting ellipses: (1) boundary-based and (2) region-based methods. Detailed descriptions of these can be found in [188, 191, 192]. Boundary-based methods consider that the arbitrary region consists of a set of points sampled from the region. Prior research in image analysis and computer vision have employed a variety of techniques including linear least squares, weighted least squares, Kalman filtering and robust estimation methods[192, 193]. Region-based methods are frequently used in image processing and were chosen here to determine some geometric characteristics of flames. These methods are detailed by Gonzales and Wintz [191]. They use the moments of a region in calculating the best-fit ellipse [188, 194, 195], and equalise the second order moment of a region in order to determine the best-fit ellipse. In the case of regular shapes (i.e., region close to an ellipse) the aforementioned methods show no major difference in the result. For in-

cylinder flames, region-based methods are more appropriate as they are less affected by boundary irregularities.

The moment of $(w + q)$ order of a 2 dimensional arbitrary region (B) is given by [196].

$$M_{wq} = \iint_B f(x, y)x^w y^q dx dy \quad (60)$$

calculated over (B) . For regions where no properties are varied, function f has a value of unity. When $(w + q)$ equals zero, i.e., the zeroth moment is the area of region (B) , the centroids are given by the quotient of the first and zeroth moments:

$$\bar{x} = \frac{M_{10}}{M_{00}} \quad (61)$$

$$\bar{y} = \frac{M_{01}}{M_{00}} \quad (62)$$

Then, the central moments can be determined evaluating the following integral:

$$U_{wq} = \iint_B f(x - \bar{x})^w (y - \bar{y})^q dx dy \quad (63)$$

or can be written in terms of moments:

$$U_{00} = M_{00} \quad (64)$$

$$U_{10} = U_{01} = 0 \quad (65)$$

$$U_{20} = M_{20} \frac{M_{10}^2}{M_{00}} = \quad (66)$$

$$U_{02} = M_{02} \frac{M_{01}^2}{M_{00}} \quad (67)$$

$$U_{11} = M_{11} \frac{M_{10}M_{01}}{M_{00}} \quad (68)$$

Finally, the best-fit ellipse can be determined using the central moments:

$$O = \sqrt{4U_{11}^2 + (U_{20} - U_{02})^2} \quad (69)$$

$$\epsilon = \frac{1}{2} \tan^{-1} \left(\frac{2U_{11}}{U_{20} - U_{02}} \right) \quad (70)$$

$$SA_{maj} = \sqrt{\frac{2(U_{20} + U_{02} + O)}{U_{11}}} \quad (71)$$

$$SA_{min} = 2 \sqrt{\frac{2(U_{20} + U_{02} - O)}{U_{11}}} \quad (72)$$

where, SA_{maj} ; SA_{min} and ϵ are the semi-major, minor axes and the orientation angle respectively. In this work bitmap images were acquired from the high-speed camera, from which the central moment integral were obtained from:

$$U_{20} = \frac{1}{n} \sum_{i=1}^n (x_i - \bar{x})^2 \quad (73)$$

$$U_{02} = \frac{1}{n} \sum_{i=1}^n (y_i - \bar{y})^2 \quad (74)$$

$$U_{11} = \frac{1}{n} \sum_{i=1}^n (x_i - \bar{x})(y_i - \bar{y}) \quad (75)$$

and can be calculated fairly easily using a computer code.

3.6 Determining flame speed from fitted ellipses

Once the semi-major and minor axes were calculated for each image, the difference in their length was determined by:

$$\Delta da_{(t)} = da_{(t)} - da_{(t-1)} \quad (76)$$

where, in this case da is SA_{max} or SA_{min} . Dividing the change in length with the known time interval gives the instantaneous flame speed at the given time:

$$S_{n(t)} = \frac{\Delta da_{(t)}}{\Delta t} \quad (77)$$

This instantaneous flame speed $S_{n(t)}$ provides an insight into the local disturbances at a given time after ignition, but provides no information of the overall propagation of the combustion. The time-averaged flame speed $\overline{S_{n(t)}}$ is required for calculating the burned mass fraction or for determining the exact position of the flame fronts.

$$\overline{S_{n(t)}} = \frac{\Delta da_{(t)}}{t} \quad (78)$$

This averaged value is less affected by random errors and is more pronounced for fuels that are less stable and are likely to have higher fluctuation in flame front movement.

3.7 Shape factor

There are many ways to arrange geometric parameters of a shape non-dimensionally. Details of shape descriptors can be found in [188]. Usually geometric

regions are circular when their descriptor value approaches unity. Here the shape evolution of SA_{max} and SA_{min} are of interest. Their most suitable descriptor is roundness RNS , which does not vary with the boundary irregularities (local shape wrinkles or disturbances).

$$RNS = \frac{4A}{\pi D_f^2} \quad (79)$$

where, A is the area of a region and D_f is Feret's diameter, the longest distance between any two points along the boundary of a region.

3.8 The data processing code

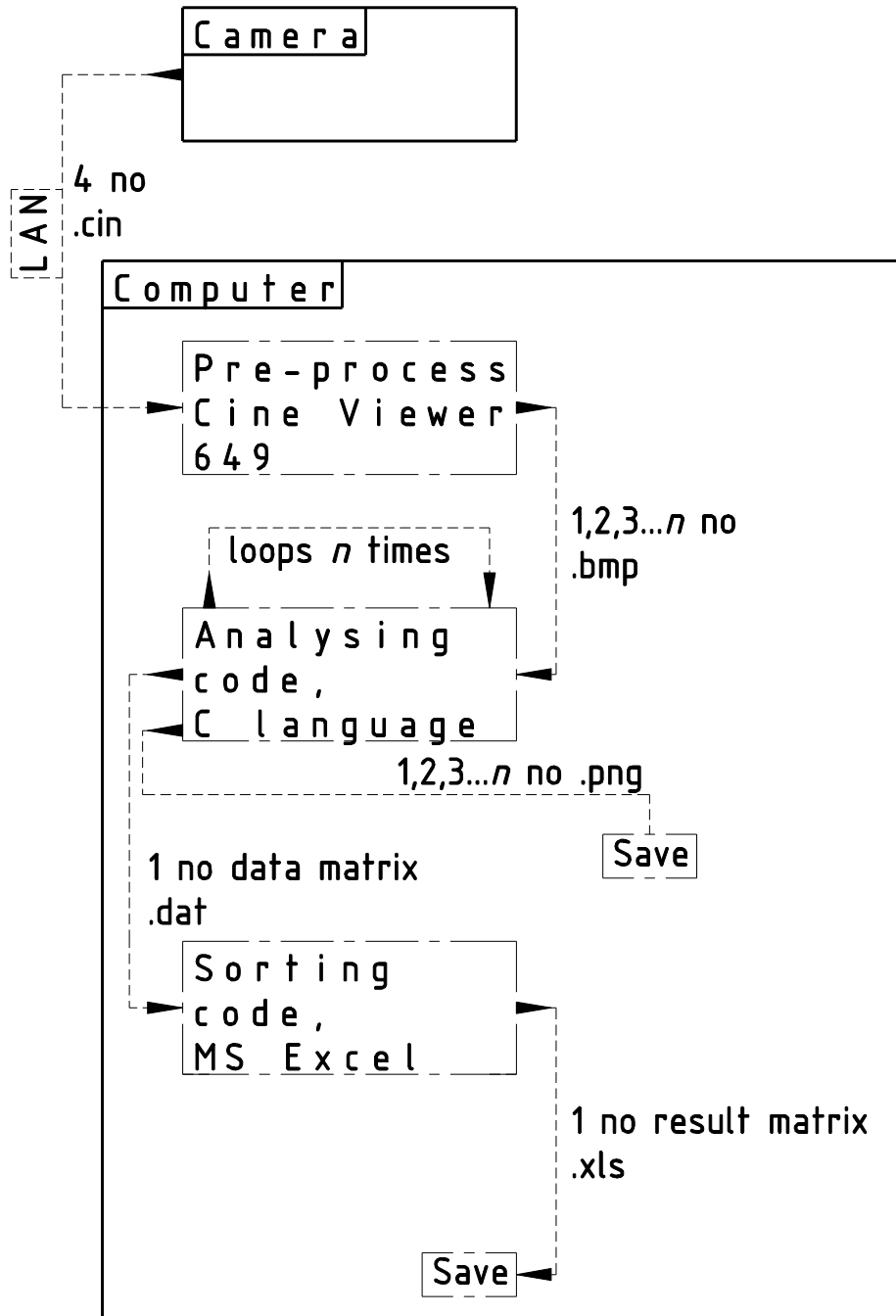


Figure 43. Flow chart of the analysing computer code

As explained earlier, the camera's internal memory could store only about 30 to 33 combustion events. Therefore the camera's memory had to be cleared regularly; the data had to be transferred four times to a computer at each test condition to obtain at least 120-125 full combustion processes. At this stage of the analysis, the optical data was in Kodak Cineon Image files (.cin). The four, 1 GB sized .cin files were transferred to a computer via a LAN cable.

In the next step, the large video file was saved in a series of bitmap files by a program called Cine Viewer 649 supplied by Vision Research, [197]. The images were saved as 24-bit .bmp files. The actual images had only 256 greyscales (8-bit) but the analysing code worked faster with the larger (98 kB), 24-bit bitmaps rather than the memory saving 8-bit ones. Altogether, about 132000 .bmp files were created from the four video files.

Once the conversion to images was completed, the C language analysing code was executed. The files in the series were opened one by one until the last one in the series. The same set of operations was carried out on each of them and the results were saved in a data matrix. Firstly, each image was cropped. The edges where there was some noise concentration were trimmed off, as shown in Figure 37. It was a systematic error; therefore the size of the trimmed of area was easily determined and could be kept the same for the whole analysis. Then, the background noise was removed; a constant threshold value was subtracted from the value of every pixel. In order to determine this threshold, the pixel value histogram was analysed. The

pixel value for the occurrence of the first sharp rise was determined and pixels with this value were considered as flame. Pixel values below this were categorised as noise.

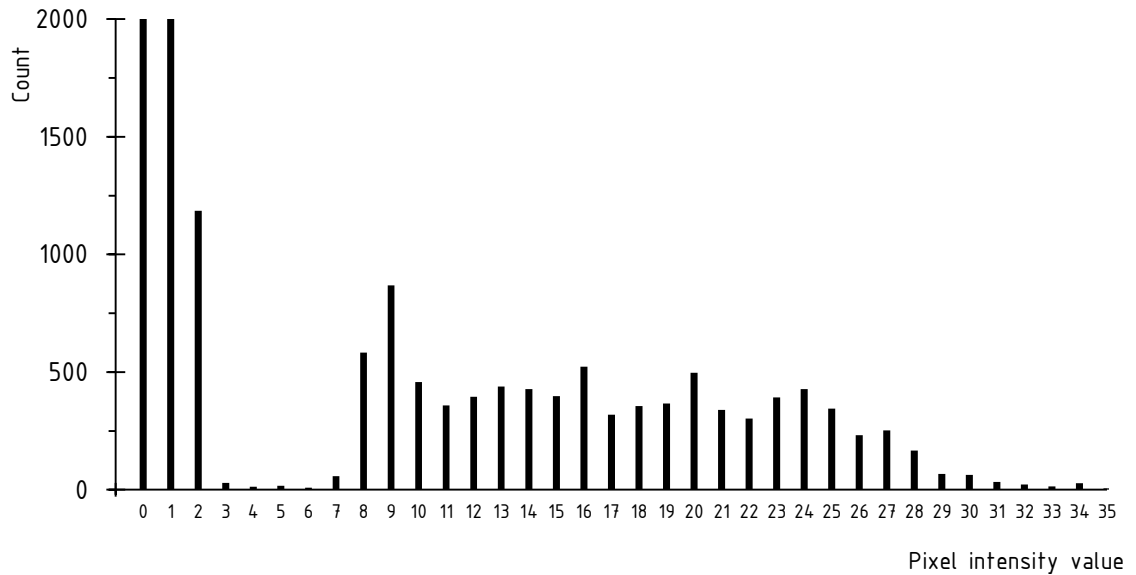


Figure 44. A typical histogram of pixel values on recorded raw image

After this, the image was binarised, i.e. all of the remaining pixels with any value were turned into the maximum value of 255. Edges of the main flame area were detected and then all the pixels outside the main boundaries were deleted from the image. Typically, these discrete scattered points or small cluster of pixels had a total area of less than 0.2% of the main flame. The code was to send an error message if this area exceeded 0.4%, but would carry on with the analysis. Finally, the ellipse fitting subroutine was applied to the region representing the flame. The code saved the results in a matrix as a .dat file. Before the next image was opened, the code saved the binarised image as .png file in a separate folder (see Figure 45). The image

manipulating operations and the ellipse fitting algorithm were called from a freeware, ImageJ [198].

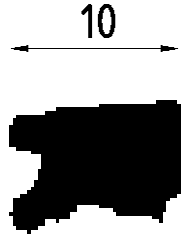


Figure 45. Sample .png binarised image, E85 at CR: 5.00 and 1500 rpm, this image is the 9th in the series after spark onset

The data file was then fed into a sorting spread sheet. Here, from the data matrix, the ignition events were detected – roughly, 120 of them. For each ignition event 30 images, set of data were separated. The first line of data corresponding to the first image only had the striking spark, then the next one captured the flame kernel 67 μ s later, and so on up to

$$30 \times 67\mu\text{s} = 2010\mu\text{s} \quad (80)$$

Then 30 matrices were created – one for each time after stark onset. Each matrix had 120 lines of results of the analysis (area of flame, fitted ellipse, roundness, etc.). The computer code had a comparison loop that compared the four series of data to each other to check the stability of conditions and to look for contamination on the window.

Finally, the data organised by time after ignition was opened in MS Excel for statistical analysis and presentation of results.

4 Experimental results and discussion

4.1 Statistical analysis

4.1.1 Sources of systematic and random error in measurements

During recording, especially during the early stages of flame initiation, the experimental apparatus had to capture flames with lowlight intensity for short times. Therefore, the optical setup was calibrated to its highest sensitivity. This meant that one of the major sources of uncertainties was light entering the optical path from outside. The underground location of the laboratory helped to provide nearly complete darkness for the tests. High-transparency window material and a high reflectivity optical mirror were used; therefore errors arising from scattering, absorption, etc. were neglected. Errors from the complementary metal-oxide semiconductor (CMOS) sensor and the computer's internal clock were considered not to be significant. Changes in the air fuel mixture, quality of sparks, distance of engine and CMOS sensor were considered as random uncertainties and the result of the combination of these was an overall error in each measurement.

This resultant error was considered to arise from a combination of an infinitely large number of infinitesimally small errors, which was expected to show a normal frequency data distribution, according to the Central Limit Theorem in statistics [199].

4.1.2 Data distribution and relative standard error

Figure 46 is typical of statistical data obtained for all conditions in this research. It illustrates that the data has a normal distribution, and that statistical analysis of the data with normal-distribution statistics is a justified approach. The only exception was the very first data point, images recorded at 67 μs after spark onset, as it was explained in the Imaging system section. Some the reflection of the brighter sparks from the bottom of the combustion chamber was captured. The additional and not true bright area resulted in a skewed histogram of measurements Figure 40.

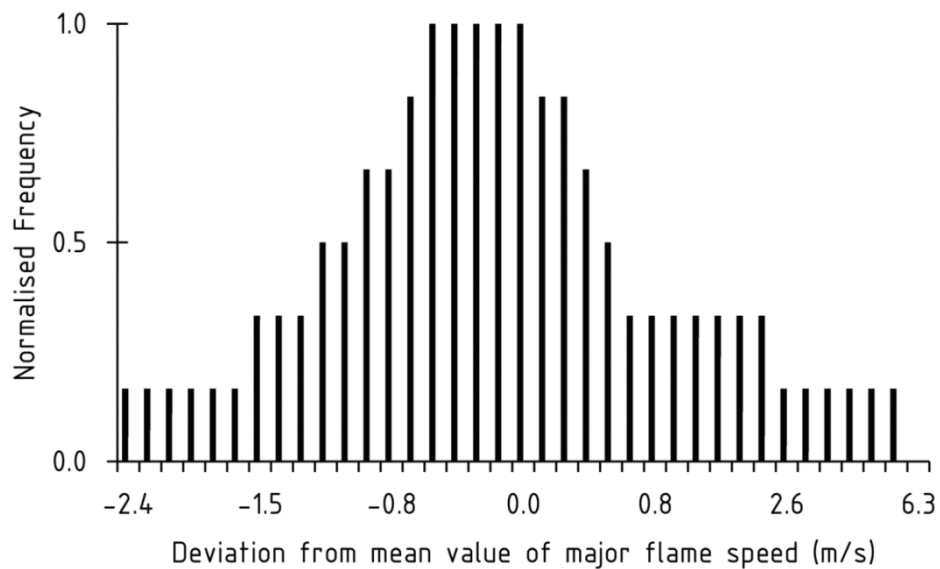
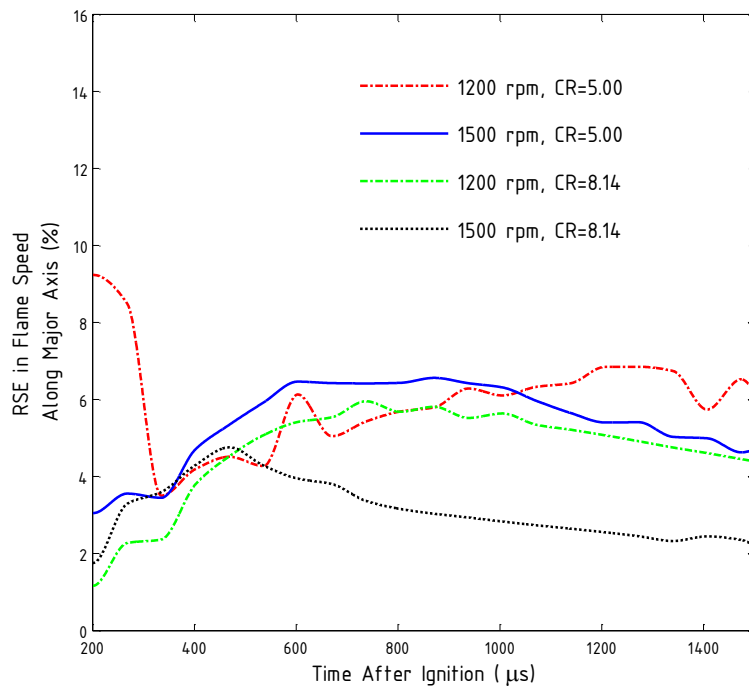


Figure 46. Sample data distribution, in this case for M85, 1200 rpm, CR = 5.00, 804 μs ,

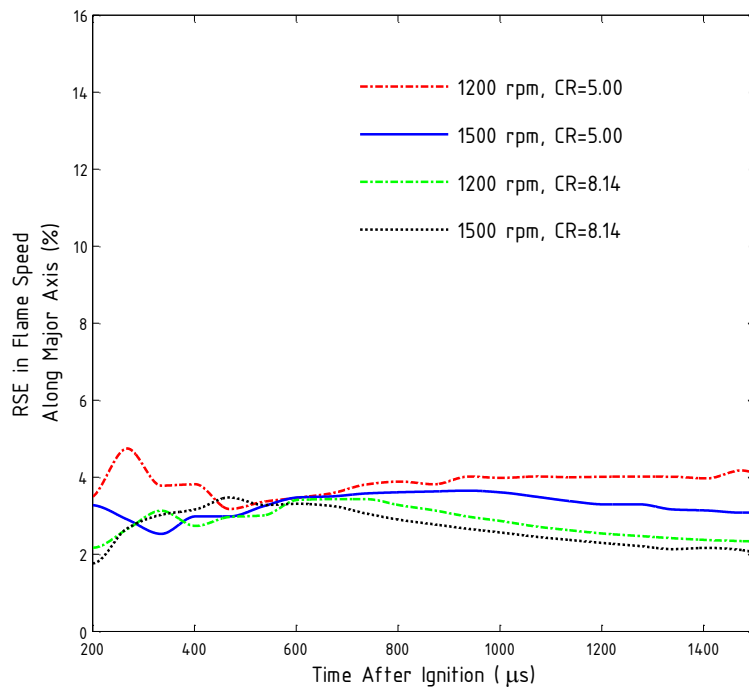
$$S_{t=804} = (5.9 \pm 0.15)\text{m/s}$$

The values of the relative standard error (RSE) in major flame speed measurements for data point recorded at 134 μs and later were plotted in separate graphs for each

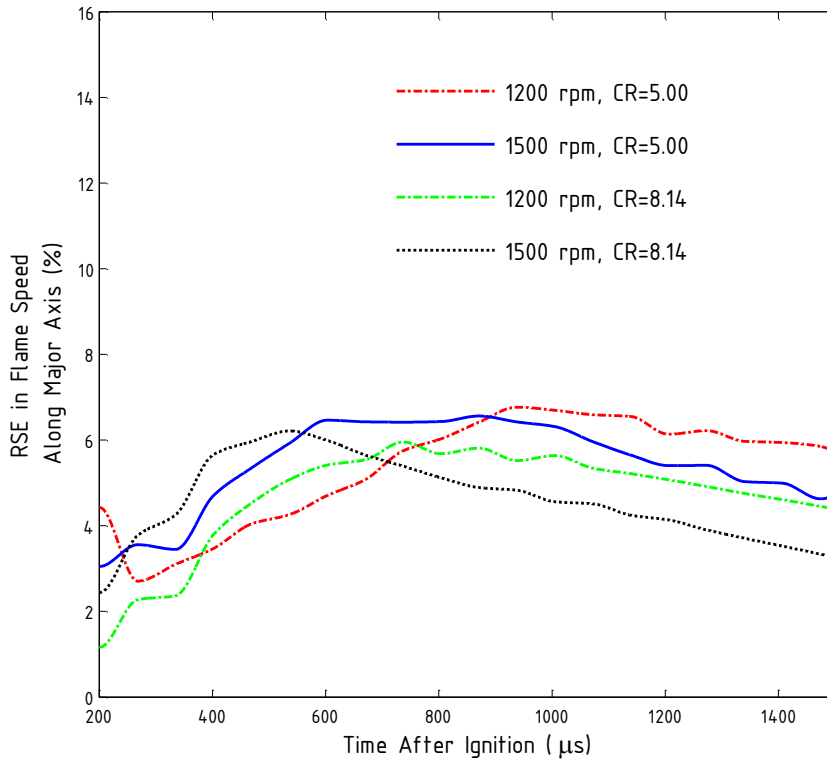
fuel in Figure 47. The absolute values of errors of all data points were plotted on the flame speed graphs Figure 49, Figure 50 and Figure 51. Similar uncertainty values were found for minor flame speed and roundness (these figures are not included for brevity). In general, uncertainty analysis showed that at lower speeds and CR the errors were higher, suggesting a worse air fuel mixing, bigger large scale eddies caused by lower level of turbulence and more spacious combustion chamber respectively, and higher coefficient of variation in these conditions.



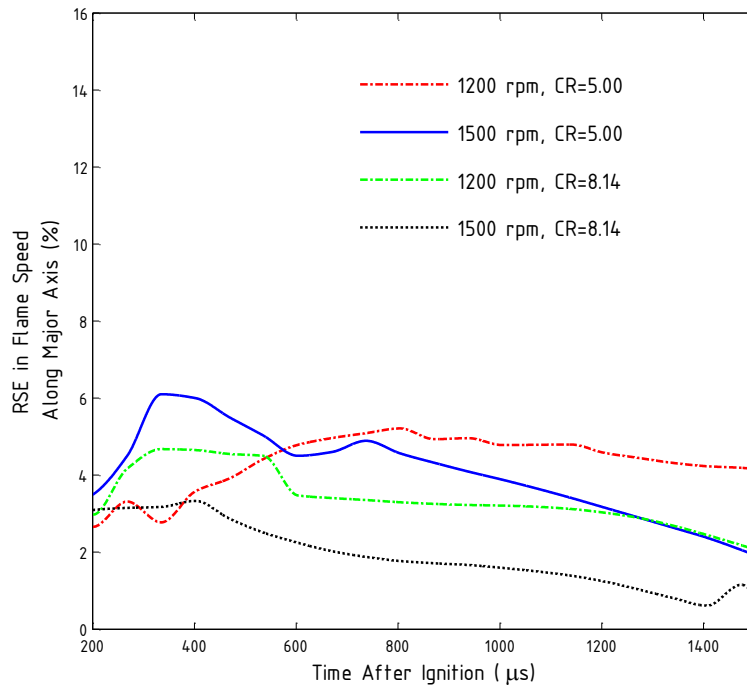
a,
isooctane



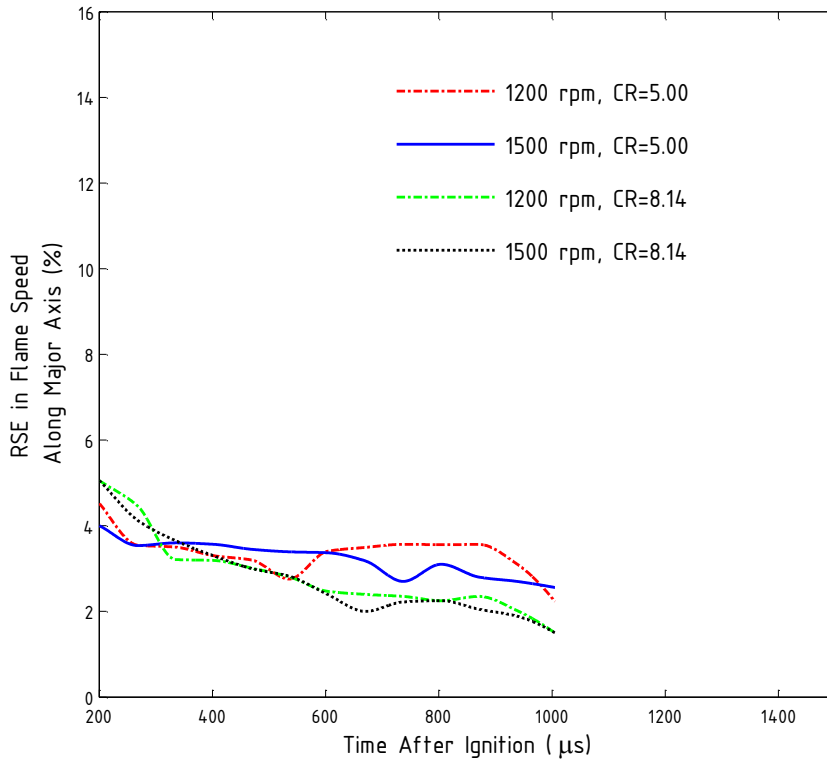
b,
gasoline



c,
E85



d,
M85



e,
hydrogen

Figure 47. RSE in calculated flame speed along the major axis at selected CRs and engine speeds for a, isoctane b, gasoline c, E85 d, M85 e, Hydrogen

Variations in the energy, the striking location of the spark and some reflection caused higher uncertainty values near 67 μs after ignition. The lower energy flame propagation at times near 134 μs after ignition resulted in moderate uncertainty values from those near 67 μs after ignition. The exothermic combustion kinetics dominates at 200 μs after ignition and later on. The relative magnitude of turbulent fluctuating velocity to flame speed affects uncertainty of measurements. Therefore when the flame speeds are lower (soon after 200 μs) the uncertainties are higher than when flame speeds are higher (e.g. near 1200 μs).

Higher speeds and higher compression ratios promote better mixing, so that uncertainties are lower in these cases for all fuels. It can also be seen that the RSE decreases with time.

The RSE graph for Hydrogen fuel showed a significantly different characteristic from the liquid fuels. Firstly, there was no local minimum visible on the curves between 134 and 200 μs . From the high laminar flame speed value of Hydrogen and its simpler molecular structure, it can be seen that Hydrogen needs less time to form radicals and become oxidised.

4.2 Flame speed curves as function of fuel type and engine conditions

Figure 49, Figure 50 and Figure 51 show the result of image analysis as instantaneous flame speed and roundness curves against time after ignition.

A set of curves were plotted for each liquid fuels. The chart on the top shows the whole investigated time period. This chart allows the direct comparison of the fuel types and shows the large initial peak values. Then, the next graph shows a closer view with a reduced time range to give a better view of the flame speed and roundness curves of the combustion kinetics ruled flame propagation. Finally, the error bars are shown on the major flame speed curves. There are two charts showing the results for each fuel, in total there are four graphs with error bars in the figures for the liquids. The first graph indicates the spark boosted, shorter period of time 0-

134 μ s. Then the second plot is for the time after 200 μ s. In order to differentiate between the fuels all the curves are colour coded.

Some of the engine conditions were chosen to be similar to the ones that had been used by other authors, so that some of the results can be directly compared to the already published data for cross-comparison and validation. The ignition time was kept the same for test conditions and fuels, 20 degree BTDC. Table 13 summarises some of the most important variables that describes the conditions in the combustion chamber at the time of the ignition.

Table 13. Geometric and thermodynamic conditions in the combustion chamber at the time of spark onset

Variable	Engine speed (rpm)	CR	Value
Clearance Height (mm) at Tol / Eol	1200	5.00	32.10 / 30.74
		8.14	14.76 / 13.40
	1500	5.00	32.10 / 30.57
		8.14	14.76 / 13.23
Estimated Residual Mass Fraction (%)		5.00	~25
		8.14	~14
Volumetric Efficiency of Engine for Liquid Fuels (%)	1200	5.00	27.02±1.35
	1500	8.14	27.93±1.4
Volumetric Efficiency of Engine for Hydrogen (%)	1200	5.00	23.60±1.67
	1500	8.14	24.61±1.67
Pressure at Time of Ignition (bar)	1200	5.00	3.78±0.19
		8.14	6.29±0.31
	1500	5.00	3.97±0.20
		8.14	7.41±0.37
Spark Duration (ms)			1.48±0.19

Figure 49, Figure 50 and Figure 51 indicate that the visible flame area right after spark onset expands quickly; this fast propagation rate was measured to be around 50 m/s for the liquids but it exceeded 100 m/s for hydrogen. These large numbers are the results of the initial high energy input from the spark and some random error as it was discussed earlier. Then, the flame area undergoes a similarly fast contraction.

This flame contraction soon after the beginning of ignition might be caused by rapid endothermic dissociation of fuel molecules and the formation of radicals in the mixture [200-202].

In order to investigate this flame contraction further and to isolate the effect of the spark, experiments were carried out of discharging the spark plug at motored conditions in air. The same analysis procedure was carried out on the collected data and the results were presented in Figure 48. In this case, the maximum and minimum “flame speeds” of the gas ionised by the spark plug are about 12 m/s. When the plasma stabilised 200 μ s after spark discharge, its value of roundness remained stationary at around 0.75. This value describes the shape of the electric arc between the spark plug electrodes well. The shape and frequency trend of the growth and contractions of the “flame speed” curves were similar to the ones with the fuel added until about 250 μ s after Tol. On the other hand, the magnitude of these peaks and drops were significantly higher when fuel particles were present in the mixture. From the results, it can be seen that the fluctuating properties of the flame speed curves originated from nature of spark discharge. After 250 μ s, the curves that described the combustion supported growth still had some fluctuation, but the relative magnitude of these peaks and drops was significantly lower than the ones seen in Figure 48.

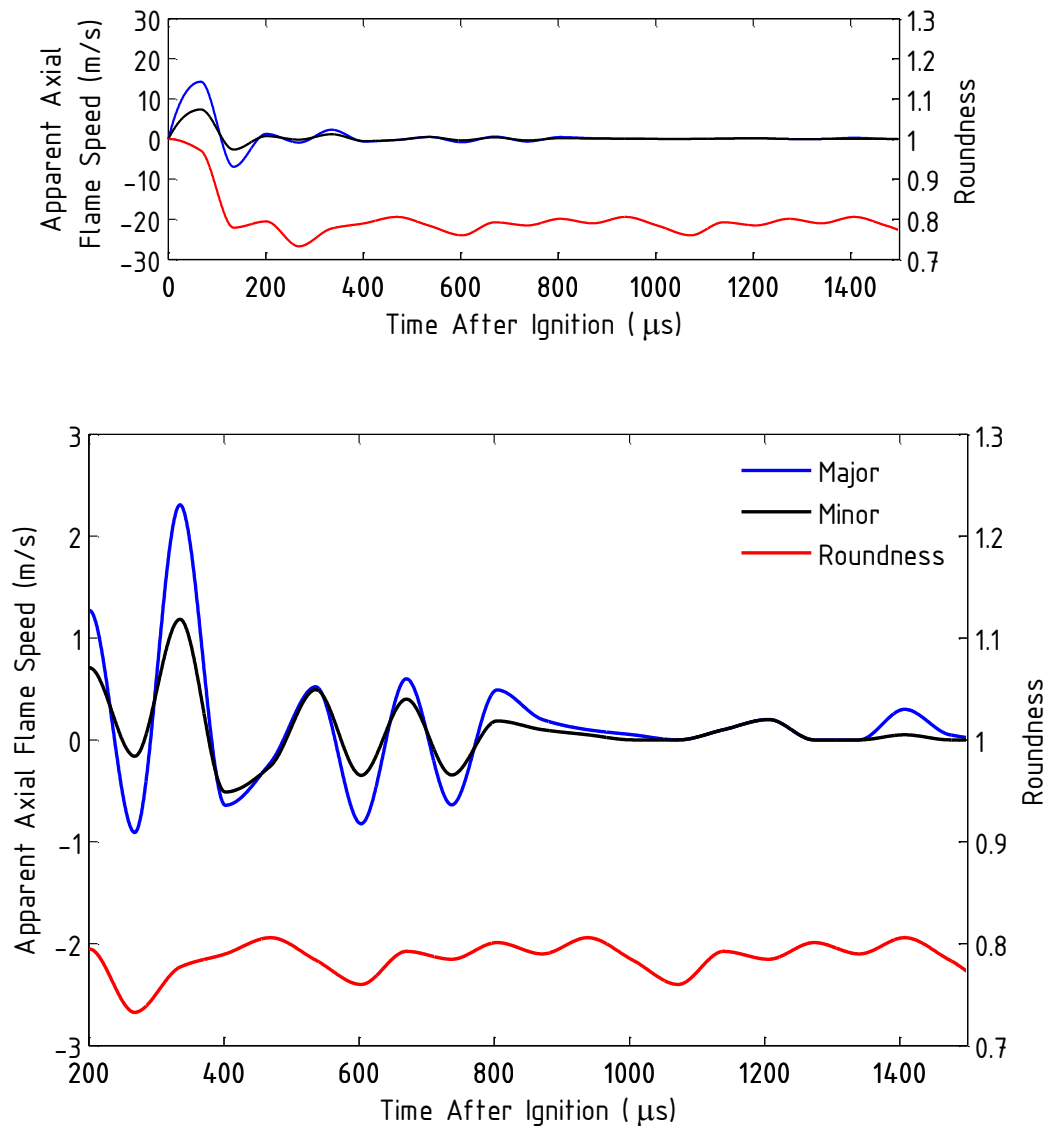


Figure 48. Apparent flame speed and roundness values of a spark discharging at 1500 rpm and CR: 8.14 in a non-combustible charge (air, plasma was considered to be flame)

In Table 15 flame speed results are shown for all conditions and fuels as a single value measured at 1000 μs after ignition. Flame speed values have been normalised to the results obtained from isoctane as base-fuel. This is discussed further under Isooctane result section.

Moreover, Table 16 summarises the effect of different engine speeds and higher CRs on the flame speeds of the tested fuels. In this table the major and minor flame speeds were normalised to the highest value condition (CR: 8.14, engine speed: 1500 rpm) in order to provide an easy comparison between the engine conditions. A general result is that flame speeds along the major axis are closer to the corresponding maximum values than the ones along the minor axis. This is a direct result of the initially highly distorted shapes becoming more circular as the minor axis elongated more during the flame development. It can be seen that M85 produced somewhat different results among the liquid fuels. This is probably the result of the aforementioned combustion kinetics, [203, 204]. The normalised values for isooctane, gasoline and E85 were quite similar (within about $\pm 10\%$), indicating that the flame propagation characteristics of these fuels tend to react similarly to changes of engine conditions. It is somewhat surprising to see that the results gained from hydrogen are similar to the ones from M85.

Table 14 shows a data matrix of the indicated mean effective pressure (IMEP) values and the corresponding coefficient of variance (COV) for each condition and fuel. The ignition timing was kept the same in order to provide a similar flow field for all fuels. The values of IMEP were below the levels of pressure produced of production engines. This was a result of number factors: the L-head has relatively larger surface where heat loss occurs, even the maximum CR was low compared to ones of the production engines and the engine was operating at a low volumetric efficiency.

Although, the data presented in Table 14 is only informative; it can be used for cross-comparison of the fuels. It is important to note that this work aimed to investigate the early stages of flame kernel formation and not the full combustion process which is described by the IMEP.

Table 14. Data matrix of IMEPs and the corresponding COVs for all conditions and fuels.

		Engine conditions							
		1200 rpm				1500 rpm			
		5.00		8.14		5.00		8.14	
Fuel		IMEP (bar)	COV (%)	IMEP (bar)	COV (%)	IMEP (bar)	COV (%)	IMEP (bar)	COV (%)
Gasoline		1.41	1.84	2.25	1.19	1.49	1.90	2.45	1.47
Isoctane		1.33	2.38	2.10	1.31	1.52	2.27	2.31	1.75
E85		1.23	2.45	2.07	1.33	1.32	2.08	2.27	1.77
M85		1.40	1.80	2.32	1.16	1.59	1.80	2.48	1.59
Hydrogen		1.47	1.84	2.49	1.17	1.64	1.88	2.49	1.61

Table 15. Flame speed values calculated using the EQR method and along the major and minor axes at 1000 μ s after Tol; for an easy comparison of fuels the EQR method speed values were normalised to flames speeds values of isoctane.

CR	-	5.00	5.00	8.14	8.14	
Engine Speed	(rpm)	1200	1500	1200	1500	
Isooctane	Major	(m/s)	3.10	5.66	10.11	13.76
	Minor	(m/s)	1.21	2.44	4.70	7.05
	EQR method	(m/s)	1.57	3.70	6.90	10.40
	Ratio to isoctane	-	1.00	1.00	1.00	1.00
Gasoline	Major	(m/s)	2.48	5.31	10.45	13.26
	Minor	(m/s)	1.36	2.58	4.70	6.70
	EQR method	(m/s)	1.80	4.12	7.05	10.31
	Ratio to isoctane	-	1.15	1.11	1.02	0.99
E85	Major	(m/s)	2.87	7.71	8.03	12.97
	Minor	(m/s)	1.30	3.57	4.42	7.55
	EQR method	(m/s)	1.91	5.20	7.14	9.10
	Ratio to isoctane	-	1.21	1.41	1.04	0.88
M85	Major	(m/s)	7.29	14.69	16.74	19.13
	Minor	(m/s)	3.88	7.36	7.63	9.69
	EQR method	(m/s)	4.95	11.01	11.84	14.40
	Ratio to isoctane	-	3.15	2.98	1.72	1.38
Hydrogen ¹	Major	(m/s)	10.39	19.40	24.72	27.10
	Minor	(m/s)	4.24	7.44	10.09	10.40
	EQR method	(m/s)	6.98	13.80	18.71	19.70
	Ratio to isoctane	-	4.44	3.73	2.71	1.89

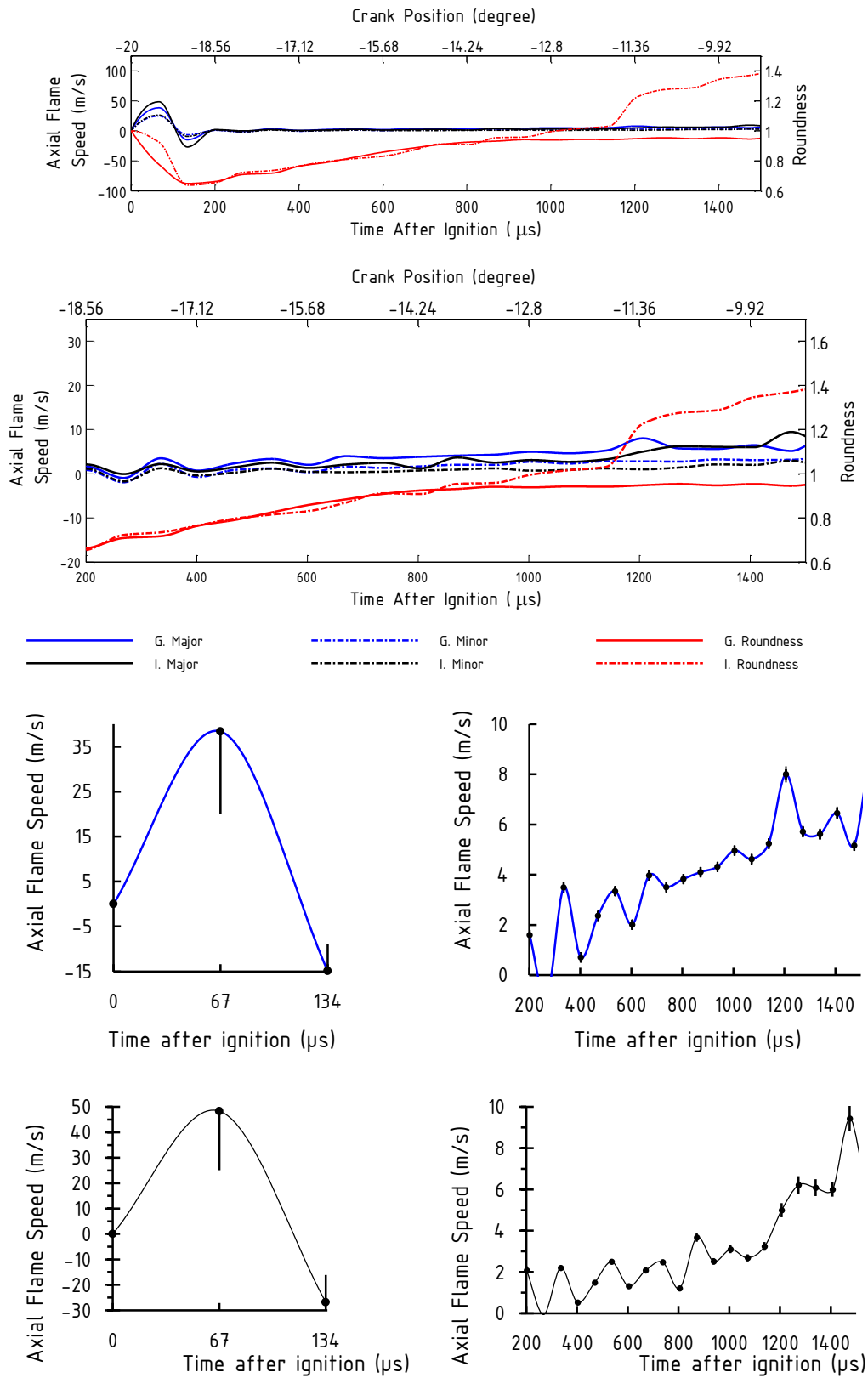
¹ values at 804 μ s after ignition

Table 16. Flame speed values along the major and minor axes at 1000 μ s AIT; for an easy comparison of the results from different engine conditions, a normalised value is shown for each result and condition.

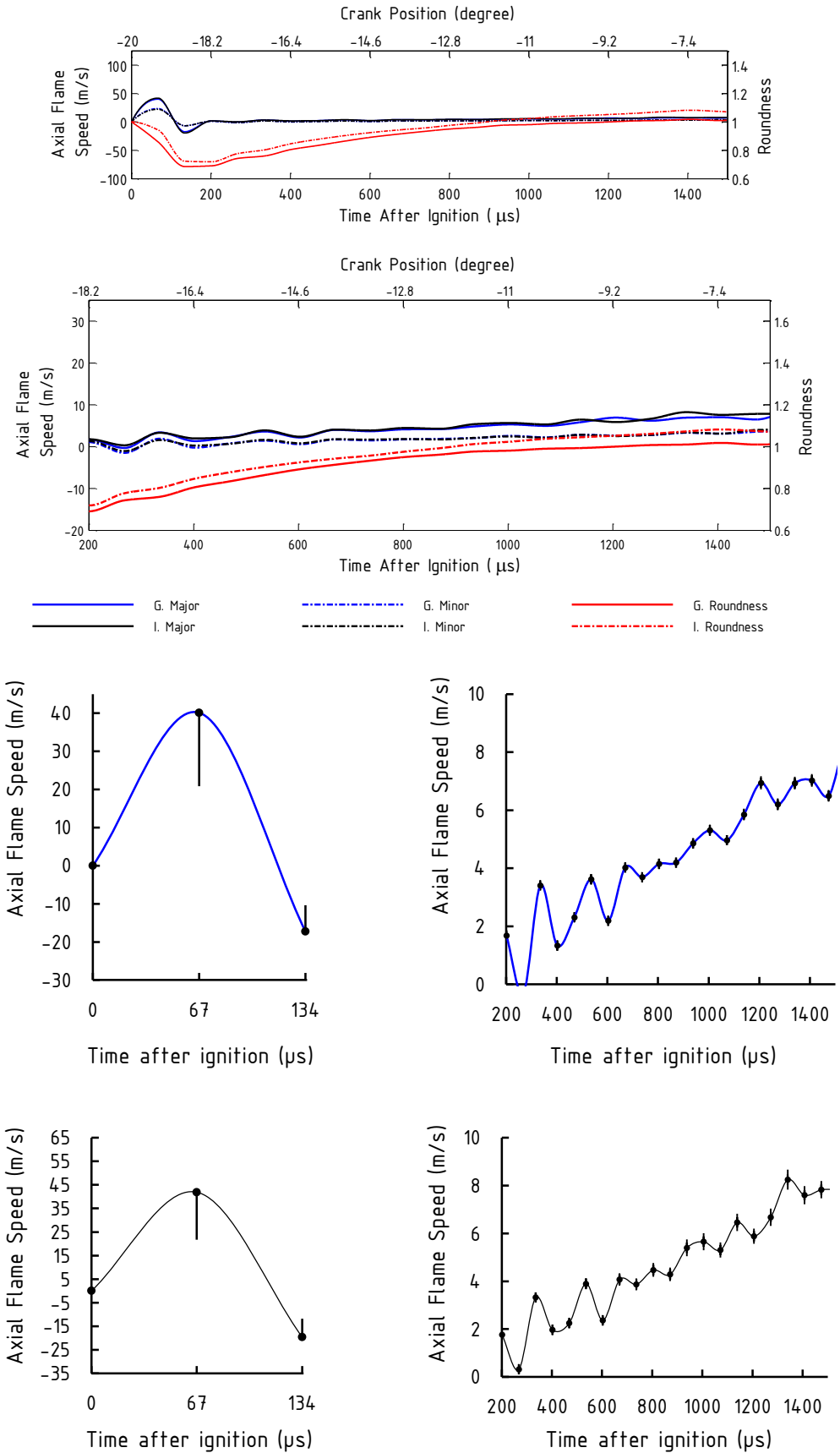
CR	-	5.00	5.00	8.14	8.14	
Engine speed	(rpm)	1200	1500	1200	1500	
Isooctane	Major	(m/s)	3.10	5.66	10.11	13.76
	Condition ratio	-	0.23	0.41	0.73	1.00
	Minor	(m/s)	1.21	2.44	4.70	7.05
	Condition ratio	-	0.17	0.35	0.67	1.00
Gasoline	Major	(m/s)	2.48	5.31	10.45	13.26
	Condition ratio	-	0.19	0.40	0.79	1.00
	Minor	(m/s)	1.36	2.58	4.70	6.70
	Condition ratio	-	0.20	0.39	0.70	1.00
E85	Major	(m/s)	2.87	7.71	8.03	12.97
	Condition ratio	-	0.22	0.59	0.62	1.00
	Minor	(m/s)	1.30	3.57	4.42	7.55
	Condition ratio	-	0.17	0.47	0.59	1.00
M85	Major	(m/s)	7.29	14.69	16.74	19.13
	Condition ratio	-	0.38	0.77	0.87	1.00
	Minor	(m/s)	3.88	7.36	7.63	9.69
	Condition ratio	-	0.40	0.76	0.79	1.00
Hydrogen ¹	Major	(m/s)	10.39	19.40	24.72	27.10
	Condition ratio	-	0.38	0.72	0.91	1.00
	Minor	(m/s)	4.24	7.44	10.09	10.40
	Condition ratio	-	0.41	0.72	0.97	1.00

¹ values at 804 μ s after ignition

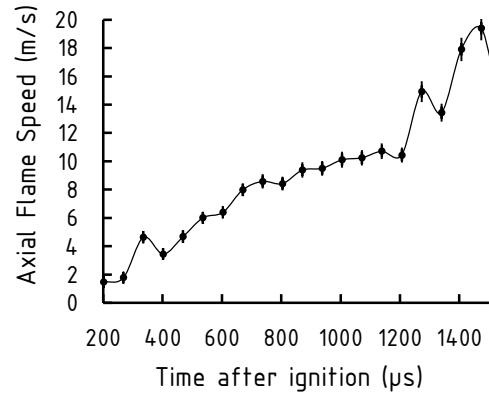
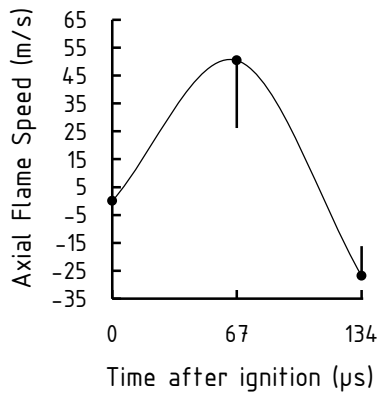
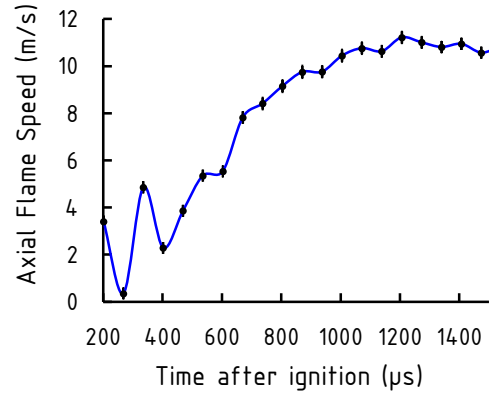
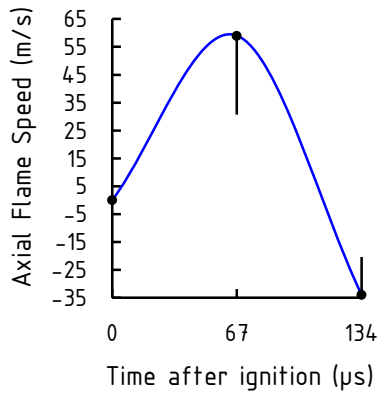
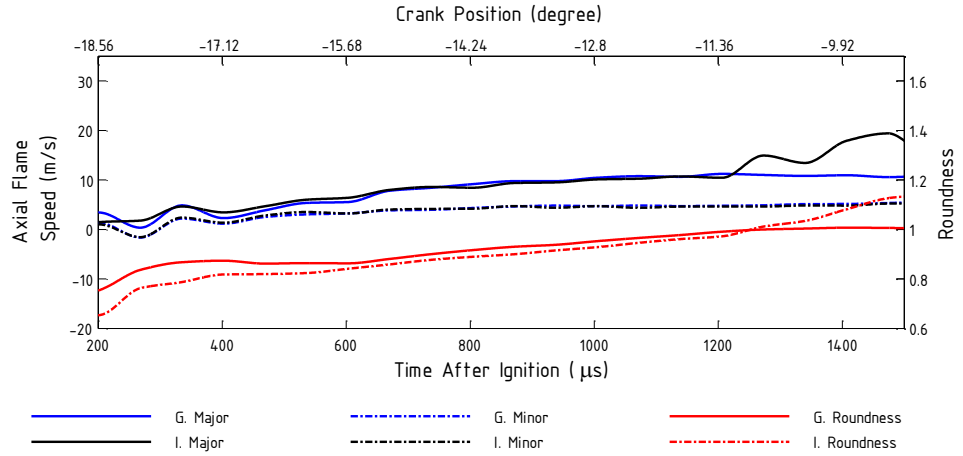
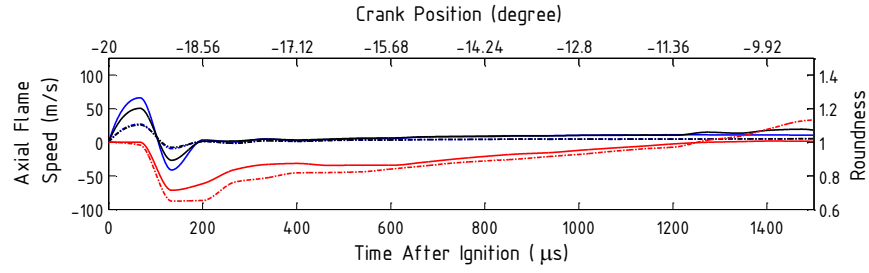
4.2.1 Isooctane and gasoline



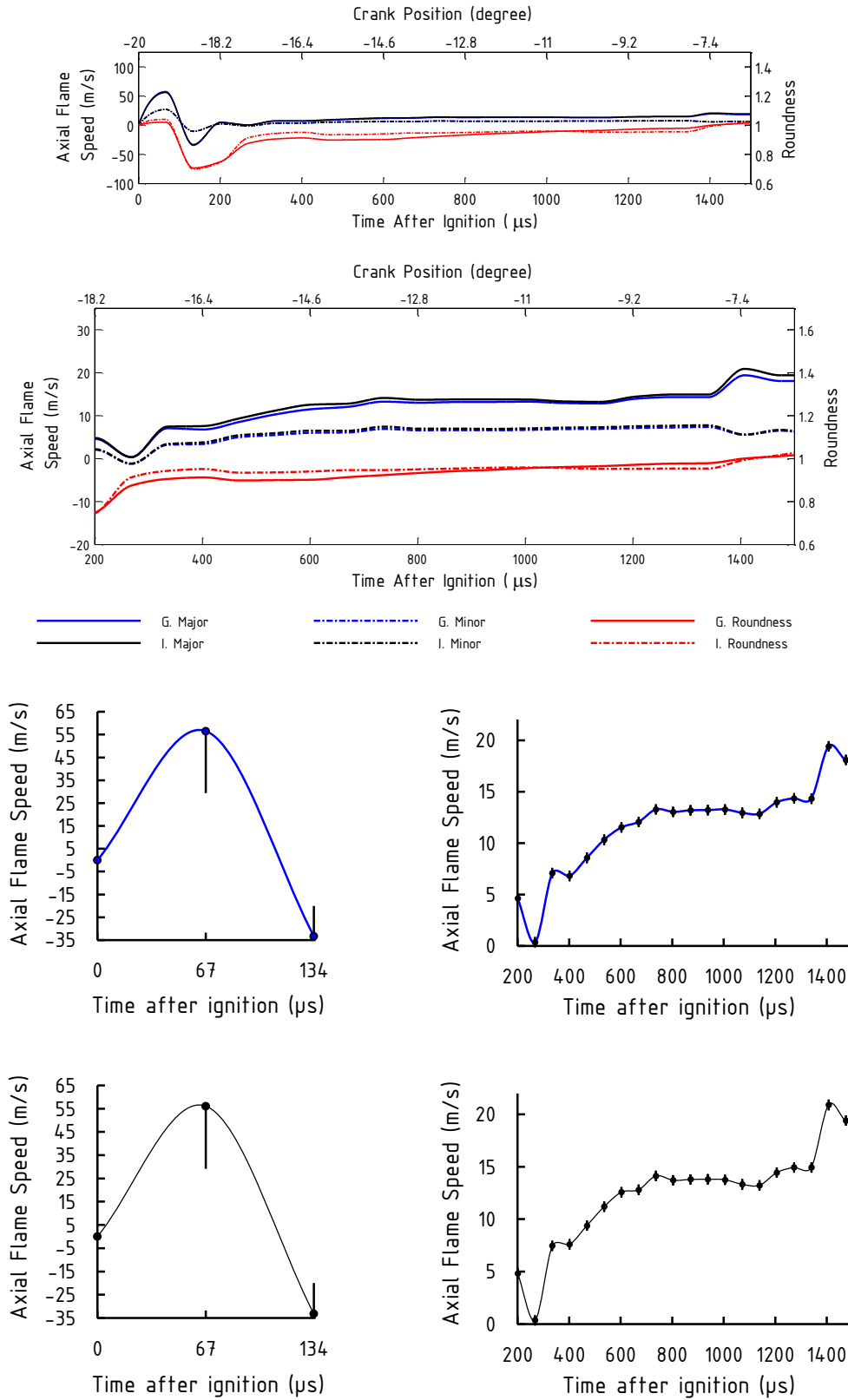
a, CR:5.00; 1200 rpm



b, CR: 5.00 1500 rpm



c, CR: 8.14 1200 rpm



d, CR: 8.14 1500 rpm

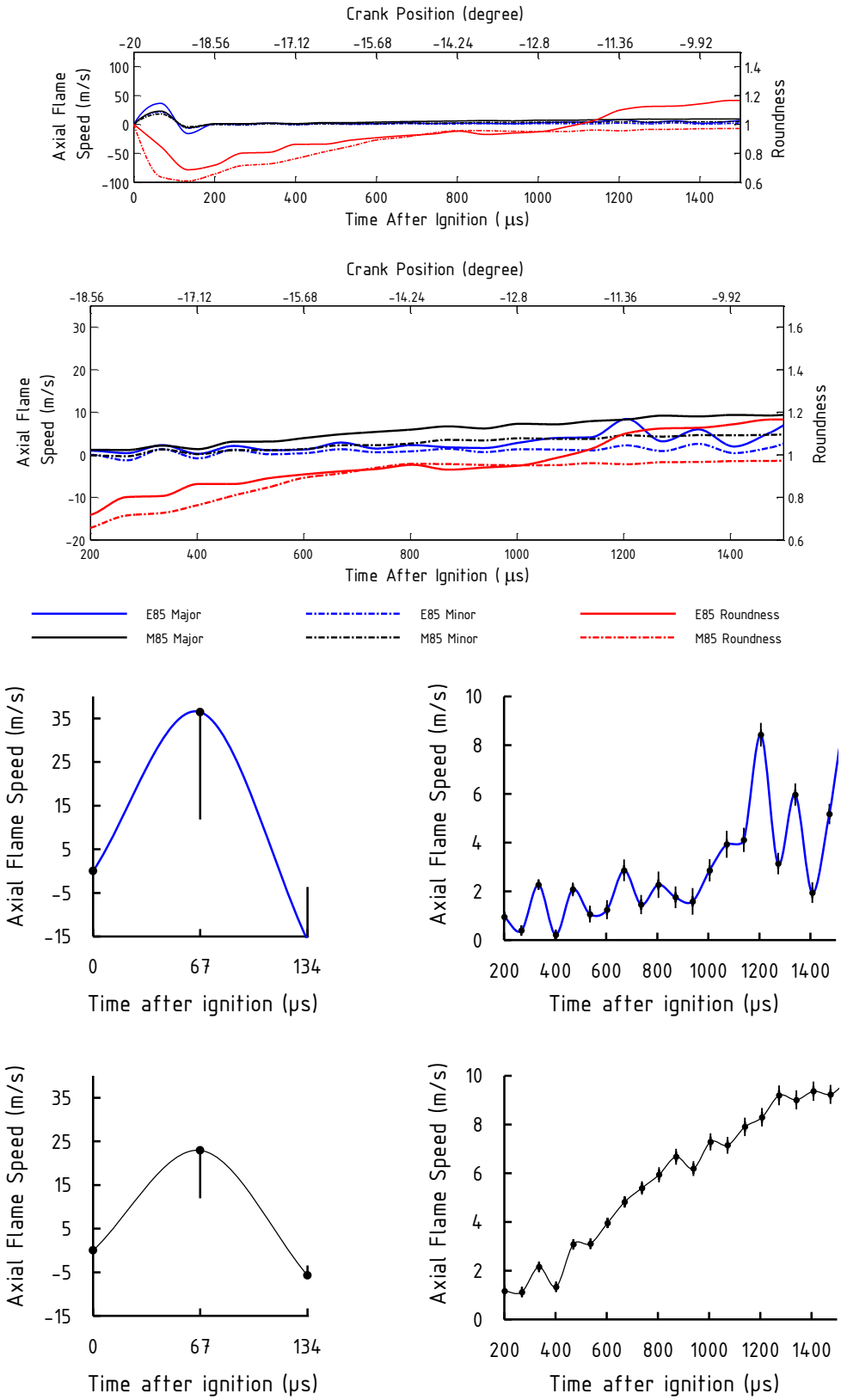
Figure 49. Instantaneous flame speed and roundness curves of isooctane and gasoline at different engine conditions; a, CR: 5.00 engine speed: 1200 rpm; b, CR: 5.00 engine speed: 1500 rpm; c, CR: 8.14 engine speed: 1200 rpm; d, CR: 8.14 engine speed: 1500 rpm

Isooctane and gasoline flames and some fitted ellipses are shown in Figure 53 at the condition of 1200, 1500 rpm and CR: 5.00. The slowest flame propagation was observed at 1200 rpm and CR: 5.00. The last image is the 41st in the particular series where the travelling flame reaches the edge of field of view. In Figure 53, only seven images are shown. The first three are continuous with temporal resolution of 67 μ s. Then the next three were selected randomly, and the final one is the last image in the series. Figure 49 and Figure 50 indicate that the visible flame area first expands and reaches maximum flame speeds of the order 50 m/s at about 67 μ s, then it contracts as indicated by minimum flame speeds of the order of -30 m/s at about 134 μ s, and then the flame speeds become positive again.

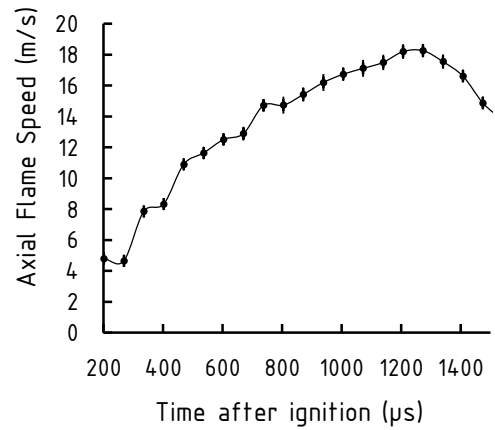
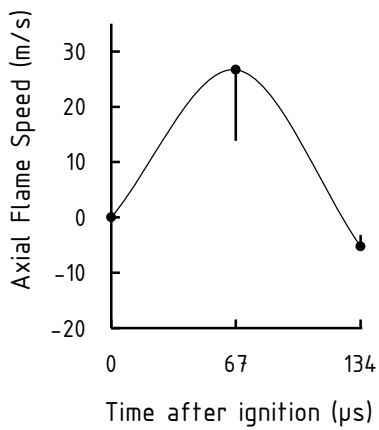
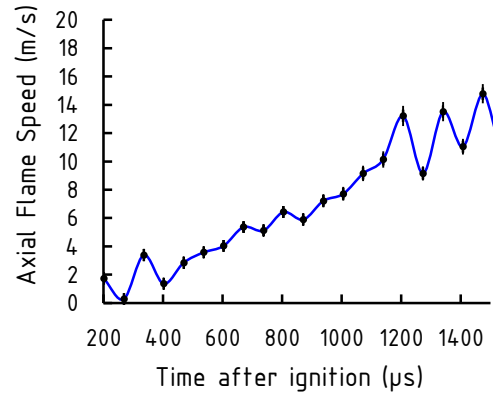
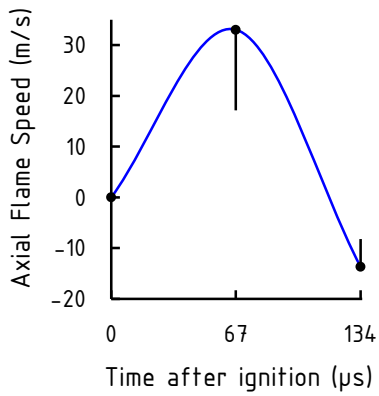
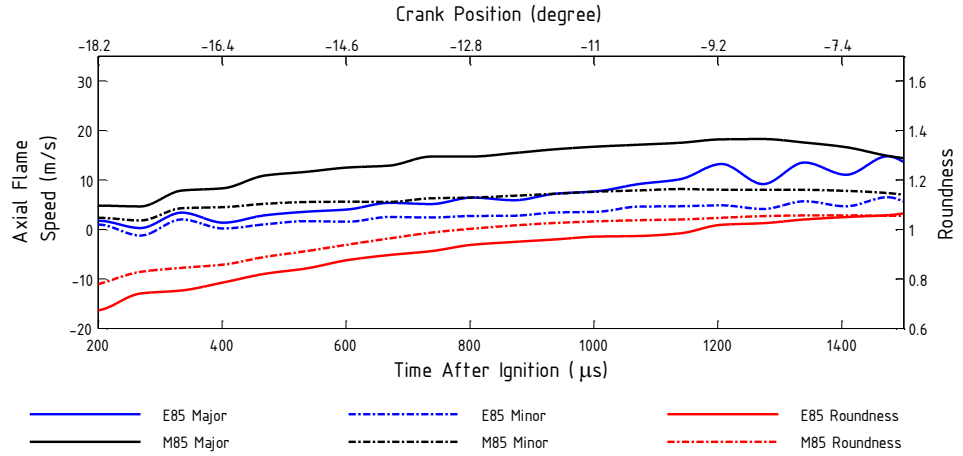
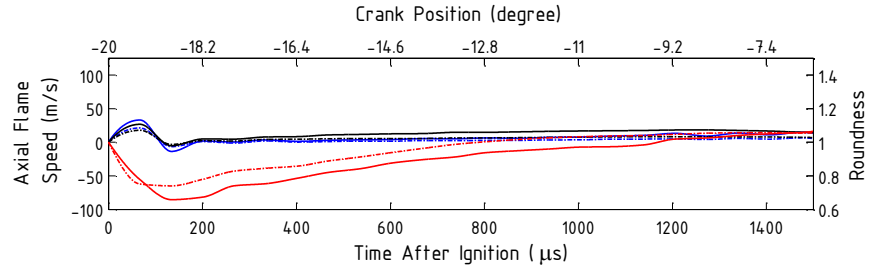
Isooctane (major: 13.76, minor: 7.05) [all flame speed data have a unit of m/s and at condition of CR: 8.14; engine speed: 1500 rpm; TAI: 1000 μ s] and E85 (major: 12.97, minor: 7.55) were found to have more unstable behaviour in combustion; their flame speed curves had more fluctuations than the other two fuels. These two fuels showed the largest changes in shape, sometimes exceeding unity of their shape factors. It seemed that all fuels would sooner or later reach a fairly stable flame speed value depending on the operating conditions. The rate of stabilising was found to be the lowest for isooctane, which in most cases had increasing flame speeds until the end of recording. In Table 15 flame speed results are shown for all conditions and fuels. Moreover, in order to compare fuels directly with each other, the EQR method values were normalised by ones of isooctane. Similar flame speed values

were measured for isooctane and gasoline (major: 13.20, minor: 6.70), and most of the time, the trend of their change in flame shape showed agreement. As it can be seen from Figure 49, their flame speed curves were overlapping, apart from the earliest times which were associated with higher uncertainties. Their similarity was more obvious at higher speed and CR where the normalised values showed only a couple of percentage points difference, but the largest difference was only about 15 %. In the case of gasoline, the results were only informative as its chemical properties were not guaranteed.

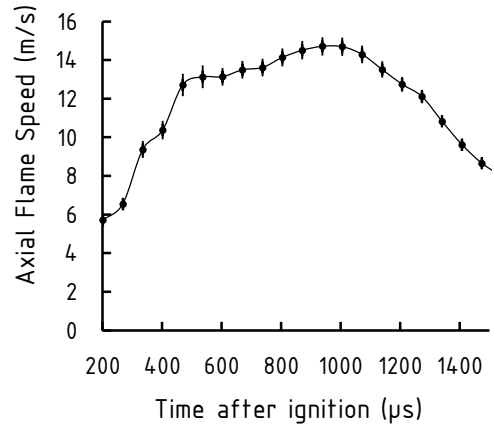
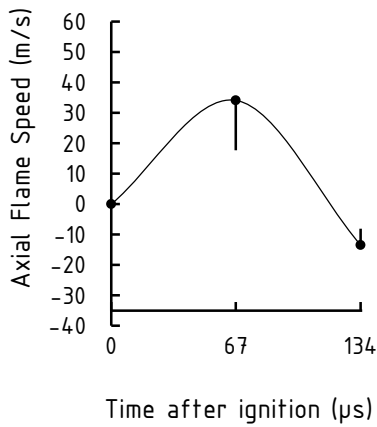
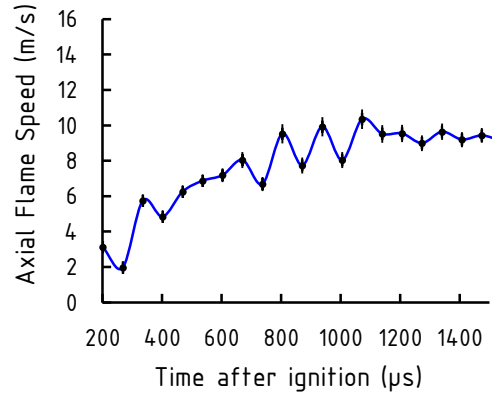
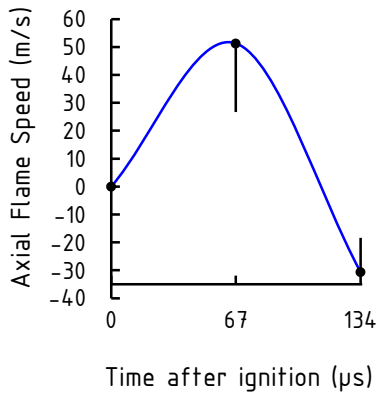
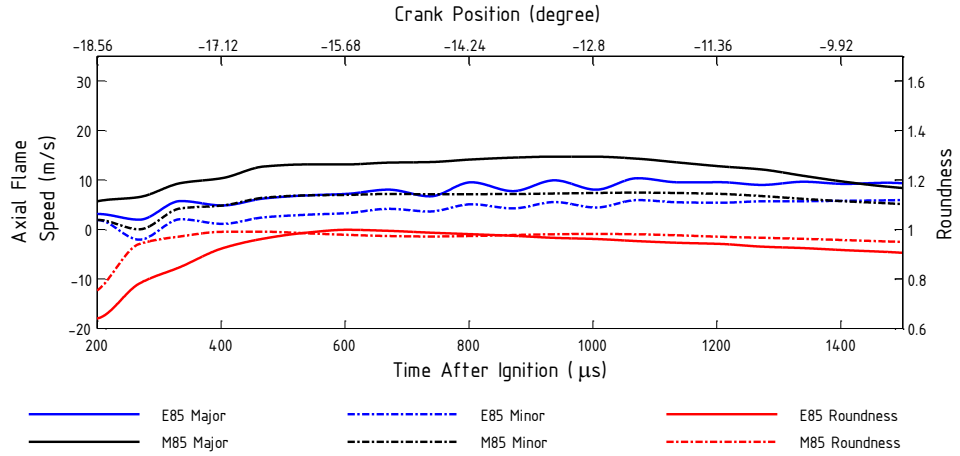
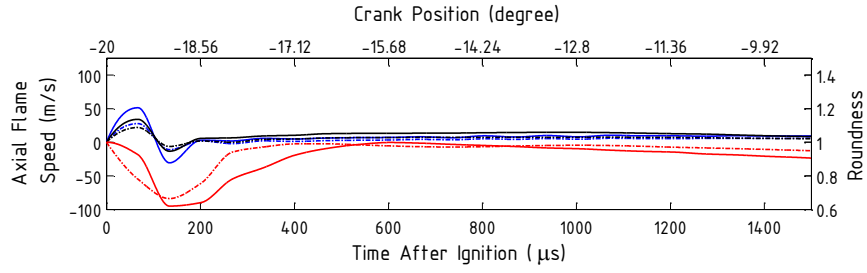
4.2.2 Alcohol blends



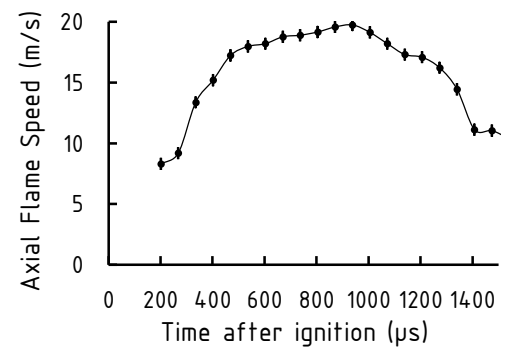
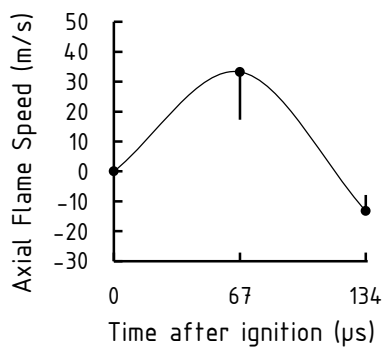
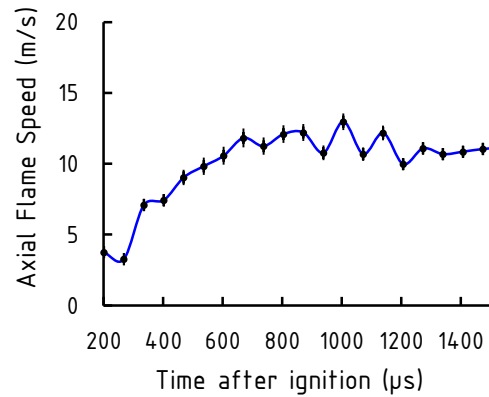
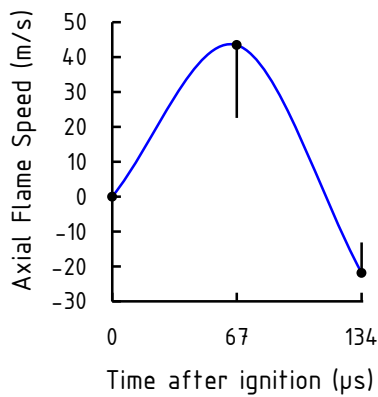
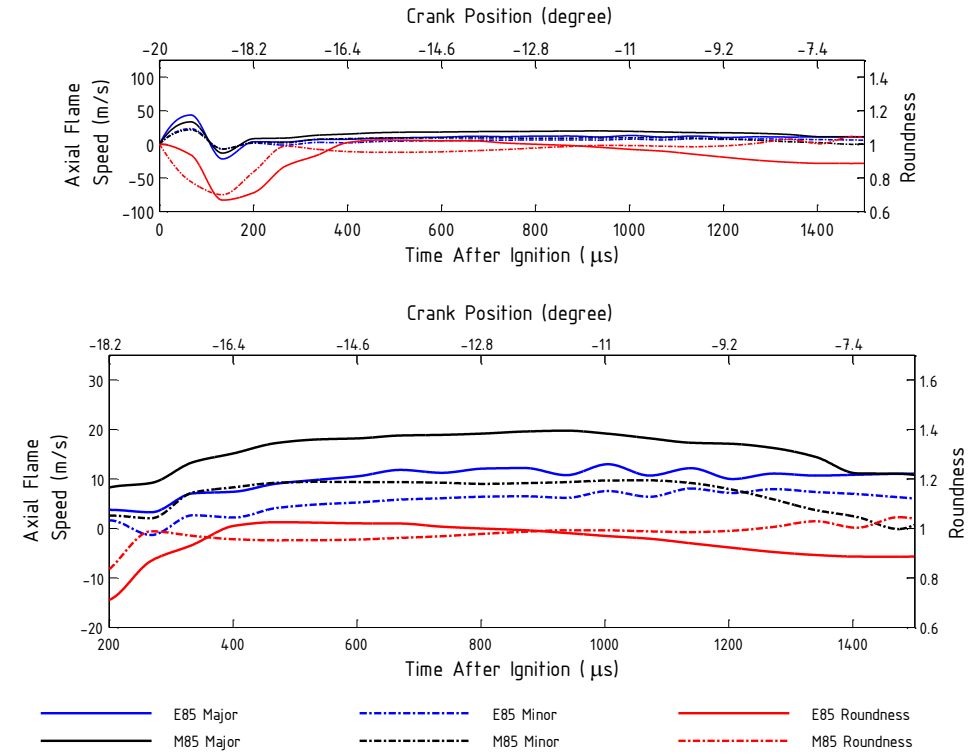
a, CR:5.00; 1200 rpm



b, CR: 5.00 1500 rpm



c, CR: 8.14 1200 rpm



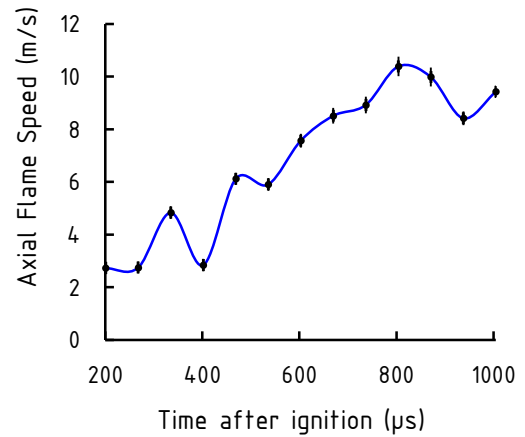
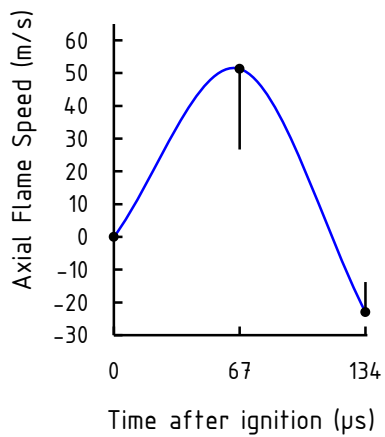
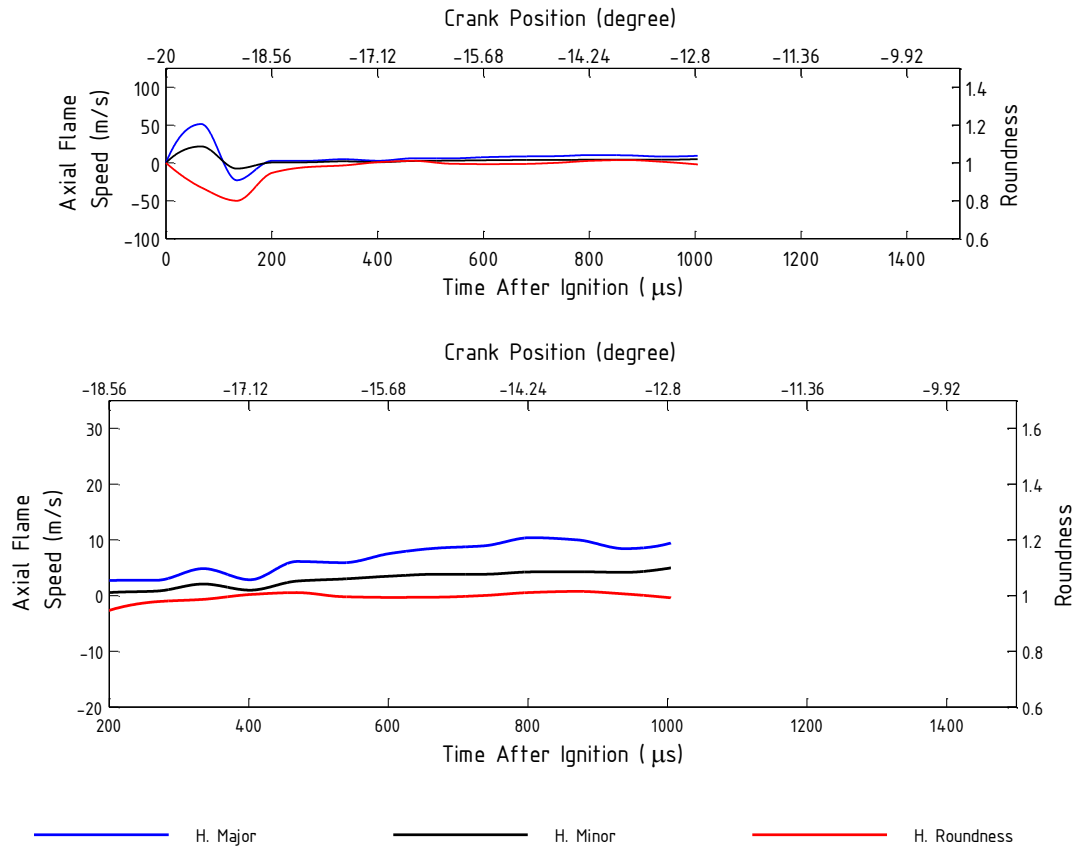
d, CR: 8.14 1500 rpm

Figure 50. Instantaneous flame speed and roundness curves of E85 and E85 at different engine conditions; a, CR: 5.00 engine speed: 1200 rpm; b, CR: 5.00 engine speed: 1500 rpm; c, CR: 8.14 engine speed: 1200 rpm; d, CR: 8.14 engine speed: 1500 rpm

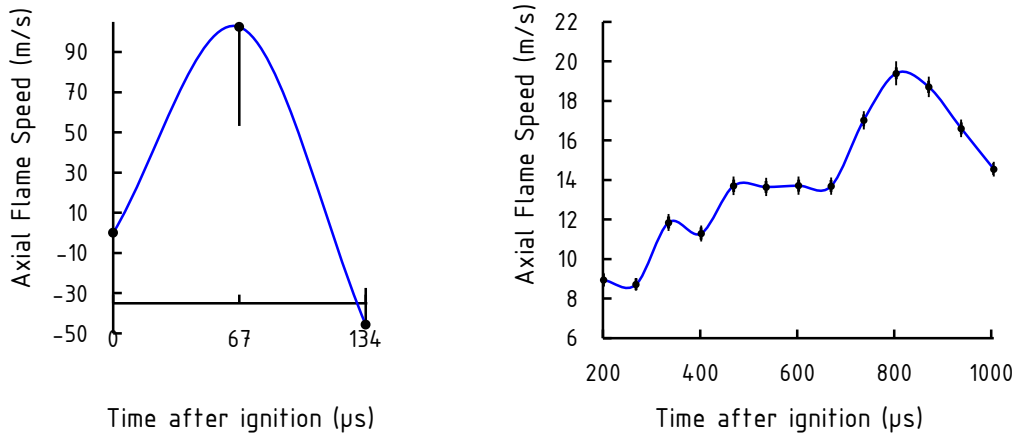
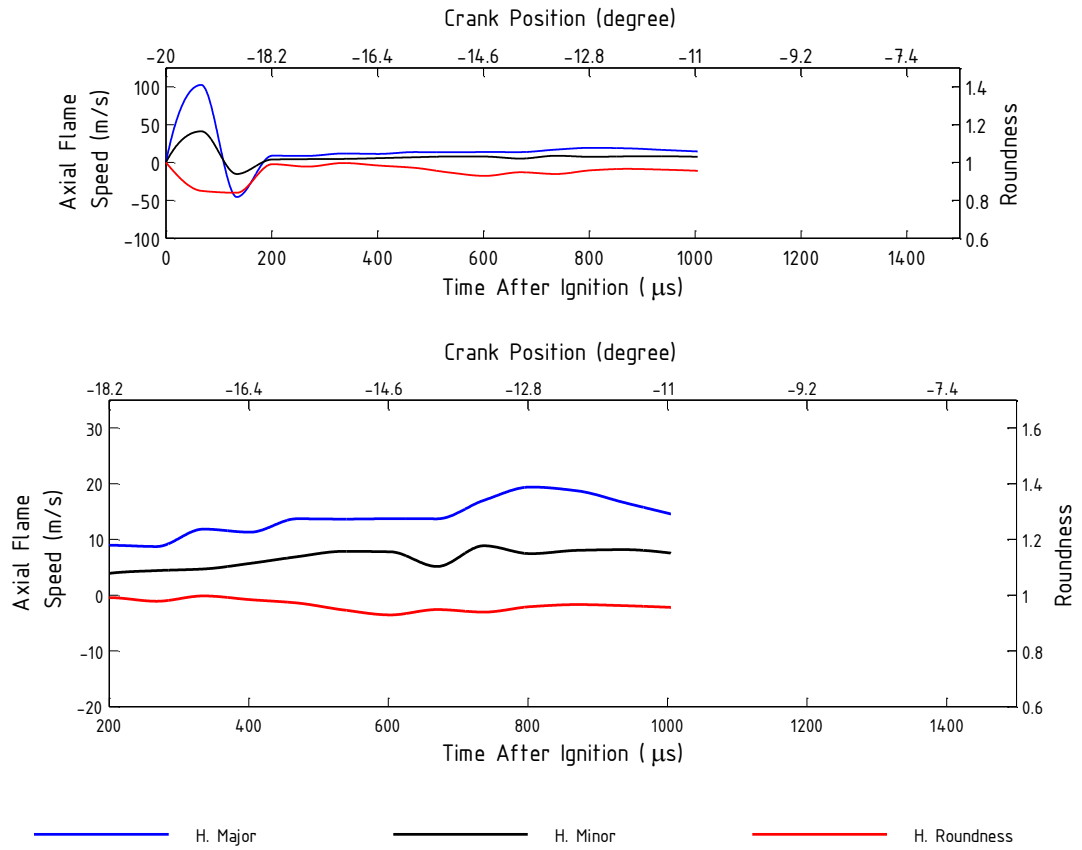
Among the liquid fuels, the highest and most stable flame speeds were found in the case of M85 (major: 19.13, minor: 9.69) which reached its stationary values first, as shown in Figure 50. Also, the roundest contours were recorded for this fuel, with fairly low errors in the measurements. This might be a result of the higher flame speed as fluctuating and random in-cylinder flows had less effect on the flame propagation. A large difference in flame speed was observed from the other fuels, especially for the low-speed, CR measurements. It was interesting to see the difference in the behaviour of the two oxygenated fuel blends: while E85 seemed to be showing similar flame propagation characteristics to isooctane, M85 clearly stood apart from E85. As the geometry of the combustion chamber and the operating conditions were the same, it is likely that this behaviour of M85 can be explained by the combustion kinetics of methanol. The high laminar flame speed of methanol was explained on the basis of the successive dehydrogenations of the methoxyl radical by Veloo et al., [204] in Ranzi et al., [203].

It was interesting to observe the similarity between the combustion characteristics of M85 and hydrogen. Their shape analysis showed similar results, and these two fuels produced the highest rate of flame growth. The reason behind this could be the similarity of the molecular structure of M85 and hydrogen – namely the fact that they do not have carbon to carbon bonds.

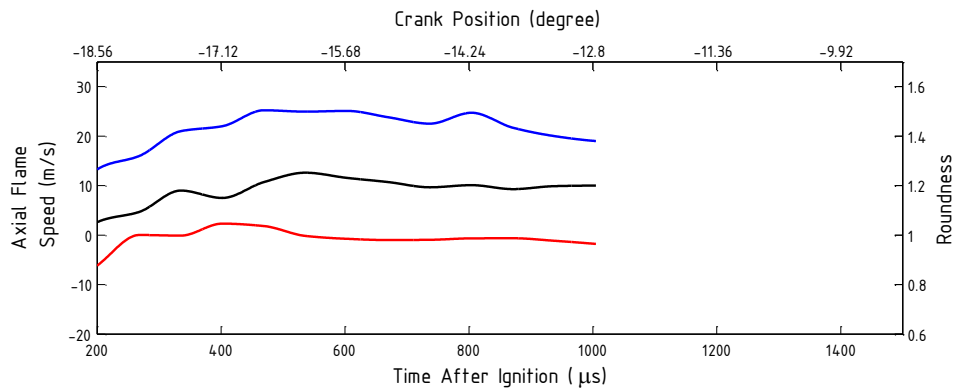
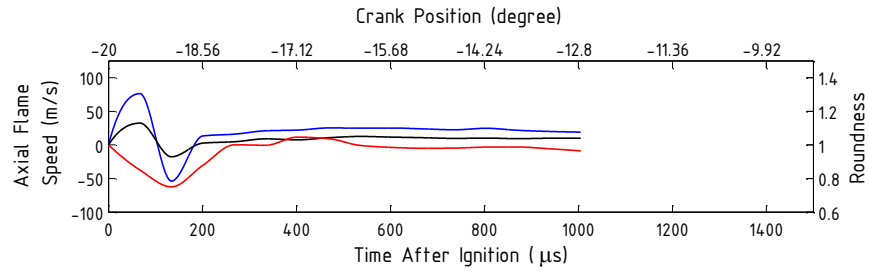
4.2.3 Hydrogen



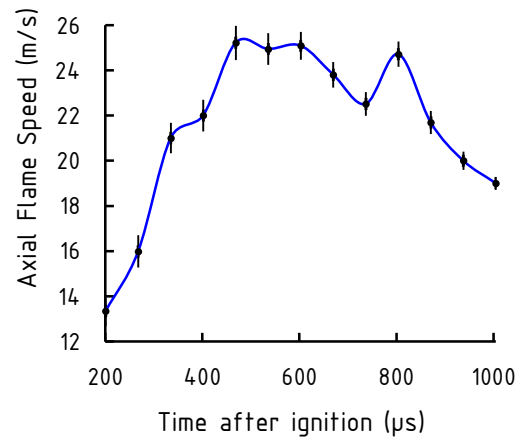
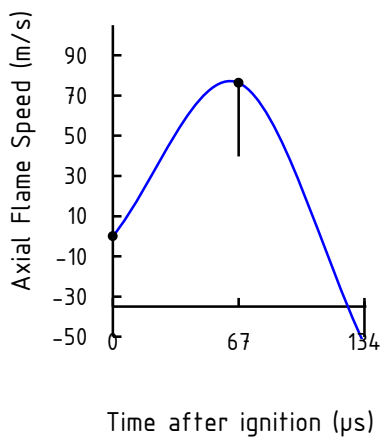
a, CR:5.00 1200 rpm



b, CR: 5.00 1500 rpm



— H. Major — H. Minor — H. Roundness



c, CR: 8.14 1200 rpm

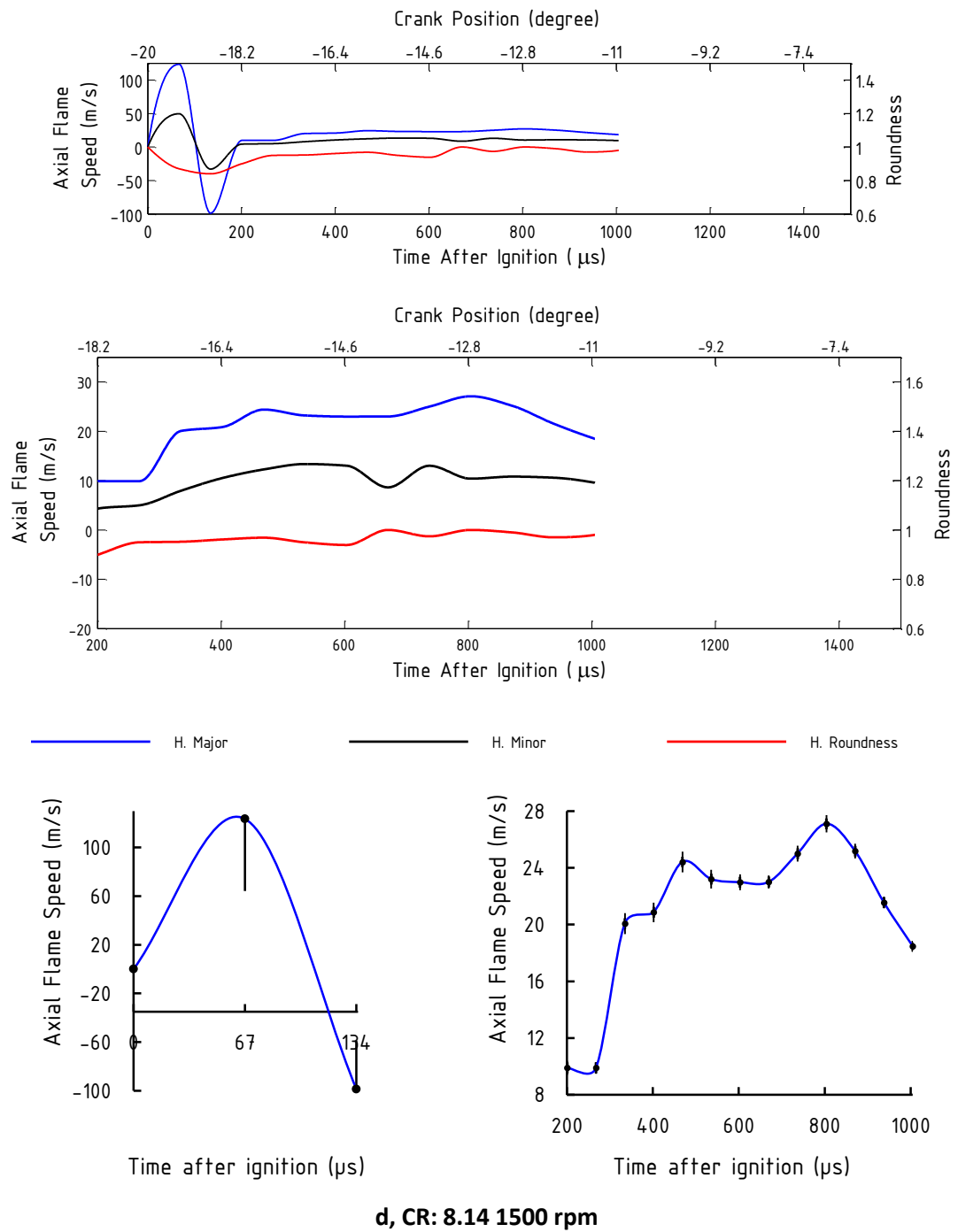


Figure 51. Instantaneous flame speed and roundness curves of hydrogen at different engine conditions; a, CR: 5.00 engine speed: 1200 rpm; b, CR: 5.00 engine speed: 1500 rpm; c, CR: 8.14 engine speed: 1200 rpm; d, CR: 8.14 engine speed: 1500 rpm

Ideally, the hydrogen would have been tested at its stoichiometric mixture as well as the chosen 0.67 normalised fuel to air ratio (FAR) for direct cross-analysis with the other fuels. Unfortunately, strong knocking, backfiring and pre-ignition did not allow the tests to be carried out over about 0.8 FAR. The abnormal combustion behaviour of hydrogen is well known and has been investigated by a number of authors [205-208]. Moreover, as the hydrogen flames propagated significantly faster than flames observed from the liquids, they reached the walls of the combustion chamber earlier. Therefore, meaningful data could only be plotted up until 1000 μs , Figure 51.

In case of the liquids, a steadily increasing flame speed trend was observed. As opposed to this, after some large spark influenced the peaks and drops, from approximately 250 μs there was a steady increase in the flame speed. Then a plateau followed, and finally the curves started decreasing. At the steadiest plateau region, the major flame speeds were found to be between 18 and 32 m/s and minor speeds were between 8 and 18 m/s. These values were found to be two to four times higher depending on the engine condition than the findings for isooctane, as shown in Table 15.

4.2.4 Cross comparison of results

The quantitative and direct comparison of flame speed measurements in optical engines is difficult. The wide selection of fuels, operating conditions and the optical

engines themselves produce very different in-cylinder conditions. Many parameters – such as air/fuel mixing, ignition modes [53], electrode gaps, spark plugs [30], valve motion and timing [25], and engine geometries – differ from engine to engine, not to mention operational factors like engine speed or compression ratio, as shown in Table 3. Every factor, such as a relatively small change in the direction of a spark plug electrode, could have a significant effect on the flame development [29]. Therefore, the best comparison can be made between fuels or operating points if the data are collected from the same engine with the same setup. For the purpose of putting the results in context and for cross-discussion, the flame speed was re-calculated from the recorded optical data based on the equivalence radius method. Then, the results were summarised in Table 17 and shown along with results from other researchers.

Table 17. Summary of flame speed, EQR, values for cross-discussion purposes

Author	Ref.	Engine speed (rpm)	Fuel	FAR	CR	Combustion chamber geometry	S_n @ 1000 μ s after ToI (m/s)	S_n max. value (m/s)
Ihracska	[13]	1500	Isooctane	1.00	8.14	Rectangular	10.4	10.8
Ihracska	[13]	1500	Gasoline	1.00	8.14	Rectangular	10.3	11.4
Ihracska	[13]	1500	E85	1.00	8.14	Rectangular	9.1	10.2
Ihracska	[13]	1500	M85	1.00	8.14	Rectangular	14.4	14.6
Ihracska	[14]	1500	Hydrogen	0.67	8.14	Rectangular	19.7 ¹	19.7
Pischinger	[27]	1400	Propane	1.00	6.70	Square	4.1	-
Keck	[25]	1400	Propane	0.87	5.75	Square	6.1	12.5
Herweg	[53]	1250	Propane	1.00	7.30	Cylindrical	10.1	10.2
Aleiferis	[40]	1500	Isooctane	0.60	7.90	Pentroof	4.9	7.6
Aleiferis	[61]	1500	Gasoline	1.00	11.15	Pentroof	5.0	12.2
Aleiferis	[61]	1500	E85	1.00	11.15	Pentroof	4.0	11.4
Aleiferis	[209]	1000	Hydrogen	0.67	7.50	Pentroof	13.0	-
Meier	[210]	1000	Hydrogen	0.5	-	Cylindrical	15.0	-
Kirchweger	[211]	1000	Hydrogen	0.67	-	Pentroof	18.9	-
Ihracska	[14]	1000	Hydrogen	0.67	8.14	Rectangular	20.9	-

¹ maximum flame speed at 804 μ s

Despite of the fact that the flame speed values were collected from varied engine geometries and operating conditions, the results had the same magnitude for each fuel. It should be noted that there is very little flame speed data available for the early stages of combustion in SI engines, and especially for those with satisfactory temporal resolution, a wider quantitative comparison appears impossible.

The flame speed measurement results of gasoline and E85 were compared to Aleiferis' findings [61], as the engine conditions of that study were the closest to the current ones. It was found that the ratio of the flame speeds for these two fuels in

the current study was similar to the ratio found in Aleiferis' work. At the early stages, E85 produced faster travelling flames, and then beyond about 400 μs after ignition, gasoline exceeded E85. The flame speed values were approximately the same at around 450 μs , being 4.5 m/s and 5.0 m/s for gasoline and E85 respectively. Then, a steady increase in flame speed values could be seen. However, the flame speed values increased at a higher rate in the current study than according to Aleiferis' measurements. Interestingly, the maximum values found in the two studies were similar and are given in Table 17. The significant difference was that the maximum values were reached in the current study at around 1000 μs , whereas in Aleiferis' engine the fastest flame propagation occurred at about 3000 μs after ignition. This difference in the characteristics of the flame speed function is a combined outcome of the dissimilar in-cylinder flow field. Furthermore, it is speculated that the direct injection used by Aleiferis may have delayed the development of a fast flame front, as there was less time for thorough fuel–air mixing.

Qualitatively, the flame speed trend obtained among different experiments is consistent. It has an initial high value due to the spark boosted combustion, followed by a minimum value for the liquids that occurs between 200 and 500 μs , and then a fairly steady increase until the end of the investigated period. Such a trend shows good agreement with the computational model of Herweg and Maly [71] for flame kernel formation in spark ignition engines. Considering the very different engine

geometries, ignition modes and fuel mixing methods, the result is surprisingly well matched.

The results obtained from hydrogen were compared to the findings of the papers by Meier [210] , Aleiferis [209] and Kirchweger [211]. All of these optical studies were performed using an engine speed of 1000 rpm, which was covered in this work. Other parameters, such as the ignition time, load and air/fuel ratio, were slightly different. The engine geometry and measurement method were significantly dissimilar, which weakens the validity of the cross-discussion. Nevertheless, the flame speed data is shown in Table 17 at 1000 μ s after ignition. Surprisingly, the flame speed values of the four studies were quite similar and exhibited good agreement. This agreement indicated that the flame propagation of hydrogen was not significantly affected by the other parameters mentioned above, most likely because of its high flammability and laminar burning velocity.

Apart from the absolute values, which shall be different for different works, the results are comparable, which suggests that the flame propagation characteristics are similar in SI engines for the earliest stages and is not engine geometry dependent. It is likely that the main controlling factor for early flame speed shall be the initial high energy input from the spark. Consequently, the finding of this study can be extrapolated to other engines.

4.3 Flame shape analysis and comparison of equivalent radius and ellipse fitting methods

Numerous methods have been proposed in the literature to calculate shape parameters. For this work, roundness was chosen as only the overall shapes was of interest and the local disturbances (wrinkling) could not be captured accurately due to the limitation in the spatial resolution. No roundness data has been found on in-cylinder flame in the literature and on validation or analysis of the EQR method.

The fit of the circles and ellipses onto the region of the flames was evaluated and compared with one another using the fit ratio (FR_c for circles, FR_e for ellipses). Once the images were processed and binarised, the number of pixels outside of the fitted geometry was divided by the total number of pixels of the flame to determine the corresponding fit ratios. The hydrogen in-cylinder flames are shown in Figure 52, where a number of fitted circles and ellipses can be observed with their FR. Ellipses described the inflamed areas better. In the case of well-elongated regions, the FR was significantly less for ellipses than for circles. The analysis of fit ratios indicated that – depending on the exact shape – ellipses had two to three times less uncaptured pixels.

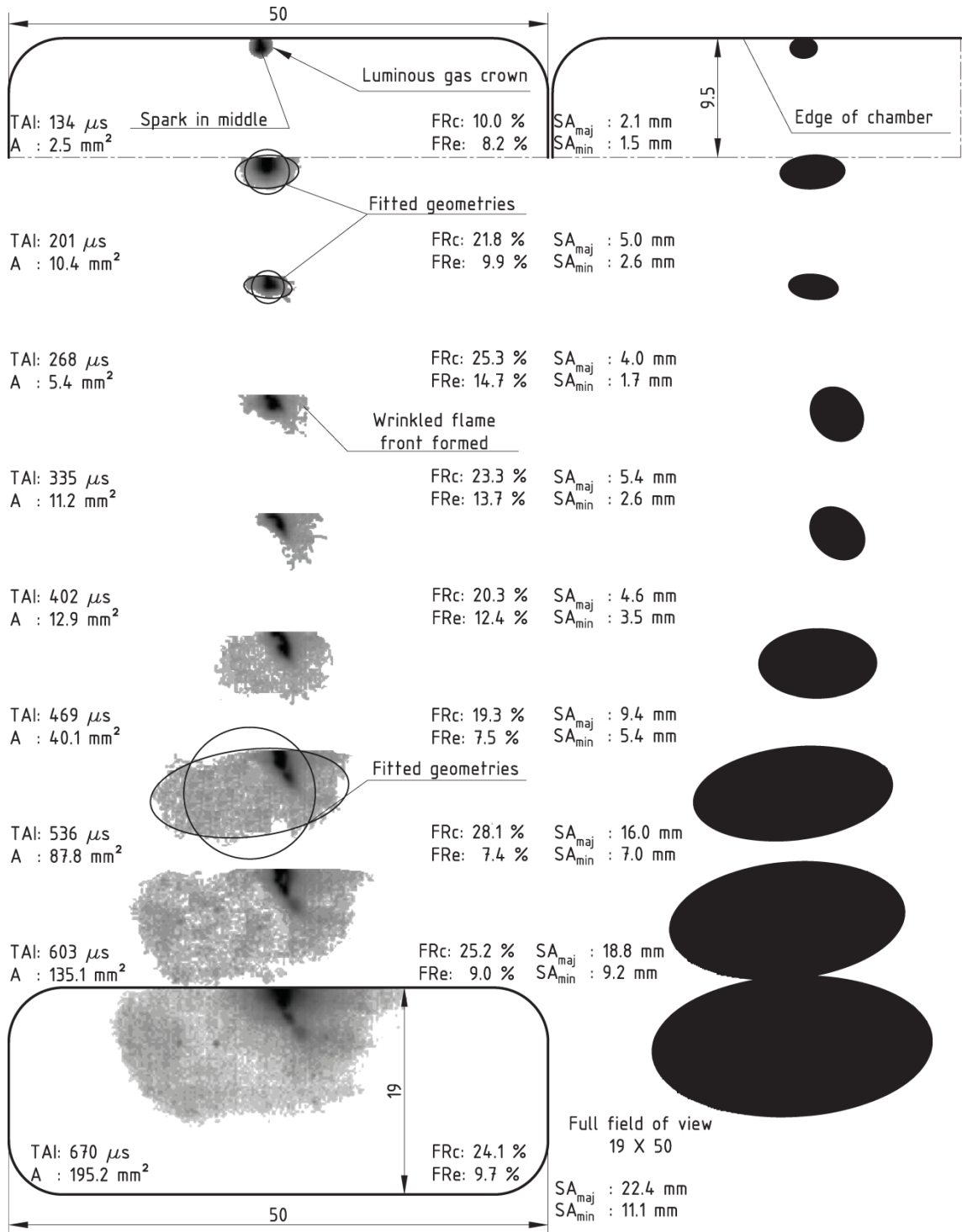


Figure 52. Development of a hydrogen flame kernel at 1500 rpm and CR: 8.14 with fitted ellipses and circles; fit ratios are also shown

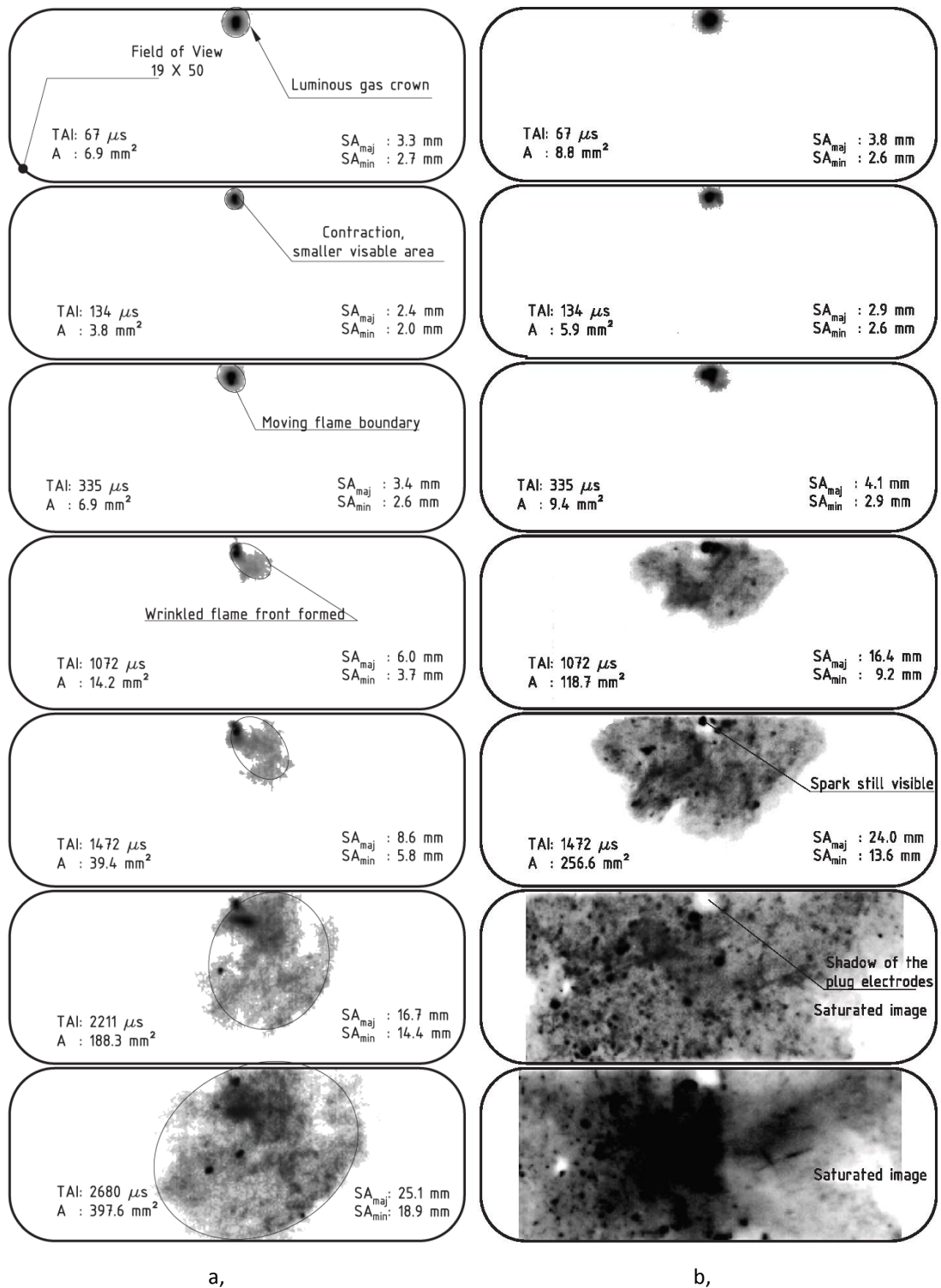


Figure 53. Sample flame images a, isooctane, conditions: 1200 rpm and CR = 5.00 b, gasoline conditions: 1500 rpm and CR = 5.00

In 3D the flame boundary reached the combustion chamber long before it reached the edges of the visible area, as it is explained in Figure 27. Considering the geometry of the combustion chamber, it was assumed that the flame speed vector in the z direction had always the same or smaller absolute values than the major flame speed vector at a given time. In the 3D space, the most distorted flames and the fastest ones did reach the combustion chamber walls and the piston at the end of the investigated period (1500 μs for liquid fuels and 1000 μs for hydrogen). However, for the vast majority of cases, there was no contact between the flames and the walls (apart from the spark plug). When the contact did happen, a number of new variables should be added to the flame propagation equations to derive true values of flame speeds. However, since there were only relatively small number of data points with contact and its area was small, the effect of it was considered as a small random error. The visual analysis of the gathered images showed a distinct difference in the physical appearance of the flame for the two fuel types, hydrocarbons and alcohols blends. Less luminous flames were found for the latter and higher intensity was seen in images of isooctane and gasoline with local maximums randomly distributed. This is likely to be the result of the simpler and shorter molecule structure of the alcohols. As the longer chains of hydrogen and carbon atoms of isooctane and gasoline required more time for dissociate and complete combustion, there was more unburnt carbon and soot present in flames

than in the case of alcohols. The higher soot concentration resulted in greater broad spectrum luminosity.

The flame shape and its changes in time are important information in the understanding and prediction of in-cylinder processes. Therefore the ellipse method can provide useful data for CFD and emissions predictions in studies of fuel-engine combinations, and engine design processes. Flame speed and shape factor measurements showed that an ellipses described the contour of combustion better than circles in the first stages of combustion. About the first 800 μ s of propagation were severely affected by the spark causing well elongated flames. This phenomenon was not dependent on fuel or engine operating conditions. At time of ignition, the value of roundness was found to be close to unity in all cases, which was confirmed by images showing a circular glowing area. Then, when the initial high energy got absorbed, the projection of the flame was elongated as the arc and the roundness dropped to about 0.7. Finally, in all investigated cases the calculated value of shape factors started increasing and approaching unity again. There was no description available of the flow field but the phenomenon of the flame becoming more circular later was expected. There is always a larger flux of unburnt charge passing through planes that contain the major axis (or in a general case Feret's diameter) simply because these cross sections have larger areas. This of course is not valid for uniform flows where there is just one plane for the charge to flow through. In an internal combustion engine there are main directions of flows but as it is

turbulent, it could be approximated as a highly random field. The changes in shape were found to be dependent on the engine conditions and fuel. Higher engine speeds and CRs appeared to cause rounder contours; fuels with faster flame speeds also tended to have more regular shapes. Utilising the properties of the ellipse fitting method two flame speed values were calculated normal to each other. It was observed that changes in the magnitude of one flame speed component corresponded to the change in the magnitude of the other one. Therefore, these peaks were caused by a large scale in-cylinder process rather than some local disturbance.

Overall, it was found that EQR method provides valid measurements for well-developed flames. However, at the early combustion stages or spark assisted flame kernel formation the flames are distorted. Ellipses fit on these elongated boundaries significantly better than circles. Using the EQR method for these conditions would result in high errors in the measurements.

5 Conclusions

The in-cylinder flame propagation characteristics of fuels have fundamental effects on ICE performance. The rate of this propagation can be measured in optically accessible engines, traditionally, by applying the so-called circle method. One of the main aims of this work was to check and verify this method which, though widely accepted, to the author's best knowledge has never been validated before. A novel and more accurate analysis method using ellipses was proposed and compared against the circle method. Moreover, using and comparing these methods, new flame speed data was collected for different alternative fuels with the same boundary conditions allowing a direct comparison between them. The optical measurements in engines are vital for understanding the underlying fundamentals of combustion these can only be carried out in optically accessible ICEs. Other aims of this research were to investigate the design process of these engines, the collection and a new interpretation of the relevant design standards and procedures. In addition, in order to simplify and aid the design process the research aimed to develop new relations and functions.

These experimental engines must be able to withstand the high thermal and fluctuating mechanical loads. Moreover, a part or parts of the assembly are required to be transparent to some ranges of electromagnetic waves, to allow the optical sensors to record data. There are standards and data available in the existing literature on heated pressure vessel design and optical element design. However,

there has been no attempt made before to investigate, interpret and presents the design procedure of optically transparent and heated pressure vessels.

In this work a significant number of data sources were surveyed to produce a comprehensive review of the most relevant optical, thermal and mechanical properties of some optical materials. The resulting database allows for a convenient and direct comparison to aid material selection for other designers and researchers in the field. The relevant standards and the limited design data that were available on the topic in the literature were presented, while also taking into account practical, mechanical and optical design considerations. The aspects of the design for optical performance were described in depth. Based on this review newly developed equations, relations and functions were added to the literature. The relevant types of design criteria were considered in detail and suggestions of values of constants were given for different opto-mechanical applications.

Furthermore, as a result of this research work it was concluded that larger safety factor values are required for optical element design, typically ranging from two to five depending on operating conditions, manufacturing technology, risks and hazards and so on. The safety factor selection procedure and criteria was clearly described. The high values suggested is the result of the inconsistency found in available data sourced from suppliers and from the literature of the thermal and mechanical properties of optical materials under room temperature conditions. Moreover, the databases lack the relevant design data considering the mechanical

properties at elevated temperatures and fatigue for optical materials. The utilisation of the database created, the novel interpretation of the design process, and the presented design criteria allowed a number of case studies of pressure chambers with optical elements under high mechanical and thermal load to be demonstrated.

Research rigs, designed by procedures presented herewith, were used in this work to target gaps in the combustion science literature.

In general, it was found that there is not much data available on in-cylinder flame growth rates. The literature especially lacks data on the early stages of flame kernel formation. The little data that can be found is obtained from different fuels, in significantly different engine conditions which make it difficult to establish a benchmark for comparison purposes. In order to compare the characteristics of different fuels to each other, in this work, the data was acquired from the same engine at the same operating conditions. It is generally accepted that the flame speed and flame shape have an effect on cyclic variability and thus on performance.

However, it is a usual approximation that cylinder flames propagate isotropically. In order to analyse and evaluate this assumption, a novel method for the combustion analysis is proposed in this work. This method consists of using ellipse fits to approximate the projected flame boundaries (instead of the conventional use of circles fits) in an innovative approach that has never been used before to describe the propagation characteristics of in-cylinder flames. The novel ellipse fitting method

elucidated details of the combustion properties and added valuable data to the existing literature on these fuels. Furthermore, the conventional method of isotropic assumption with circle fitting was evaluated and verified.

- A fit analysis indicated that for the tested flame geometries, ellipses provided more accurate measurement results than the conventional equivalent radius method. In the case of elongated flames, the fit was significantly better for the ellipse method.
- The spherical flame propagation assumption has certain limitations. Results showed that for some cases the spherical flame front assumption is reasonably valid; but one needs to consider non-isotropic flame propagation in order to model in-cylinder processes more accurately. This is especially true for the earlier combustion stages when the spark causes highly distorted flame contours.
- For all fuels the flames were more elliptical rather than circular immediately after ignition, which caused the least round flame-kernel shapes. It is nonetheless true that, in all cases after the first 200 μs , the elliptical shapes gradually became more circular. However, the elliptical method, being more general than the circular one, can be used with good accuracy for any flame shape geometry.

The flame propagation characteristics of isooctane, gasoline, M85, E85 and hydrogen were recorded using a high-specification camera. The high temporal-resolution pictures were analysed with a purpose-built code and statistically compiled. In-cylinder combustion processes with these fuels were investigated in the visible spectra. The high-temporal resolution enabled evaluation of the flame kernel formation. The flame speed data was recorded at various engine speeds and compression ratios. The relevant thermodynamic conditions were also determined to provide a more complete picture of the experimental conditions. To the author's knowledge this is the first study on detailed flame speed measurements for M85 from optical engines. Specifically, the following conclusions were made:

- Higher flame speeds were observed with increasing engine speed and compression ratio for all fuels. This finding showed good agreement with the published flame speed and burning velocity trends as function of engine condition.
- For all of the tested liquid fuels, the changes and trends in flame speed as a function of time showed good agreement with those in similar studies. These experimentally obtained flame speed curves were also comparable to some computational results. The similar findings in different engine properties suggest that the flame propagation characteristic is similar in SI engines for, at least, the earliest stages and is not engine geometry dependent. It is likely that the main controlling factor for early flame speed is the initial high energy

input from the spark. Consequently, the findings of this study can be extrapolated to other engines.

- The standard deviation of the measured values and uncertainty decreased at higher speeds and compression ratios. The roundness and lower fluctuations of flame speed also indicated more stable flames at those conditions, as a result of higher flame speed, better mixing, and smaller large-scale eddies.
- For all tested fuels at every operating condition a contraction of the flame was observed on the second recorded image. This may have been the result of an endothermic process associated with the formation of radicals in the mixture.
- The phenomenon of ignition delay can be defined for SI engines utilising the observed flame-kernel contraction and the relatively slow establishment of the combustion kinetics supported flame growth. Ignition delay is defined as the time between spark ignition and establishment of the steadily expanding flame kernel.
- A large number of sample observations were plotted and the distribution function showed good agreement with the normal distribution curve.
- The cross-discussion with existing, hydrogen combustion literature revealed surprisingly good agreement between the findings, despite the different test

conditions: ignition, chamber geometry and air/fuel ratio. This finding suggested that hydrogen flame propagation was less affected by the engine conditions than by the engine speed. This behaviour was most likely the result of the high flammability and laminar flame speed of hydrogen.

- The detailed analysis of the earliest stages of the kernel formation indicated that there was no relationship between the engine speed and the flame propagation. Until approximately 250 μs after ignition, the flame propagation was not affected by the moving piston generated flow field. Similar findings by others using different fuels suggested that the first 200-250 μs of the flame kernel formation primarily depends on the ignition and on the properties of the ignition system.

6 Future work

The research and results explained in this study added new information to the background of in-cylinder combustion science. It is clear that a lot more can be done in order to fill in the gaps that were identified in the literature.

The investigation of ignition and flame kernel formation can be investigated further. There are a large number of engine conditions that still can be tested: CRs that are closer to the ones that can be found in modern engines; higher engine speeds that are similar to ones in performance engines; full load conditions; and different mixture formation strategies. The combustion characteristics and the performance of alternative fuels and their mixtures are still relatively unexplored. Therefore, there is more experimental and computational work to be done to explore the properties of different alcohols, natural gas, liquefied petroleum gas, hydrogen and their mixtures.

According to the findings of this study, supported by previous research, the flame kernel development is strongly dependent on the properties of the discharging spark. It would be interesting to see comparison studies between different ignition systems, where voltage and current data acquisition is synchronised with the image recording equipment. Moreover, the process of the burning charge becoming combustion kinetics driven is still not understood clearly. With the aid of the

advances in high speed data recording, it is now possible to explore this phenomenon with a significantly better resolution.

It seems to be clear that the best resemblance to production engines is provided by optical engines equipped with a cylindrical liner. This liner should ideally be manufactured out of a material that has thermal conductivity in the same range as the thermal conductivity of steel and iron. If the thermal conductivity cannot be kept the same, then the heat flux to the fresh charge is required to be controllable. The distortion caused by the curvature needs to be investigated further. It is suggested by the author that instead of a complex optical system, the distortion should be corrected by software built specifically for this purpose. In order to design a liner, that would allow the full load and high speed operation, further research is required to unfold the mechanical properties of optical materials at elevated temperatures. It would be especially beneficial to obtain data for the fatigue failure behaviour of ceramics and glass at high temperatures.

7 Appendices

Appendix A.

Design of the optical element on the HPC, design requirements

The main purpose of the window is to provide a transparent barrier between the combustion and the instrumentation. An underlying requirement was to allow use of three different sensors (cameras) with differing spectral responses; the curves are shown in Figure 11. As the wavelength of the laser is in the visible range, there were two bands of electromagnetic radiation that needed to be considered – 380-985 and 2800-5200 nm. In these regions, a minimum of 80% transmittance was required. The tolerance on the OPD had to be kept in the photographic range: 10 nm/cm. As the three sensors were robust and their measurements were not overly sensitive, the maximum allowed lens power of the distorted window was 0.01 dioptre. The maximum expected pressure difference on the optical element was 20 bar. The required safety factor was required to be four for stresses arising from mechanical and thermal loads, with a maximum probability failure of 10^{-4} . Finally the operating temperature of the window had to stay under the maximum permitted level.

Material choice

The spectral requirement is shown in Figure 11 along with the transmittance curves. The ideal design solution was to select only one material type to cover the required

wavelength ranges. It can be seen that the two possible material types that cover the needed large range of EM wavelengths are sapphire and magnesium fluoride. The thermal analysis of the optical section indicated that the steel blanks and windows would need cooling to survive. The calculations and simulations were carried out for both materials. It was found that MgF_2 can be a valid option for low-temperature and low-humidity environments. Extra caution is required when a temperature gradient is applied to the MgF_2 material, as its high expansion coefficient and middle-range conductivity combined with low strength makes it sensitive to thermal shock. It is also suggested by manufacturers that MgF_2 can react with high temperature steam similar that found in the HPC as a combustion product. Therefore, sapphire was chosen instead as a material for the windows as it combines good transmittance in all the required wavelength bands with good thermo-mechanical strength.

Design and validation

The diameter of the window was determined by the maximum available space in the optical section. The maximum possible diameter was 82 mm with 64 mm aperture. The thickness of the window was estimated by using the equations and relations that were explained earlier in this paper and then validated by FEA. The maximum temperature of the window was found to be 284 °C then, the design stress was determined using Figure 34.

$$\sigma_{des} = 178\text{MPa} \quad (81)$$

The minimum thickness was calculated for two requirements: maximum allowable stress and OPD. Substituting values into Equations (16) and (30) the resulting thicknesses were 5.88 and 0.05 mm respectively.

$$t_{ck|\sigma \min} = \left(\frac{1}{2}D_o\right) \left[\frac{K_w SF_\delta \Delta p}{\sigma_{des}}\right]^{1/2} =$$

$$= \left(\frac{1}{2}64 \cdot 10^{-3}\text{m}\right) \left[\frac{0.75 \cdot 4 \cdot 2 \cdot 10^6\text{Pa}}{178 \cdot 10^6\text{Pa}}\right]^{1/2} = 5.88\text{mm} \quad (82)$$

$$t_{ck|ODP \min} = \sqrt[5]{8.89 \cdot 10^{-3}(n-1) \frac{\Delta p^2 D^6}{OPD \cdot E^2}} =$$

$$= \sqrt[5]{8.89 \cdot 10^{-3}(1.76-1) \frac{(2 \cdot 10^6\text{Pa})^2 \cdot (64 \cdot 10^{-3}\text{m})^6}{10^{-10} \frac{\text{m}}{\text{m}^2} \cdot (335 \cdot 10^9\text{Pa})^2}} = 0.07 \text{ mm} \quad (83)$$

Then, the estimated window thickness was modelled and simulated. The stress and deflection results were substituted in Equations (18), (19) and (27) in order to check the design for failure probability and image distortion. It was found that the limiting factors were the probability failure and lens deflection. In order to keep these values at an acceptable level the thickness of the window was chosen to be 10 mm.

$$P_f = 1 - \exp\left[-\left(\frac{\sigma}{\sigma_0}\right)^m\right] = 1 - \exp\left[-\left(\frac{42.8 \cdot 10^6 \text{Pa}}{485 \cdot 10^6 \text{Pa}}\right)^5\right] = \quad (84)$$

$$= 5.35 \cdot 10^{-6}$$

$$R = \frac{x^2 + D_0^2}{8x} = \frac{(0.281 \cdot 10^{-3} \text{m})^2 + (64 \cdot 10^{-3} \text{m})^2}{8 \times 0.281 \cdot 10^{-3} \text{m}} = 1.83 \text{m} \quad (85)$$

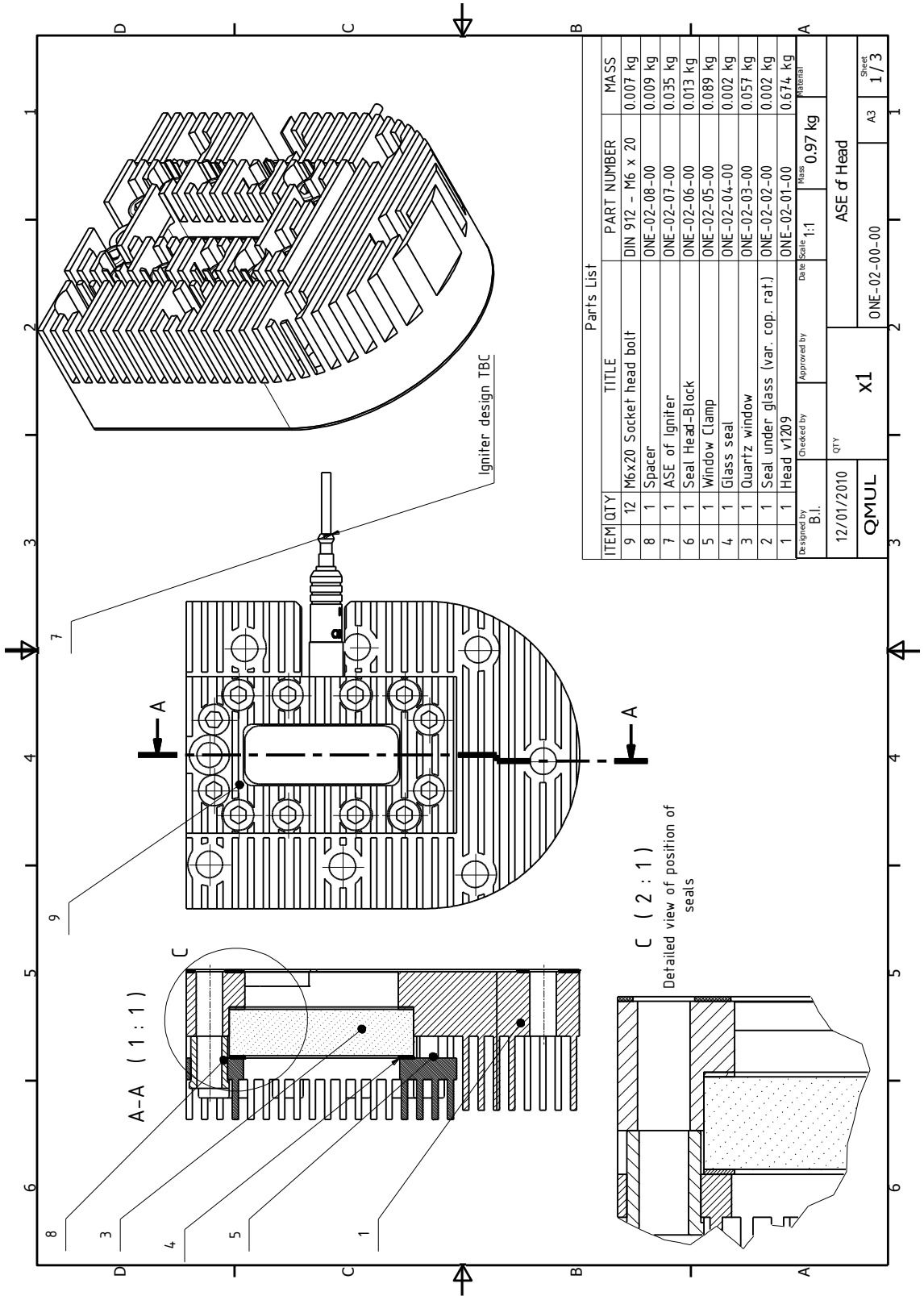
$$P_{lens} = (n - 1) \frac{-t_{ck}}{R^2 + Rt_{ck}} =$$

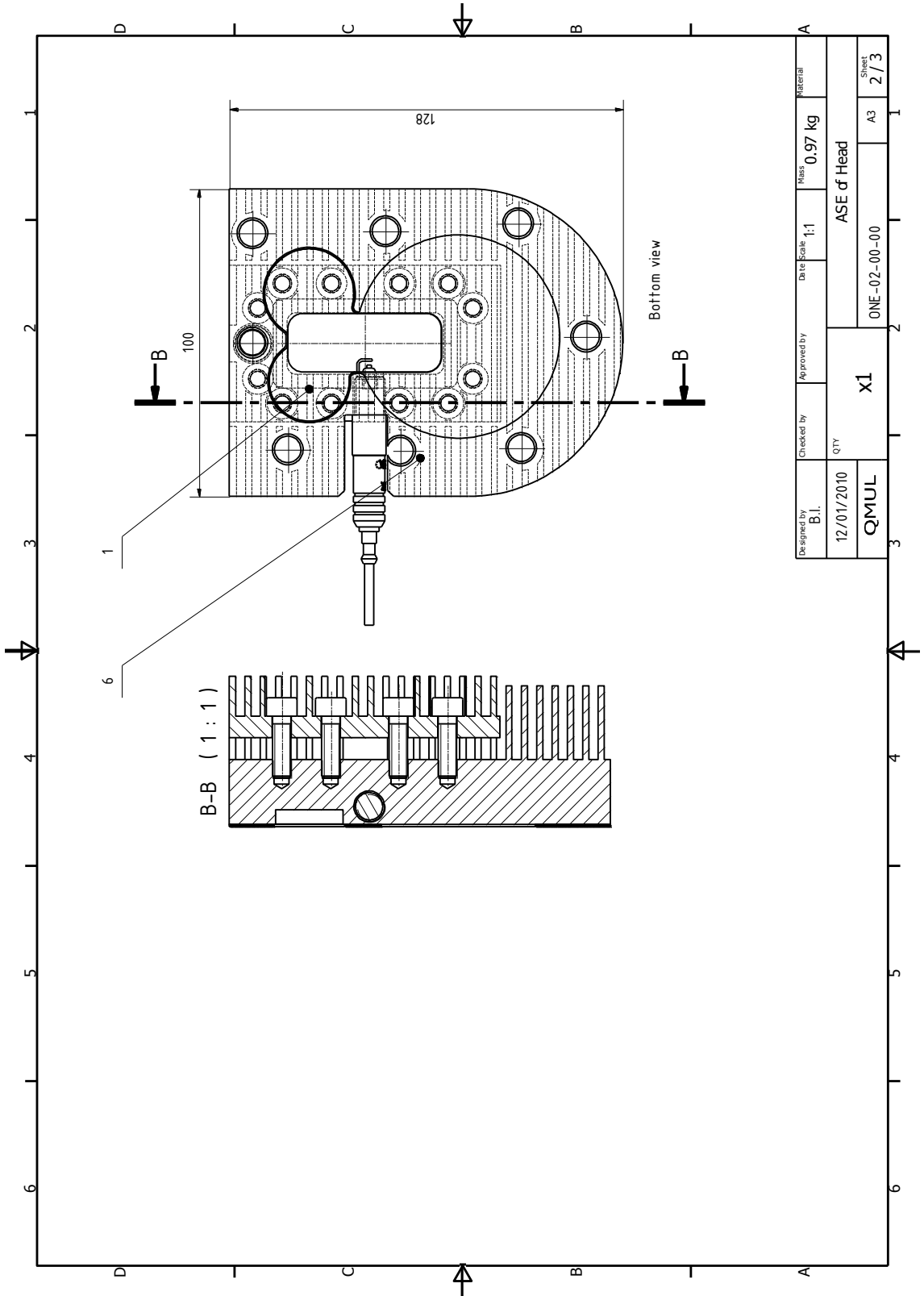
$$= (1.76 - 1) \frac{-10 \cdot 10^{-3} \text{m}}{(1.83 \text{m})^2 + 3.41 \text{m} \cdot 10 \cdot 10^{-3} \text{m}} = \quad (86)$$

$$= -2.28 \cdot 10^{-3} \text{dioptre}$$

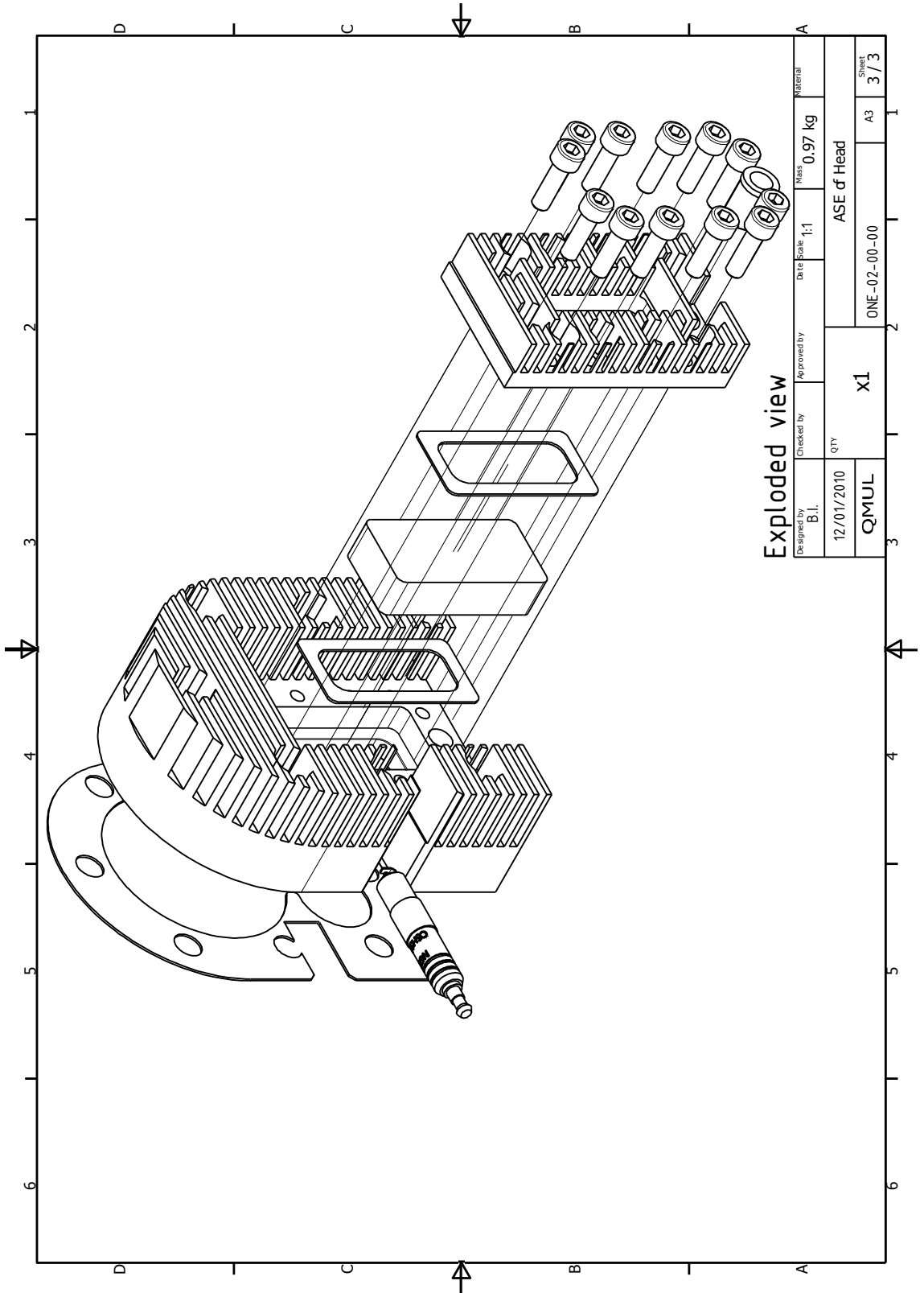
where, x and σ were obtained form FAE simulations and σ_0 was taken from Table 4.

Appendix B.



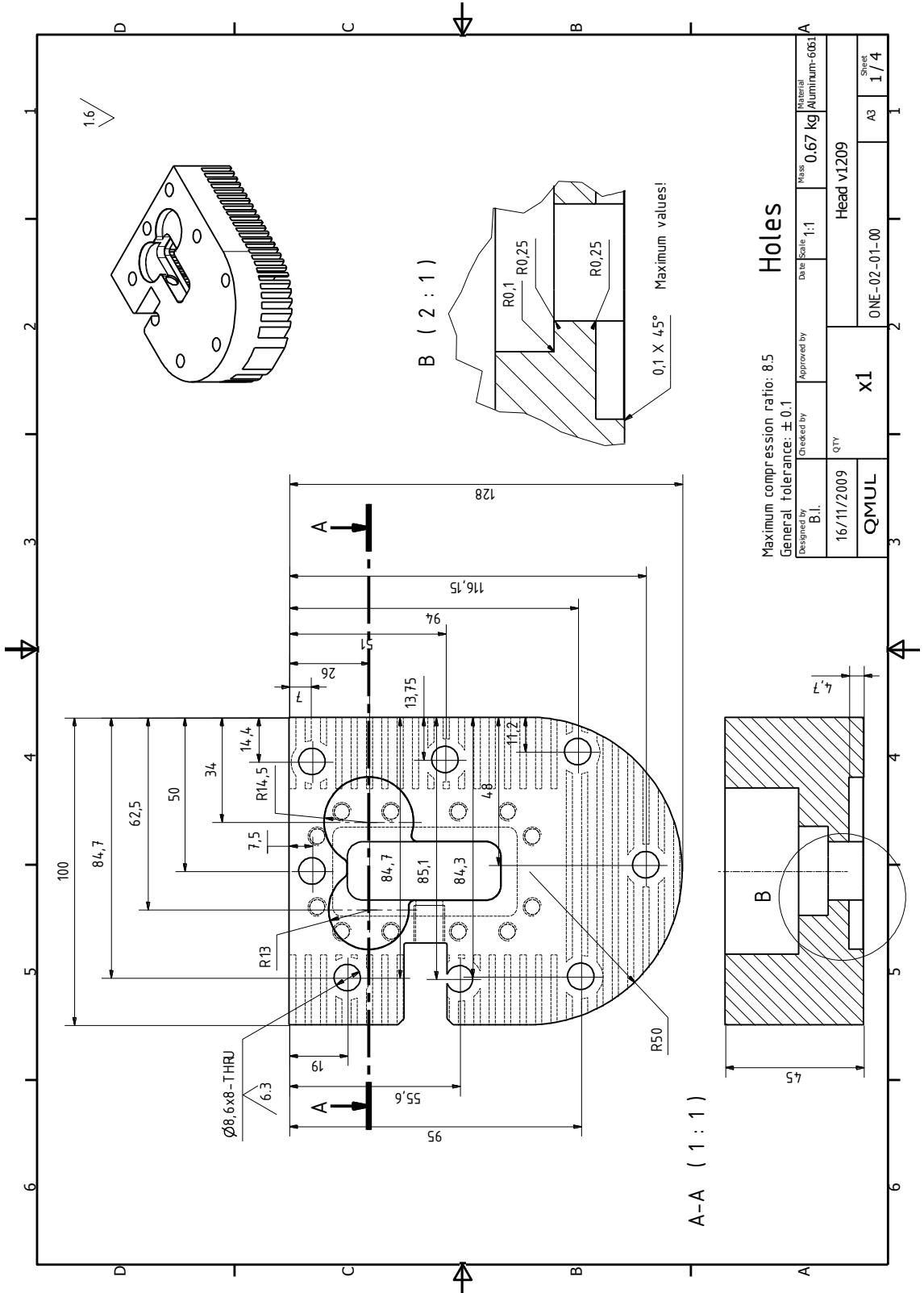


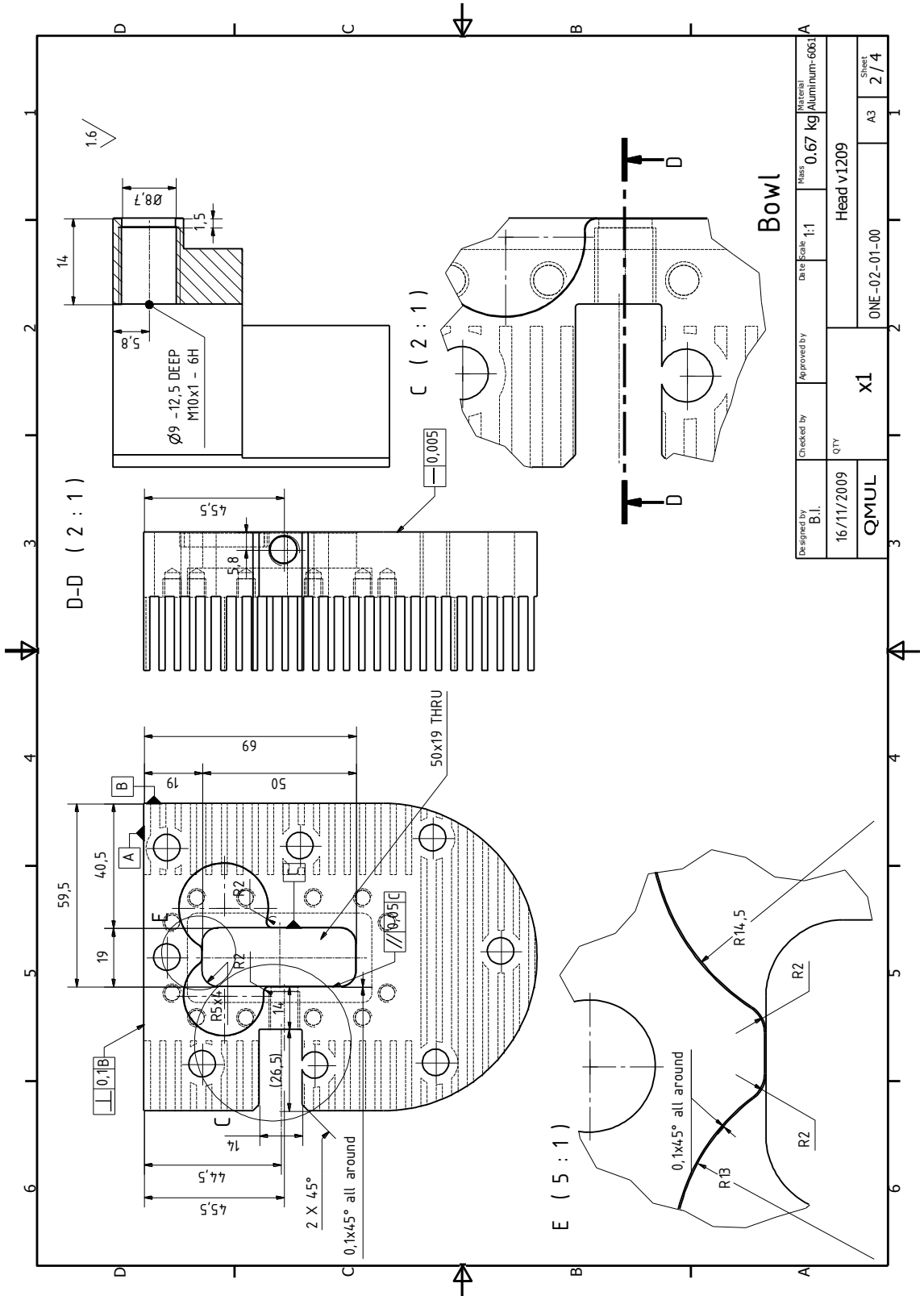
Designed by B.I.	Checked by	Approved by	Date/Scale 1:1	Mass 0.97 kg	Material
12/01/2010	QTY QMU	X1	ASE of Head		
			ONE-02-00-00	A3	Sheet 2 / 3



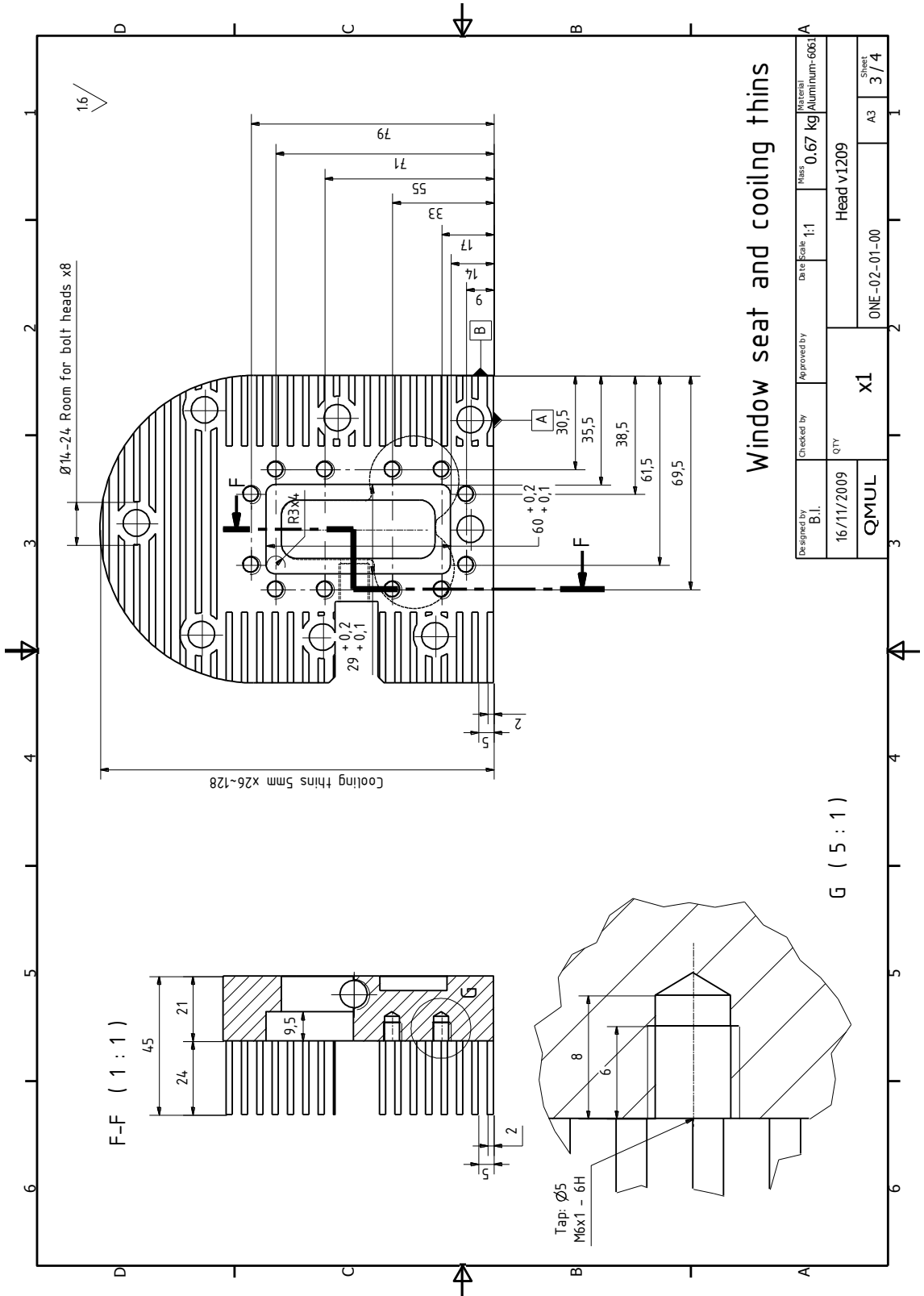
Exploded view

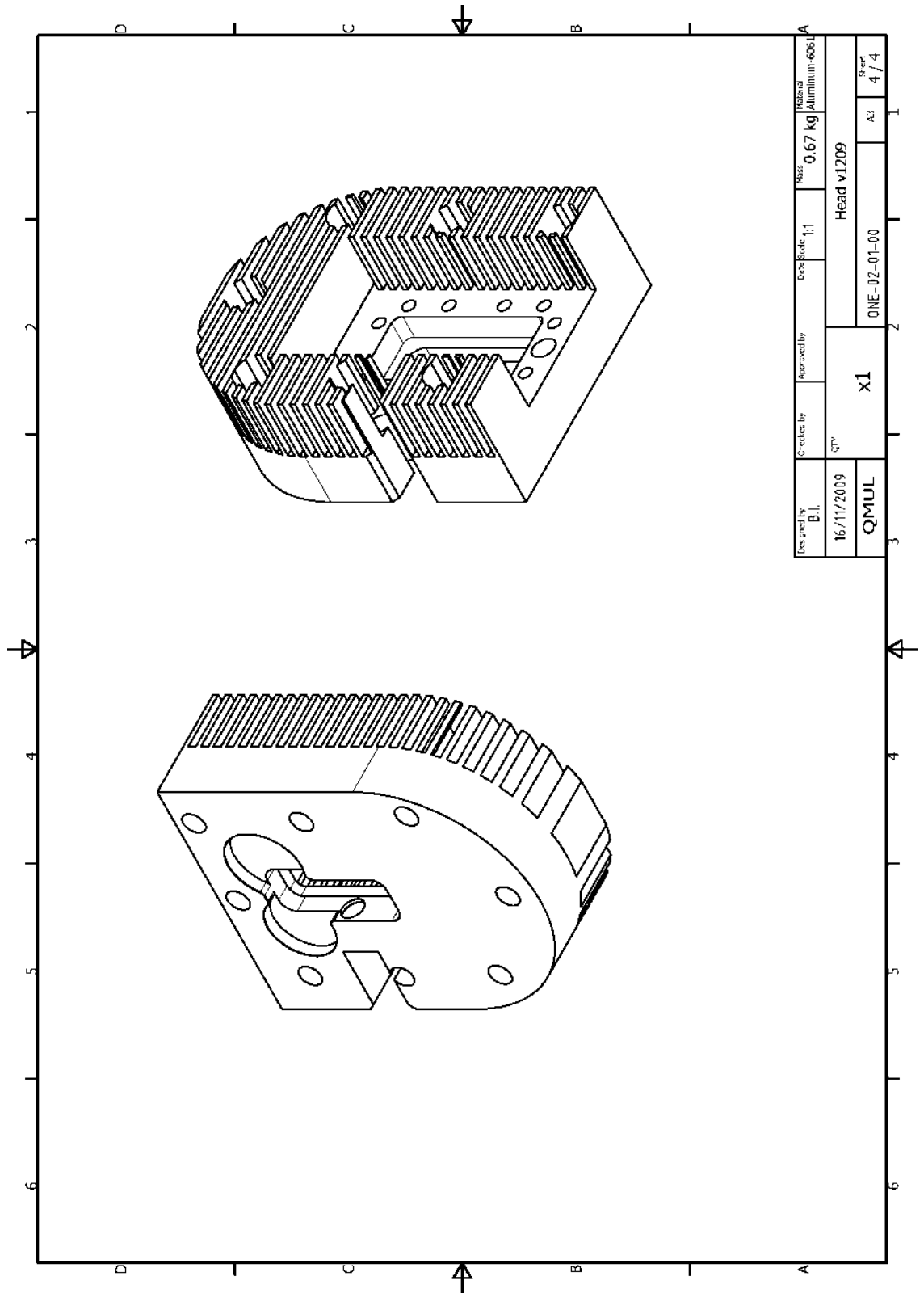
Designed by B.I.	Checked by	Approved by	Date Scale 1:1	Mass 0.97 kg	Material
12/01/2010	QTY QMUL	x1	ASE of Head		
ONE-02-00-00			A3	3 / 3	

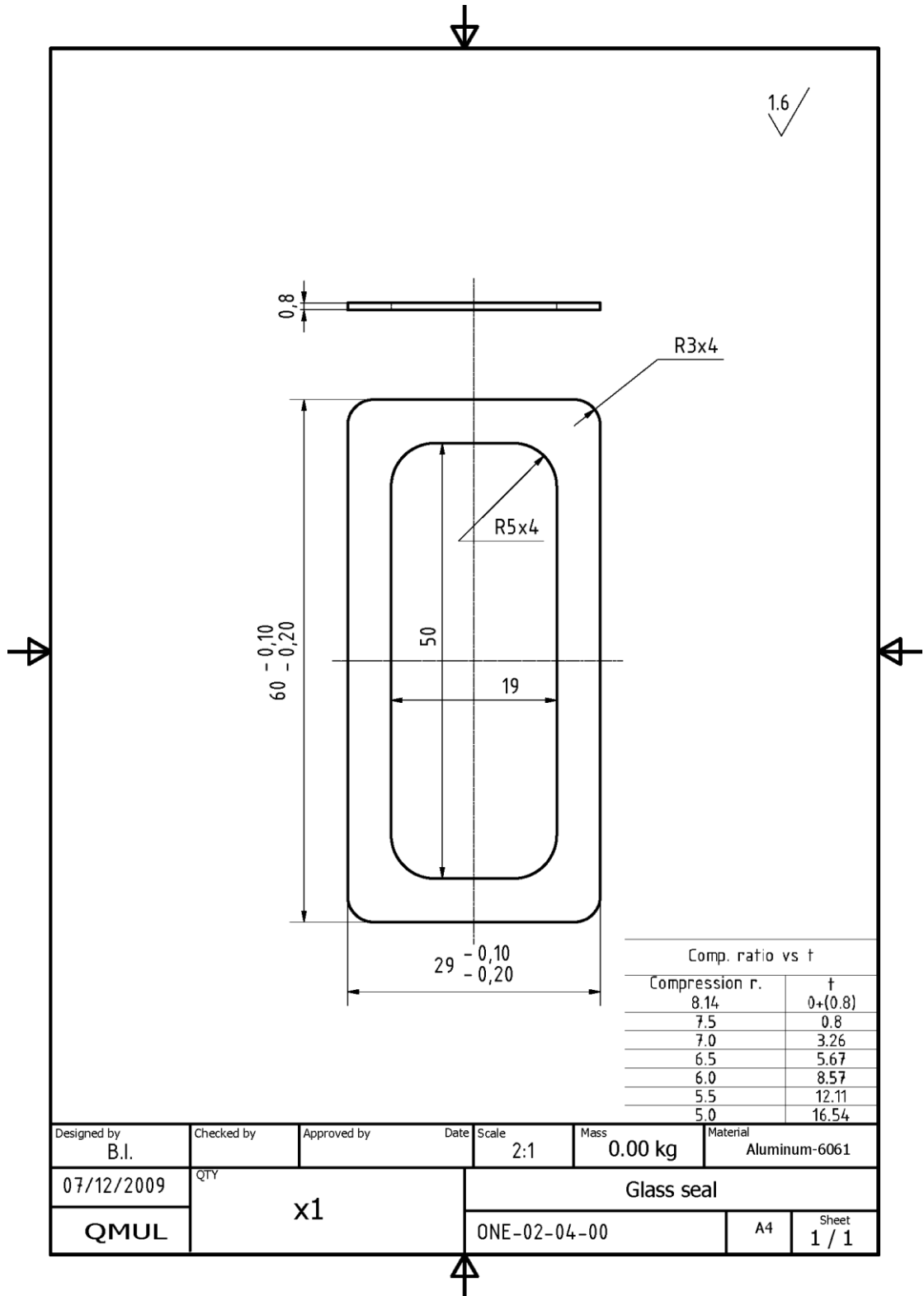


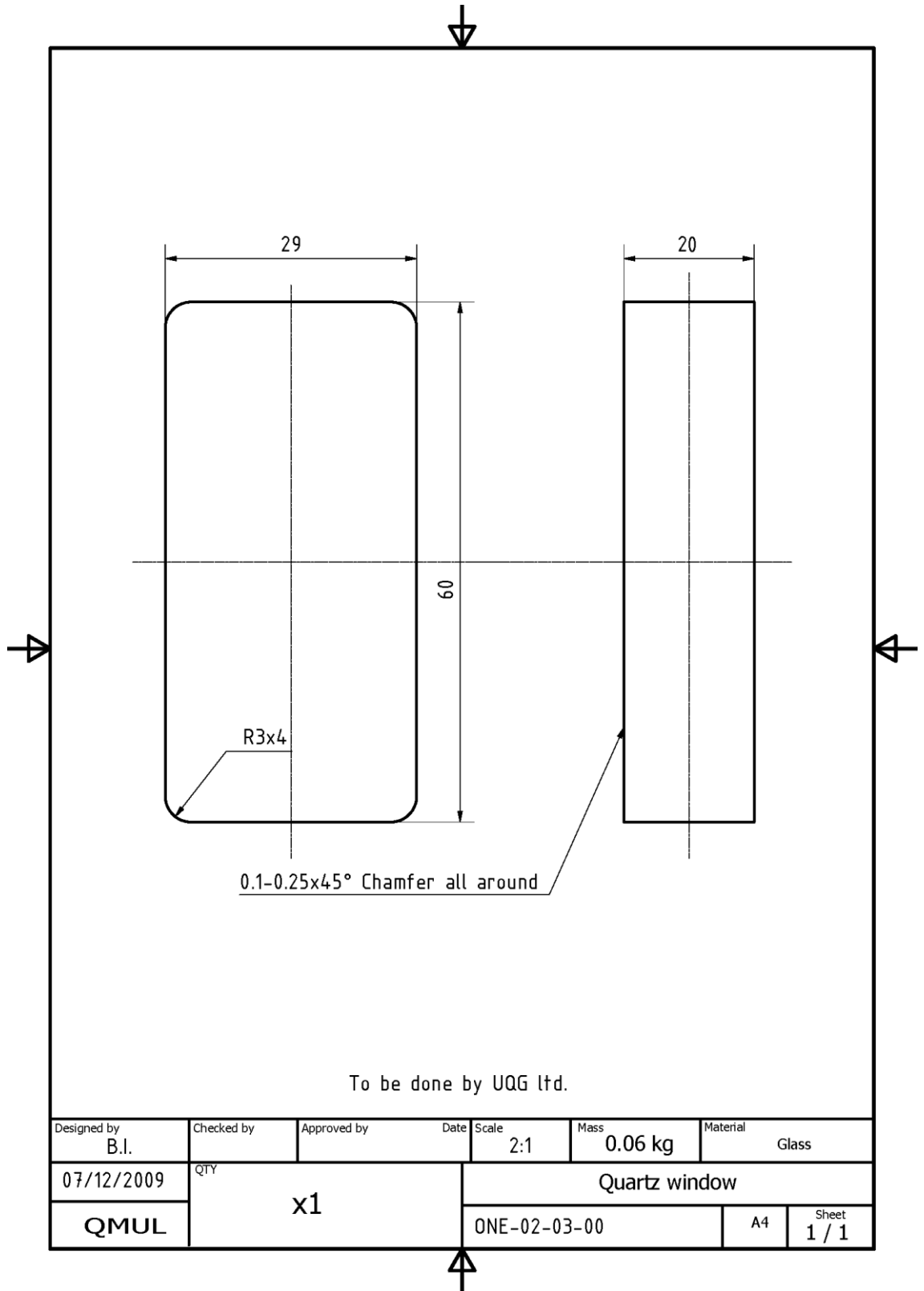


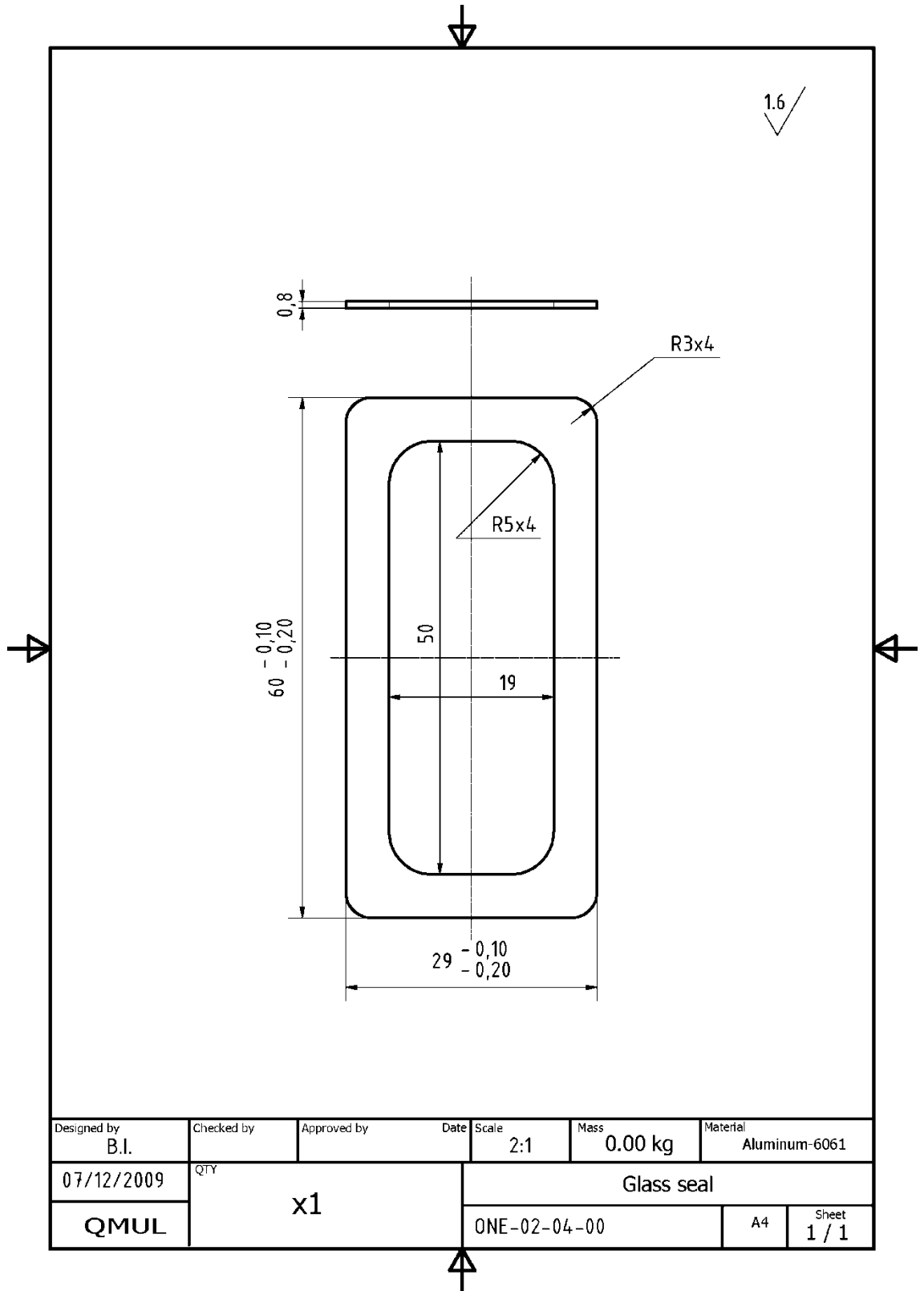
Designed by B.I.	Checked by	Approved by	Date Scale 1:1	Material Aluminum-6061
16/11/2009	QTY	X1	ONE-02-01-00	Mass 0.67 kg
QMUL			Head v1209	
			A3	Sheet 2 / 4

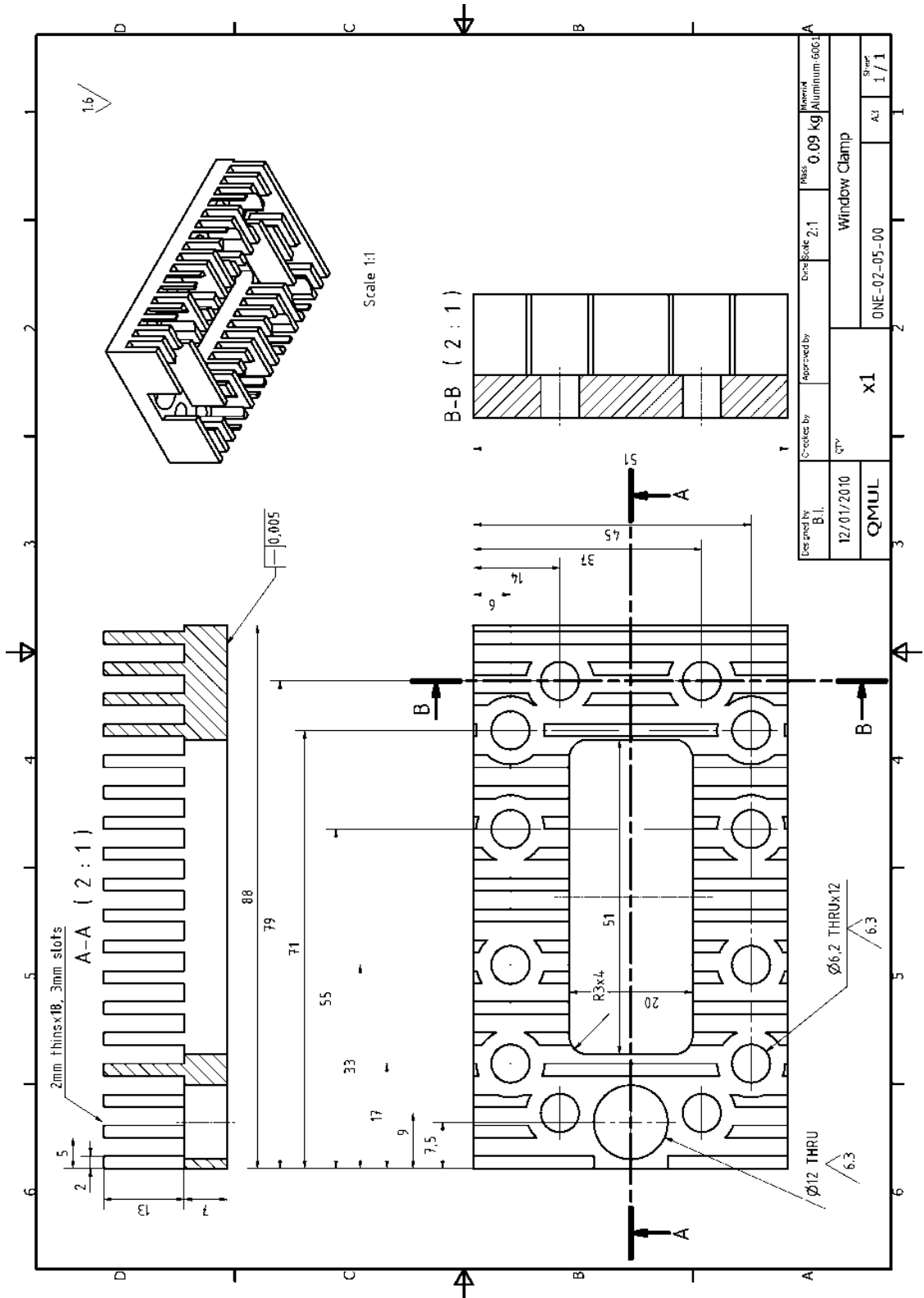




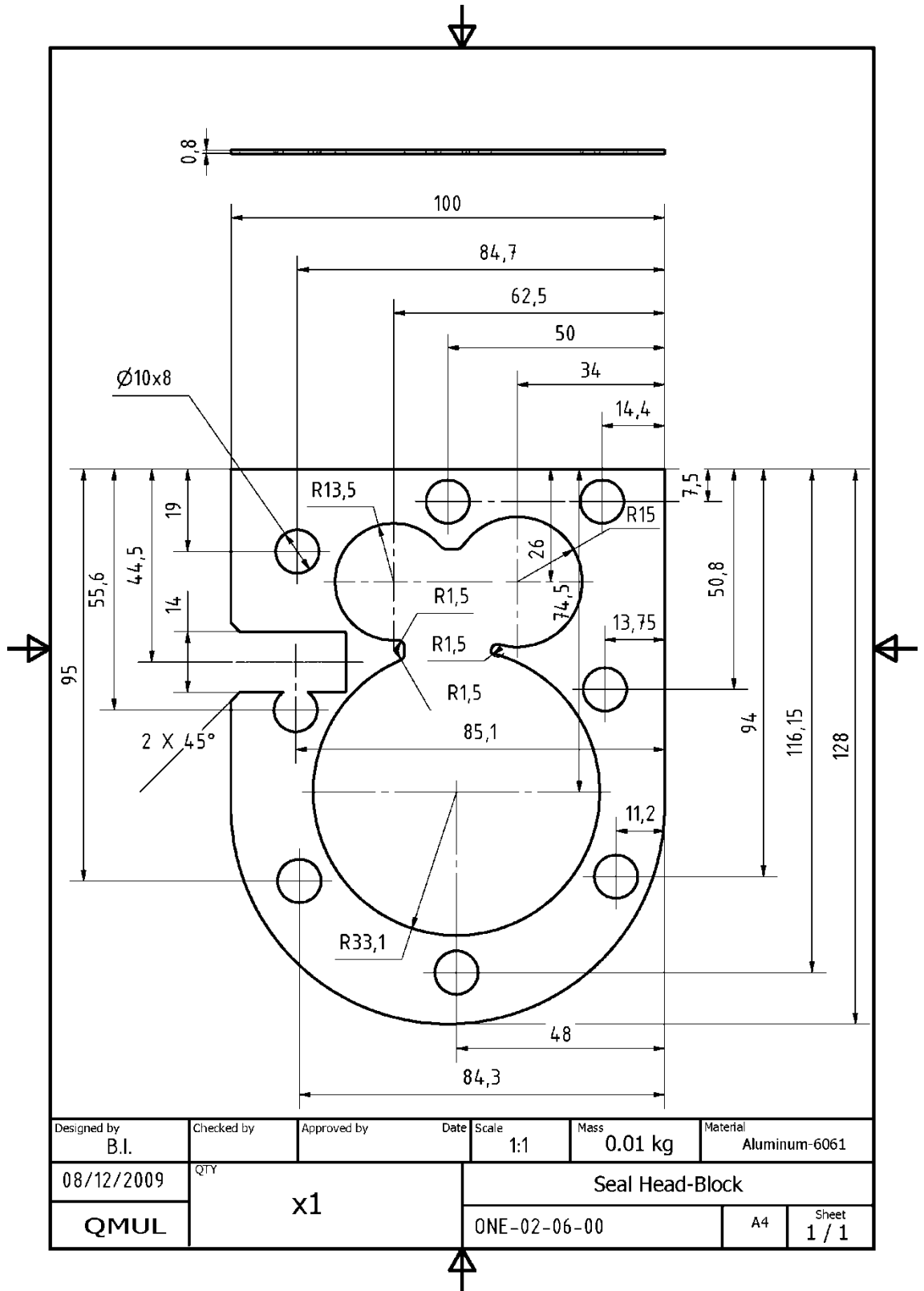


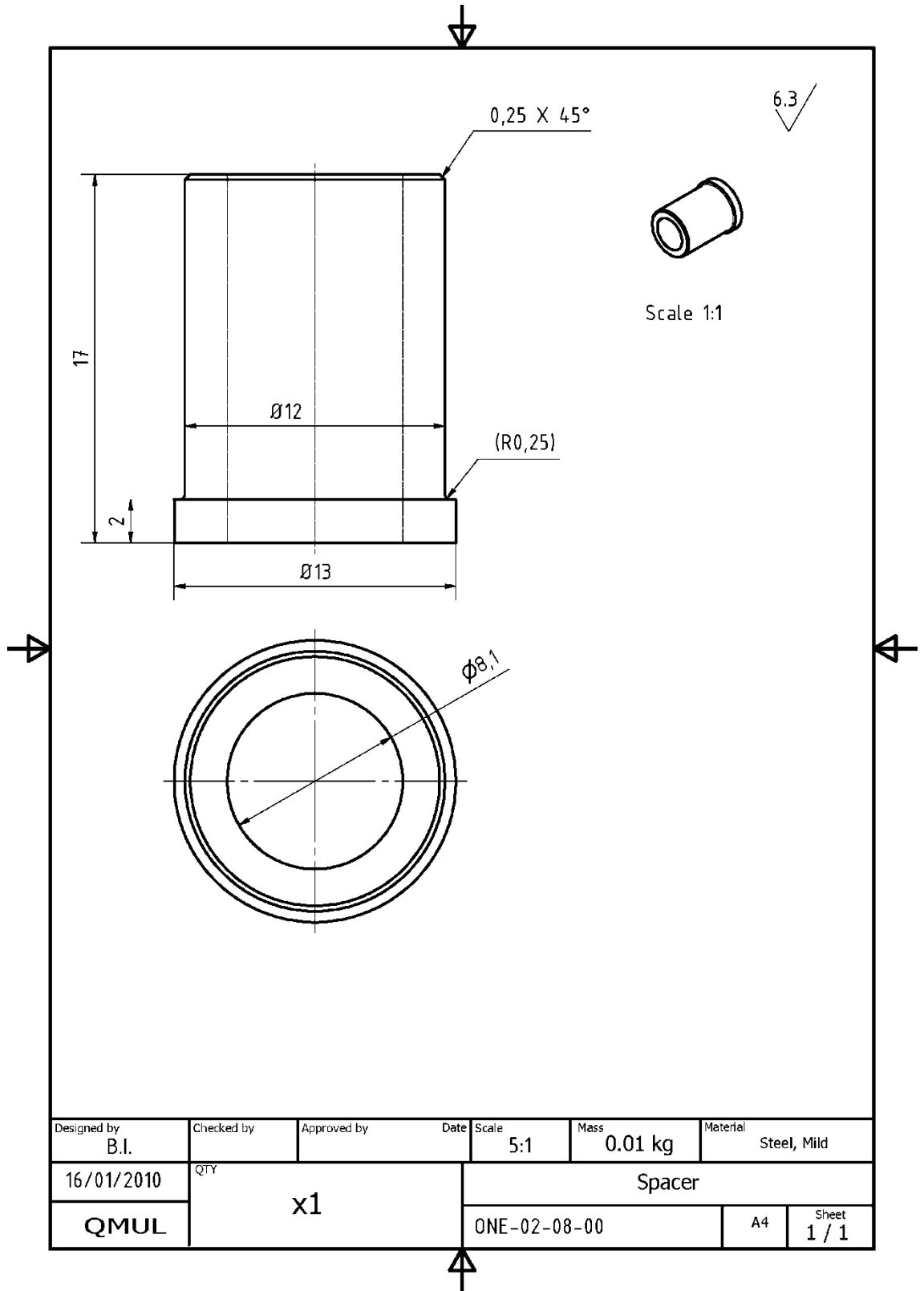


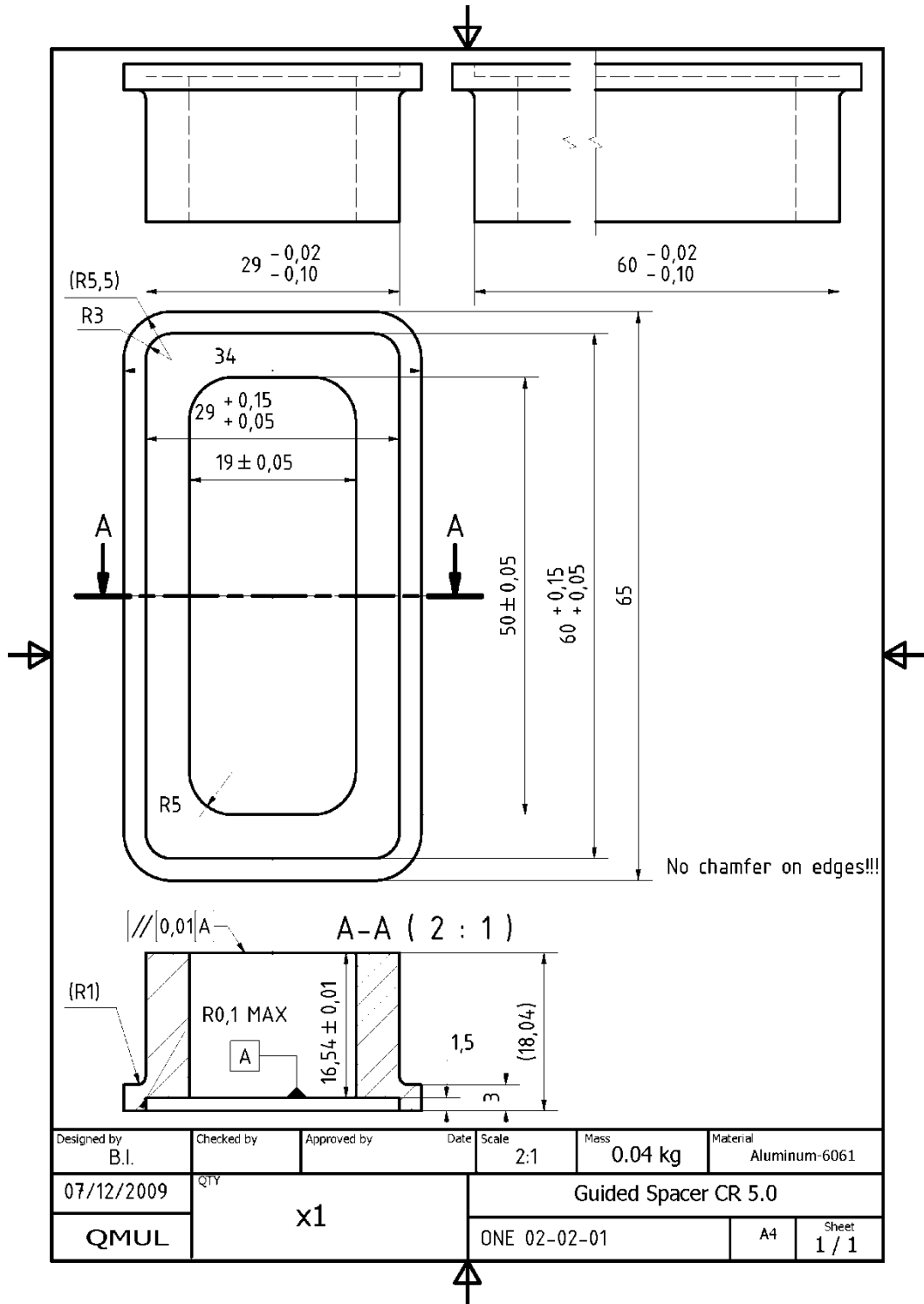




Designed By B.L.	Checked By QTM	Approved By X1	Drawn Scale 2:1	Material Aluminum 6061
12/01/2010	QTM	X1	ONE-02-05-00	Part A3
Window Clamp				Rev 1 / 1







Appendix D.



BORN FROM THE CAMERA THAT STARTED IT ALL

Every day previous versions of the Phantom v4 camera system are successfully collecting data from critical tests. The v4.2 and v4.3 continue this tradition of performance and customer confidence by incorporating new and useful features that further extend this camera's horizons.

Both the v4.2 and v4.3 cameras received our latest advanced CMOS sensor to improve the already excellent image quality that has always been expected from previous versions. Our customers expect excellent performance and both of these camera models delivers by effectively tripling the ASA/ISO sensitivity of previous models.

Now all image sizes (aspect ratios) selected during setup are centered on the sensor's midpoint, and

Phantom v4.3/v4.2

Provide 8-bit image depth, at 1,000 frames per second (v4.3) or 2,100 fps (v4.2) at a full resolutions of 800 x 600 pixels (v4.3), 512 x 512 pixels (v4.2)



the Continuously Adjustable Resolution feature permits screen size adjustment in 16 x 8 pixel increments. These slightly smaller cameras include Gigabit Ethernet to simplify camera network communications and speed file transfers.

- 8-bit CMOS sensor composed of 800 x 600 pixels (v4.3), 512 x 512 (v4.2); color or monochrome
- 1,000 frames per second full resolution (v4.3), 2,100 fps (v4.2), up to 90,000 fps maximum (both)
- "CAR" (Continuously Adjustable Resolution) in 16 x 8 pixel increments
- 4800 ISO/ASA monochrome, 1200 ISO/ASA color sensitivity equivalency
- Global (snap-shot) on-chip shuttering to 10 microseconds, (optional 2 μs)
- "EDR" Extreme Dynamic Range™ exposure control
- Auto Exposure control
- Up to 4 Gigabytes DRAM, 6 Gigabytes non-volatile flash memory (optional)
- IRIG-B timing capture, modulated or unmodulated, IRIG lock w/phase shift
- Continuous video output RS-170 (NTSC, PAL)
- Rugged HI-G configuration (optional); Airborne also available for Phantom v4.2 camera
- Gigabit Ethernet or RS232 control

Appendix E.

AF Micro-Nikkor 60mm f/2.8D

★★★★★ 31 reviews

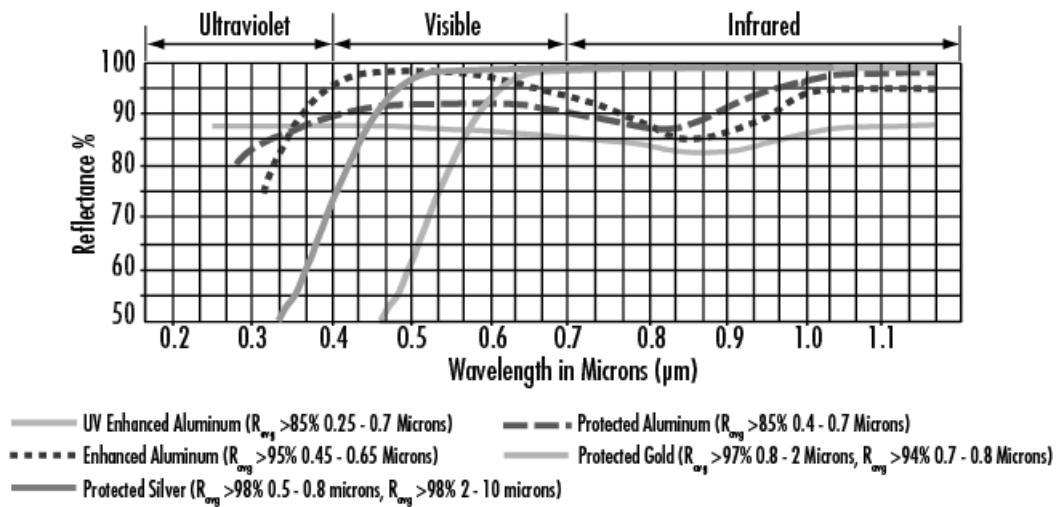
Mount Type	Nikon F-Bayonet
Focal Length	60mm
Maximum Aperture	f/2.8
Minimum Aperture	f/32
Format	FX/35mm
Maximum Angle of View (DX-format)	26°30'
Maximum Angle of View (FX-format)	39°40'
Maximum Reproduction Ratio	1.0x
Lens Elements	8
Lens Groups	7
Compatible Format(s)	FX DX FX in DX Crop Mode 35mm Film
Diaphragm Blades	7
Distance Information	Yes
Autofocus	Yes
Minimum Focus Distance	0.72 ft. (0.22m)
Close Range Correction	Yes
Focus Mode	Auto Manual
Filter Size	62mm
Accepts Filter Type	Screw-on
Approx. Dimensions (Diameter x Length)	2.8 in. (70 mm) x 2.9 in. (74.5 mm)
Approx. Weight	15.5 oz. (440 g)

Appendix F.

51mm diameter, enhanced, first surface, aluminium mirror

Diameter (mm)	51
Dimensional Tolerance (mm)	0
Thickness (mm)	13
Thickness Tolerance (mm)	0
Surface Accuracy (λ)	$\frac{1}{4}$ @ 632.8 nm
Surface Quality	60 - 40
Edges	Fine Ground
Substrate	BOROFLOAT®
Coating Specification	$R_{avg} > 95\%$ @ 450 - 650 nm
Typical Energy Density Limit	0.2 J/cm ² @ 532 nm, 10 ns
Wavelength Range (nm)	450 - 650
Type	Flat Mirror
Coating	Enhanced Aluminium

Reflectance Curves for Metallic (Mirror) Coatings



Metallic Mirror Coating Reflectance Curves, retrieved from Edmund Optics [172]

Appendix G.

High-Temperature Pressure Sensor for Engine Measuring Technology

Type 6052C...

Patent No. US 6,105,434

High-temperature pressure sensor with very small dimensions are ideal for use in internal combustion engines with complex structural geometry of the cylinder head. The sensor is installed with front sealing in an M5x0,5 bore.

- Good temperature stability of the sensitivity
- High sensitivity
- Low thermal shock error
- Long service life due to front seal

Description

Type 6052C... uses a piezoelectric crystal which achieves high sensitivity in conjunction with an extremely small sensor structure. This sensitivity varies by not more than $\pm 0,5\%$ in the temperature range from 150 ... 250 °C. The passive acceleration compensation patented by Kistler keeps the influence of engine vibrations to a minimum.

The front seal provides very good heat transfer and keeps the sensor at a save operating temperature. The diaphragm, optimized by finite element calculation, produces good measuring results and ensures a long service life.

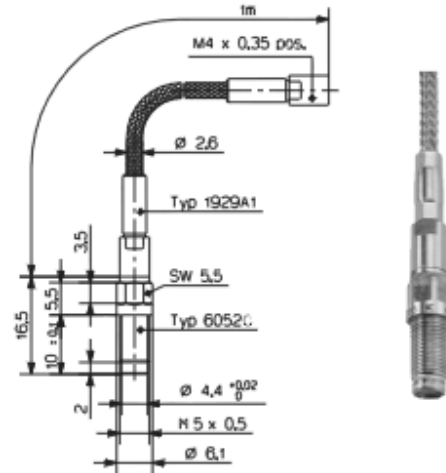
Application

The sensor Type 6052C... is an excellent all-rounder. Its rugged construction makes it suitable for measurements at the knock limit as well as for thermodynamic investigations. This sensor is used mainly for complex cylinder head geometry. As well as for motor cycles and other small engines and for combustion analysis in vehicles.

For applications mainly in the knocking range or at very high peak pressures, use of Type 6052C...U20 with reinforced diaphragm (heavy duty version) is recommended.

Type 6052C...U40 is provided with additional damping and is suitable for applications on engines with extremely high vibrations, e.g. racing engines.

These sensors are always provided with an integrated cable. For standard applications, a rugged cable with steel braiding Type 1929A1 is used. If the sensor connector is exposed directly to engine oil, e.g. when installed through the valve cover, the oil proof cable (IP67) Type 1983AA1 is recommended.



Technical Data

Type 6052C...

Measuring range	bar	0 ... 250
Calibrated partial ranges	bar	0 ... 50, 0 ... 100, 0 ... 150, 0 ... 250
Overload	bar	300
Sensitivity	pC/bar	≈ -20
Natural frequency (measuring element)	kHz	≈ 160
Linearity, all ranges (at 23 °C)	%/FSO	$\leq \pm 0,3$
Acceleration sensitivity		
axial	bar/g	$< 0,0002$
radial	bar/g	$< 0,0005$
Operating temperature range	°C	-20 ... 350
Temperature min./max.		-50 ... 400
Sensitivity change		
200 °C ± 50 °C	%	$\leq \pm 0,5$
23 ... 350 °C	%	$\leq \pm 2$
Thermal shock error		
(at 1500 1/min, $p_{mi} = 9$ bar)		
Δp (short time drift)	bar	$\leq \pm 0,5$
Δp_{mi}	%	$\leq \pm 2$
Δp_{max}	%	$\leq \pm 1,0$
Insulation resistance at 23 °C	Ω	$\geq 10^{11}$
Shock resistance	g	2 000
Tightening torque	N-m	1,5
Capacitance, without cable	pF	5
Weight with cable	gram	30
Connector, ceramic insulator	-	M4 x0,35

Technical Data

Type 6052C...U20 (other specifications as for Type 6052C...)

Measuring range	bar	0 ... 300
Calibrated partial ranges	bar	0 ... 100, 0 ... 200, 0 ... 300
Overload	bar	350
Sensitivity	pC/bar	≈-19
Linearity, all ranges (at 23 °)	%/FSO	≤±0,5
Acceleration sensitivity		
axial	bar/g	<0,0005
radial	bar/g	<0,0005
Sensitivity change		
23 ... 350 °C	%	≤±3
Thermal shock error		
(at 1500 1/min, p _{mi} = 9 bar)		
Δp (short time drift)	bar	≤±0,7
Δp _{mi}	%	≤±3
Δp _{max}	%	≤±1,5

Type 6052C...U40 (other specifications as for Type 6052C...)

Operating temperature range	°C	-20 ... 200
Temperature min./max.	°C	-50 ... 250
Sensitivity shift		
23 ... 200 °C	%	≤±2
Calibrated partial ranges	bar	0 ... 100, 0 ... 200, 0 ... 250

Mounting

Direct mounting:

Sensor Type 6052C... can be mounted directly in the cylinder head, see Fig. 2. Machining of the bore must correspond exactly to the bore specifications shown in Fig. 1.

The Kistler tools:

- Step drill Type 1300A51
- Special tap Type 1357A and the
- Finishing tool for bore Type 1300A79

must be used in order to comply with the tolerances required. The bore must be machined in one clamping. Before mounting the sensor, the sealing surface in particular must be checked; use of the finishing tool (reamer) Type 1300A79 is mandatory. When mounting the sensor, it is essential to comply with the tightening torque of 1,5 N-m. The sensor should therefore be mounted with the cable connected using the socket wrench Type 1300A9 and the torque wrench Type 1300A17. You will find additional information for machining the bore and mounting in the instruction manual. Your Kistler distributor will provide you with information, for example concerning the preferred position of the indicating bore in the combustion chamber.

Mounting sleeve:

When space allows or if the water jacket of the cylinder head will be breached, a mounting sleeve is recommended. Mounting sleeves are manufactured to customer requirements; Fig. 3 shows a version with M7x0,75 thread. An additional advantage of mounting sleeves is that the actual sensor bore in the sleeve can be very precisely machined. On request, Kistler will provide custom made adapters for your particular mounting situation.

Spark plug adapter:

Sensor 6052C... can also be used in the spark plug adapter 6517B..., see data sheet 6517B_000-491.

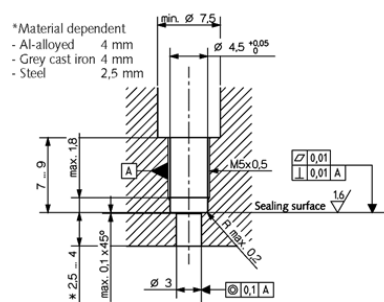


Fig. 1: Mounting bore

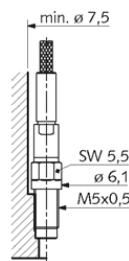


Fig. 2: Direct mounting

6052C_000-552e-02.10

Appendix H.

513.802

Measure & Analyze -- MCA



1 ... 4

Ladungsverstärker
Amplificateur de charge
Charge Amplifier

5037B1.... 5037B3...

Beschreibung

Ladungsverstärker für industriellen Einsatz. Das in ein robustes, dichtes Kunststoffgehäuse angepasste Gerät ist, mit einem oder drei Kanälen, bereits abgeglichen oder vor Ort einstellbar (siehe Bestellbezeichnung Seite 4).

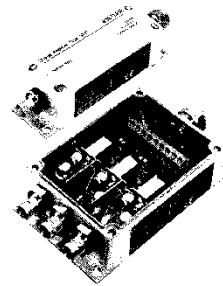
Description

Amplificateur de charge pour l'industrie. L'appareil, incorporé dans un boîtier en matière plastique étanche et robuste, est disponible en version à un ou trois canaux déjà ajusté ou réglable in situ. (Voir désignation de commande, page 4).

Description

Charge amplifier for industrial use. This instrument is housed in a rugged, sealed plastic case and is supplied with either one or three channels already adjusted or adjustable in situ (see order designation Page 4).

- Industrieller Ladungsverstärker für vor-Ort Einsatz
 Amplificateur de charge industriel pour utilisation sur place
 Industrial charge amplifier for on-site application
- Robustes, dichtes Gehäuse, nach Schutzart IP 65
 Boîtier étanche et robuste selon degré de protection IP 65
 Rugged, sealed case per degree of protection IP 65
- Bereich auf bestimmten Sensor abgeglichen lieferbar
 Disponible avec gamme ajustée pour un capteur défini
 Range can be supplied adjusted to a specific sensor
- Option: Halbleiter-Reset anstelle Relais-Reset
 Option: Reset par semi-conducteur au lieu de reset par relais
 Option: Semiconductor reset instead of relay reset
- CE-konform
 Conforme au CE
 Conforming to CE



Technische Daten

Données techniques

Technical Data *

Bereich	Gamme	Range		
für ±10 V Ausgangsspannung vor Ort einstellbar innerhalb	pour tension de sortie de ±10 V réglable in situ au dedans	for ±10 V output voltage adjustable in situ within	pC	±200 ... ±1000
bereits abgeglichen innerhalb (in der Bestellung angeben)	déjà ajustée au dedans (préciser dans la commande)	already adjusted within (specify in the order)	pC	±20 ... ±200/300
Verstärkung, mit Potentiometer stufenlos einstellbar	Gain, réglable en continu avec potentiomètre	Gain, continuously adjustable with potentiometer	V	1 ... 5
Ausgangsspannung	Tension de sortie	Output voltage	V	±10
Ausgangsstrom	Courant de sortie	Output current	mA	±5
Ausgangswiderstand	Impédance de sortie	Output impedance	Ω	≈10
Toleranz	Tolérance	Tolerance	%	±2
Linearität	Linéarité	Linearity	%FS	±0,2
Rauschen (0,1 Hz ... 10 MHz)	Bruit de fond (0,1 Hz ... 10 MHz)	Noise (0,1 Hz ... 10 MHz)	mV _{eff}	±5
Kabelsörnsignal	Bruit de fond du câble	Cable noise	pC _{int} /pF	<2*10 ⁶
Frequenzbereich (-3 dB)	Gamme de fréquence (-3 dB)	Frequency range (-3 dB)	Hz	0 ... 30'000
Drift bei 25 °C (typ./max.)	Dérive à 25 °C (typ./max.)	Drift at 25 °C (typ./max.)	pC/s	±1,0/7
Drift mit Halbleiter reset bei 25 °C (±0 °C)	Dérive reset par semi-conducteur bei 25 °C (±0 °C)	Drift with semiconductor reset bei 25 °C (±0 °C)	pC/s	<±0,1 (<±0,5)
Speisespannung	Alimentation	Power	V DC (%)	±15 (±5)
Stromaufnahme	Courant	Current	mA	±30 (±15) ±80 (±40)
5037B1... +15 V (-15 V) 5037B3... -15 V (-15 V)	5037B1... +15 V (-15 V) 5037B3... +15 V (-15 V)	5037B1... +15 V (-15 V) 5037B3... +15 V (-15 V)		
Reset-Funktion Ansteuerung mit 15V-Logik	Fonction Reset Réglage avec logique 15 V	Reset function Control with 15 V logic		LOW: OPERATE HIGH: RESET
Zulässige Umgebungstemperatur	Température ambiante admissible	Working temperature range	°C	0 ... 60
Messanschlüsse	Connexions de mesure	Measuring connections		(Fig. 1)
Schutzart	Degré de protection	Degree of protection		IP 65 (exc. BNC + IG-32 I/F)
Gewicht 5037B1 (5037B3)	Poids 5037B1... (5037B3...)	Weight 5037B1... (5037B3...)	g	≈180 (≈300)
Konformität mit EG-Richtlinie EMV Störaussendung EMV Störfestigkeit	Conformité à la Directive CE CEM Emission CEM Immunité	Conformity to EC Directive EMC Emission EMC Immunity		EN 50081-1 EN 50082-1

5037B_000-302m-1104

* In all Kistler documents, the decimal sign is a comma on the line (ISO 31-0:1992)

Appendix I.

HENGSTLER

TECHNICAL DATASHEET

Absolute Encoder AC 58 - SSI-P

- Compact design: 59 mm mounting depth for single or multiturn
- Aids for start up and operation: diagnostic LED, preset key with optical response
- Parameterization: Resolution, code type, direction, output format, warning, alarm
- Parameters can be stored in a non-volatile memory
- Integrated RS232 interface



Clamping flange



TECHNICAL DATA
mechanical

Housing diameter	58 mm
Shaft diameter	6 mm / 10 mm (Solid shaft) 10 mm / 12 mm (Hub shaft)
Flange (Mounting of housing)	Synchro flange, Clamping flange, Tether, Square flange
Protection class shaft input (EN 60529)	IP64 or IP67
Protection class housing (EN 60529)	IP64 (IP67 optional)
Shaft load axial / radial	40 N / 60 N
Max. speed	max. 10 000 rpm (continuous), max. 12 000 rpm (short term)
Starting torque typ. ¹	≤ 0.01 Nm
Moment of inertia	ca. 3.8 x 10 ⁻⁶ kgm ²
Vibration resistance (DIN EN 60068-2-6)	100 m/s ² (10 ... 500 Hz)
Shock resistance (DIN EN 60068-2-27)	1000 m/s ² (6 ms)
Operating temperature	-40 °C ... +100 °C
Storage temperature	-40 °C ... +85 °C
Material shaft	Stainless Steel
Material housing	Aluminum
Weight	approx. 260 g (ST) / 310 g (MT)
Connection	Cable, axial or radial M23 connector (Conin), 12 pole, axial or radial

¹ at 20°C

TECHNICAL DATA
electrical

Supply voltage	DC 10-30 V
Max. current w/o load	250 mA (ST / MT)
Resolution singleturn	10 - 17 Bit
Resolution multiturn	12 Bit
Output code	Binary, Gray
Drives	Clock and Data / RS422
Parameterization	Resolution, Code type, Direction, Output format, Warning, Alarm
Control inputs	Direction, Preset 1, Preset 2
Alarm output	Alarm bit
Status LED	Green = ok, red = alarm

Data sheet created	© Hengstler GmbH, Umlandstr. 49, D-78554 Aldingen/ Germany ☎ +49 74 24 - 89 0 Fax +49 74 24 - 89 500	Page
2009-12-15 12:07:08	E-mail: info@hengstler.com Internet: www.hengstler.com	1

Appendix J.



Technical overview

The pressure transmitters of type 680 with piezoresistive measuring elements have compensated, calibrated and amplified sensor signals which are available as standard voltage or current outputs.

The transmitter housing is available with various pressure and electrical connections.

Manufactured from stainless steel, its welded construction provides a watertight seal. With its sophisticated building block system, individual designs to meet specific applications are possible.

The distinct advantages

- Effective overload protection due to chemically etched chip diaphragm and specially designed glass gland
- Fast and affordable customer-specific solutions due to building-block system, even for small quantities
- Compact construction with SMD technology enhances operational reliability in the presence of shock and vibration
- Welded construction provides 100% sealing against media

Pressure ranges

Relative pressure (differential measurements to ambient pressure) -1 ... +25 bar

Absolute pressure (absolute measurement; reference point vacuum) 0 ... +25 bar

Overpressure (absolute measurement; reference point ambient pressure on manufacture) > 25 ... 1000 bar

DIN categories see order code selection table. Other pressure ranges available.

Overload

3 x Measuring range, min. 3 bar, maximum rupture pressure

Rupture pressure

> 200 bar (0.1 ... 25 bar)
> 850 bar (> 25 ... 600 bar)
1500 bar (> 600 ... 1000 bar)

Characteristic line deviation

Acc. initial point setting DIN 16086, inclusive hysteresis and repeatability
≤ 0.5% fs
≤ +/- 0.25% fs
≤ +/- 0.10% fs on request

Material

Stainless steel 1.4435 (316L)
Titanium or Hastelloy C on request

Temperature influences

Compensated temperature range:
0 ... 70 °C, -25 ... +85 °C

Temperature error

Zero point (0 ... 70 °C)
0 ... < 0.5 bar ≤ +/- 0.06 % fs/°C

0.5 ... < 2 bar ≤ +/- 0.03 % fs/°C
2 ... < 600 bar ≤ +/- 0.015 % fs/°C

Zero point (-25 ... +85 °C)

0 ... < 0.5 bar ≤ +/- 0.08 % fs/°C
0.5 ... < 2 bar ≤ +/- 0.04 % fs/°C
2 ... < 600 bar ≤ +/- 0.02 % fs/°C

Operating range (0 ... 70 °C)

≤ +/- 0.015% fs/°C

Operating range (-25 ... +85 °C)

≤ +/- 0.02% fs/°C

Storage

- 40 ... + 125 °C

Dynamic response

Suitable for static and dynamic measurements.
Response time: < 1 ms / 10 ... 90% FS

Outputs and power supply

0 – 5 V	15 – 30 VDC	3-wire
0 – 10 V	15 – 30 VDC	3-wire
0 – 20 mA	9 – 33 VDC	3-wire
4 – 20 mA	9 – 33 VDC	2-wire

Short circuit-proof, with polarity reversal protection. Other signal outputs on request.

Adjustable versions

Potentiometer for adjustment of all pressure ranges (only with DIN EN 175301-803 connector and round binder connector 723, can be screwed up)

Load

0 – 20 mA $\frac{\text{supply voltage} - 6 \text{ V}}{0.02 \text{ A}}$ [Ohm]

max. 1 kOhm

4 – 20 mA

max. $\frac{\text{supply voltage} - 9 \text{ V}}{0.02 \text{ A}}$ [Ohm]

Intrinsically safe version

Intrinsic safety II 1G EEx ia IIC T3 ... T6

Output 4 – 20 mA

Power supply 10 – 30 VDC

Load

max. $\frac{\text{Speisepannung} - 10 \text{ V}}{0.02 \text{ A}}$ [Ohm]

Current consumption

0 – 5 V	2.5 mA
0 – 10 V	2.5 mA
0 – 20 mA	2.6 mA fs (max. 30 mA)
4 – 20 mA	2.0 mA fs (max. 31 mA)

Electrical connections / Protection class

See order code selection table.
Other connections on request.

Test voltage 500 VDC

Appendix K.

Technical data (red-y compact series)

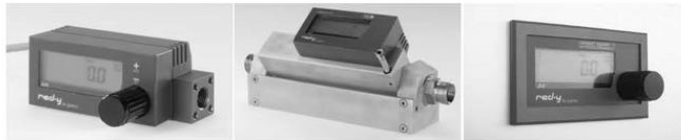
Instrument types



compact meter GCM
Thermal mass flow meter

compact regulator GCR
Thermal mass flow meter
with manual valve

compact switch GCS
Thermal mass flow meter
with alarm functions



compact all-in GCA
Thermal mass flow meter with
manual valve & alarm functions

OEM version
For customer-specific
requirements

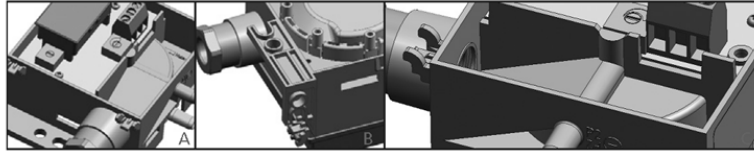
Panel mounting kit
Panel mounting kits for
IP-50 and IP-65 protection

Measuring ranges (Air)	Full scale freely selectable	Type	Measuring range (Air)	Connection		
	compact meter GCM	GCX-A	from 0 ... 50 mln/min to 0 ... 500 mln/min	G $\frac{1}{2}$ "		
	compact regulator GCR	GCX-B	from 0 ... 500 mln/min to 0 ... 5000 mln/min	G $\frac{1}{2}$ "		
	compact switch GCS	GCX-C	from 0 ... 5 l/min to 0 ... 50 l/min	G $\frac{1}{2}$ "		
	compact all-in GCA	GCX-D	from 0 ... 50 l/min to 0 ... 300 l/min	G $\frac{1}{2}$ "		
Performance data	Media (real gas calibration)	Air, O ₂ , N ₂ , He, Ar, CO ₂ , H ₂ , CH ₄ , C ₃ H ₈ , SF ₆ Other gases and gas mixtures on request (real gas calibration or conversion factors)				
	Accuracy	± 1.0% of full scale; GCX-D ± 2.0% of full scale				
	Turndown ratio	1 : 50				
	Response time	500 ms (accuracy better than 99%)				
	Power supply					
	Meter & Regulator	Lithium battery (Lifetime about 2 years with constant flow) Option: External supply + 24 Vdc ± 10%				
	Switch & All-in	External supply + 24 Vdc ± 10%				
	Pressure	Up to 11 bar a				
	Temperature	0 – 50°C				
	Materials	Aluminium, optional stainless steel electropolished				
Seals	FKM, optional EPDM					
Integration	Display	6-digit LCD in engineering units and bar graph				
	Gasanschluss	G $\frac{1}{2}$ " female up to 50 l/min, G $\frac{1}{2}$ " female up to 300 l/min				
	Inlet section	None required				
	Mounting orientation	Any orientation (horizontal only above 5 bar)				
	Front plate dimensions	48x96 mm (DIN-Standard)				
	Connection cable	For external power supply: 2 m and 5 m with loose ends				
	Optional flow switch	Settings				
Function		Min. or max. alarm				
Threshold		Adjustable between 0 and full scale, normally open or closed				
Failsafe Condition		User configurable				
Alarm delay		Adjustable 0 – 180 s				
Alarm hysteresis		Fully adjustable				
Alarm suppression		User configurable				
Alarm reset		Automatic or manual				
Contact		Floating changeover contact (24 V, 1 A)				
Safety		Test pressure	16 bar a			
	Leak rate	< 1 x 10 ⁻⁸ mbar l/s He				
	Environmental protection	IP-50, with panel mounting kit IP-65				
	EMC	EN 50081, EN 50082				
Dimensions	Dimensions in mm	A	B	C	D	
		GCM, GCR, GCS, GCA G $\frac{1}{2}$ "	114	44	25	44*
		GCM, GCS G $\frac{1}{2}$ "	160	54	35	54
		GCR, GCA G $\frac{1}{2}$ "	207	54	35	80**
		*Regulator knob (GCR, GCA): D+26mm **Valve mounted				

Subject to technical alterations

Appendix L.

E



Versions

- A – 2 potentiometers for full scale and zero point adjustment
- B – Housing with built-in fixing brackets
- C – Self-retaining screw in cover and angled surface for easy cable entry

Accuracy

Transmitter Type Parameter	Unit	± 0.5 mbar	0 ... 1 mbar	0 ... 3 mbar	0 ... 5 mbar	0 ... 10–50 mbar
Tolerance zero point ¹⁾	max. % fs	± 1.0	± 1.0	± 0.7	± 0.7	± 0.7
Tolerance full scale ¹⁾	max. % fs	± 1.0	± 1.0	± 0.7	± 0.7	± 0.7
Resolution	% fs	0.2	0.2	0.1	0.1	0.1
Total of linearity, hysteresis and repeatability	max. % fs	± 3.0	± 2.0	± 1.0	± 1.0	± 0.6
Long term stability acc. to DIN IEC 60770	% fs	± 1.0	± 1.0	± 1.0	± 1.0	± 1.0
TC zero point ²⁾	typ. % fs/10 K	± 0.2	± 0.2	± 0.2	± 0.1	± 0.1
TC zero point ²⁾	max. % fs/10 K	± 1.0	± 1.0	± 0.5	± 0.4	± 0.4
TC sensitivity ²⁾	typ. % fs/10 K	+ 0.3	+ 0.3	+ 0.2	+ 0.1	± 0.1
TC sensitivity ²⁾	max. % fs/10 K	+ 0.6	+ 0.6	+ 0.5	+ 0.5	± 0.2

With root-extracted output (2 ... 100% pressure)

Absolute error: (% of full scale)

TC zero point: (% fs) ²⁾

$$\text{max. } \pm 0.6 \sqrt{\frac{P_{fs}}{P}} + 1.5$$

$$\text{max. } \pm 0.3 \sqrt{\frac{P_{fs}}{P}} + 1.5$$

$$\text{max. } \pm 0.6 \sqrt{\frac{P_{fs}}{P}} + 1.5$$

Test conditions: 25 °C, 45% RH, Power supply 24 VDC
TC z. p. / TC s. 0 ... 70 °C

Order code selection table

694. 9 X X X X X X X X X

Pressure range ³⁾	mbar (hPa)	Pa	mmWC (mmH ₂ O)	inH ₂ O															
-0.5 ... +0.5	-50 ... +50	-5 ... +5	-0.2 ... +0.2		3	1													
0 ... 1	0 ... 100	0 ... 10	0 ... 0.4		1	1													
0 ... 3	0 ... 300	0 ... 30	0 ... 1.2		1	2													
0 ... 5	0 ... 500	0 ... 50	0 ... 2		1	3													
0 ... 10	0 ... 1000	0 ... 100	0 ... 4		1	4													
0 ... 16	0 ... 1600	0 ... 160	0 ... 6.4		1	5													
0 ... 25	0 ... 2500	0 ... 250	0 ... 10		1	6													
0 ... 50	0 ... 5000	0 ... 500	0 ... 20		1	7													
Unit of pressure	mbar (hPa)							0											
	Pa							2											
	mmWC (mmH ₂ O)							3											
	inH ₂ O							1											
Output signal / Adjustment	Linear									1									
	Linear Full scale and zero point adjustable by customer									2									
	Square root extracted									4									
	Square root extracted Full scale and zero point adjustable by customer									3									
Output ⁴⁾ and power supply	0 ... 10 V	13.5 ... 33 VDC / 24 VAC ±15%	3-wire																
	0 ... 20 mA	13.5 ... 33 VDC / 24 VAC ±15%	3-wire																
	4 ... 20 mA	13.5 ... 33 VDC / 24 VAC ±15%	3-wire																
	4 ... 20 mA	11.0 ... 33 VDC	2-wire																
Display 3 digit	Without																		
	In pressure unit chosen above																		
	In % fs																		
Pressure connections / Pressure orifices	Connection pipe Ø 6.2 mm without pressure orifice																		1
	Connection pipe Ø 6.2 mm pressure orifice on P1																		2
	Connection pipe Ø 6.2 mm pressure orifice on P2																		3
	Connection pipe Ø 6.2 mm pressure orifices on P1 and P2																		4
Version	IP 54: Without connection kit																		0
	IP 54: With connection kit (metal), 90° angled including tube 2 m long (Fig. 1) ⁵⁾																		1
	IP 54: With connection kit (plastic), straight including tube 2 m long (Fig. 2) ⁵⁾																		2
	IP 65: Without connection kit																		3
	IP 65: With connection kit (metal), 90° angled including tube 2 m long (Fig. 1) ⁵⁾																		4
	IP 65: With connection kit (plastic), straight including tube 2 m long (Fig. 2) ⁵⁾																		5
Variation (optional)	Of pressure range or output signal																		
	Indicate W and state on order (e.g. 0 ... 9 mbar / Out 0 ... 10 V)																		W

Accessories

	Order number
Connection kit for vent duct (metal), 90° angled including tube 2 m long (Fig. 1) ⁵⁾	104312
Connection kit for vent duct (plastic), straight including tube 2 m long (Fig. 2) ⁵⁾	100064
DIN-rail mounting adaptor	112854
Calibration certificate	104551

¹⁾ For changing diaphragm position see installation arrangement page 6
²⁾ TC = Temperature coefficient
³⁾ Other pressure ranges on request
⁴⁾ Other output signals on request
⁵⁾ See page 8

8 Bibliography

1. Kosnik, L., *The potential for small scale hydropower development in the US*. Energy Policy, 2010. **38**(10): p. 5512-5519.
2. Siebert, H., *The Problem*, in *Economics of the Environment*. 2008, Springer Berlin Heidelberg. p. 3-6.
3. Stern, N., *The Economics of Climate Change, The Stern Review*. 2007: Cambridge University Press.
4. Stern, N., *The Economics of Climate Change*. American Economic Review, 2008. **98**(2): p. 1-37.
5. Chu, S. and A. Majumdar, *Opportunities and challenges for a sustainable energy future*. Nature, 2012. **488**(7411): p. 294-303.
6. Inman, M., *Natural gas: The fracking fallacy*. Nature, 2014. **516**(7529): p. 28-30.
7. Olah, G.A., A. Goepfert, and G.K.S. Prakash, *Beyond Oil and Gas: The Methanol Economy*. 2009: Wiley VCH.
8. Rifkin, J., *The hydrogen economy*. 2002: Polity Press.
9. Panel on Climate Change, *Climate Change 2014: Synthesis Report*. 2014.
10. McGlade, C. and P. Ekins, *The geographical distribution of fossil fuels unused when limiting global warming to 2 [deg]C*. Nature, 2015. **517**(7533): p. 187-190.
11. Höök, M. and X. Tang, *Depletion of fossil fuels and anthropogenic climate change - A review*. Energy Policy, 2013. **52**(0): p. 797-809.
12. Hoffert, M.I., K. Caldeira, G. Benford, D.R. Criswell, C. Green, H. Herzog, A.K. Jain, H.S. Kheshgi, K.S. Lackner, and J.S. Lewis, *Advanced technology paths to global climate stability: energy for a greenhouse planet*. science, 2002. **298**(5595): p. 981-987.
13. Ihracska, B., T. Korakianitis, P. Ruiz, D.R. Emberson, R.J. Crookes, A. Diez, and D. Wen, *Assessment of elliptic flame front propagation characteristics of iso-octane, gasoline, M85 and E85 in an optical engine*. Combustion and Flame, 2014. **161**(3): p. 696-710.

14. Ihracska, B., D. Wen, S. Imran, D.R. Emberson, L. Maria Ruiz, R.J. Crookes, and T. Korakianitis, *Assessment of elliptic flame front propagation characteristics of hydrogen in an optically accessible spark ignition engine*. International Journal of Hydrogen Energy, 2013. **38**(35): p. 15452-15468.
15. Schuetzle, D., W.O. Siegl, T.E. Jensen, M.A. Dearth, E.W. Kaiser, R. Gorse, W. Kreucher, and E. Kulik, *The relationship between gasoline composition and vehicle hydrocarbon emissions: a review of current studies and future research needs*. Environmental health perspectives, 1994. **102**(Suppl 4): p. 3.
16. Rakopoulos, C.D., G.M. Kosmadakis, and E.G. Pariotis, *Evaluation of a combustion model for the simulation of hydrogen spark-ignition engines using a CFD code*. International Journal of Hydrogen Energy, 2010. **35**(22): p. 12545-12560.
17. Turns, S.R., *An Introduction to Combustion: Concepts and Applications*. 2000: McGraw-Hill Education.
18. Veynante, D. and L. Vervisch, *Turbulent combustion modeling*. Progress in Energy and Combustion Science, 2002. **28**(3): p. 193-266.
19. Daintith, J., *Oxford dictionary of physics*. 2005, Oxford University Press Oxford.
20. Kalghatgi, G.T. and M.D. Swords, *Flame-Speed Measurements In An Internal-Combustion Engine*. Combustion and Flame, 1983. **49**(1-3): p. 163-169.
21. Rallis, C.J. and A.M. Garforth, *The determination of laminar burning velocity*. Progress in Energy and Combustion Science, 1980. **6**(4): p. 303-329.
22. Lancaster, D.R., R.B. Krieger, S.C. Sorenson, and W.L. Hull, *Effect of Turbulence on Spark Ignition Engine Combustion*. SAE International Journal, 1976(760160).
23. Bates, S.C., *Flame Imaging Studies in a Spark-Ignition Four-Stroke Internal Combustion Optical Engine*. SAE Technical Paper, 1989(890154).
24. Bates, S.C., *Further Insights Into Si 4-Stroke Combustion Using Flame Imaging*. Combustion and Flame, 1991. **85**(3-4): p. 331-352.
25. Keck, J.C., J.B. Heywood, and G. Noske, *Early Flame Development and Burning Rates in Spark Ignition Engines and Their Cyclic Variability*. SAE Technical Paper, 1987(870164).
26. Ozdor, N., M. Dulger, and E. Sher, *Cyclic Variability in Spark Ignition Engines A Literature Survey*. SAE Technical Paper, 1994(940987).

27. Pischinger, S. and J.B. Heywood, *A Study of Flame Development and Engine Performance with Breakdown Ignition Systems in a Visualization Engine*. SAE Technical Paper, 1988(880518).
28. Maly, R., *Spark Ignition: Its Physics and Effect on the Internal Combustion Engine*. 1984: Plenum Press, New York. 91-129.
29. Aleiferis, P.G., A.M.K.P. Taylor, J.H. Whitelaw, and K.U.Y. Ishii, *Cyclic Variations of Initial Flame Kernel Growth in a Honda VTEC-E Lean-Burn Spark-Ignition Engine*. SAE Technical Paper, 2000(2000-01-1207).
30. Keck, J.C., *Turbulent flame structure and speed in spark-ignition engines*. Symposium (International) on Combustion, 1982. **19**(1): p. 1451-1466.
31. Matekunas, F.A., *Modes and Measures of Cyclic Combustion Variability*. SAE International Journal, 1983(830337).
32. Beretta, G.P., M. Rashidi, and J.C. Keck, *Turbulent Flame Propagation And Combustion In Spark-Ignition Engines*. Combustion and Flame, 1983. **52**(3): p. 217-245.
33. Bradley, D. *How fast can we burn?* in *Symposium (International) on Combustion*. 1992. Elsevier.
34. Gillespie, L., M. Lawes, C.G.W. Sheppard, and R. Woolley, *Aspects of Laminar and Turbulent Burning Velocity Relevant to SI Engines*. SAE Technical Paper, 2000(2000-01-0192).
35. Bradley, D., R.A. Hicks, M. Lawes, C.G.W. Sheppard, and R. Woolley, *The Measurement of Laminar Burning Velocities and Markstein Numbers for Iso-octane-Air and Iso-octane-n-Heptane-Air Mixtures at Elevated Temperatures and Pressures in an Explosion Bomb*. Combustion and Flame, 1998. **115**(1-2): p. 126-144.
36. Heywood, J.B., *Internal Combustion Engine Fundamentals*. 1988: McGraw-Hill.
37. Driscoll, J.F., *Turbulent premixed combustion: Flamelet structure and its effect on turbulent burning velocities*. Progress in Energy and Combustion Science, 2008. **34**(1): p. 91-134.
38. zur Loye, A.O. and F.V. Bracco, *Two-Dimensional Visualization of Premixed-Charge Flame Structure in an IC Engine - SP-715*. SAE Technical Paper, 1987(870454).

39. Korakianitis, T., A.M. Namasivayam, and R.J. Crookes, *Natural-gas fuelled spark-ignition (SI) and compression-ignition (CI) engine performance and emissions*. Progress in Energy and Combustion Science, 2011. **37**(1): p. 89-112.
40. Aleiferis, P.G., Y. Hardalupas, A. Taylor, K. Ishii, and Y. Urata, *Flame chemiluminescence studies of cyclic combustion variations and air-to-fuel ratio of the reacting mixture in a lean-burn stratified-charge spark-ignition engine*. Combustion and Flame, 2004. **136**(1-2): p. 72-90.
41. Crua, C., D.A. Kennaird, and M.R. Heikal, *Laser-induced incandescence study of diesel soot formation in a rapid compression machine at elevated pressures*. Combustion and Flame, 2003. **135**(4): p. 475-488.
42. Yang, C. and H. Zhao, *In-cylinder studies of hybrid combustion in a direct injection single-cylinder optical engine*. International Journal of Engine Research, 2010. **11**(6): p. 515-531.
43. Yang, C. and H. Zhao, *In-Cylinder Studies of CAI/HCCI Combustion with Negative Valve Overlap in a Direct Injection Gasoline Optical Engine*. Combustion Science and Technology, 2011. **183**(5): p. 467-486.
44. Efthymiou, P., M.H. Davy, C.P. Garner, G.K. Hargrave, J.E.T. Rimmer, and D. Richardson, *Insights into Cold-Start DISI Combustion in an Optical Engine Operating at -7°C*. SAE Int. J. Engines, 2013. **6**(2): p. 1059-1074.
45. Shen, H. and D. Jiang, *Investigation on the Flame Initiation and Early Development in a Spark Ignition Engine*. SAE Technical Paper, 1992(922239).
46. Zhao, H. and N. Ladommatos, *Engine Combustion Instrumentation and Diagnostics*. 2001: SAE International.
47. Bates, S.C., *Flame Imaging Studies of Cycle-by-Cycle Combustion Variation in a SI Four-Stroke Engine*. SAE Technical Paper, 1989(892086).
48. Rashidi, M., *The nature of cycle-by-cycle variation in the si-engine from high-speed photographs*. Combustion and Flame, 1981. **42**(2): p. 111-122.
49. Heywood, J.B. and F.R. Vilchis, *Comparison of flame development in a spark-ignition engine fueled with propane and hydrogen*. Combustion Science and Technology, 1984. **38**(5-6): p. 313-324.
50. Gatowski, J.A., J.B. Heywood, and C. Deleplace, *Flame photographs in a spark-ignition engine*. Combustion and Flame, 1984. **56**(1): p. 71-81.

51. Tagalian, J. and J.B. Heywood, *Flame initiation in a spark-ignition engine*. Combustion and Flame, 1986. **64**(2): p. 243-246.
52. Baritaud, T.A., *High Speed Schlieren Visualization of Flame Initiation in a Lean Operating S.I. Engine*. SAE Technical Paper, 1987(872152).
53. Herweg, R. and Z. G.F.W, *Flame Kernel Formation in a Spark-Ignition Engine*. Proceedings of the Second International Symposium COMODIA 90, 1990: p. 173-178.
54. Nakamura, A., K. Ishii, and T. Sasaki, *Application of Image Converter Camera to Measure Flame Propagation in S.I. Engine*. SAE Technical Paper, 1989(890322).
55. Conte, E. and K. Boulouchos, *Experimental investigation into the effect of reformer gas addition on flame speed and flame front propagation in premixed, homogeneous charge gasoline engines*. Combustion and Flame, 2006. **146**(1-2): p. 329-347.
56. Gerke, U., K. Steurs, P. Rebecchi, and K. Boulouchos, *Derivation of burning velocities of premixed hydrogen/air flames at engine-relevant conditions using a single-cylinder compression machine with optical access*. International Journal of Hydrogen Energy, 2010. **35**(6): p. 2566-2577.
57. Lee, K. and J. Ryu, *An experimental study of the flame propagation and combustion characteristics of LPG fuel*. Fuel, 2005. **84**(9): p. 1116-1127.
58. Aleiferis, P.G., A. Taylor, K. Ishii, and Y. Urata, *The nature of early flame development in a lean-burn stratified-charge spark-ignition engine*. Combustion and Flame, 2004. **136**(3): p. 283-302.
59. Faure, M., M. Sadler, K. Oversby, J. Stokes, S. Begg, L. Pommier, and M. Heikal, *Application of LDA and PIV techniques to the validation of a CFD model of a direct injection gasoline engine*. 1998, SAE Technical Paper.
60. Gold, M., G. Li, S. Sapsford, and J. Stokes, *Application of Optical Techniques to the Study of Mixture Preparation in Direct Injection Gasoline Engines and Validation of a CFD Model*. 2000, SAE International.
61. Aleiferis, P.G., J. Serras-Pereira, Z. van Romunde, J. Caine, and M. Wirth, *Mechanisms of spray formation and combustion from a multi-hole injector with E85 and gasoline*. Combustion and Flame, 2010. **157**(4): p. 735-756.
62. Aleiferis, P.G., J. Serras-Pereira, and D. Richardson, *Characterisation of flame development with ethanol, butanol, iso-octane, gasoline and methane in a direct-*

- injection spark-ignition engine*. Fuel, 2013(In Press
Doi:10.1016/j.fuel.2012.12.088): p. -.
63. Tahtouh, T., F. Halter, C. Mounaïm-Rousselle, and E. Samson, *Experimental Investigation of the Initial Stages of Flame Propagation in a Spark-Ignition Engine: Effects of Fuel, Hydrogen Addition and Nitrogen Dilution*. SAE International Journal of Engines, 2010(2010-01-1451).
 64. Niven, R.K., *Ethanol in gasoline: environmental impacts and sustainability review article*. Renewable and Sustainable Energy Reviews, 2005. **9**(6): p. 535-555.
 65. Agarwal, A.K., *Biofuels (alcohols and biodiesel) applications as fuels for internal combustion engines*. Progress in Energy and Combustion Science, 2007. **33**(3): p. 233-271.
 66. J.S. Malcolm, P.G.A.A.R. and et al., *Internal Combustion Engines: Performance, fuel economy and emissions: A study of alcohol blended fuels in a new optical spark-ignition engine*. 2007: Institution of Mechanical Engineers.
 67. Metghalchi, M. and J.C. Keck, *Burning velocities of mixtures of air with methanol, isooctane, and indolene at high pressure and temperature*. Combustion and flame, 1982. **48**: p. 191-210.
 68. Sileghem, L., V. Alekseev, J. Vancoillie, E. Nilsson, S. Verhelst, and A. Konnov, *Laminar burning velocities of primary reference fuels and simple alcohols*. Fuel, 2014. **115**: p. 32-40.
 69. Verhelst, S., *A Study of the Combustion in Hydrogen-Fuelled Internal Combustion Engines*, in *Department of Flow, Heat and Combustion Mechanics*. 2005, Ghent University: Gent, BELGIUM.
 70. Verhelst, S., R. Woolley, M. Lawes, and R. Sierens, *Laminar and unstable burning velocities and Markstein lengths of hydrogen-air mixtures at engine-like conditions*. Proceedings of the Combustion Institute, 2005. **30**: p. 209-216.
 71. Herweg, R. and R. Maly, *A Fundamental Model for Flame Kernel Formation in S. I. Engines*. SAE Technical Paper, 1992(922243).
 72. Cant, S., *High-performance computing in computational fluid dynamics: progress and challenges*. Philosophical Transactions of the Royal Society of London A: Mathematical, Physical and Engineering Sciences, 2002. **360**(1795): p. 1211-1225.

73. Vervisch, L., R. Hauguel, P. Domingo, and M. Rullaud, *Three facets of turbulent combustion modelling: DNS of premixed V-flame, LES of lifted nonpremixed flame and RANS of jet-flame*. Journal of turbulence, 2004. **5**(4): p. 1-8.
74. Fureby, C., *A fractal flame-wrinkling large eddy simulation model for premixed turbulent combustion*. Proceedings of the Combustion Institute, 2005. **30**(1): p. 593-601.
75. Mantzaras, J., P. Felton, and F. Bracco, *Fractals and turbulent premixed engine flames*. Combustion and Flame, 1989. **77**(3): p. 295-310.
76. Gouldin, F., *An application of fractals to modeling premixed turbulent flames*. Combustion and Flame, 1987. **68**(3): p. 249-266.
77. Zhao, H., *Laser Diagnostics and Optical Measurement Techniques in Internal Combustion Engines*. 2012.
78. Baert, R.S., P.J. Frijters, B. Somers, C.C. Luijten, and W. de Boer, *Design and operation of a high pressure, high temperature cell for HD diesel spray diagnostics: guidelines and results*. 2009, SAE Technical Paper.
79. Allen, C., G. Mittal, C.-J. Sung, E. Toulson, and T. Lee, *An aerosol rapid compression machine for studying energetic-nanoparticle-enhanced combustion of liquid fuels*. Proceedings of the Combustion Institute, 2011. **33**(2): p. 3367-3374.
80. Diez, A., R.J. Crookes, and T. Løvås, *Experimental studies of autoignition and soot formation of diesel surrogate fuels*. Proceedings of the Institution of Mechanical Engineers, Part D: Journal of Automobile Engineering, 2013. **227**(5): p. 656-664.
81. Nazha, M.A.A. and R.J. Crookes, *Design and Operation of a High-Pressure Combustion System for Study of Soot Formation*. 1992.
82. Nazha, M.A.A. and R.J. Crookes, *Design and Operation of a High-Pressure Combustion System for Study of Soot Formation*. 1992, SAE International.
83. Olsen, J., R.J. Crookes, and K.D.H. Bob-Manuel, *Experiments in dual fuelling a compression ignition engine by injecting di-methyl ether as a pilot fuel to ignite varying quantities of natural gas*. 2007.
84. Emberson, D.R., *Diesel fuel and Diesel fuel with Water Emulsions Spray and Combustion Characterization*, in *Department of Engineering and Material Sciences*. 2015, Queen Mary University of London: London.

85. Abdi Aghdam, E., *Wall effect on determination of laminar burning velocity in a constant volume bomb using a quasi-dimensional model*. Applied Mathematical Modelling, 2014. **38**(24): p. 5811-5821.
86. Schott, *TIE-35: Transmittance of optical glass*. 2005.
87. Schott, *TIE-31: Mechanical and Thermal Properties of Optical Glass*. 2004.
88. Doyle, K.B. and M.A. Kahan, *Design strength of optical glass*. Proceedings of SPIE, 2003. **5176 Optomechanics**: p. 14-25.
89. Hoya, *Optical Glass: Specifications*.
90. Schott, *Technical Glasses*, in *Physical and technical properties*. 2010.
91. ISO, *Optics and photonics -- Specification of raw optical glass*. 2010.
92. Weber, M.J., *Handbook of Optical Materials*. 2002: CRC Press.
93. Koenig Spilman, A.K., *Stress-Engineered Optical Elements*. 2007, School of Engineering and Applied Sciences, University of Rochester.
94. Klein, C.A., *Characteristic strength, Weibull modulus, and failure probability of fused silica glass*. Optical Engineering, 2009. **48**(11): p. 113401-113401-10.
95. Detrio, J., D. Iden, F. Orazio, S. Goodrich, and G. Shaughnessy. *Experimental validation of the Weibull area-scaling principle*. in *Proc. 12th DoD Electromagnetic Windows Symp*. 2008.
96. Voloshyn, O.V., L.A. Lytvynov, and E.V. Slyunin, *Potentialities for sapphire strength enhancement*. Functional Materials, 2007. **14**(4): p. 569-569.
97. Ditmars, D.A., S. Ishihara, S.S. Chang, G. Bernstein, and E.D. West, *Enthalpy and Heat-Capacity Standard Reference Material: Synthetic Sapphire Al₂O₃ From 10 to 2250 K*. JOURNAL OF RESEARCH of the National Bureau of Standards, 1982. **87**(2): p. 159-159.
98. Combes, L.S., S.S. Ballard, and K.A. McCarthy, *Mechanical and Thermal Properties of Certain Optical Crystalline Materials*. J. Opt. Soc. Am., 1951. **41**(4): p. 215-221.
99. Harris, D.C. *High-temperature strength of sapphire*. in *International Symposium on Optical Science and Technology*. 2000. International Society for Optics and Photonics.

100. Schmid, F. and D.C. Harris, *Effects of crystal orientation and temperature on the strength of sapphire*. Journal of the American Ceramic Society, 1998. **81**(4): p. 885-893.
101. Icenogle, H.W., B.C. Platt, and W.L. Wolfe, *Refractive indexes and temperature coefficients of germanium and silicon*. Applied Optics, 1976. **15**(10): p. 2348-2351.
102. Duncanson, A. and R.W.H. Stevenson, *Some Properties of Magnesium Fluoride crystallized from the Melt*. Proceedings of the Physical Society, 1958. **72**(6): p. 1001-1001.
103. Laporte, P., J.L. Subtil, M. Courbon, M. Bon, and L. Vincent, *Vacuum-ultraviolet refractive index of LiF and MgF₂ in the temperature range 80--300 K*. Journal of the Optical Society of America, 1983. **73**(8): p. 1062-1069.
104. Jarvis, S., T. Justham, A. Clarke, C. Garner, G. Hargrave, and N. Halliwell. *Time resolved digital PIV measurements of flow field cyclic variation in an optical IC engine*. in *Journal of Physics: Conference Series*. 2006. IOP Publishing.
105. Felton, P.G., J. Mantzaras, D. Bomse, and R. Woodin, *Initial two-dimensional laser induced fluorescence measurements of OH radicals in an internal combustion engine*. 1988, SAE Technical Paper.
106. Konig, G. and C. Sheppard, *End gas autoignition and knock in a spark ignition engine*. 1990, SAE Technical Paper.
107. Scott, W., *Understanding Diesel Combustion Through the Use of High-Speed Moving Pictures in Color*. 1969.
108. Rassweiler, G.M. and L. Withrow, *Motion pictures of engine flames correlated with pressure cards*. 1938, SAE Technical Paper.
109. Rassweiler, G.M. and L. Withrow, *High-speed motion pictures of engine flames*. Industrial & Engineering Chemistry, 1936. **28**(6): p. 672-677.
110. Bowditch, F., *New Tool for Combustion Research A Quartz Piston Engine*. SAE Technical Paper, 1961(610002).
111. Begg, S., D. Mason, and M. Heikal, *Spark ignition and spark-assisted controlled auto-ignition in an optical gasoline engine*. 2009, SAE Technical Paper.
112. Tornatore, C., L. Marchitto, G. Valentino, F. Esposito Corcione, and S.S. Merola, *Optical diagnostics of the combustion process in a PFI SI boosted engine fueled with butanol-gasoline blend*. Energy, 2012. **45**(1): p. 277-287.

113. Lee, S., J.M. McGee, B.D. Quay, and D.A. Santavicca, *A comparison of fuel distribution and combustion during engine cold start for direct and port fuel injection systems*. 1999, SAE Technical Paper.
114. Bates, S.C., *A transparent engine for flow and combustion visualization studies*. 1988, SAE Technical Paper.
115. Fujikawa, T., T. Ozasa, and K. Kozuka, *Development of transparent cylinder engines for schlieren observation*. 1988, SAE Technical Paper.
116. Richman, R. and W. Reynolds, *The development of a transparent cylinder engine for piston engine fluid mechanics research*. 1984, SAE Technical Paper.
117. Namazian, M., S. Hansen, E. Lyford-Pike, J. Sanchez-Barsse, J.B. Heywood, and J. Rife, *Schlieren visualization of the flow and density fields in the cylinder of a spark-ignition engine*. 1980, SAE Technical Paper.
118. Kashdan, J.T. and B. Thirouard, *A Comparison of Combustion and Emissions Behaviour in Optical and Metal Single-Cylinder Diesel Engines*. SAE Int. J. Engines, 2009. **2**(1): p. 1857-1872.
119. Williams, J.G., R.E. Anley, D.H. Nash, and T.G.F. Gray, *Analysis of externally loaded bolted joints: Analytical, computational and experimental study*. International Journal of Pressure Vessels and Piping, 2009. **86**(7): p. 420-427.
120. Bouzid, A.-H., *Comparative study of bolt spacing formulas used in bolted joint designs*. International Journal of Pressure Vessels and Piping, 2014. **120-121**: p. 47-54.
121. Manuccia, T.J., J.R. Peele, and C.E. Geosling, *High temperature ultrahigh vacuum infrared window seal*. Review of Scientific Instruments, 1981. **52**(12): p. 1857-1859.
122. Yoder Jr, P.R., *Mounting Optics in Optical Instruments*. 2008: SPIE Press.
123. Yoder Jr, P.R., *Opto-mechanical systems design*. 2006: SPIE Press.
124. Dunn, G. and J. Stachiw. *Acrylic windows for underwater structures*. in *Underwater Photo Optics I*. 1966. International Society for Optics and Photonics.
125. Dunn, G.M. and J.D. Stachiw, *Acrylic Windows For Underwater Structures*. Proceedings of SPIE, 1966. **0007**: p. 157-168.

126. Abid, M. and D.H. Nash, *A parametric study of metal-to-metal contact flanges with optimised geometry for safe stress and no-leak conditions*. International Journal of Pressure Vessels and Piping, 2004. **81**(1): p. 67-74.
127. BS EN, *13445-3: Unfired pressure vessels - Part3: Design*. 2009.
128. ASME, *ASME Boiler and Pressure Vessel Code, in Section VIII, Division 3*. 2004: New York.
129. Diamantoudis, A.T. and T. Kermanidis, *Design by analysis versus design by formula of high strength steel pressure vessels: a comparative study*. International Journal of Pressure Vessels and Piping, 2005. **82**(1): p. 43-50.
130. Harris, D.C., *Materials for infrared windows and domes: properties and performance*. 1999: SPIE press.
131. Roark, R.J., *Formulas for Stress and Strain*. 1954, New York: McGraw-Hill Book Co Inc.
132. Young, W.C. and R.G. Budynas, *Roark's formulas for stress and strain*. Vol. 7. 2002: McGraw-Hill New York.
133. Fischer, R.E., B. Tadic-Galeb, P.R. Yoder, and R. Galeb, *Optical system design*. 2000: McGraw Hill New York.
134. Hearn, D.R. *Vacuum window optical power induced by temperature gradients*. in *SPIE's International Symposium on Optical Science, Engineering, and Instrumentation*. 1999. International Society for Optics and Photonics.
135. Kingslake, R. and R.B. Johnson, *Lens design fundamentals*. 2009: academic press.
136. Klein, C.A. and J. Pappis, *ZnS, ZnSe, and ZnS/ZnSe windows: their impact on FLIR system performance*. Optical Engineering, 1986. **25**(4): p. 254519-254519-.
137. Lim, T.-C., *Optimal Poisson's ratios for laterally loaded rectangular plates*. Proceedings of the Institution of Mechanical Engineers, Part L: Journal of Materials Design and Applications, 2013: p. 1464420712472634.
138. Lim, T.-C., *Auxetic Materials and Structures*. 2015: Springer.
139. Ashby, M.F., *Materials selection in mechanical design*. 2005, Butterworth-Heinemann, Oxford.

140. Doyle, K.B. and M.A. Kahan. *Design strength of optical glass*. in *Optical Science and Technology, SPIE's 48th Annual Meeting*. 2003. International Society for Optics and Photonics.
141. Vukobratovich, D., *Optomechanical Design Principles*. 1999: CRC Press LLC.
142. Wannenburg, J., G.C. Klintworth, and A.D. Raath, *The use of probability theory in fracture mechanics—A case study*. International Journal of Pressure Vessels and Piping, 1992. **50**(1–3): p. 255-272.
143. Shigley, J.E., R.G. Budynas, and C.R. Mischke, *Mechanical engineering design*. 2004.
144. Hoag, K., *Vehicular engine design*. 2007: Springer.
145. Dabbs, T., B.R. Lawn, and P. Kelly, *Dynamic fatigue study of soda-lime silicate and borosilicate glasses using small scale indentation flaws*. Physics and Chemistry of Glasses, 1982. **23**(2): p. 58-66.
146. Han, L.X. and S. Suresh, *High-Temperature Failure of an Alumina-Silicon Carbide Composite under Cyclic loads: Mechanisms of Fatigue Crack-Tip Damage*. Journal of the American Ceramic Society, 1989. **72**(7): p. 1233-1238.
147. Harrison, C.B. and G.N. Sandor, *High-temperature crack growth in low-cycle fatigue*. Engineering Fracture Mechanics, 1971. **3**(4): p. 403-420.
148. Asoo, B., J. McNancy, Y. Mitamura, and R. Ritchie, *Cyclic fatigue-crack propagation in sapphire in air and simulated physiological environments*. Journal of biomedical materials research, 2000. **52**(3): p. 488-491.
149. Porter, M., *Aspects of structural design with glass*. 2001, University of Oxford.
150. Sglavo, V., M. Gadotti, and T. Micheletti, *Cyclic loading behaviour of soda-lime silicate glass using indentation cracks*. Fatigue & Fracture of Engineering Materials & Structures, 1997. **20**(8): p. 1225-1234.
151. Lawn, B.R., *Fracture of brittle solids*. 1993: Cambridge university press.
152. Hertzberg, R.W., *Deformation and fracture mechanics of engineering materials*. Vol. 89. 1996: Wiley.
153. Sparks, M. and M. Cottis, *Pressure-induced optical distortion in laser windows*. Journal of Applied Physics, 1973. **44**(2): p. 787-794.

154. ISO, *Optics and photonics -- Preparation of drawings for optical elements and systems -- Part 8: Surface texture; roughness and waviness*. 2010.
155. Kimmel, R.K. and R.E. Parks, *ISO 10110 Optics and Optical Instruments: Preparation of Drawings for Optical Elements and Systems: a User's Guide*. 2002: Optical Society of America.
156. Delgado, R. and M. Hallinan, 'Mounting of Lens Elements. *Opt. Eng*, 1975. **14**: p. 11.
157. Yoder Jr, P.R. *Parametric investigations of mounting-induced axial contact stresses in individual lens elements*. in *SPIE's 1993 International Symposium on Optics, Imaging, and Instrumentation*. 1993. International Society for Optics and Photonics.
158. Chen, W. and C. Nelson, *Thermal stress in bonded joints*. *IBM Journal of Research and Development*, 1979. **23**(2): p. 179-188.
159. Timoshenko, S., J. Goodier, and H.N. Abramson, *Theory of elasticity*. *Journal of Applied Mechanics*, 1970. **37**: p. 888.
160. Greivenkamp, J.E., *Field Guide to Geometrical Optics*. Vol. FG01. 2004: Spie Press.
161. Barnes Jr, W.P., *Some effects of aerospace thermal environments on high-acuity optical systems*. *Applied optics*, 1966. **5**(5): p. 701-711.
162. Dudzik, M.C., *Electro-Optical Systems Design, Analysis, and Testing*. Vol. 4. 1993: SPIE Optical Engineering Press.
163. Mackerle, J., *Finite elements in the analysis of pressure vessels and piping, an addendum: A bibliography (2001–2004)*. *International Journal of Pressure Vessels and Piping*, 2005. **82**(7): p. 571-592.
164. Mayer, H., H. Stark, and S. Ambrose, *Review of fatigue design procedures for pressure vessels*. *International journal of pressure vessels and piping*, 2000. **77**(13): p. 775-781.
165. Preiss, R., *Design-by-analysis of a chemical reactor's head under sustained and thermal loads*. *International journal of pressure vessels and piping*, 2000. **77**(6): p. 277-288.
166. Staat, M., M. Heitzer, H. Lang, and K. Wirtz, *Direct finite element route for design-by-analysis of pressure components*. *International Journal of Pressure Vessels and Piping*, 2005. **82**(1): p. 61-67.

167. Hyder, M.J. and M. Asif, *Optimization of location and size of opening in a pressure vessel cylinder using ANSYS*. Engineering Failure Analysis, 2008. **15**(1-2): p. 1-19.
168. Chattopadhyay, S., *Pressure Vessels: Design and Practice*. 2005: CRC Press LLC.
169. Spence, J. and D.H. Nash, *Milestones in pressure vessel technology*. International Journal of Pressure Vessels and Piping, 2004. **81**(2): p. 89-118.
170. Nash, D. and M. Abid, *Combined external load tests for standard and compact flanges*. International journal of pressure vessels and piping, 2000. **77**(13): p. 799-806.
171. Nadarajah, C. and L. Foo, *Finite element study of keyed backing ring design for floating head*. International journal of pressure vessels and piping, 1998. **75**(6): p. 521-526.
172. Edmund Optics. *Technical Information*. 2010 [cited 2010 /07/17]; Available from: <http://www.edmundoptics.co.uk/optics/optical-mirrors/flat-mirrors/quarter-wave-first-surface-mirrors/1927>.
173. Sigma-Aldrich. *Technical Documents*. 2010 [cited 2010 /07/17]; Available from: <http://www.sigmaaldrich.com/united-kingdom/technical-services/datasheets.html>.
174. BOC. *Safety Data Sheets*. 2010 [cited 2010 /07/17]; Available from: <http://www.boconline.co.uk/en/sheq/safety-data-sheets/index.html>.
175. Autodesk. *Inventor*. 2010; Available from: www.autodesk.co.uk.
176. Dassault Systems. *SolidWorks 3D CAD Software*. 2011; Available from: <http://www.solidworks.co.uk/>.
177. Agrira, A., D.R. Buttsworth, and T. Yusaf. *Instantaneous heat flux simulation of SI engines: comparison of unsteady thermal boundary layer modelling with experimental data*. in *Energy and Environment, 2009. ICEE 2009. 3rd International Conference on*. 2009. IEEE.
178. Finol Parra, C., *Heat transfer investigations in a modern diesel engine*. 2008, University of Bath.
179. Agrira, A.I.A., *Internal combustion engine heat transfer-transient thermal analysis*. 2012, University of Southern Queensland.

180. Chana, K., T. Wilson, P. Bryanston-Cross, M. Burnett, and T. Jones, *High bandwidth heat transfer measurements in an internal combustion engine under low load and motored conditions*. 2003, DTIC Document.
181. Qi, B., N. Tessier-Doyen, and J. Absi, *Young's modulus evolution with temperature of glass/andalusite model materials: Experimental and numerical approach*. Computational Materials Science, 2012. **55**(0): p. 44-53.
182. Wenning, L., S. Xin, and K. Moe, *Behavior of Aging, Micro-Void, and Self-Healing of Glass/Ceramic Materials and Its Effect on Mechanical Properties*. Advances in Ceramics - Characterization, Raw Materials, Processing, Properties, Degradation and Healing. 2011.
183. Bright, D.S., D.E. Newbury, and E.B. Steel, *Visibility of objects in computer simulations of noisy micrographs*. Journal of Microscopy, 1998. **189**: p. 25-42.
184. Rose, A., *Television pickup tubes and problem of vision*. Advances in Electronics, 1948. I: p. 131-166.
185. Smith, S.W., *The scientist and engineer's guide to digital signal processing*. 1997.
186. Gross, H., H. Zügge, M. Peschka, and F. Blechinger, *Aberration Theory and Correction of Optical Systems, volume 3 of Handbook of Optical Systems*. 2007, Wiley-VCH.
187. Sasián, J., *Introduction to aberrations in optical imaging systems*. 2013: Cambridge University Press.
188. Russ, J.C., *The Image Processing Handbook*. 1999: CRC Press.
189. Whybrew, A., *D.2.7. High Speed Imaging*, in *Handbook of Laser Technology and Applications: Laser design and laser systems*, C.E. Webb and J.D. Jones, Editors. 2004, CRC Press.
190. West, P., *High Speed, Real-Time Machine Vision*. 2001.
191. Gonzalez, R.C. and P. Wintz, *Digital Image Processing*. 1987: Addison-Wesley.
192. Mulchrone, K.F. and K.R. Choudhury, *Fitting an ellipse to an arbitrary shape: implications for strain analysis*. Journal of Structural Geology, 2004. **26**(1): p. 143-153.
193. Ji, Q., M.S. Costa, R.M. Haralick, and L.G. Shapiro, *A robust linear least-squares estimation of camera exterior orientation using multiple geometric features*. ISPRS Journal of Photogrammetry and Remote Sensing, 2000. **55**(2): p. 75-93.

194. Jähne, B., *Digital Image Processing: Concepts, Algorithms, and Scientific Applications*. 1997: Springer-Verlag.
195. Jain, A.K., *Fundamentals of Digital Image Processing*. 1989: Random House.
196. Anderson, T.W., *Multivariate Statistical Analysis*. 1984: John Wiley.
197. Vison Research. *Software: Cine Viewer*. 2014; Available from: <http://www.visionresearch.com/Service--Support/Downloads/Software/>.
198. Rasband, W., *ImageJ*. 2014, National Institutes of Health: USA.
199. Barford, N.C., *Experimental Measurements: Precision, Error and Truth*. 1994: John Wiley and Son.
200. Korakianitis, T., R. Dyer, and N. Subramanian, *Pre-integrated nonequilibrium combustion-response mapping for gas turbine emissions*. *Journal of engineering for gas turbines and power*, 2004. **126**(2): p. 300-305.
201. Dyer, R. and T. Korakianitis, *Pre-integrated response map for inviscid propane-air detonation*. *Combustion Science and Technology*, 2007. **179**(7): p. 1327-1347.
202. Sazhin, S.S., G. Feng, M.R. Heikal, I. Goldfarb, V. Goldshtein, and G. Kuzmenko, *Thermal ignition analysis of a monodisperse spray with radiation*. *Combustion and Flame*, 2001. **124**(4): p. 684-701.
203. Ranzi, E., A. Frassoldati, R. Grana, A. Cuoci, T. Faravelli, A.P. Kelley, and C.K. Law, *Hierarchical and comparative kinetic modeling of laminar flame speeds of hydrocarbon and oxygenated fuels*. *Progress in Energy and Combustion Science*, 2012. **38**(4): p. 468-501.
204. Veloo, P.S., Y.L. Wang, F.N. Egolfopoulos, and C.K. Westbrook, *A comparative experimental and computational study of methanol, ethanol, and n-butanol flames*. *Combustion and Flame*, 2010. **157**(10): p. 1989-2004.
205. Ciatti, S.A., T. Wallner, H. Ng, W.F. Stockhausen, and B. Boyer. *Study of combustion anomalies of H₂-ICE with external mixture formation*. in *ASME 2006 Internal Combustion Engine Division Spring Technical Conference*. 2006. American Society of Mechanical Engineers.
206. Lee, S., H. Yi, and E. Kim, *Combustion characteristics of intake port injection type hydrogen fueled engine*. *International Journal of Hydrogen Energy*, 1995. **20**(4): p. 317-322.

207. Sierens, R. and E. Rosseel, *Backfire mechanism in a carburetted hydrogen fuelled engine*. HYDROGEN ENERGY PROGRESS XII, VOLS 1-3, 1998: p. 1537-1546.
208. Verhelst, S. and T. Wallner, *Hydrogen-fueled internal combustion engines*. Progress in Energy and Combustion Science, 2009. **35**(6): p. 490-527.
209. Aleiferis, P.G. and M.F. Rosati, *Flame chemiluminescence and OH LIF imaging in a hydrogen-fuelled spark-ignition engine*. International Journal of Hydrogen Energy, 2011. **37**(2): p. 1797-1812.
210. Meier, F., J. Köhler, W. Stolz, W.H. Bloss, and M. Al-Garni, *Cycle-Resolved Hydrogen Flame Speed Measurements with High Speed Schlieren Technique in a Hydrogen Direct Injection SI Engine*. SAE Technical Paper, 1994(942036).
211. Kirchweger, W., R. Haslacher, M. Hallmannsegger, and U. Gerke, *Applications of the LIF method for the diagnostics of the combustion process of gas-IC-engines*. Experiments in Fluids, 2007. **43**(2-3): p. 329-340.